Journal of Earth Observation and Geospatial Applications

Volume 1, Number 1 October 2025

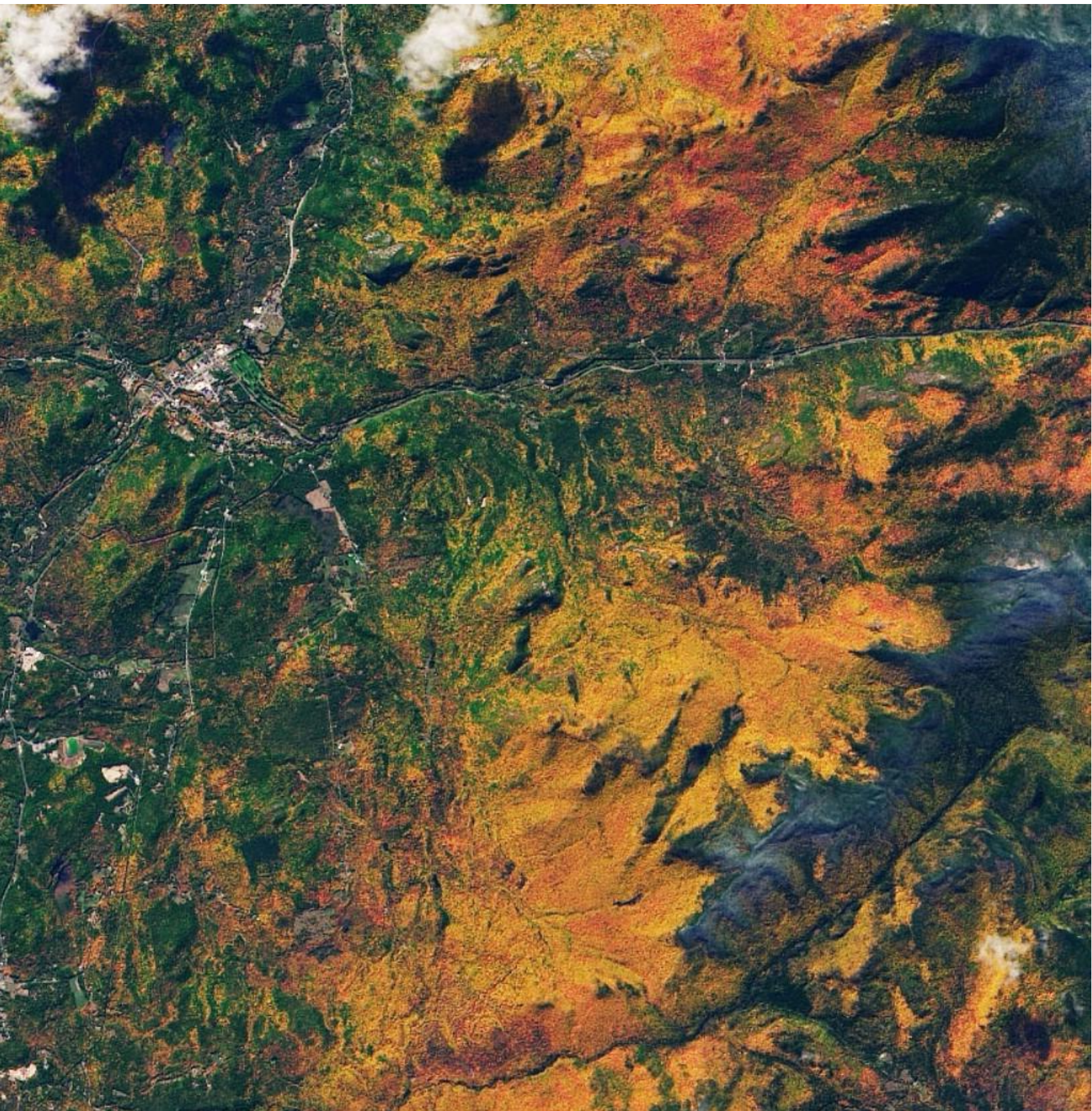

FORWARDS

Christopher McGinty
Executive Director
AmericaView

AmericaView is a nationwide, university-based network that promotes Earth observation education, research, and practical applications for communities, agencies, and industry.

I am pleased to announce the new AmericaView-sponsored Journal of Earth Observation and Geospatial Applications (JEOGA), which expands the AmericaView mission by offering a platform for young researchers to publish their Earth observation and remote sensing work alongside their mentors. The journal will highlight studies that help inform decision-makers while enhancing authors' research and writing skills through peer reviews and editorial standards. JEOGA will strengthen the pathways from education to practice by sharing methods, datasets, and providing valuable input on key issues across the United States and around the world.

To learn more about AmericaView and JEOGA, please visit the AmericaView website (https://AmericaView.org).

Dr. Donna M. Delparte
Chair, Board of Directors
AmericaView

It is my privilege to introduce this edition of the Journal of Earth Observation and Geospatial Applications, a publication that reflects AmericaView's vision of "Empowering Earth Observation Education." As a nationwide consortium, AmericaView brings together a collaborative network of remote sensing scientists, educators, students, and industry leaders who are contributing to innovations in Earth observation.

The articles in this issue demonstrate the diverse applications of remote sensing to advance knowledge. Featured case studies explore the use of Earth observation data in analyzing urban heat island effects, monitoring land cover dynamics, and mapping fluvial terraces. Additionally, a best-practices article offers insights into the challenges and solutions of earth observation technology for emergency management.

On behalf of the AmericaView Board of Directors, I extend sincere appreciation to our authors, reviewers, and the editorial team for their contributions and commitment. This journal not only showcases the depth of expertise within the AmericaView network but also highlights the dedication of our emerging scientists and educators who carry our mission forward. Together, as exemplified by articles in this issue, we strive to expand the power of remote sensing by transforming knowledge into action for the benefit of our nation and the global community.

EDITORIAL NOTES

Dr. Jeong Chang Seong
Chief Editor, JEOGA
University of West Georgia

It is with great pleasure that we introduce the inaugural issue of the Journal of Earth Observation and Geospatial Applications (JEOGA). This first volume features nine original research papers spanning diverse themes—from evapotranspiration and vegetation dynamics to urban heat islands, geomorphic mapping, biomass estimation, drought assessment, and the use of Earth observation for emergency management. Collectively, these studies showcase the power of geospatial science to reveal patterns and processes that shape our changing planet. They examine vegetation and hydrological correlations in Colorado, restoration effects in Maryland, seasonal greenness shifts in the Great Smoky Mountains, urban heat disparities in Louisiana and Colorado, terrace mapping in Georgia, urban biomass modeling in Texas, drought patterns across the U.S. Corn Belt, and NASA's efforts to enhance emergency management applications. Together, these contributions advance our understanding of environmental change and demonstrate how remote sensing continues to transform Earth science, workforce development, and applied research.

We extend our deepest gratitude to the authors for their outstanding scholarship and dedication to this first issue. We also sincerely thank AmericaView for their steadfast support of this endeavor, as well as our nine editors, copyeditors, and layout editors whose meticulous efforts made this publication possible. Our appreciation also goes to the University of West Georgia's Office of Research and Sponsored Projects (ORSP), Information Technology Services (ITS), and the Ingram Library for their invaluable institutional and technical support. The promotion of research, writing, and workforce development in the geospatial STEM disciplines is essential to fostering innovation and resilience in a rapidly changing world. We also acknowledge the ongoing contributions of U.S. Geological Survey, NASA, and NOAA in monitoring Earth's dynamic natural systems through satellite imagery—tools that underpin much of the work presented here. Looking ahead, JEOGA aims to publish at least two issues each year, continuing to serve as a platform for advancing geospatial science, workforce training, and environmental research for the public good.

October 2025
Volume 1, Number 1

Journal of Earth Observation and Geospatial Applications

Research Article

Analysis of ET and NDVI Correlation in Different Land Cover Types of Colorado

Zhibin Sun[1,2], Runqing Liu[2], Kate Laidlaw[1,3], Maosi Chen[1] and Wei Gao[1,3,*]

[1] United States Department of Agriculture UV-B Monitoring and Research Program, Natural Resource Ecology Laboratory, Colorado State University, Fort Collins, Colorado 80521 USA; zhibin.sun@colostate.edu (Z.S.), kate.laidlaw@colostate.edu (K.L.), maosi.chen@colostate.edu (M.C.), wei.gao@colostate.edu (W.G.)

[2] School of Mathematical Sciences, Ministry of Education Key Laboratory of NSLSCS, Nanjing Normal University, Nanjing, Jiangsu 210023, China; zhibin.sun@njnu.edu.cn (Z.S.), 220902056@njnu.edu.cn (R.L.)

[3] Department of Ecosystem Science and Sustainability, Colorado State University, Fort Collins, Colorado 80523 USA; kate.laidlaw@colostate.edu (K.L.), wei.gao@colostate.edu (W.G.)

[*] Corresponding Author: wei.gao@colostate.edu; +1-970-491-3609.

Academic Editor: Carter Wang
Received: 21 May 2025
Revised: 28 July 2025; 30 July 2025
Accepted: 31 July 2025
Published: 24 October 2025

Abstract: Climate change and water scarcity are pressing public concerns, severely impacting agricultural production and ecological balance. Leveraging advanced remote sensing, this study analyzed 30m-resolution Landsat normalized difference vegetation index (NDVI) and evapotranspiration (ET) data during Colorado's growing seasons (April–August) from 2000 to 2018. Examining correlations across various land cover types, it detailed data processing, relation analysis at different lead times, and correlation classification. Results show a mostly positive correlation in Colorado, aligning with coarser-resolution studies, with some negative exceptions. Uniquely, ET's influence on NDVI weakens as lead time extends, regardless of correlation. Combining with land cover analysis, forests with high water storage maintain stable ET. Additionally, human intervention significantly affects these correlations.

Keywords: Landsat, NDVI, ET, land cover, Colorado

1. Introduction

Plant production is a function of many variables. Besides obvious factors like sunlight and precipitation, plant growth is also affected by other variables like soil moisture, surface temperature, and evapotranspiration. Plants of all species can exhibit metabolic responses to extremes in moisture and even temperature, not just sunlight. Briggs *et al*. (1995) highlighted that the majority of interannual variations in net primary productivity (NPP) cannot be explained solely by a single factor, such as precipitation. This finding aligns with the concept that the NPP patterns in high grassland ecosystems are a result of both spatial and temporal fluctuations in light, water, and nutrients.

The normalized difference vegetation index (NDVI) is a widely used metric for assessing Earth's vegetation (Crow *et al*., 2012). It is robust, versatile, and easy to interpret. Regardless of vegetation type, NDVI shows a strong correlation with ground observations. It is versatile across various fields. NDVI values range from −1 to 1, with 0 representing a vegetation-free region. As vegetation abundance and vitality increase, NDVI increases over time or space. A maximum NDVI of 1.0 indicates dense, healthy vegetation. Values below zero indicate the absence of terrestrial vegetation, and a lake or ocean exhibits an NDVI of −1.

The NDVI exhibits a correlation with vegetation biomass, making it a useful proxy for assessing habitat quality across a wide range of species where ground-based observational data is lacking. However, the accuracy of NDVI may be limited in sparsely vegetated arid and semi-arid environments due to signal contamination from substrate reflectance (Formica *et al*., 2017). Numerous studies have indicated a linear relationship between NDVI and NPP or aboveground net primary productivity (ANPP) under specific conditions. Multiple investigations have demonstrated a positive correlation between NDVI derived from AVHRR/NOAA satellite data and biomass or annual ANPP in different geographical regions and ecosystems

Citation: Sun, Z., Liu, R., Laidlaw, K., Chen, M., & Gao, W. (2025). Analysis of ET and NDVI correlation in different land cover types of Colorado. *Journal of Earth Observation and Geospatial Applications, 1*(1), 1–20. DOI: https://doi.org/10.65372/4z6zq224

(Paruelo *et al*., 1997). Strong correlations were observed between NDVI and annual ANPP at five study sites in cumulative growing season (i.e., from May to September), suggesting that NDVI can serve as an alternative indicator for ANPP. In the Great Plains region of the United States, the correlation between county-level accumulated actual evapotranspiration (AET) from April to July, and ANPP was higher than that with precipitation, especially in dry areas. After considering the ratio of AET to potential evapotranspiration (PET), the correlation was improved with integrated NDVI (iNDVI) and county-level NRCS ANPP (Chen *et al*., 2019). In addition, Zeng *et al*. (2013) has found that precipitation and temperature are powerful controlling factors for NDVI variability, exhibiting distinct spatial patterns.

Evapotranspiration (ET), a variable influencing plant growth and crop production, is poorly understood and difficult to calculate directly. It is the combination of two key parts of water cycle: evaporation and transpiration. ET is the conversion of liquid water to water vapor from land surfaces, water body surfaces, and plant stomata, so it represents a loss of usable water from plants. Therefore, high ET rates are a limit on plant growth. Variables contributing to ET include latent heat flux, sensible heat flux, ground heat flux, relative humidity, wind, temperature, and solar radiation (Rocha *et al*., 2020). Areas with high ET are mainly arid, sunny, and windy, such as the Great Plains of the United States and entire Colorado. ET is a key variable of the hydrologic cycle and agricultural water demand, especially in arid and semi-arid places like Colorado.

In the Great Plains region of the United States, the cumulative AET and transpiration (Tr) from April to July are closely associated with annual ANPP, particularly in arid areas, where AET and Tr show a stronger correlation with ANPP compared with precipitation. In more humid regions, the accumulated precipitation from April to July exhibits the highest interannual variation in relation to ANPP (Chen *et al*., 2019). It has been found that late July is the optimal period for predicting ANPP using NDVI, with a Pearson correlation coefficient of 0.86. A linear model called TAM (tallgrass ANPP model) was developed, confirming the linear association between ANPP and NDVI (An *et al*., 2013). In addition, by studying the relationship between various variables related to water changes and plant growth, one can gain a deeper insight into the consequences arising from water scarcity and climate change (Mukheibir *et al*., 2010), thereby formulating more efficient agricultural development strategies (Nikolaou *et al*., 2020).

Grassland ANPP is strongly influenced by the amount and distribution of annual precipitation (PPT) (Sala *et al*., 1988). The magnitude and direction of precipitation changes associated with climate change are highly uncertain, leading to uncertainties in ecosystem responses. Periods with above or below-average rainfall over multiple years may indicate consequences of changing precipitation conditions. Long-term data on ANPP and PPT were compiled for eight North American grasslands, quantifying the relationships between ANPP and PPT during the periods of above and below-average rainfall, applicable to temperate, semi-arid cool, and semi-arid warm grassland types (Petrie *et al*., 2018). On the other hand, understanding the dynamics of the global carbon cycle relies on the functional relationship between PPT and NPP (Wilcox *et al*., 2016).

As a categorical variable, land cover has a significant impact on ET and NDVI. Accurate information regarding land cover is crucial for the study of global change. In the past decade, data sources and methods for creating global land cover maps through remote sensing have rapidly advanced. The National Land Cover Database (NLCD) is an extensive resource that provides comprehensive nationwide data on land cover and land cover change in the United States. It utilizes a 30-meter resolution and follows a 16-class legend based on the modified Anderson Level II classification system. The version of NLCD used in this study (i.e., NLCD 2019) focuses on delivering innovative information on land cover and land cover change for the entire country (Dewitz *et al*., 2021; Wickham *et al*., 2021; Homer *et al*., 2020; Jin *et al*., 2019; Yang *et al*., 2018). It includes eight integrated epochs of land cover data, spanning the years of 2001, 2004, 2006, 2008, 2011, 2013, 2016, and 2019. The developed classes for these years are derived directly from the percentage of developed impervious surface and are accompanied by descriptor labels that specify the type of impervious surface found in each image pixel. Appendix A provides specific information on land cover in Colorado.

Moreover, research has revealed that global water resources are significantly impacted by human interventions (Haddeland *et al*., 2014). For example, human activities led to an 11%–16% increase in evapotranspiration over the Yellow River between 2003 and 2010 (Zhang *et al*., 2020).

The Great Plains region of the United States serves as a vital agricultural production hub in the global market and constitutes a significant source of greenhouse gas emissions (Parton *et al*., 2015). In spite of its arid and highly variable climate, Colorado is a key state for agricultural production in the United States. Livestock, especially cattle along with alfalfa, sugar beets, corn, melons, peaches, apples, and wheat are the most important parts of Colorado's agriculture industry (USDA/NASS, 2021). However, drought is one of the most devastating afflictions on agricultural success, sustainability, and production in Colorado (Bauman *et al*., 2013). Drought conditions persist almost continually throughout the state, with scarce periods where

some regions are not affected to some extent (McKee *et al*., 2000). Droughts are usually accompanied by extremely high temperatures (Hood *et al*., 2020), adding stresses to plants. The changing climate is likely to decrease water availability and agricultural yields in Colorado (What Climate Change Means for Colorado, 2016). As a result, this study was undertaken in order to investigate what and if any effects ET have on agricultural plant growth in Colorado.

To investigate the impact of ET or cumulative ET (cu ET) on NDVI and its variation across different land types, thereby shedding light on the close relationship between water availability and agriculture, this study incorporates three variables: ET, NDVI, and land cover.

Long-term datasets, which are essential for advancing research in ecology and guiding agricultural production, offer vital information for ecosystem management and evidence-based policymaking at appropriate scales (Lindenmayer *et al*., 2012). For example, Joiner *et al*. (2018) utilized long-term ET and NDVI data from 2003 to 2016 to conclude that ET generally exhibits a quicker response to water deficits and enhancements compared with NDVI. Using a similar length of the above time span, this study explores the relationship between ET and NDVI across diverse land cover types in the region within the growing seasons from April to August between 2000 and 2018.

ET and NDVI are hard to measure since it depends on so many variables that can extremely change over spatiotemporal scales. Additionally, monitoring any hydro-meteorological in-situ variable requires expensive sensors and frequent maintenance. Consequently, satellite remote sensing has emerged as an effective way to obtain these kinds of data worldwide, fill in data coverage gaps since sensors cannot be installed everywhere, and calibrate in-situ physical sensors. National Aeronautics and Space Administration (NASA) and United States Geologic Survey's (USGS) Landsat mission is the longest-lasting continuous remote sensing survey of the Earth's surface. It provides trustworthy geospatial raster data in the form of tagged image file format (TIFF or TIF) at fine resolutions with extensive, informative metadata at the levels of understanding ranging from professional to amateur. These factors make Landsat data trustworthy and frequently used in geographic information systems (GIS). In addition, the relationship between NDVI and ANPP is linear for the data obtained from NOAA/AVHRR and Landsat TM (Paruelo *et al*., 2000).

2. Data and Methodology

In this study, ET and NDVI data are sourced from NASA's USGS Landsat mission and are treated as temporally continuous variables, renowned for its impressive 30m resolution. There are some limitations for both data. For example, (1) there are missing values in some areas; (2) some pixels are contamination by clouds/rain/snow, and (3) there are overlapping pixels at scene boundaries for the same acquisition date. We selected the data sets spanning from the year 2000 to 2018, specifically focusing on the growing seasons of each year, from April to August. The land cover data, obtained from the National Land Cover Database (NLCD), encompasses the entire state of Colorado and comprises only 16 land cover types. Consequently, the land cover data is treated as a categorical variable with 16 categories, as presented in Table A1 in Appendix A. The specific information for all variables is detailed in Table 1. The download process for all variables started on EarthExplorer with setting Colorado as the predefined area.

Table 1. Data sources and resolution characteristics of satellite products.

Variable	Dataset	Data Source/ Landsat Mission/ Sensor	Spatial Resolution	Temporal Resolution
ET	Landsat C2 Level-2 (L2)	Landsat 7 and 8 (ETM+, OLI/TIRS) C2 L2	30m	about half monthly
NDVI	Landsat C2 Level-2 (L2)	Landsat 7 and 8 (ETM+, OLI/TIRS) C2 L2	30m	about half monthly
Land Cover	Landsat Collection 2 (C2) U.S. Analysis Ready Data (ARD)	Landsat 7 and 8 (ETM+, OLI/TIRS) C2 L2	30m	2001, 2004, 2006, 2008, 2011, 2013, 2016, 2019

Each variable exhibits distinct spatial and temporal distributions, reflecting changes over space and time. To uncover the relationships among these variables, it is necessary to firstly process the downloaded raw remote sensing data. The data processing techniques, as shown in Figure 1, take into account the temporal and spatial characteristics of the raw data, enabling the establishment of the linear relationship between ET

and NDVI. This processing facilitates the analysis of correlations and potential influences across different land covers. Initially, the linear relationships are examined following spatial and temporal alignment and interpolation. Moreover, specific land types are selected to study the correlation between ET and NDVI, allowing for a focused analysis of their relationship within a specific area. All programs were executed using MATLAB R2022a on two Intel Xeon Silver 4215 CPUs. The computer has 128GB of memory.

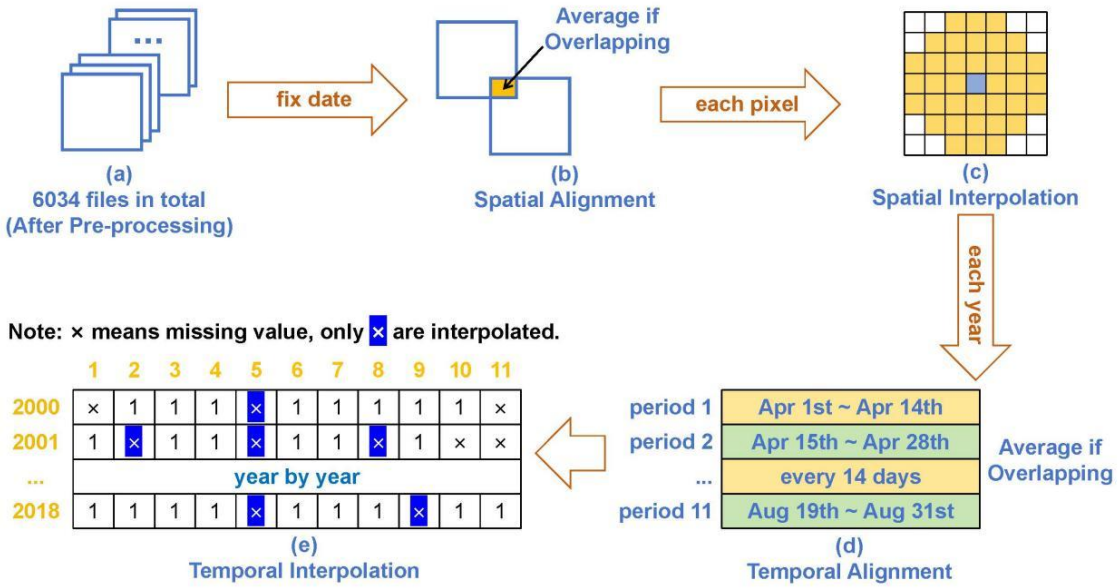

Figure 1. Data Processing Workflow. (a) Preprocess the downloaded data and convert a ".tif" file into ". mat" format compatible with MATLAB. (b) When a fixed date is considered, there may be multiple valid values in a pixel within the yellow area. The average value is taken as the value at that pixel. (c) Illustration of Spatial Interpolation. The blue square represents a pixel requiring interpolation, indicating its original missing values. The yellow squares represent the area involved in interpolating the pixel at the blue square. Each pixel has a resolution of 30 meters, and these yellow squares encompass a radius of 100 meters around the pixel requiring interpolation. (d) From April 1st to August 31st, there are a total of 153 days, divided into 11 periods of 14 days each, starting from April 1st. This may result in a pixel having multiple values within the same period. The average of these values is taken as the value of the pixel for that period. (e) Linear interpolation is performed on an annual basis, excluding the missing values only during the periods between years, as the last period of one year and the first period of the following year have a substantial time gap.

The detailed processing method represented by Figure 1 is outlined as follows:

1) Pre-processing (Figure 1a)
   - 1.1) Remove pixel values affected by cloud, cloud shadow, and snow from the QA_pixel dataset (in Landsat product) and set them to NaN.
   - 1.2) Based on the vertex coordinates in the source data, delineate the areas captured by the satellite images, primarily to distinguish NaN values originating from blank edges or remote sensing algorithms.
2) Spatial Alignment (Figure 1b)
   - 2.1) Extract dates and UTM projection zones from 6034 files, categorize them, and generate all possible combinations of dates and zones.
   - 2.2) Read all combinations, iterate through each spatial coordinate in the zones, and examine the uniqueness of variable values within all files in that combination.
   - 2.3) If all values at the same coordinate across files are NaN, assign NaN as the value for that coordinate. Otherwise, calculate the average of all non-NaN values at the coordinate as the pixel value.
   - 2.4) Based on the combinations of dates and zones, derive the final outcome associated with dates and zones.

3) Spatial Interpolation (Figure 1c)
   3.1) Identify the date and zone, read the results from the previous step, and perform spatial interpolation.
   3.2) As depicted in Figure 1c, for each pixel (blue pixel), compute the average of all valid values (i.e., yellow pixels) within a circle of 90-meter radius.
   3.3) If all values at the same coordinate across files are NaN, assign NaN as the value for that coordinate. Otherwise, calculate the average of all non-NaN values as the pixel value at that location.
   3.4) The interpolated results are linked to the date and zone.
4) Temporal Alignment (Figure 1d)
   4.1) Divide each year from April to August into periods of two weeks (14 days), resulting in 11 periods per year.
   4.2) Determine the year and period, and retrieve all files within the specified time range.
   4.3) If all values at the same coordinate across files are NaN, assign NaN as the value for that coordinate. Otherwise, calculate the average of all non-NaN values as the pixel value at that location.
   4.4) Iterate through different years and periods to obtain final results.
5) Temporal Interpolation (Figure 1e)
   5.1) Fix the year and spatial coordinates, examine the values of the corresponding pixels across 11 periods, sorted chronologically.
   5.2) For each period, perform linear interpolation if non-NaN values are present both before and after that period.
   5.3) Ultimately, results are obtained for different years and periods.

2.1. Preprocessing of Raw Data

The datasets preprocessed in this study consist of two variables: ET and NDVI. Both variables exhibit the same spatial and temporal distribution. Therefore, in order to explain the data processing methodology, we will focus on elucidating the approach using the ET variable. Our data processing approach follows a two-step principle: first, focusing on maximizing the utilization of raw data (i.e., fine-grained processing), and then employing a coarser approach that involves merging overlapping data and performing interpolation (i.e., rough-grained processing). The data processing is carried out in a sequential order, prioritizing spatial considerations before temporal aspects.

Taking the ET variable as an example, we obtained a total of 6034 products from the EarthExplorer website (https://earthexplorer.usgs.gov/) based on the metadata. These products covered the period from 2000 to 2018, specifically from April to August of each year, and were located in different spatial and temporal contexts. The downloaded products had a resolution of 30m and provided information about variable value, pixel quality, and coordinate information for each pixel. To prepare the raw data for further analysis, we performed preprocessing, which involved two steps: removing pixels with bad quality and annotating the valid measurement areas.

In the raw data, certain pixels were affected by factors such as clouds, cloud shadows, and snow, resulting in poor quality. To address this, we utilized the QA_pixel product, where "QA" stands for Quality Assessment. By referring to this product, we identified and removed pixels that were affected by cloud, cloud shadow, and snow. This process involved replacing the values of these pixels with missing values, effectively excluding them from subsequent analyses.

Additionally, we observed that the actual measurement areas of the products differed from the entire represented regions. Upon visual examination of products, we identified missing values within the actual measurement area, which corresponds to a rectangular-like region in the image, as well as the region outside the actual measurement area. We refer to the actual measurement area as the valid region, while the rest is considered invalid. During subsequent spatial interpolation, it is crucial to exclude the invalid regions from the interpolation process. Therefore, our first step was to annotate the valid and invalid regions of the products. The metadata files provided the latitude and longitude coordinates of the vertices that defined the actual measurement area for each product. By utilizing these coordinates, we constructed a quadrilateral in the latitude and longitude coordinate system and labeled the boundaries and interior of the quadrilateral as the valid region, while the exterior was labeled as the invalid region. This labeling process is illustrated in Figure 2, where the left image represents the annotated result, with the yellow color indicating the valid region and

the blue color representing the invalid region. The consistency between the annotated valid region and the right image confirms the accuracy of our labeling approach.

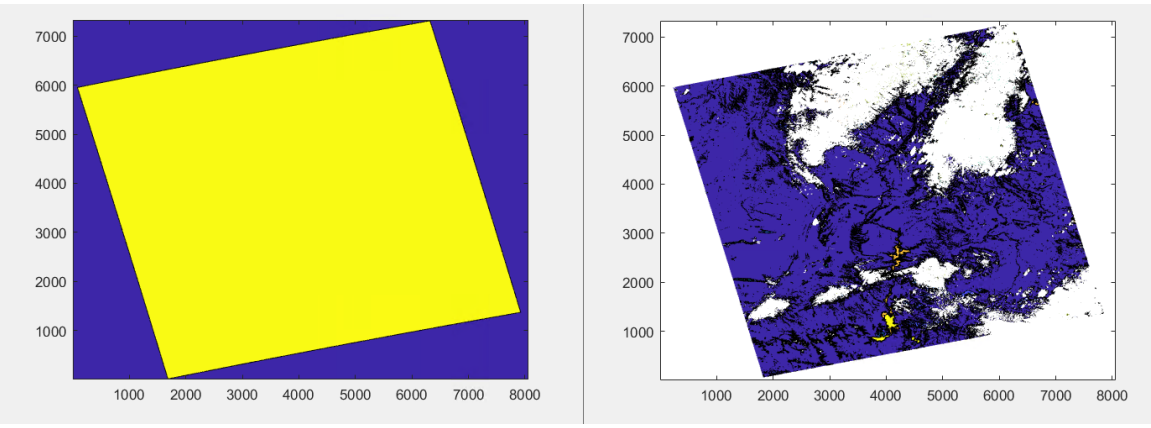

Figure 2. Illustration of the annotated valid region for a specific .tif product. An image from a randomly selected tile on a particular day was chosen as an example for annotating the valid region. In the left image, the yellow area represents the valid region, while the blue area represents the invalid region. The right image shows the white area indicating missing values, and it is noticeable that there is a substantial block of missing values outside the edges of the valid region.

2.2. Spatial Alignment and Interpolation

Within a given day, a product may consist of multiple tiles, and upon comparison, overlapping areas between adjacent tiles can be identified. In these overlapping regions, pixels representing the same geographic coordinates may possess values derived from at least two distinct tiles. On a given date, variations in the time of image acquisition (including hour, minute, and second) and disparities resulting from the utilization of different algorithms to calculate satellite variables using diverse raw data can potentially lead to multiple distinct values for the same variable at a specific pixel within the same day. As shown in Figure 1b, disregarding invalid values, we compute the average of these divergent data values to determine the pixel value, thereby ensuring a more representative and reliable estimate of the variable's value for further analysis and interpretation.

Upon processing the overlapping areas, it can be observed from Figure 2 that numerous missing values exist within valid regions. To ensure the data reflects the overall characteristics of the entire area, spatial interpolation is conducted on the regions with missing values. Let $X_{date} = \left(x_{date}^{(location)}\right)$ represents all variable values on the same date, with location fixed. Let $N^{(location)} = \{neighbour \mid 0 < distance(location, neighbour) < 100\ \text{m}\}$ denotes all locations within 100 meters of the given location. For each location, compute

$$y_{date}^{(location)} = mean\,\{x_{date}^{(neighbour)} \mid neighbour \in N^{(location)}\}, \tag{1}$$

resulting in $Y_{date} = \left(y_{date}^{(location)}\right)$. Let $M_{date} = \left(m_{date}^{(location)}\right)$ be the mask for X_{date}: if there is a value at $x_{date}^{(location)}$, then $m_{date}^{(location)} = 1$; otherwise, $m_{date}^{(location)} = 0$.

After interpolation, the interpolated X^* is given by Equation (2) where $\odot$ represents the Kronecker product.

$$X^* = X + Y \odot (1 - M) \tag{2}$$

As depicted in Figure 1c, we perform interpolation at the center blue pixel by taking the average of all valid values (i.e., yellow pixels) within a radius of 100 meters. This interpolation expands the area with available values while preserving the similarity of values in neighboring regions. During the interpolation process, only the data after handling the overlapping areas is utilized, and no additional spatial interpolation

data is employed. Consequently, some missing values still exist within the valid regions after the completion of spatial interpolation. Due to inadequate satellite data and models for computing these missing values, we consider them as genuinely missing and therefore do not subject them to further spatial interpolation.

2.3. Temporal Alignment and Interpolation

As depicted in Figure 1d, considering an average of approximately two data points per month for each pixel, we conducted temporal interpolation by partitioning the time into discrete 14-day periods and consolidating data from different dates within the same period. The analysis focused on utilizing data from April to August, encompassing the years from 2000 to 2018. Specifically, each year from April 1st to August 31st, totaling 153 days, was divided into 11 periods of 14 days. After considering valid values, the pixel value was assigned as the mean value across different dates within the same period.

Then, we performed linear interpolation for each of the 11 periods, progressing year by year. Let $X_{year}^{(location)} = \left(x_{year,period}^{(location)}\right)$ denotes all variables for a certain location within a given year across all periods. For each location and year, linear interpolation was applied from the first non-missing period to the last valid period. If $x_{year,period}^{(location)}$ was missing, interpolation was performed via

$$x_{year,period}^{(location)} = (1-\alpha)x_{year,period_0}^{(location)} + \alpha x_{year,period_1}^{(location)}, \quad (3)$$

where $\alpha = \frac{period - period_0}{period_1 - period_0}$. Here, $period_0$ and $period_1$ denote the periods to which the nearest valid values preceding and following the missing value belong, respectively. As illustrated in Figure 1e, linear interpolation was applied for areas where the first and last valid values of each year were present. However, no interpolation was conducted for the regions where there were no valid values at the beginning or end of the time period.

2.4. ET Control on NDVI

Previous studies have identified the controlling effect of precipitation on NDVI (Zeng *et al*., 2013), indicating a potential lagged relationship between precipitation and NDVI (Joiner *et al*., 2018). To further investigate this mechanism, this study introduces a variable called Lead, varying from 0 to 9. This involves comparing ET data and NDVI data within same periods, with ET data leading by Lead periods respectively. Pearson correlation coefficients are calculated, and the proportion of significant correlations ($p<0.05$) is determined.

After performing spatial and temporal alignment and interpolation on the data, for each pair of longitude and latitude, we obtain a column of time-related data $\{x_{year,period}\}$, where x can represent ET or NDVI, as depicted in Figure 3. It is important to note that when calculating the correlation coefficients and their corresponding p-values, the specific dates corresponding to the periods in this study are not continuous. For

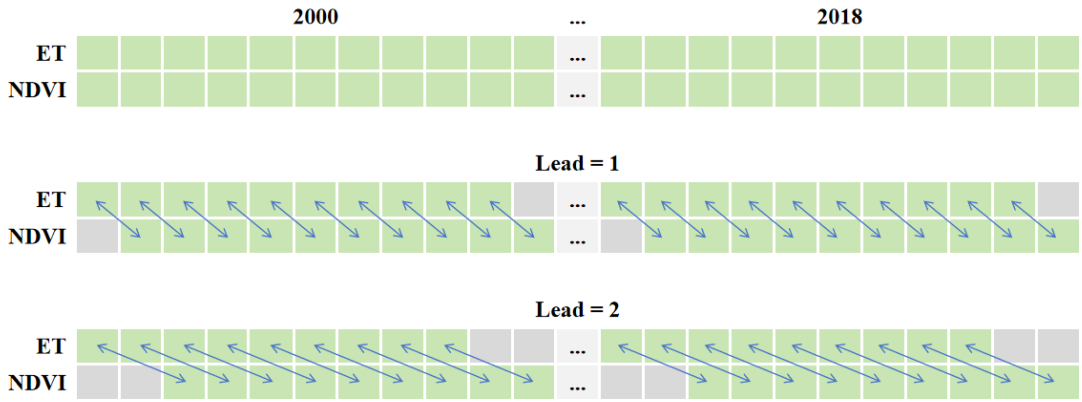

Figure 3. Illustration of calculating correlation coefficients at different Lead levels. The green squares represent the data utilized in the analysis, while the gray squares indicate the data that were not included. The bidirectional arrows demonstrate how ET and NDVI data from different time points correspond to each other.

instance, the last period of 2001 ends on August 31st, while the first period of 2002 begins on April 1st. Given this discontinuity, we do not consider the preceding period of the first period in 2002 as the last period of 2001, but rather replace it with missing values. Additionally, when calculating the correlation coefficients, the calculation is performed only when both the leading ET and NDVI values are non-missing. Introducing the variable Lead, we define the following two sequences:

$$E_{Lead} = \{ET_{year,period} \mid period = 1, 2, \ldots, 11 - Lead\}, \quad (4)$$

$$N_{Lead} = \{NDVI_{year,period} \mid period = Lead + 1, Lead + 2, \ldots, 11\}. \quad (5)$$

The correlation between E_{Lead} and N_{Lead} at different Lead levels is evaluated using Pearson correlation coefficients and their corresponding p-values.

2.5. Cumulative ET Control on NDVI

Previous studies have demonstrated the controlling effect of cumulative precipitation on NDVI (Zeng *et al*., 2013; Koster *et al*., 2014). To investigate this mechanism, this study also introduces a variable called CuLead, varying from 0 to 9. In this context, Lead refers to the cumulative ET data obtained by summing the ET values from the preceding CuLead periods up to the current period. This cumulative ET data is then compared with the NDVI data of the current period, as illustrated in Figure 4. To examine whether the NDVI during the growing season (i.e., from late July to August) is influenced by cumulative precipitation, this study selects the last two periods of each year for NDVI data. These NDVI data points are paired with their corresponding cumulative ET data, and Pearson correlation coefficients and p-values are calculated for analysis. Introducing the variable CuLead, we define the following two sequences:

$$E_{CuLead} = \{\sum_{period=n-CuLead}^{n} ET_{year,period} \mid n = 10, 11\}, \quad (6)$$

$$N_{CuLead} = \{NDVI_{year,period} \mid period = 10, 11\}. \quad (7)$$

The correlation between E_{CuLead} and N_{CuLead} at different CuLead levels is evaluated using Pearson correlation coefficients and their corresponding p-values.

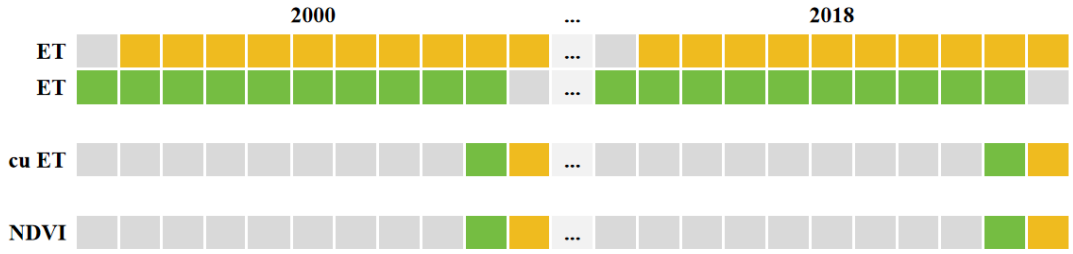

Figure 4. Illustration of calculating correlation coefficients at CuLead = 9 level. The yellow and green squares representing cu ET for each year are obtained by summing the yellow and green squares of ET, respectively. These cu ET squares are then matched with the corresponding yellow and green squares of NDVI to calculate the correlation coefficients.

3. Results

This presenting study consists of three main parts: the influence of individual monthly ET on NDVI, the influence of cumulative ET over multiple months on NDVI, and the impact of land cover on the correlation coefficient between ET and NDVI.

3.1. Influence of ET on NDVI

Individual monthly ET may exert control on NDVI. The control of ET on NDVI could exhibit a lag effect, differing across different regions. To investigate this mechanism, we separately examined the control of ET on NDVI, with ET leading by different periods.

Through observing Figure 5a, it can be noticed that the majority of regions in the image exhibit significant positive correlation, while a few regions show significant negative correlation. Building upon this observation, approximately 92% of the regions display positive correlation, with approximately 86% of the regions exhibiting statistical significance. Notably, the correlation appears to be less stable in the western regions of Colorado, whereas the eastern regions demonstrate more pronounced and consistent positive correlation. In Section 3.3., we will introduce the variable land cover to explore the reasons behind the negative correlation and lack of correlation in certain regions.

Upon examining the comparison between the left and right pictures in Figure 5, a clear pattern emerges: the regions with stronger positive or negative correlation exhibit a more significant correlation. Figure 6 provides a detailed depiction of the distribution of correlation coefficients (Lead=0) between ET and NDVI in Colorado. From the graph, it is evident that when the correlation coefficient is near zero, it is predominantly non-significant. Conversely, when the correlation coefficient deviates from zero, it tends to be statistically significant. This result suggests that the relationship between the two variables in these regions is non-random and likely exhibits a systematic connection. On the other hand, for the regions with lower correlation, various factors may influence the relationship, resulting in a larger p-value and non-significant correlation between the variables. To investigate this phenomenon, it is necessary to introduce additional variables and conduct further research to uncover the relationships among these variables and identify generalized patterns.

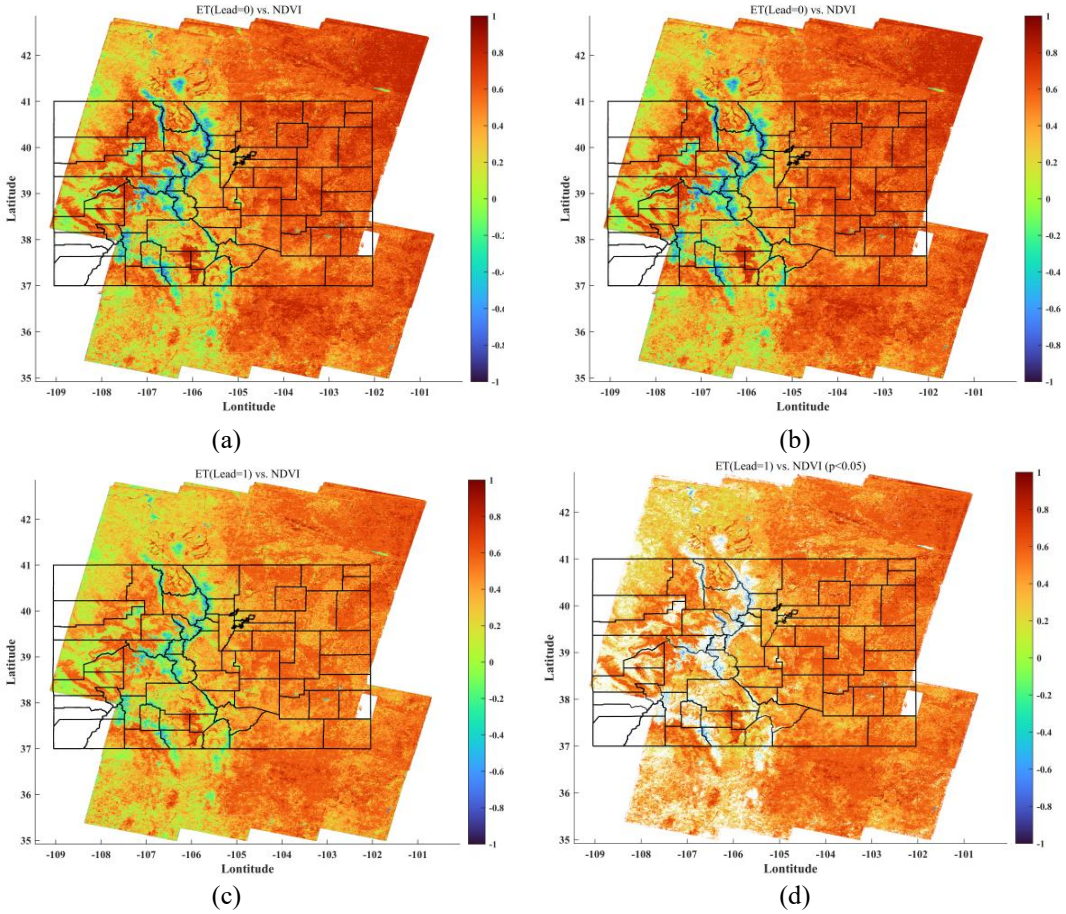

Figure 5. Pearson correlation coefficients between ET and NDVI in Colorado. The black box represents the state of Colorado and its administrative regions. Panels (a) and (c) represent the Pearson correlation coefficients for ET and NDVI at lead times of 0 and 1, respectively. Panels (b) and (d) display the Pearson correlation coefficients that are statistically significant ($p<0.05$) between ET and NDVI at lead times of 0 and 1, respectively.

We also discover that for the majority of regions in Colorado, the lagged control of ET on NDVI gradually weakens as the Lead increases, regardless of whether it is positive or negative correlation, through the comparison of results in Figure 5a & 5c. This phenomenon can be attributed to two main factors. Firstly, as

the Lead increases, the replacement of missing values between two-year intervals leads to a reduction in data volume, increasing the uncertainty of the results. Secondly, it could be related to the vegetation types in Colorado, which will be discussed in detail in Section 3.3.

Figure 7 illustrates the proportion of positive and negative correlation coefficients between ET and NDVI, as well as their significance, at different Lead levels within Colorado. Observation of the image reveals that as Lead increases, the proportion of statistically significant data decreases for both positive and negative correlations. Furthermore, by calculating the distance between the probability distribution curves in Figure 6 and other Lead levels, which we refer to as significant distance, Figure 8 is obtained. The significant distance increases with the growth of Lead, indicating a gradual weakening of the lagged control of ET on NDVI. Additionally, Figure 9 shows a decreasing trend in the expected correlation coefficients as Lead increases, further emphasizing the diminishing lagged control of ET on NDVI with increasing Lead.

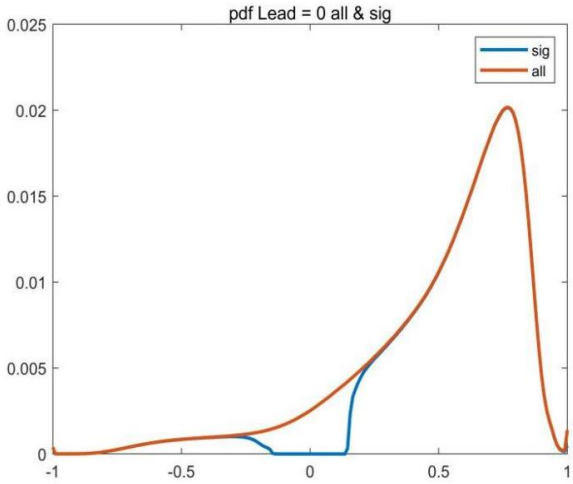

Figure 6. The probability density depicts the correlation between ET and NDVI when Lead=0. The horizontal axis represents the values of the correlation coefficient between ET and NDVI, while the vertical axis represents the proportion of the overall distribution. The upper curve represents the probability distribution of the correlation coefficient, while the lower curve represents the distribution that is statistically significant ($p<0.05$).

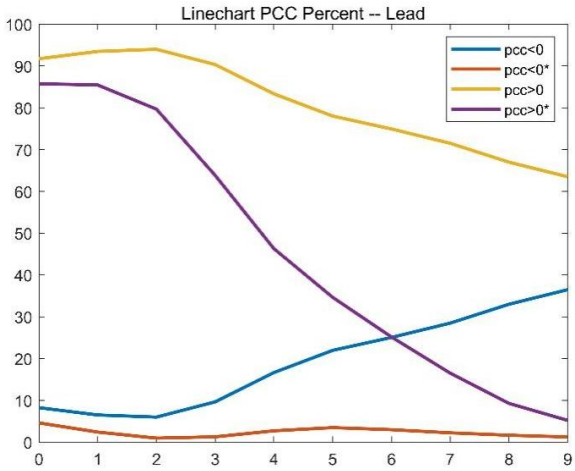

Figure 7. The line graph illustrates the proportion of positive and negative correlation coefficients as Lead increases. The horizontal axis represents Lead, while the vertical axis represents the proportion. The yellow and blue curves represent positive and negative correlation coefficients, respectively, while the purple and orange curves represent their statistically significant occurrences.

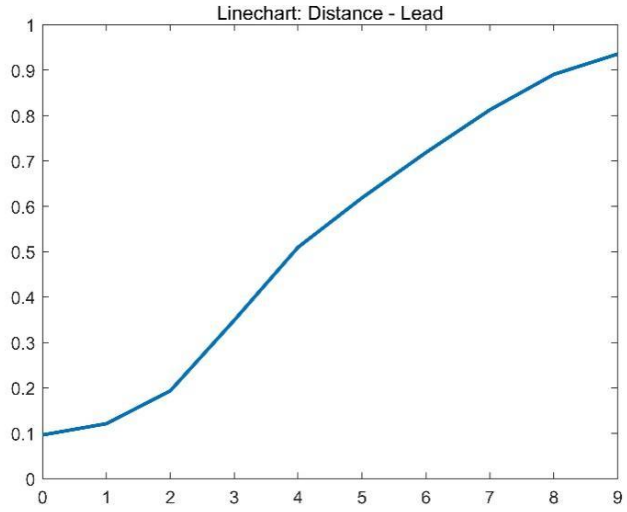

Figure 8. The graph presents the significant distance at different Lead levels. The horizontal axis represents Lead, while the vertical axis represents the significant distance, given by $\text{Distance} = \int_{-1}^{1} \text{p(x)} - \text{p}^{*}\text{(x)dx}$.

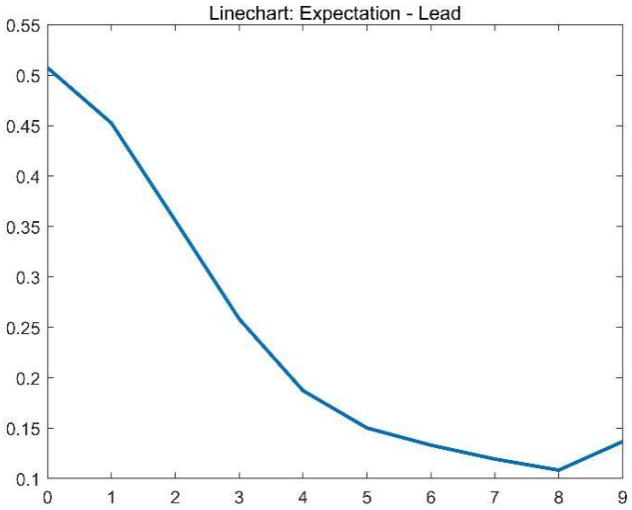

Figure 9. The graph illustrates the expected correlation coefficients at different Lead levels. The horizontal axis represents Lead, while the vertical axis represents the expected correlation, given by $\text{Expectation} = \int_{-1}^{1} \text{x p(x)dx}$.

3.2. Control of Cumulative ET on NDVI

Previous studies have demonstrated the controlling effect of cumulative precipitation on plant growth. In this study, we investigated the relationship between NDVI and cumulative ET during late growing seasons, specifically from late July to August. The NDVI were selected for the last two periods of each year, while the cumulative ET were calculated for the accumulation of ET over from 0 to 9 months. We computed the Pearson correlation coefficient and p-value between NDVI and cumulative ET.

As shown in Figure 10, almost all regions exhibit a positive correlation between cumulative ET and NDVI, indicated by positive correlation coefficients. However, upon comparing the two panels, it can be observed that this positive correlation is not very significant, with only a few regions (36%) showing statistical significance ($p < 0.05$). There are hardly any regions with significant negative correlation (<1%) or lack of correlation. Furthermore, Figure 10 vividly illustrates that the proportion of statistically significant positive correlation coefficients notably decreases compared with Figure 5.

By comparing the upper and lower panels in Figure 10, a slight enhancement in both positive and negative

correlation can be observed as the cumulative ET periods increase from 8 to 9. This phenomenon is further illustrated in Figure 11, which demonstrates the varying influence of cumulative ET on NDVI as the ET accumulation period lengthens. Specifically, it indicates a diminishing effect followed by a strengthening effect. This observation suggests that the NDVI during the late growth season is significantly influenced by both the end of the growth period and the cumulative ET throughout the entire growth season. In other words, the final growth state of the plants is influenced by the entire growth process and recent conditions, while the impact of intermediate processes on plant growth outcomes is relatively minor.

Upon observing Figure 10, it becomes apparent that the regions displaying significant positive correlation are predominantly concentrated in the eastern part of Colorado. Moreover, certain regions exhibit variations in correlation as the cumulative periods increase. Further investigation is required to delve into the mechanisms underlying these fluctuations. These phenomena are closely related to land cover, which will be explored in Section 3.3.

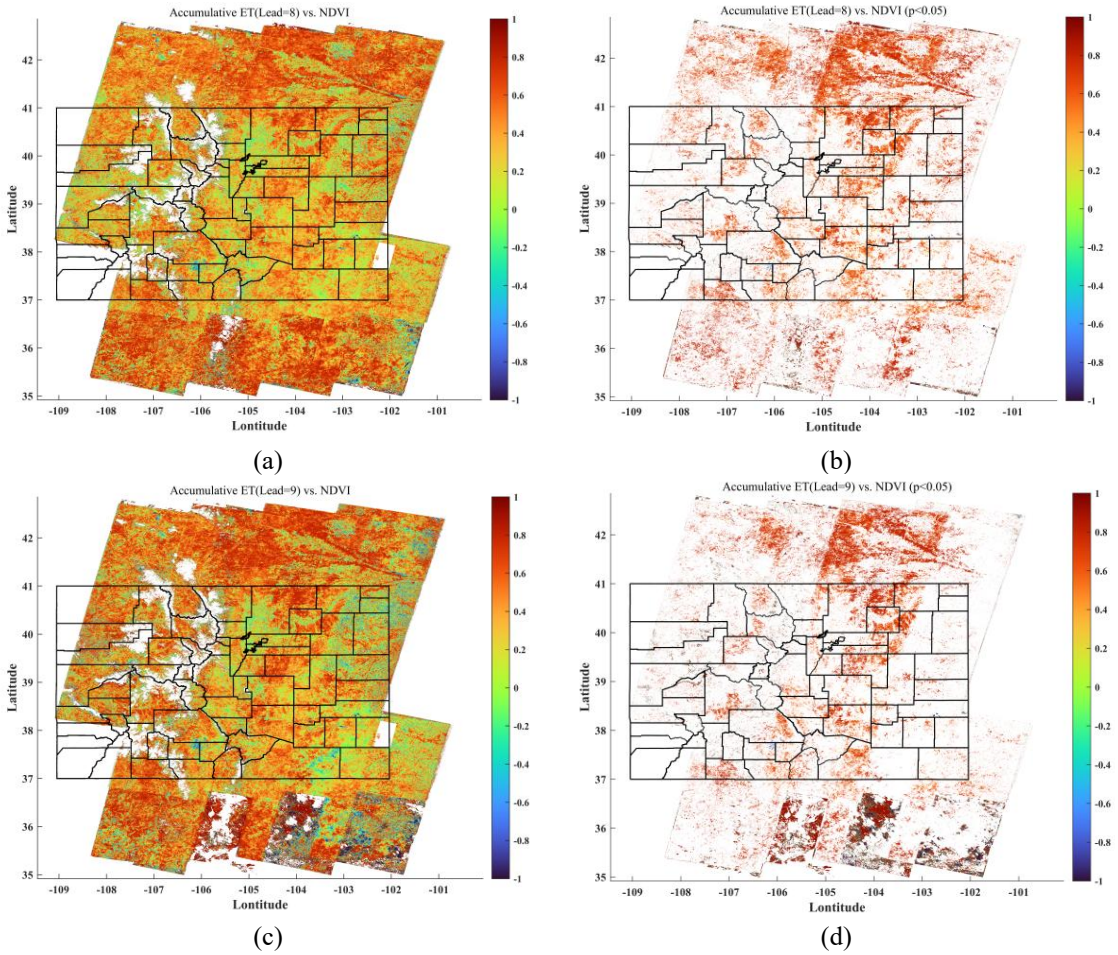

Figure 10. Pearson correlation coefficients between the cumulative ET and NDVI in Colorado. Panels (a) and (c) represent the Pearson correlation coefficients for ET and NDVI at lead times of 8 and 9, respectively. Panels (b) and (d) display the Pearson correlation coefficients that are statistically significant ($p < 0.05$) between cumulative ET and NDVI at lead times of 8 and 9, respectively.

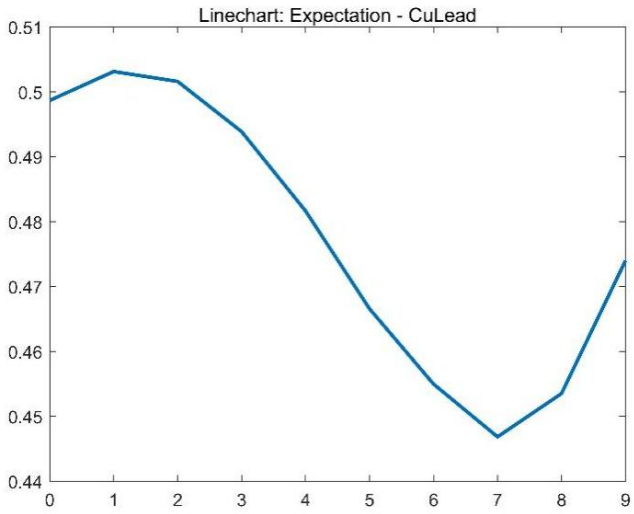

Figure 11. The graph illustrates the expectation of correlation coefficients at different levels of CuLead. The horizontal axis represents CuLead, while the vertical axis represents the expected correlation.

3.3. Impact of Land Cover on the PCC between ET and NDVI

Figure 12 presents a schematic map depicting the land cover distribution in Colorado, where different colors represent distinct land types. The proportions of each land cover category can be observed in Figure 13. By combining these two figures, it becomes evident that the western half of Colorado is predominantly comprised of Evergreen Forest and Deciduous Forest, whereas the eastern half is mainly characterized by Grassland/Herbaceous and Cultivated Crops. Additionally, Shrub/Scrub and Developed Lands also contribute to a portion of the land cover. From Figure 5 and Figure 10, it is apparent that in many areas, ET (or cumulative ET) displays a negative correlation with NDVI. By statistically analyzing the correlation coefficients between ET (or cumulative ET) and NDVI for each land cover category, we can generate Figure 14, Figure 15, and Figure 16.

Based on Figure 14 and Figure 16, it is evident that Perennial Ice/Snow, Barren Land (Rock/Sand/Clay), and Open Water, regardless of ET or cumulative ET, exhibit a predominant negative correlation with NDVI. These three land cover types are characterized by a scarcity of vegetation, resulting in ET primarily driven by water evaporation and minimal or no involvement of plant transpiration. Consequently, the dominant relationship between NDVI and ET is negative. In Figure 15, when Lead=0, the proportion of pixels with significant correlation reveals that Open Water and Barren Land exhibit a similar number of pixels with both positive and negative correlations. This indicates that ET is unrelated to NDVI in these land cover types, suggesting that evaporation is not influenced by vegetation and primarily driven by water evaporation processes.

Both trees and the land they inhabit a higher water storage capacity, allowing for stable and continuous water evaporation and plant transpiration throughout the entire growing season. This indicates that trees possess strong control over water dynamics within their surroundings, including water acquisition, storage, and consumption. As shown in Figure 14, among the remaining land cover categories, Forests, which includes Evergreen Forest, Mixed Forest, and Deciduous Forest, exhibit a higher proportion of negatively correlated regions compared with other land cover types. When considering the cumulative effect of ET on NDVI throughout the growing season, as depicted in Figure 16, the number of pixels with both positive and negative correlations is nearly equal in all Forest categories. This suggests that trees have a stable capacity for water regulation, enabling them to adapt well to environmental changes and provide a relatively consistent water cycle within ecosystems.

On the other hand, human intervention has a significant impact on correlation coefficients. Specifically, land cover categories influenced by human activities include Developed Space with different intensities, Pasture/Hay, and Cultivated Crops. As depicted in Figure 14, due to human intervention, plants can effectively utilize water and grow healthily, with most of the ET originating from plant transpiration. Therefore, there is a high positive correlation at various stages. As shown in Figure 16, due to human intervention, the cumulative ET exhibits a decreased positive correlation with end-of-growing-season NDVI compared with the influence of ET on NDVI. This phenomenon can be attributed to the "marginal effect",

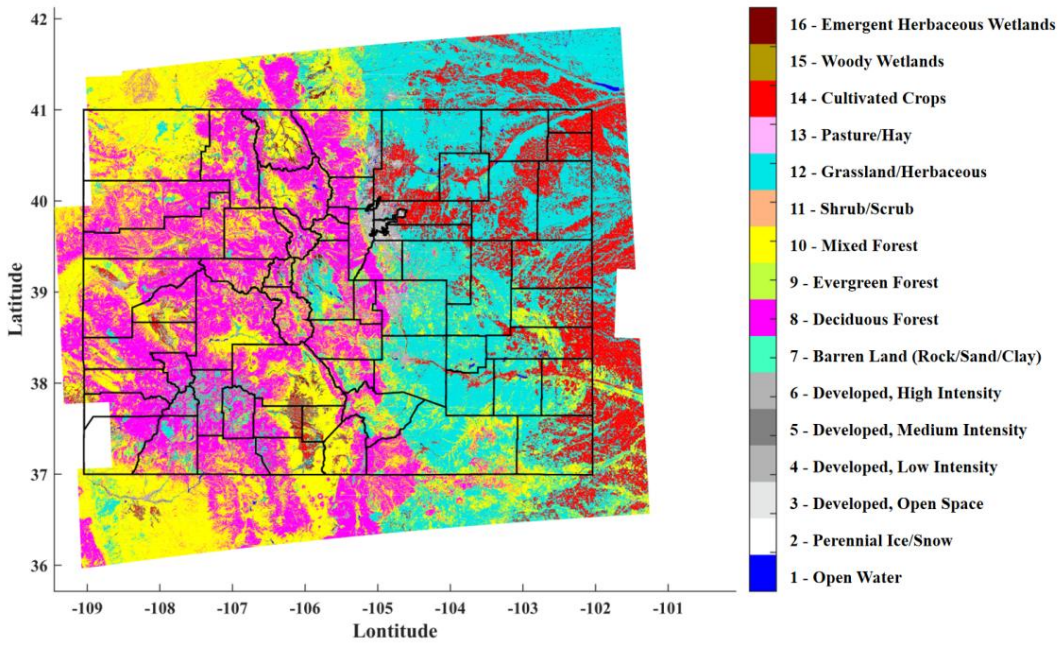

Figure 12. The schematic representation of land cover in Colorado. Land cover is a categorical variable, where integers ranging from 1 to 16 are used to represent the 16 land types in Colorado. The specific meaning of each number can be found in Table A1 of Appendix A, under the Analysis ID column.

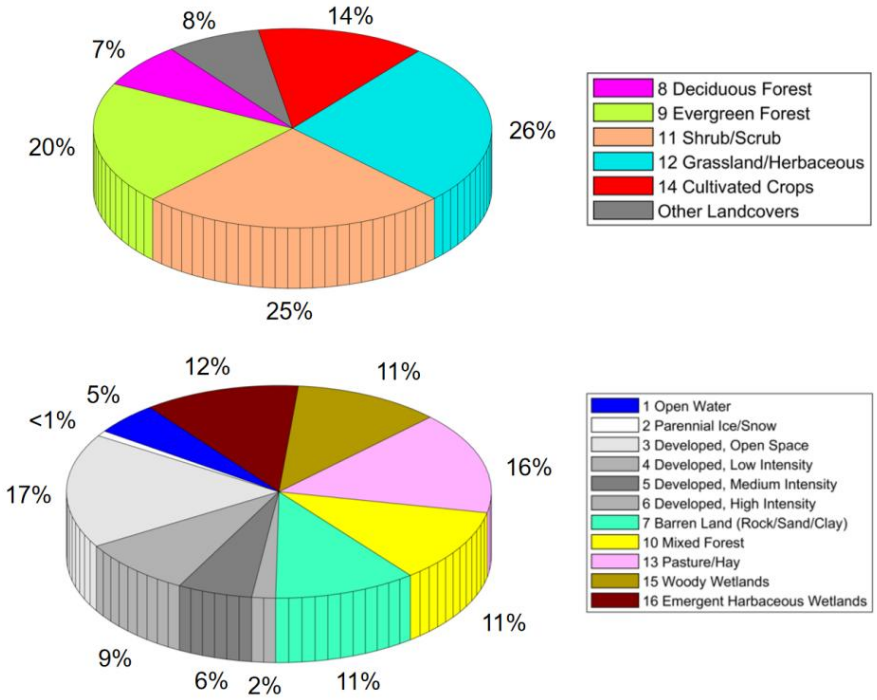

Figure 13. The pie chart illustrates the land cover composition in Colorado state. (Upper panel): It presents the proportion of the top 5 land cover categories with the largest share in Colorado, while the remaining land cover categories, each accounting for less than 1%, are combined into a single category. (Lower panel): It displays the proportion of the remaining land cover categories in Colorado, excluding the top 5 categories mentioned in upper panel.

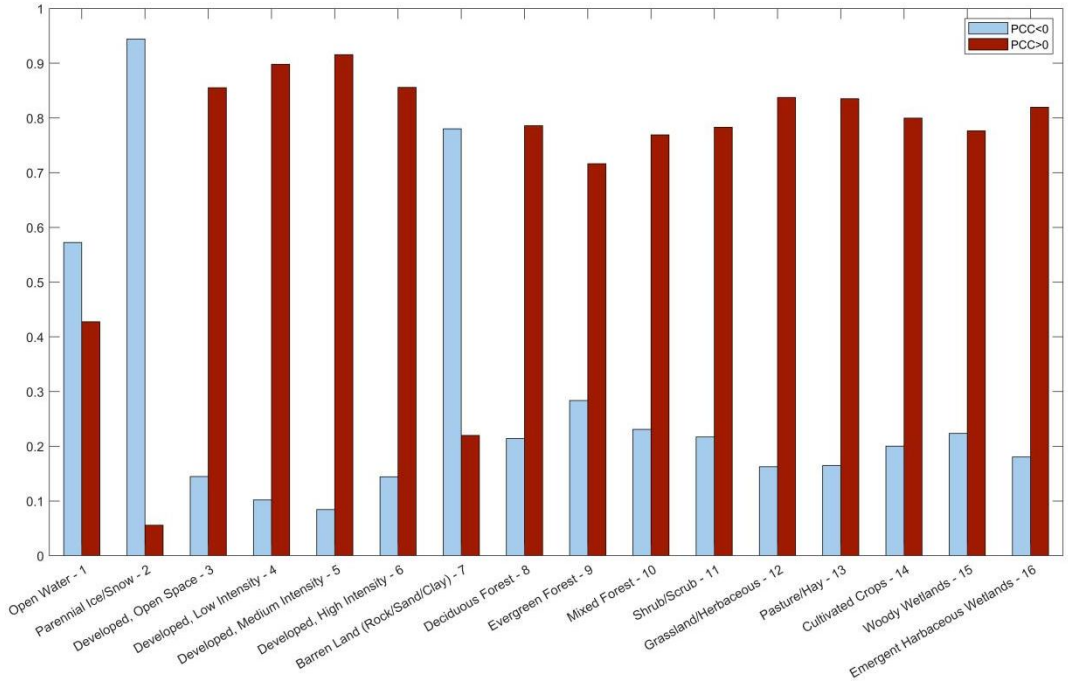

Figure 14. The bar chart illustrates the proportion of positive and negative correlation coefficients for different land cover types when Lead=0. In the chart, the blue bars represent the proportion of pixels with negative correlation coefficients, while the red bars represent the proportion of pixels with positive correlation coefficients. The combined values of the blue and red bars sum up to one.

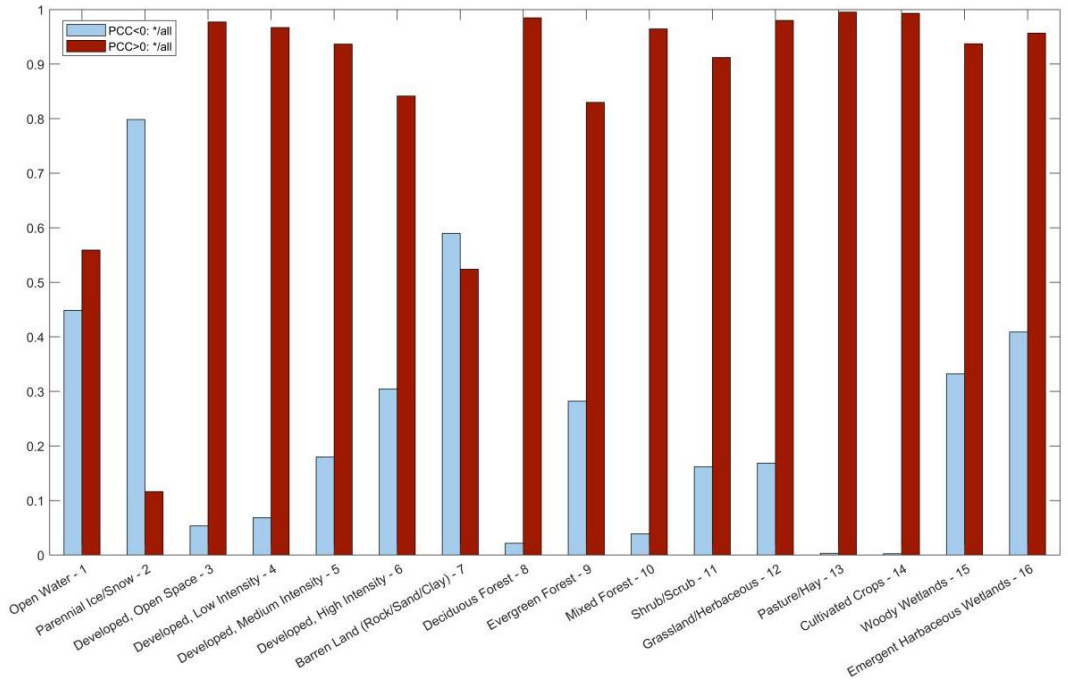

Figure 15. The bar chart illustrates the proportion of significant positive and negative correlation coefficients for different land cover types when Lead=0. Within each land cover category, the blue bars represent the proportion of pixels with significantly negative correlations among the significant pixels, while the red bars represent the proportion of pixels with significantly positive correlations.

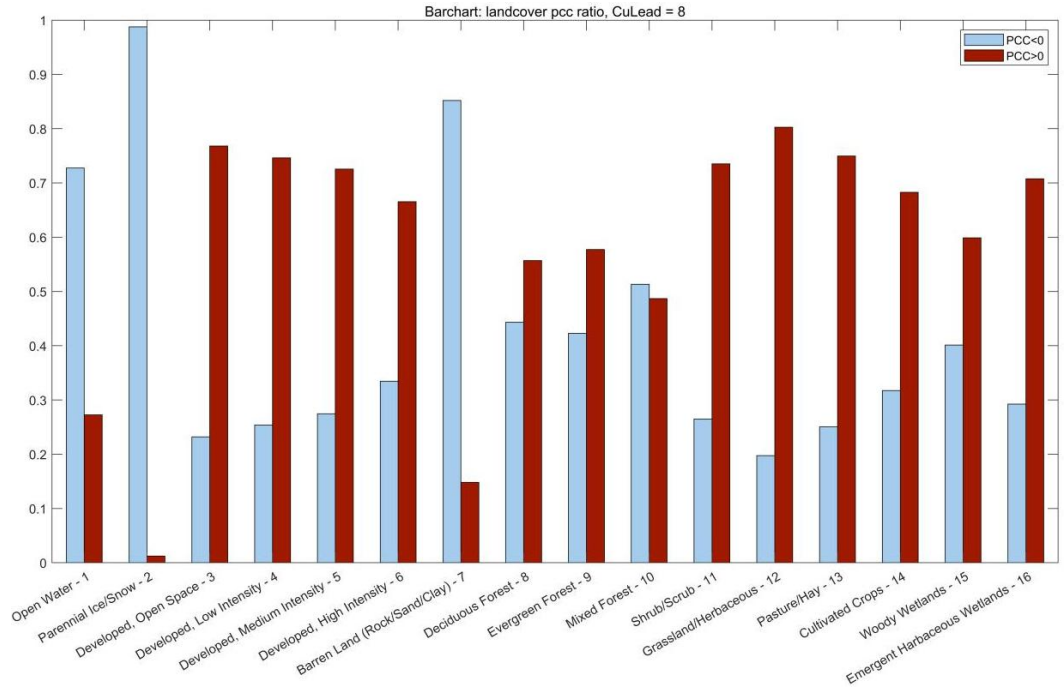

Figure 16. The bar chart illustrates the proportion of positive and negative correlation coefficients for different land cover types when CuLead=8. In the chart, the blue bars represent the proportion of pixels with negative correlation coefficients, while the red bars represent the proportion of pixels with positive correlation coefficients. The combined values of the blue and red bars sum up to one.

where the impact of water availability on plant growth diminishes as sufficient water is provided. Proper and scientifically managed agricultural practices can provide adequate water at different stages of plant growth, resulting in a cost-effective relationship between plant growth and water input. As illustrated in Figure 15, considering significance, both Pasture/Hay and Cultivated Crops land cover categories exhibit significant positive correlations.

Analyzing the results from Section 3.1. and Section 3.2., it becomes evident that the eastern regions generally exhibit stronger and more significant positive correlation compared with the western regions. Considering Figure 12, we can infer that the eastern and western sides of Colorado have distinct predominant land types, which contribute to the varying effects of ET (or cumulative ET) on NDVI. The red areas represent Cultivated Crops, which often display stronger and more significant positive correlation. Therefore, these regions are well-suited for crop cultivation, and this knowledge can inform agricultural planning and development strategies based on these findings.

4. Discussion

Chen *et al*. (2017) conducted a study that revealed a strong relationship between ET and NDVI with vegetation productivity (ANPP). Specifically, AET demonstrated a high correlation with ANPP, and there was also a significant correlation between NDVI and ANPP. These findings indicate the close relationship between ET and NDVI in influencing grassland productivity, providing valuable insights into the climate–vegetation interactions within grassland ecosystems.

By utilizing NDVI as an indicator of vegetation abundance and vitality, we observed that both ET and land cover had significant influences on plant production. Moreover, different land cover types demonstrated varying sensitivities to ET. These findings have significant implications for agriculture and environmental management, providing insights into the factors that affect plant growth and crop production. For example, planners can use NDVI as a proxy for water demand, optimizing irrigation schedules to reduce water waste. A comprehensive understanding of the relationship between ET, land cover, and NDVI can inform the development of more effective strategies for agricultural resource management. However, it is important to acknowledge certain limitations of this study, such as its focus on a specific region and time period, its

reliance on remote sensing data rather than direct measurements of plant growth, and possibly degrading usable scene availability due to Landsat's cloud-contaminated data. Future research should aim to expand the study's scope and incorporate more detailed data sources to address these limitations.

In other previous studies, DayCent model has been employed to simulate the impacts of climate and land use changes on various crops, grassland, and forest systems worldwide (Del Grosso *et al*., 2011). Regardless of rainy or non-rainy conditions, eMODIS NDVI explains approximately 50–52% of the variability in AET (Del Grosso *et al*., 2018). Del Grosso *et al*. conclude that remote sensing NDVI, when combined with the knowledge of Volumetric Soil Water Content (VSWC) and rainfall events, serves as a powerful tool for predicting Net Ecosystem Exchange (NEE) and AET across multiple temporal scales (from daily to seasonal) in semiarid grasslands.

In the future, additional research is necessary to precisely uncover the causal link between ET and NDVI. Supplementary datasets, such as soil moisture data, will be incorporated into the study. This exploration might uncover the fundamental mechanisms that dictate their relationship, thereby enhancing our understanding of the positive correlation in different land types.

Previous studies have shown a stronger correlation between ET and biomass. For instance, Ritchie *et al*. (1983) proposed an alternative approach for calculating biomass production independently of ET and T. Purcell *et al*. (2007) assessed the relationship between yield and estimated cumulative transpiration (T) or ET in well-watered soybean crops. Benjamin *et al*. (2015) found that soil water dynamics and soil water storage are critical for determining irrigation scheduling and impact various factors such as soil water use, water content, biomass production, grain yield, and water use efficiency in a continuous corn system in Colorado. Based on those existing research findings, as well as the results of this study, the future study will progress to predicting end-of-season biomass by utilizing ET, NDVI, land cover, and other relevant variables.

Through these potential studies, we expect to introduce usable methods using cutting-edge remote sensing technologies and recommend practical mathematical models for policymaking in agriculture area. Simultaneously, we seek to address issues such as water scarcity and climate change, providing support for the future sustainable development of agriculture.

5. Conclusions

This study aimed to investigate the correlation between ET, NDVI and land cover. By employing remote sensing data and statistical methodologies, our investigation revealed that approximately 92% of regions demonstrated a notable positive correlation between ET and NDVI. However, incorporating land cover into the analysis unveiled consistent patterns in Colorado, where Perennial Ice/Snow, Barren Land (Rock/Sand/Clay), and Open Water consistently showed a predominant negative correlation, ranking as the top three land types with NDVI, regardless of ET or cumulative ET. The findings presented in this study are comparable to those studies from Joiner *et al*. (2018) and Zeng *et al*. (2013). However, this study distinguishes itself by employing data with an unprecedentedly high spatial resolution of 30 meters, a novelty in this field.

Specific land types characterized by extensive root systems, enabling stable and continuous water evaporation and plant transpiration throughout the growing season, such as various forest types, exhibited a significant negative correlation with ET. Additionally, human intervention significantly influences correlation coefficients. Pasture/Hay and Cultivated Crops, two primary land types where plants are directly affected by human activity, exhibit correlation coefficients close to 1 between ET and NDVI, which is statistically significant.

In investigating the relationship between ET and NDVI through the introduction of Lead and CuLead variables, we noted that during the growing season, the lagged influence of ET on NDVI is less prominent compared with its concurrent month. Initially, the cumulative impact of ET on NDVI diminishes gradually, but it starts to intensify when CuLead≥7. This suggests that NDVI exerts a stronger influence on the cumulative ET throughout the entire growing season than during the recent period within the season.

In summary, this study pioneers the use of two-decade (2000–2018), high-resolution (30m) Landsat data to resolve fine-scale ET-NDVI dynamics in semi-arid Colorado, uncovering land cover-dependent mechanisms overlooked in coarse-scale studies. It demonstrates that agricultural systems (e.g., Cultivated Crops) exhibit strong positive correlations, indicating efficient conversion of water inputs to productivity, whereas natural ecosystems (e.g., Forests) show buffered responses due to soil water storage and canopy interception. Perennial Ice/Snow and Barren Land consistently display negative correlations. Temporally,

cumulative ET effects intensify at CuLead≥7 months, revealing legacy impacts on seasonal biomass. These findings deliver actionable pathways: optimizing irrigation to reduce agricultural water waste, guiding conservation planning for climate resilience for arid regions.

Data Availability Statement: Data are available for public at the sources in Table 1.

Acknowledgment: This work is partly supported by the US Department of Agriculture (USDA) UV-B Monitoring and Research Program, Colorado State University, under USDA National Institute of Food and Agriculture Grant 2022-34263-38472. This material is based upon work supported by the U.S. Geological Survey under Grant/Cooperative Agreement No. G18AP00077 (for GY18-GY22) or G23AP00683 (GY23-GY27).

Conflicts of Interest: The authors declare no conflicts of interest. The funders had no role in the design of the study; in the collection, analyses, or interpretation of data; in the writing of the manuscript; or in the decision to publish the results.

References

An, N., Price, K. P., & Blair, J. M. (2013). Estimating above-ground net primary productivity of the tallgrass prairie ecosystem of the central Great Plains using AVHRR NDVI. *International Journal of Remote Sensing, 34*(11), 3717–3735.

Bauman, A., Goemans, C., Pritchett, J., & McFadden, D. T. (2013). Estimating the economic and social impacts from the drought in Southern Colorado. *Journal of Contemporary Water Research & Education, 151*(1), 61–69.

Benjamin, J. G., Nielsen, D. C., Vigil, M. F., Mikha, M. M., & Calderon, F. (2015). Cumulative deficit irrigation effects on corn biomass and grain yield under two tillage systems. *Agricultural Water Management, 159*, 107–114.

Briggs, J. M., & Knapp, A. K. (1995). Interannual variability in primary production in tallgrass prairie: Climate, soil moisture, topographic position, and fire as determinants of aboveground biomass. *American Journal of Botany, 82*(8), 1024–1030.

Chen, M., Parton, W. J., Del Grosso, S. J., Hartman, M. D., Day, K. A., Tucker, C. J., … Gao, W. (2017). The signature of sea surface temperature anomalies on the dynamics of semiarid grassland productivity. *Ecosphere, 8*(12), e02069.

Chen, M., Parton, W. J., Hartman, M. D., Del Grosso, S. J., Smith, W. K., Knapp, A. K., … Gao, W. (2019). Assessing precipitation, evapotranspiration, and NDVI as controls of US Great Plains plant production. *Ecosphere, 10*(10), e02889.

Crow, W. T., Kumar, S. V., & Bolten, J. D. (2012). On the utility of land surface models for agricultural drought monitoring. *Hydrology and Earth System Sciences, 16*(9), 3451–3460. https://www.hydrol-earth-syst-sci.net/16/3451/2012/

Del Grosso, S. J., Parton, W. J., Derner, J. D., Chen, M., & Tucker, C. J. (2018). Simple models to predict grassland ecosystem C exchange and actual evapotranspiration using NDVI and environmental variables. *Agricultural and Forest Meteorology, 249*, 1–10.

Del Grosso, S. J., Parton, W. J., Keough, C. A., & Reyes-Fox, M. (2011). Special features of the DayCent modeling package and additional procedures for parameterization, calibration, validation, and applications. In *Methods of introducing system models into agricultural research* (Vol. 2, pp. 155–176).

Dewitz, J., & U.S. Geological Survey. (2021). National Land Cover Database (NLCD) 2019 Products (ver. 2.0, June 2021) [Data set]. U.S. Geological Survey. https://doi.org/10.5066/P9KZCM54

ESPA - LSRD. (n.d.). https://espa.cr.usgs.gov/. Last access: 15 May 2023.

Formica, A. F., Burnside, R. J., & Dolman, P. M. (2017). Rainfall validates MODIS-derived NDVI as an index of spatio-temporal variation in green biomass across non-montane semi-arid and arid Central Asia. *Journal of Arid Environments, 142*, 11–21.

Haddeland, I., Heinke, J., Biemans, H., Eisner, S., Flörke, M., Hanasaki, N., … Wisser, D. (2014). Global water resources affected by human interventions and climate change. *Proceedings of the National Academy of Sciences, 111*(9), 3251–3256.

Homer, C., Dewitz, J., Jin, S., Xian, G., Costello, C., Danielson, P., … Riitters, K. (2020). Conterminous United States land cover change patterns 2001–2016 from the 2016 national land cover database. *ISPRS Journal of Photogrammetry and Remote Sensing, 162*, 184–199. https://doi.org/10.1016/j.isprsjprs.2020.02.019

Jin, S., Homer, C., Yang, L., Danielson, P., Dewitz, J., Li, C., … Howard, D. (2019). Overall methodology design for the United States national land cover database 2016 products. *Remote Sensing, 11*(24), 2971. https://doi.org/10.3390/rs11242971

Joiner, J., Yoshida, Y., Anderson, M., Holmes, T., Hain, C., Reichle, R., … Zeng, F. W. (2018). Global relationships among traditional reflectance vegetation indices (NDVI and NDII), evapotranspiration (ET), and soil moisture variability on weekly timescales. *Remote Sensing of Environment, 219*, 339–352.

Koster, R. D., Walker, G. K., Collatz, G. J., & Thornton, P. E. (2014). Hydroclimatic controls on the means and variability of vegetation phenology and carbon uptake. *Journal of Climate, 27*(14), 5632–5652.

Lindenmayer, D. B., Likens, G. E., Andersen, A., Bowman, D., Bull, C. M., Burns, E., … Wardle, G. M. (2012). Value of long-term ecological studies. *Austral Ecology, 37*(7), 745–757.

McKee, T. B., Doesken, N. J., Kleist, J., Shrier, C. J., & Stanton, W. P. (2000). A history of drought in Colorado: Lessons learned and what lies ahead.

Mukheibir, P. (2010). Water access, water scarcity, and climate change. *Environmental Management, 45*, 1027–1039.

Nikolaou, G., Neocleous, D., Christou, A., Kitta, E., & Katsoulas, N. (2020). Implementing sustainable irrigation in water-scarce regions under the impact of climate change. *Agronomy, 10*(8), 1120.

Parton, W. J., Gutmann, M. P., Merchant, E. R., Hartman, M. D., Adler, P. R., McNeal, F. M., & Lutz, S. M. (2015). Measuring and mitigating agricultural greenhouse gas production in the US Great Plains, 1870–2000. *Proceedings of the National Academy of Sciences, 112*(34), E4681–E4688.

Paruelo, J. M., Epstein, H. E., Lauenroth, W. K., & Burke, I. C. (1997). ANPP estimates from NDVI for the central grassland region of the United States. *Ecology, 78*(3), 953–958.

Paruelo, J. M., Oesterheld, M., Di Bella, C. M., Arzadum, M., Lafontaine, J., Cahuepé, M., & Rebella, C. M. (2000). Estimation of primary production of subhumid rangelands from remote sensing data. *Applied Vegetation Science, 3*(2), 189–195.

Petrie, M. D., Peters, D. P., Yao, J., Blair, J. M., Burruss, N. D., Collins, S. L., … Steiner, J. L. (2018). Regional grassland productivity responses to precipitation during multiyear above- and below-average rainfall periods. *Global Change Biology, 24*(5), 1935–1951.

Purcell, L. C., Edwards, J. T., & Brye, K. R. (2007). Soybean yield and biomass responses to cumulative transpiration: Questioning widely held beliefs. *Field Crops Research, 101*(1), 10–18.

Ritchie, J. T. (1983). Efficient water use in crop production: Discussion on the generality of relations between biomass production and evapotranspiration. In *Limitations to efficient water use in crop production* (pp. 29–44).

Rocha, N. S. D., Käfer, P. S., Skokovic, D., Veeck, G., Diaz, L. R., Kaiser, E. A., … Rolim, S. B. A. (2020). The influence of land surface temperature in evapotranspiration estimated by the S-SEBI model. *Atmosphere, 11*(10), 1059. https://doi.org/10.3390/atmos11101059

Sala, O. E., Parton, W. J., Joyce, L. A., & Lauenroth, W. K. (1988). Primary production of the central grassland region of the United States. *Ecology, 69*(1), 40–45.

U.S. Geological Survey. (n.d.-a). Collection 2 Landsat 8–9 OLI (Operational Land Imager) and TIRS (Thermal Infrared Sensor) Level-2 Science Product. https://doi.org/10.5066/P9OGBGM6

U.S. Geological Survey. (n.d.-b). *Collection 2 Landsat 7 Enhanced Thematic Mapper Plus (ETM+) Level-2 Science Product*. https://doi.org/10.5066/P9C7I13B

U.S. Geological Survey. (n.d.-c). *Landsat Collection 2 U.S. Landsat Analysis Ready Data (ARD) Level-2*. https://doi.org/10.5066/P960F8OC

United States Environmental Protection Agency. (2016). *What climate change means for Colorado* [PDF]. Last access: 1 July 2023.

USDA/NASS. (2021). *State agriculture overview for Colorado*. https://www.nass.usda.gov/Quick_Stats/Ag_Overview/stateOverview.php?state=COLORADO. Last access: 1 July 2023.

Wickham, J., Stehman, S. V., Sorenson, D. G., Gass, L., & Dewitz, J. A. (2021). Thematic accuracy assessment of the NLCD 2016 land cover for the conterminous United States. *Remote Sensing of Environment, 257*, 112357. https://doi.org/10.1016/j.rse.2021.112357

Wilcox, K. R., Blair, J. M., Smith, M. D., & Knapp, A. K. (2016). Does ecosystem sensitivity to precipitation at the site-level conform to regional-scale predictions? *Ecology, 97*(3), 561–568.

Yang, L., Jin, S., Danielson, P., Homer, C., Gass, L., Bender, S. M., … Xian, G. (2018). A new generation of the United States National Land Cover Database: Requirements, research priorities, design, and implementation strategies. *ISPRS Journal of Photogrammetry and Remote Sensing, 146*, 108–123.

Zeng, F. W., Collatz, G. J., Pinzon, J. E., & Ivanoff, A. (2013). Evaluating and quantifying the climate-driven interannual variability in Global Inventory Modeling and Mapping Studies (GIMMS) Normalized Difference Vegetation Index (NDVI3g) at global scales. *Remote Sensing, 5*(8), 3918–3950.

Zhang, M., & Yuan, X. (2020). Crucial role of natural processes in detecting human influence on evapotranspiration by multisource data analysis. *Journal of Hydrology, 580*, 124350.

Appendix A

Table A1. Land types and an introduction to land types in Colorado.

Analysis ID	NLCD ID	Land types
1	11	Open Water - All areas of open water, generally with less than 25% cover or vegetation or soil
2	12	Perennial Ice/Snow - All areas characterized by a perennial cover of ice and/or snow, generally greater than 25% of total cover.
3	21	Developed, Open Space - Includes areas with a mixture of some constructed materials, but mostly vegetation in the form of lawn grasses.
4	22	Developed, Low Intensity -Includes areas with a mixture of constructed materials and vegetation.
5	23	Developed, Medium Intensity - Includes areas with a mixture of constructed materials and vegetation.
6	24	Developed, High Intensity - Includes highly developed areas where people reside or work in high numbers.
7	31	Barren Land (Rock/Sand/Clay) - Barren areas of bedrock, desert pavement, scarps, talus, slides, volcanic material, glacial debris, sand dunes, strip mines, gravel pits and other accumulations of earthen material.
8	41	Deciduous Forest - Areas dominated by trees generally greater than 5 meters tall, and greater than 20% of total vegetation cover.
9	42	Evergreen Forest - Areas dominated by trees generally greater than 5 meters tall, and greater than 20% of total vegetation cover.
10	43	Mixed Forest - Areas dominated by trees generally greater than 5 meters tall, and greater than 20% of total vegetation cover.
11	52	Shrub/Scrub - Areas dominated by shrubs; less than 5 meters tall with shrub canopy typically greater than 20% of total vegetation.
12	71	Grassland/Herbaceous - Areas dominated by graminoid or herbaceous vegetation, generally greater than 80% of total vegetation.
13	81	Pasture/Hay - Areas of grasses, legumes, or grass-legume mixtures planted for livestock grazing or the production of seed or hay crops, typically on a perennial cycle.
14	82	Cultivated Crops - Areas used for the production of annual crops, such as corn, soybeans, vegetables, tobacco, and cotton, and also perennial woody crops such as orchards and vineyards.
15	90	Woody Wetlands - Areas where forest or shrub land vegetation accounts for greater than 20 percent of vegetative cover and the soil or substrate is periodically saturated with or covered with water.
16	95	Emergent Herbaceous Wetlands - Areas where perennial herbaceous vegetation accounts for greater than 80 percent of vegetative cover and the soil or substrate is periodically saturated with or covered

Research Article

Analysis of Ecological Impacts of a Stream Restoration on Riparian Vegetation in Baltimore County, Maryland

Ren Dodge[1,2] and Chuyuan Wang[1,*]

[1] Department of Geography & Environmental Planning, Towson University, Towson, MD 21252, USA

[2] Department of Cell, Molecular, Developmental Biology, and Biophysics, Johns Hopkins University, Baltimore, MD 21218, USA

[*] Corresponding Author: cwang@towson.edu; +1-410-704-3973

Academic Editor: Jeong Chang Seong
Received: 12 August 2025
Revised: 23 September 2025
Accepted: 23 September 2025
Published: 24 October 2025

Abstract: Riparian forests play a vital role in supporting wildlife, managing runoff, and enhancing human well-being, yet they have been degraded by urban development and engineered stormwater systems. Stream restorations have emerged as nature-based solution to water management, but their effect on adjacent riparian ecosystems requires more research. This study evaluates the ecological impact of the Upper Jones Falls Stream Restoration in Baltimore County, Maryland, USA, using satellite and aerial imagery to assess vegetation health and land cover. Vegetation health during the period between 2015 and 2025 was assessed using the normalized difference vegetation index (NDVI), derived from high-resolution multispectral PlanetScope satellite imagery. Results show that although mature forest canopy was substantially lost, vegetation steadily regenerated, with NDVI returning to baseline in less than 10 years. Land cover analysis confirmed some tree plantings closest to the water have been thriving in recent years and also revealed the persistence of exposed water and barren zones. These findings show that NDVI is a useful metric for monitoring vegetation recovery post-restoration, while emphasizing the importance of integrating land cover classification and direct observation. This study highlights the need for more nuanced evaluation of riparian restoration outcomes, including the use of evolving remote sensing technologies and modeling.

Keywords: riparian zone, stream restoration, remote sensing, NDVI, urban ecology

1. Introduction

1.1. Background

Set at the interface between aquatic and terrestrial ecosystems, riparian zones provide a cornucopia of vital ecosystem services including primary production, habitat, flood control, access to water, recreation and a connection to nature for humans (Cadenasso *et al.*, 2007; Ferreira *et al.*, 2023). In the urban environment, these services are scarce, and because of that, more valuable. Yet even in an extensively developed city, small patches of riparian forest can support a diverse number of species with rich spatial and temporal heterogeneity of landforms and habitat (Pennington *et al.*, 2010; Rusnák *et al.*, 2022).

Rivers and riparian zones have been heavily altered by human activity. In many cities, the built environment limits their utility for both humans and nature (Kaushal & Belt, 2012; Morin *et al.*, 2022). Common stressors include dams, flow regulation, agriculture and irrigation, human-induced modifications, and land use changes (Murphy *et al.*, 2022). These changes disrupt natural patterns that support riparian function. In particular, stormwater in Baltimore has been managed through the construction of extensive concrete infrastructure, replacing 1st- and 2nd-order streams (Pickett *et al.*, 2020). Increased volumes and velocity of stormwater then lead to erosion, lowering the water table and disconnecting urban streams from the riparian zone, impacting soil, vegetation, and microbial processes and therefore nutrient cycling (Kaushal & Belt, 2012). This outcome is known as urban stream syndrome, and is marked by rapid flow changes, lack of flood control, higher levels of pollutants and nutrients, altered stream channels, and lower biodiversity with more pollution-tolerant species (Walsh *et al.*, 2005). Because water is diverted, riparian zones are disconnected from their floodplains, streams become incised deeper into the ground due to erosion, and streams in concrete channels deny water to adjacent vegetation, degrading primary production, habitat, flood

Citation: Dodge, R., & Wang, C. (2025). Analysis of Ecological Impacts of a Stream Restoration on Riparian Vegetation in Baltimore County, Maryland. *Journal of Earth Observation and Geospatial Applications*, *1*(1), 21–34. DOI: https://doi.org/10.65372/b1sxbv26

control and other ecosystem services provided by riparian systems. This degradation has prompted cities like Baltimore to implement restoration projects to reverse this degradation (Abdul & Kang, 2023).

The objectives of many urban stream restoration efforts are focused on meeting stormwater quality standards set by the Clean Water Act, which regulates a total maximum daily load of sediment, nitrogen, phosphorous and polychlorinated biphenyls (PCBs) into major waterways. With the focus on water quality, the extent to which restorations benefit riparian ecosystems is limited (Kenney *et al.*, 2012). As an example, the city of Baltimore, MD, has undertaken major urban stream restoration projects across all local watersheds (Baltimore City Department of Public Works, 2009), successfully reducing pollution drained into the Chesapeake Bay. While replanting of destroyed forest patches is standard practice, scientists and community stakeholders are increasingly concerned that some restorations do more harm than good, particularly when large swaths of mature forest habitat are removed to facilitate the restoration (Friends of Herring Run Parks, 2022). As a relatively new engineering practice, approaches to stream restoration should continue to evolve as new information and ideas come to light.

Remote sensing is a powerful and cost-effective method for studying the landscape functionality of ecosystems (del Río-Mena *et al.*, 2023; Iskin & Wohl, 2023). Multispectral remotely sensed imagery is increasingly used to generate detailed land use and land cover (LULC) maps (Claggett *et al.*, 2022) and to measure key indicators of ecological condition. One such indicator is the normalized difference vegetation index (NDVI), a widely used metric of vegetation health. NDVI has also been applied to classify vegetation types and assess both vegetation condition and landscape structure (Pace *et al.*, 2022). The ability to observe and measure land cover at high spatial and temporal resolution makes remote sensing particularly useful for understanding the potential of riparian systems to recover following stream restoration. Recent advances in very high-resolution drone-based multispectral imaging now allow for reliable species-level identification of riparian vegetation using machine learning (Rommel *et al.*, 2022). NDVI time series analysis can reveal the trajectory and pace of vegetative regrowth across disturbed and undisturbed areas (Fitts *et al.*, 2025), making it a valuable tool for evaluating the long-term effectiveness of restoration projects.

1.2. Research Questions and Hypothesis

Stream restoration projects, while often necessary to meet regulatory water quality standards, can cause significant disturbances to riparian ecosystems. For example, the removal of concrete channels and the excavation of new stream channels require the destruction of mature trees and displace aquatic and riparian organisms. As a result, forested areas are necessarily replaced with grass or pioneer species, reducing overall vegetation biomass. This raises the question; how severely are riparian forests impacted by stream restoration, and how does their recovery unfold over time? A key justification for this research lies in the need to quantify the ecological impact of restoration activities in order to refine and improve current methods. The hypothesis is that riparian ecosystems will require a significant time to recover after restoration, due to the loss of forest cover and leading to sustained reductions in NDVI values.

Despite prior efforts to monitor stream restoration effectiveness, there remains a gap in the literature regarding the specific ecological impacts of restoration activities on riparian vegetation health. This study aims to address that gap by leveraging high-resolution remotely sensed data to observe riparian vegetation dynamics over time at the stream-reach scale. The objectives of this study are to: (1) Examine a specific stream restoration case study in Baltimore County, Maryland. (2) Measure the extent and magnitude of deforestation resulting from restoration activity using remote sensing technology. (3) Observe the rate and spatial patterns of re-vegetation following the restoration.

2. Study Area and Methods

2.1. Study Area

This study evaluates the condition of a 11,190m^2 area alongside a stream restoration site along the Upper Jones Falls, restored by Blue Water Baltimore in 2016 (BWB Communications, 2016) (Figure 2A). As a representative example of similar efforts across Baltimore and the region, the site offers a valuable case study for assessing ecological outcomes.

The Upper Jones Falls Stream Restoration Project is located in a suburban neighborhood of Baltimore County, Maryland (Figure 1A). Jones Falls is a spring-fed stream in a temperate climate in the Montane-Piedmont floodplains ecosystem, originating in the Greenspring Valley of Baltimore County. The

surrounding watershed is relatively undeveloped, characterized primarily by large estates. To illustrate the site's ecological significance. The Maryland Department of Natural Resources Fisheries Service has recorded the highest standing crop of wild trout in any Maryland stream within the Jones Falls (MDTU, 2020). The restoration project was managed by Blue Water Baltimore and executed by Environmental Quality Resources. The process involved diverting the stream, removing a 152m (500ft) section of concrete channel, then excavating a new channel with a more natural form Figure 2B. Large stones were implemented to regulate water flow, reducing erosion and pollution. After the restoration, 600 native plants were planted (Figures 1C−E). The aim was to improve aquatic habitat, and enhance water quality, as well as monitor for changes in water quality (BWB Communications, 2016). Restoration work took place between May and October of 2016, and the restored stream segment is located at 39°23'45"N, 76°39'52"W.

A site visit was conducted on February 12, 2025 and again on June 4, to observe the landforms and vegetation and document the current state using small unoccupied aircraft system (sUAS) imagery. There is a stand of American Sycamore (*Plantanus occidentalis*) extending approximately 100 meters along the northern side of the riverbank in the restored area, while further up from the stream, saplings of Swamp White Oak (*Quercus bicolor*) and Black Cherry (*Prunus serotina*), have been planted more recently, which is evidenced by the protective grow tubes (Figure 1D). In contrast, undisturbed regions supported mature stands of American Elm (*Ulmus americana*), and Bush Honeysuckles (*Genus Lonicera*), suggesting a different successional stage. These direct observations of vegetation patterns inform interpretation of remote sensed data.

2.2. Data Sources

This study integrates remote sensing techniques using two primary data sources. Multispectral imageryfrom PlanetScope, a constellation of Earth-observing satellites with high spatial and temporal resolution, was used to calculate the NDVI and assess vegetation health following the restoration until 2025. High-resolution aerial imagery from the National Agricultural Imagery Program (NAIP) complements this by enabling detailed land cover classification and detection of landscape changes over time (See Supplementary Data Sheet 1 for a complete list of data sources).

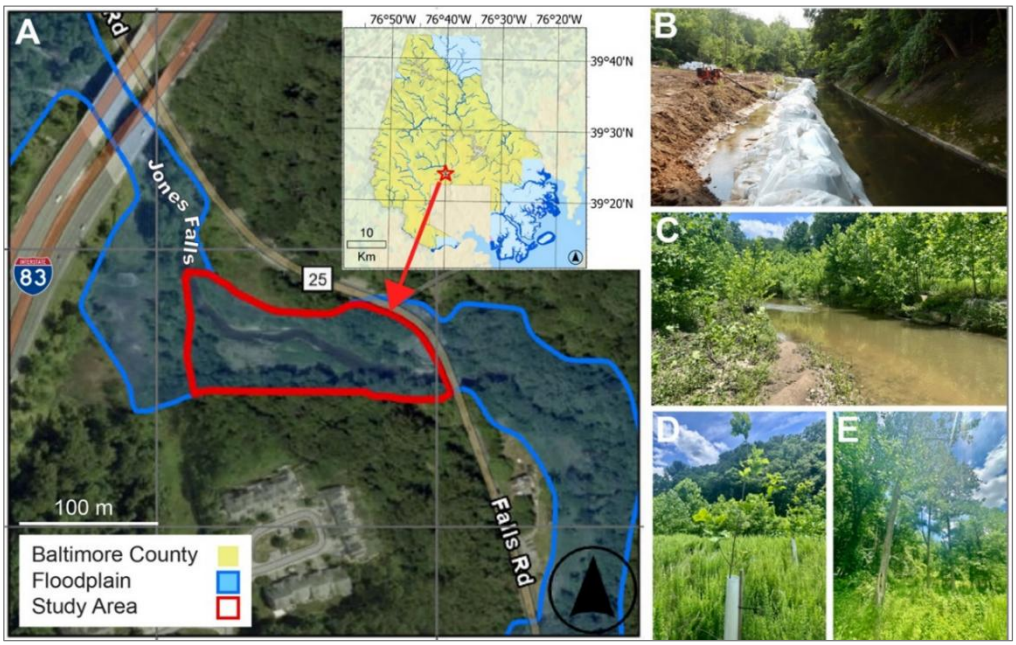

Figure 1. Study area: Upper Jones Falls stream channel removal and stream restoration. (A) The study area is bounded in red, within the floodplain (blue) located at the red star in Baltimore County, MD USA (inset, yellow). (B) Stream restoration construction in 2016, white sandbags on left for diverting the stream path, on the right is the concrete channel. Image used with permission of Blue Water Baltimore. (C) The restored channel in 2025, sycamore trees grow on both banks. (D) New plantings of oak and cherry in the meadow above the stream. (E) American elm in the older riparian forest not affected by the restoration.

The NAIP orthophotos were obtained from USGS EarthExplorer website (USDA, 2023). These high spatial resolution images are useful for identifying fine-scale characteristics of stream restoration sites, such as stone or concrete embankments, sandbars, and new tree plantings. Each image includes four bands: Red (R), Green (G), Blue (B), and Near-Infrared (NIR). Aerial image acquisition occurred before and after the restorations, on the following dates: 2015-07-24, 2017-06-11, 2021-06-17, and 2023-05-25 (Figures 2A−E). The USDA produced no images for this location in 2019, instead an aerial photo for that cycle was taken in 2018-11-06, but was not utilized for analysis because the acquisition date is well past the peak vegetation and the image is obscured by long shadows.

To obtain the most up-to-date observations of the study area, an aerial photographic survey of the study area was conducted on 2025-06-04 using a DJI Mini4Pro sUAS. The final orthorectified image was composed of 187 tiles mosaicked using PixPro software (Figure 2F).

The extent of the riparian zone was defined using the Federal Emergency Management Agency (FEMA) 100-year floodplain shapefile (Baltimore County, Maryland, 2018) from Baltimore County Open Data (Figure 2G), as the floodplain represents the area most likely to support riparian conditions due to its regular exposure to stream flow and flooding.

PlanetScope (PS) satellite imagery sourced from Planet.com (Figure 2H) was available beginning in October 2016, shortly after the restoration. This data set consists of Analysis-Ready PlanetScope imagery (Level 3B products); 3m spatial resolution, resampled from ~3.5m ground sampling distance (GSD), orthorectified surface reflectance product, radiometrically harmonized and spectrally aligned with Sentinel-2 bands: Blue (B2, 490 nm), Green (B3, 560 nm), Red (B4, 665 nm), and Narrow NIR (B4, 865 nm), facilitating consistent time-series comparisons (Planet, 2021).

Because PlanetScope images only became available beginning in 2016 after the restoration, additional images from the RapidEye satellite, also sourced from Planet.com, were used to assess vegetation conditions prior to restoration. These are orthorectified, and radiometrically corrected surface reflectance images at 5-meter spatial resolution (resampled from ~ 6.5m GSD) images (Level 3A products. The imagery includes five spectral bands: Blue (B1, 440–510 nm), Green (B2, 520–590 nm), Red (B3, 630–685 nm), Red Edge (B4, 690–730 nm), and Near-Infrared (B5, 760–850 nm) (Planet, 2019).

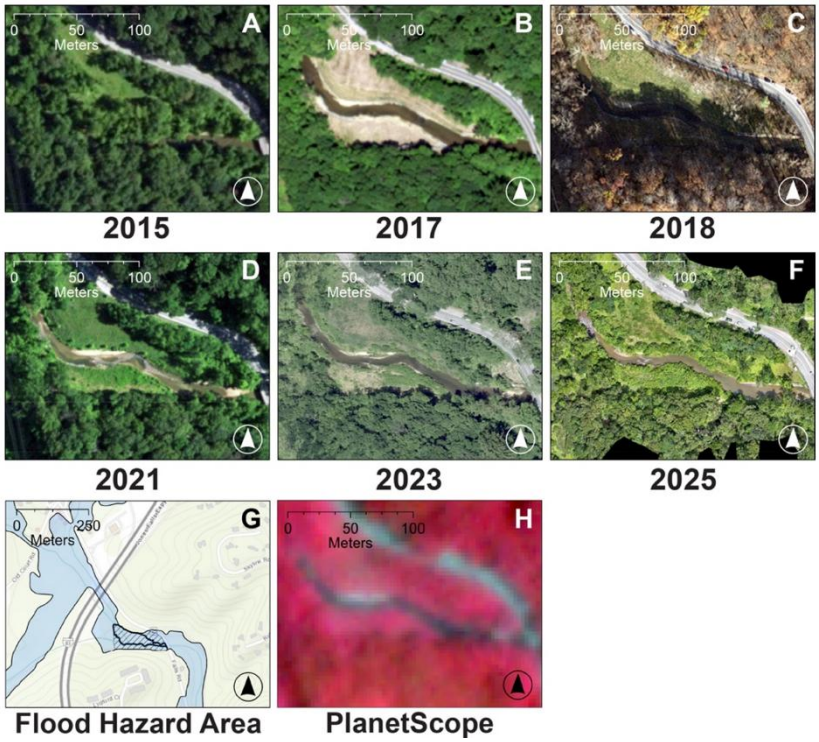

Figure 2. Data sources. (A–E) NAIP aerial orthophotos taken in the year below image. (F) sUAV aerial orthophoto taken in 2025. (G) FEMA 100-year floodplain, hatched area denotes the restoration area. (H) A representative multispectral satellite image, n=555 PlanetScope images.

2.3. Methods

To assess land cover changes, the study area was classified based on NAIP images from 2015, 2017, 2021 and 2023 and using the sUAV aerial mosaic from 2025. Images from 2015 and 2017 were first resampled from 1-m spatial resolution to 0.3-m resolution, to match the 2021 and 2023 images. The 2025 sUAV aerial mosaic was also resampled to 0.3m resolution. Images were then classified using Classification Wizard in ArcGIS Pro. Segmentation was unsupervised with spectral detail: 20, spatial detail: 10, and min. segment size: 10. Classification method was iso cluster, max. classes: 12, max. iterations: 50, max. merges 5, max. merge distance: 0.5, max samples per cluster: 2 and skip factor: 2. All classified images were then reclassified manually, to correct errors and reduce the number of classes to seven land cover classes, based on vegetation structure and surface characteristics: Canopy, Mixed Forest, Pioneer/Understory, Herbaceous, Barren, Developed, and Water (Table 1). Manual classification was informed by direct field observation and extrapolation between sequential years. These categories reflect different stages of vegetation, disturbance, and land use relevant to stream restoration monitoring.

Table 1. Land cover classification.

Class	Description	Rationale
Canopy	Tallest trees with whole crowns visible; dense upper layer of woody trees	Represents mature forest and urban forest canopy habitat
Mixed Forest	Intermediate sized vegetation; mix of small pre-canopy vegetation and shrubs	Reflects transitional forest zones and areas dominated by shrubs or low woody plants
Pioneer	Small woody vegetation, newly planted trees, or leafy understory vegetation	Indicates regrowth areas post-restoration or after disturbance, or exposed understory in canopy gaps
Herbaceous	Grass and groundcover with little vertical relief	Indicates lawns, mowed areas, and early successional vegetation
Barren	Bare ground, sandbars, trails, rocks, erosion control, recently cleared areas	Identifies unvegetated zones in the stream as well as disturbed areas
Developed	Road, bridges, guardrails, exposed concrete channel	Represents all artificial landforms in and around the area of interest
Water	Exposed water, not obscured by canopy in imagery	Marks stream channel presence

In order to focus the study on a representative area of interest, the reach of riparian zone near the removed channel was delineated using the FEMA 100-year floodplain shapefile (Figure 3). The cleared area was defined as all the Barren, Herbaceous and Water land cover that appeared in the 2017 NAIP imagery, and then intersected with the floodplain boundary to define the final cleared area shapefile. Water was included in the cleared area because it was canopy-covered in 2015 but fully exposed in 2017. As the study focuses on vegetation change, canopy removal over water is treated equivalently to that over bare ground.

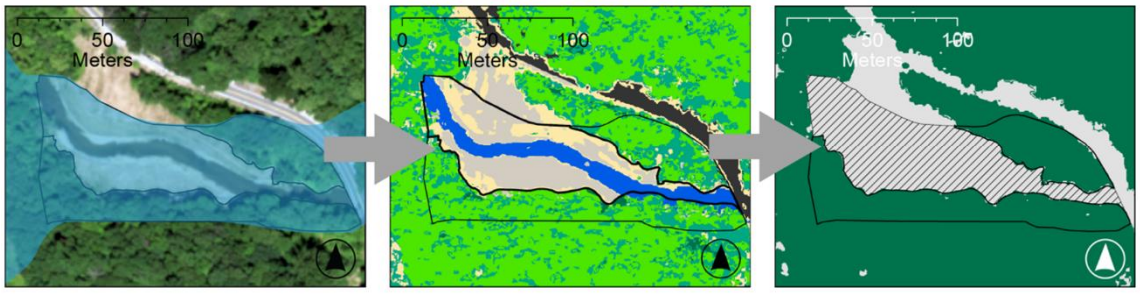

Figure 3. Generation of land cover and restoration extents. Land cover image was classified shortly after restoration using the NAIP image from 2017-06-11. The contiguous area within the floodplain classified as barren, herbaceous or water was identified as the cleared area, an uncleared region of equal size and within the floodplain was defined as the uncleared area. Both patches were converted to shapefiles for use as boundaries in subsequent analysis.

The boundary was smoothed to remove aliasing, resulting in a cleared region with an area of 5,595 m^2. As a reference area, an uncleared portion of adjacent riparian forest was also defined within the floodplain. The uncleared area serves as control to distinguish effects that are a direct result of deforestation and channel rerouting from any indirect effects like annual variations in precipitation, or from artifacts in the images like shadows. The NDVI value of the cleared area at any time point was interpreted relative to the uncleared control, rather than a theoretical baseline. One assumption is that prior to the restoration, the cleared and uncleared area had very similar properties in terms of land cover and mean NDVI. The uncleared area was drawn so that it covered the same surface area as the cleared area. These areas were then generated as shapefiles for further analysis and comparison of the cleared and uncleared areas.

To measure the impact of restoration on cleared and uncleared vegetation in the riparian zone, multispectral images from Planet were evaluated to measure NDVI for each area in each image (Figure 4). A total of 541 cloud-free and snow-free images from PlanetScope (PS2 and PS2.SD) constellations were acquired for dates between 08/14/2016 and 08/10/2025. The images were clipped using the cleared and uncleared boundaries with the Extract by Mask geoprocessing function in ArcGIS pro, then converted to NDVI rasters using the equation NDVI = (NIR−Red)/(NIR+Red). For each raster, the mean NDVI was calculated and taken as a representation of the overall vegetation index for that area. When multiple images were available for a single day, the average of their mean NDVI was used for that day, so that only one mean NDVI value was reported for each day in the time series. Because there were no PlanetScope images available prior to the restoration, four RapidEye images from 7/10/2015−8/4/2015 were used to establish a pre-restoration baseline (Supplementary Data Sheet 2 shows images used for specific dates and single image NDVI statistics). For RapidEye images bands 3 and 5 were used, for PlanetScope images bands 3 and 4 were used for red and NIR respectively. The files were batch processed using a custom ArcPy script.

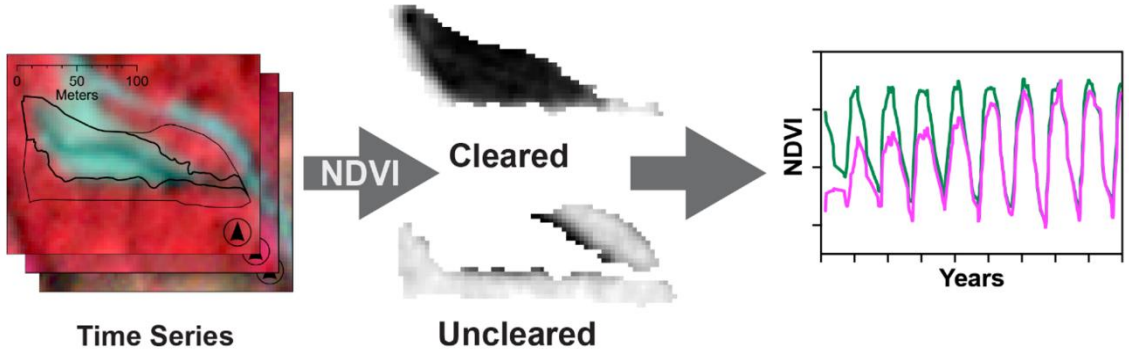

Figure 4. Calculation of NDVI. A PlanetScope image of the study area is shown in false color, where red represents the near infrared band and green represents the red band. The cleared or uncleared shapefile was used to clip a portion of the satellite images, which was then converted to an NDVI raster using the red and NIR bands. Then, mean pixel value was extracted from the layer statistics and compiled to generate a time-series.

3. Results

3.1. Land Cover Classification and Changes

Prior to clearing the area for stream restoration construction, most of the floodplain was forested. Approximately half of the areas of both the uncleared and to-be-cleared zones were classified as Canopy, with another quarter in each zone classified as Mixed Forest (Figures 5A & 5B, Table 2). The remaining land cover consisted mainly of exposed Pioneer vegetation along forest edges and a patch of Herbaceous vegetation in the area designated for clearing (Figure 4C). Notably, only a small fraction of the study area was classified as exposed Water, since nearly the entire length of the stream was shaded by late-successional canopy vegetation.

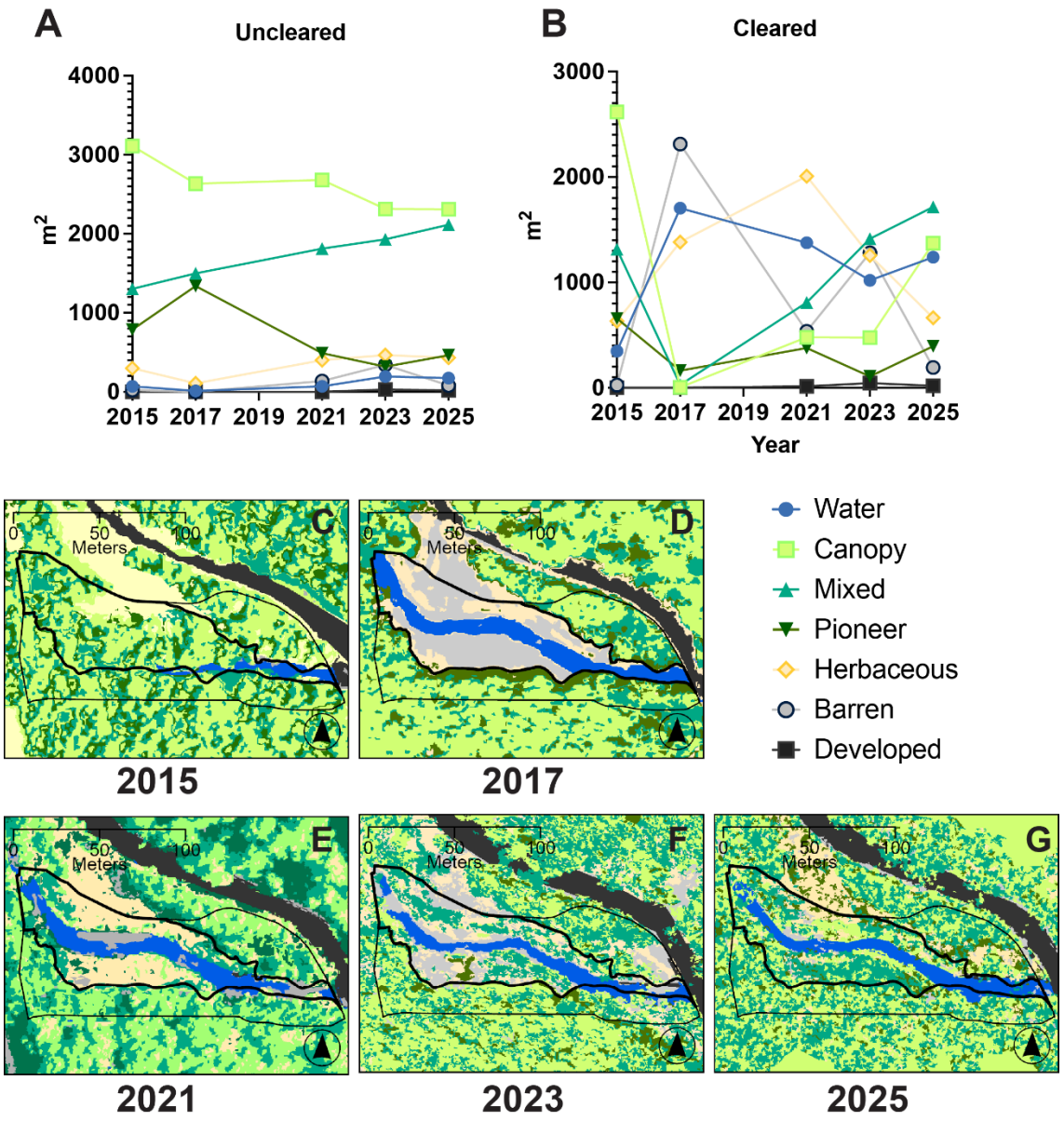

Figure 5. Land cover changes and maps. (A) Square meters of land cover for the uncleared riparian area over a 10-year timespan. (B) Square meters of land cover for the cleared area. (C−G) Land cover maps for each year that NAIP imagery was available.

Land cover was drastically altered following restoration. Forest clearing initially caused a complete loss of Canopy, Mixed Forest, and Understory vegetation within the defined cleared zone. In 2017, the first year following construction, land cover in this area consisted of 41% Barren ground, 30% open water, 25% Herbaceous vegetation, and 4% other land classes (Table 2, more detailed land cover data are in available Supplementary Sheet 3). Recovery of the Canopy and Mixed Forest classes progressed slowly through 2021 and 2023, while Pioneer vegetation expanded at a roughly linear rate. The Water area peaked in 2017 and remained relatively stable in the following years, with variation primarily driven by stream hydrology rather than canopy coverage. Between 2023 and 2025, significant vegetation recovery occurred: the cleared area regained 1,372 m² of Canopy (25% cover) and 1,715 m² (31% cover) of Mixed Forest. However, nine years post-restoration, Canopy cover remained 48% below 2015 levels, and exposed Water was still 257% greater than before the restoration.

Land cover also changed in the uncleared area over the course of the study. A loss of 477 m² of Canopy was observed in 2017, followed by another marked decline in tall trees in 2023. This decline coincided with a gradual increase in the Mixed Forest class, a decrease in Pioneer vegetation, and some gains in the Herbaceous class. A stand of trees on the north side of the stream, adjacent to the road, was removed prior to 2023 for unknown reasons (Figures 2E & 5F). The additional canopy loss in 2023 was accompanied by a 29 m² increase in Developed area, corresponding to newly visible sections of the bridge and remnants of the old concrete channel.

Overall, land cover analysis reveals that while vegetation in the cleared area is gradually returning, the landscape remains significantly changed in both structure and composition. The restoration led to substantial initial disturbance, followed by slow but measurable regrowth of forest classes. Meanwhile, even the uncleared area experienced notable shifts, underscoring the broader and more complex impacts of stream restoration on riparian land cover.

Table 2. Land cover area and change.*

Year	Class	Area (m^2)		Change Since 2015	
		Uncleared	Cleared	Uncleared	Cleared
	Total Area	**5595**	**5595**		
2015	Water	70	347		
	Canopy	3111	2618		
	Mixed	1304	1315		
	Pioneer	789	657		
	Herbaceous	298	632		
	Barren	23	26		
	Developed	0	0		
2017	Water	13	1703	–81%	391%
	Canopy	2634	5	–15%	–100%
	Mixed	1500	28	15%	–98%
	Pioneer	1338	162	70%	–75%
	Herbaceous	107	1383	–64%	119%
	Barren	0	2312	–98%	8760%
	Developed	2	1	**	**
2023	Water	194	1018	175%	193%
	Canopy	2315	475	–26%	–82%
	Mixed	1929	1414	48%	8%
	Pioneer	319	108	–60%	–84%
	Herbaceous	465	1256	56%	99%
	Barren	341	1281	1388%	4807%
	Developed	31	44	**	**
2025	Water	175	1239	149%	257%
	Canopy	2309	1372	–26%	–48%
	Mixed	2114	1716	62%	30%
	Pioneer	464	394	–41%	–40%
	Herbaceous	431	664	45%	5%
	Barren	80	192	249%	635%
	Developed	20	19	**	**

* More detailed land cover data are available in Supplementary Sheet 3.

** Percent land cover change was not reported because the Developed area coverage in 2015 was 0 m^2, therefore calculation was not possible.

3.2. NDVI Time Series Trend of NDVI

NDVI was analyzed over time to evaluate vegetation health dynamics in response to stream restoration (Figure 6A). Mean NDVI values for both cleared and uncleared areas, provide insight into the impacts of the restoration activity and recovery. Peak NDVI for both uncleared and cleared regions occurred during the months of July and August, indicated by the circled data points in Figure 6A. A minimum NDVI value was reached in the winter months, usually January.

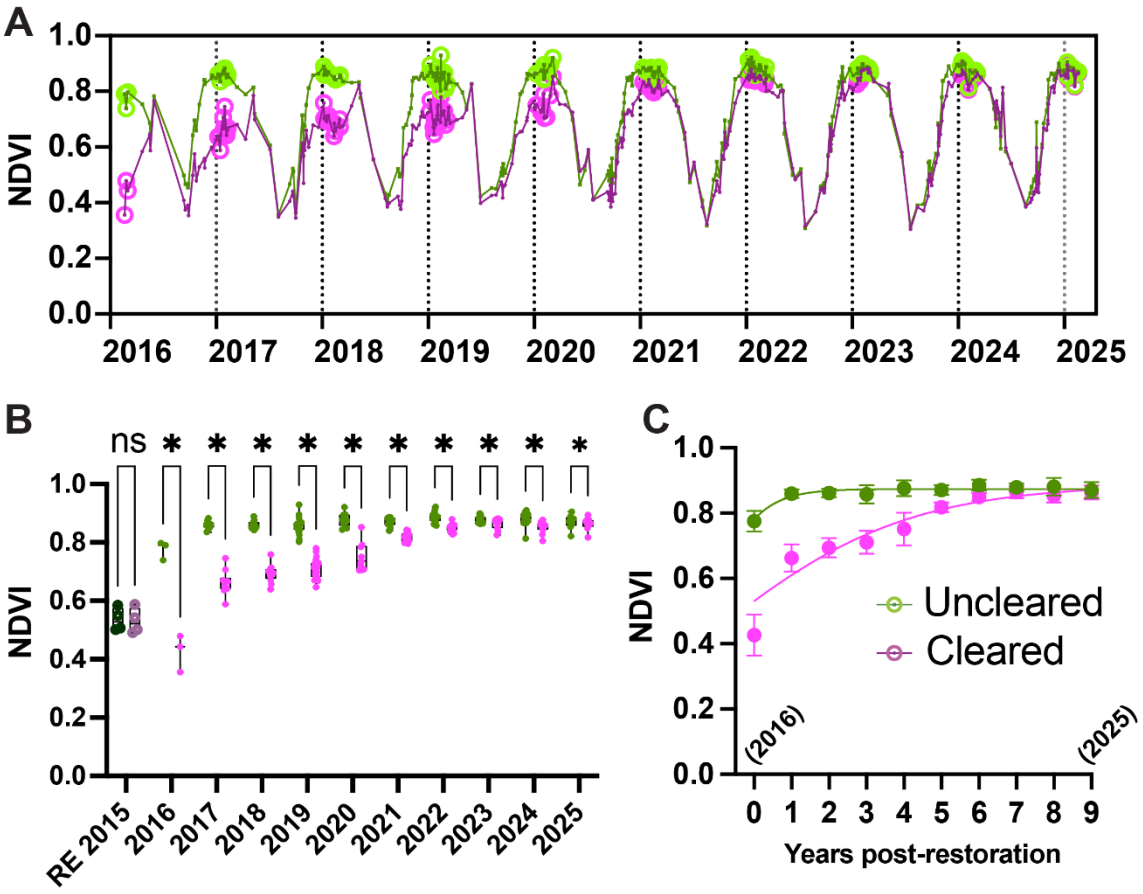

Figure 6. Restoration impacts on NDVI. (A) Time series of PlanetScope mean values for cleared and uncleared sections, n=362 days, circled points are peak vegetation days in July and August, dotted lines represent July 1st (B) Comparison of cleared and uncleared areas during peak vegetation, 2015 data is from RapidEye images, all other years are from PlanetScope, n=115 days, asterisks represent significant differences, multiple t-tests, *p*-value <0.001. (C) Logistic regression of NDVI over time, points represent mean NDVI during peak months, error bars show standard deviation, R^2= 0.3459 for uncleared and R^2= 0.8350 for cleared.

Prior to restoration in peak season 2015, the mean NDVI detected by RapidEye was not significantly different in the cleared versus the adjacent uncleared reference area (p = 0.284) (Figure 6B), indicating comparable vegetation cover at baseline. The restoration process caused a sharp decline in vegetation cover in the cleared area, as shown by the significant drop in NDVI following disturbance. In the first peak season following restoration the mean NDVI, was 0.78 and 0.43 for uncleared and cleared areas respectively. However, the cleared zone then experienced rapid vegetative growth, driven by replanting efforts and expansion of early successional species. By peak season of 2025, nine years post-restoration, NDVI in the cleared area had nearly reached equivalence with the uncleared reference zone; mean NDVI in the cleared area was 0.86, compared with 0.87 in the uncleared (Figure 6B), though it remained statistically lower (p < 0.001, t-test). The uncleared area also saw an initial reduction in mean NDVI, followed by a gradual increase during the study period, although less dramatic.

4. Discussion

4.1. Land Cover Changes

The classification of land cover within the riparian area captures the impact of the restoration activities on vegetation structure and spatial distribution. The most striking change is the complete removal of big trees in a continuous swath between the road and the stream. Water, Barren and Herbaceous classes remained dominant in the cleared area until 2025, when Mixed, Canopy and Water were the largest classes (Figure 5B). It is significant that 10 years post-restoration that canopy cover directly over the stream has not returned in a measurable way (Table 2). The loss of canopy over water is significant as streams lacking shade tend to become warmer, resulting in a loss of aquatic biodiversity (Fanelli *et al.*, 2019) and threatening the health of wild trout in particular (MDTU, 2020). In 2023 there is a spike in Barren land cover and a decrease in Herbaceous, correlated with a decrease in water coverage in the cleared area (Figure 5B); this is possibly a result of drought conditions during much of 2023 (NOAA, 2025). The recovery of canopy in 2025 to 25%, half of the 2015 coverage in the cleared area, is mainly due to the growth of the Sycamore trees along the streambanks, which accelerated between 2023 and 2025 (Figures 1D & 5F−G)), however these trees have not nearly reached the stature of the trees present before the restoration, such as the tall Elms (Figure 1E).

Changes in the uncleared portion may be influenced by clearing adjacent forest, but no direct link was demonstrated here. The first decrease in Canopy (Figure 5B) between 2015 and 2017 is most likely due to phenological differences, since the 2015 NAIP image was taken at peak growth on July 24th, while the 2017 NAIP image was acquired earlier in the year on June 11th, so the fullness of vegetation was greater in the 2015 image (Figures 2A & 2B), resulting in an apparent reduction of this class. The second decrease in canopy occurred between 2021 and 2023 when a stand of trees was removed from the northeast end of the uncleared area (Figures 2D & 5F). The expansion of Mixed class vegetation by 62% between 2015 and 2025, and the decrease in Pioneer by −41% could be due to a combination of factors, such as natural succession of understory to larger plants, and the reduction of canopy trees revealing the smaller mixed type of vegetation.

4.2. Recovery of NDVI in Cleared and Uncleared Areas during Peak Growth

The sharp NDVI decline in the cleared area immediately after restoration activity, confirms a substantial ecological disturbance. Prior to restoration, NDVI values in the cleared and uncleared zones were statistically indistinguishable ($p = 0.284$), suggesting comparable baseline vegetation cover and affirming that subsequent differences were attributable to the restoration activity. One caveat that should be addressed is the low absolute NDVI values observed in the uncleared and cleared areas prior to restoration in 2015 (Figure 6B); these values likely reflect sensor-specific calibration differences between RapidEye and PlanetScope imagery. However, it can be assumed that relative NDVI comparisons remain valid across sensors, and incorporation of RapidEye data was necessary to capture pre-restoration conditions, as PlanetScope imagery was not available prior to 2016. In the first peak season after restoration, PlanetScope images were used to measure NDVI, and they showed that the mean NDVI in the cleared zone dropped to 0.43, compared to 0.78 in the uncleared area. Over the following eight years, NDVI in the cleared section increased steadily, reaching 0.86 by the 2025 peak season. This value approached, but did not fully match, the uncleared zone's NDVI of 0.87, and the difference remained statistically significant ($p < 0.001$), indicating that recovery was strong but still incomplete. Notably, the uncleared reference area also experienced NDVI fluctuations, with a modest decrease followed by gradual increase. These changes may reflect indirect effects of the restoration, such as altered hydrology or edge effects, or broader landscape dynamics.

Seasonal variation was consistent across both zones, with NDVI peaking in July and August and reaching annual minima in the winter months, reinforcing that the observed long-term changes reflect true vegetation dynamics rather than seasonal fluctuations (Figure 6A). Between one and six years after restoration, NDVI in the cleared region began rising from the winter minimum earlier than in the uncleared area and reached peak values sooner, suggesting a shift in phenological timing potentially driven by early successional species. A recurring late-season spike in NDVI around November is also observed but is likely an artifact caused by long shadows in the imagery during that time of year (Figure 2C).

4.3. Logistic growth model predicts NDVI recovery following disturbance

To model NDVI recovery following stream restoration, a logistic model was fitted to the data using GraphPad Prism (Figure 6C). Literature has established that a logistic model is effective for evaluating bounded growth and decay of remotely sensed NDVI (Verma *et. al.*, 2016). Therefore, the logistic regression was chosen because it best captures the observed dynamics of a rapid initial recovery that slows as vegetation matures (Equation 1). In the cleared restoration area, the logistic model estimated a maximum NDVI (Y_m) of 0.8888, a starting value (Y_0) of 0.5306, a growth rate (k) of 0.3905, with a strong model fit ($R^2 = 0.8350$). In contrast, the uncleared area showed less overall change over time, with $Y_m = 0.8740$, $Y_0 = 0.7803$, k = 1.492, although a weaker fit ($R^2 = 0.3459$).

$$Y_{NDVI} = \frac{Y_m Y_0}{(Y_m - Y_0)e^{-kt} + Y_0} \quad (1)$$

This model predicts that the cleared area would reach the same NDVI value (Y_{NDVI}) after 9.44 years, a number that agrees with the observed result, suggesting that the logistic model effectively characterizes vegetation recovery in the cleared and uncleared areas, where growth followed a non-linear pattern (a table of logistic model results and example calculations are available in Supplementary Data Sheet 4). In contrast, the model showed a less precise fit for the uncleared area, consistent with more stable conditions and less directional change over time. Overall, these findings demonstrate that replanting efforts facilitated rapid vegetation regrowth in the cleared zone, though full ecological recovery, particularly in terms of vegetation density and structure, remains incomplete. According to the logistic model the mean NDVI in the cleared and uncleared areas is predicted to converge approximately 9 years post-restoration, and by year 10, the cleared zone is projected to slightly exceed the uncleared in NDVI (Supplementary Data Sheet 3). The model estimates that the uncleared area will reach its asymptotic NDVI value (Y_m) by year 25, which appears to be a reasonable recovery timescale given the observed NDVI trends and land cover changes. These results highlight the value of NDVI as a straightforward and effective metric for tracking riparian forest recovery over time.

4.4. NDVI Time Series Compared with Land Cover Analysis: Correlation and Contradiction

When interpreted alongside land cover data, the NDVI time series reveals important limitations in using greenness alone as a proxy for ecological recovery. Although NDVI values in the cleared area dropped sharply following restoration and then rebounded to nearly pre-disturbance levels, this trajectory does not fully capture the extent or quality of vegetation recovery. Prior to restoration, the cleared and uncleared areas had similar mean NDVI values (Figure 6B), which is expected given their comparable vegetation structure: 56% of the uncleared area and 47% of the cleared area were classified as Canopy (Table 2), and other land cover types were similarly distributed across both zones (Figure 5A).

A decade post-restoration, the apparent convergence of NDVI values between cleared and uncleared zones might suggest successful regrowth. However, the land cover data tells a more nuanced story. The sharp decline in biomass caused by the removal of mature trees was not reversed by the regrowth of equivalent vegetation; rather, much of the recovered NDVI can be attributed to early successional vegetation such as grass and shrubs, as well as young, small-diameter trees. These plant types have lower structural complexity and biomass than the mature forest they replaced but can nonetheless produce high NDVI values due to their chlorophyll content. Thus, the NDVI recovery reflects a return of vegetative cover in terms of greenness, but not necessarily in terms of forest structure, carbon storage, or habitat quality.

Interestingly, the NDVI in the cleared zone rebounded despite the addition of a widened stream channel, an area classified as Water, which would be expected to lower the average NDVI due to its non-vegetated surface. That NDVI still increased under these conditions highlights the dominance of low-stature, fast-growing vegetation in boosting spectral greenness measurements.

These findings challenge the initial hypothesis that NDVI would remain low in the cleared area due to the long-term loss of canopy. While NDVI recovered quickly, this appears to reflect a shift in vegetation type rather than a true return to pre-restoration forest conditions. The land cover analysis was essential for identifying persistent physical changes, such as the exposure of the streambed and the emergence of Barren

and Water classes, which NDVI alone cannot resolve. For example, while the Water class peaked in 2017 immediately following construction, it remained elevated throughout the study period, with stream hydrology driving year-to-year variation more than canopy closure. By 2025, exposed water area was still 257% greater than in 2015.

Despite signs of vegetative regrowth, forest recovery remains incomplete. Between 2023 and 2025, the cleared area regained 1,372 m² of canopy forest (25% cover) and 1,715 m² (31% cover) of mixed forest. However, this still represents a 48% reduction in canopy cover compared to baseline levels from 2015. These figures underscore the importance of supplementing NDVI time series with land cover classifications and structure-sensitive remote sensing tools to better evaluate restoration success. While NDVI is useful for tracking general vegetation recovery, it lacks the specificity to distinguish between grasses, shrubs, and mature forests, or to detect ongoing structural deficits in recovering ecosystems.

5. Conclusions

This study examined the Upper Jones Falls stream restoration, a project which replaced a concrete channel with a more natural stream form (BWB Communications, 2016). This construction involved significant ecological disruption, especially the removal of mature forest cover. The replacement of trees with grass or pioneer species reduced vegetation biomass and restructured the landscape, raising important questions about ecological impact and recovery. Replanted vegetation showed signs of health and gradual recovery over time, with NDVI values steadily increasing post-restoration.

In summary, the restoration clearly had a profound impact on riparian vegetation, initiating a rapid rebound in NDVI values. Although NDVI values returned to near pre-restoration levels, suggesting a recovery in greenness, this did not fully align with land cover analysis, which indicated a shift in vegetation type rather than a return to pre-disturbance forest conditions. This highlights a key limitation of NDVI: while it offers a useful approximation of restoration progress, it lacks ecological specificity without contextual land cover data. This study helps establish a baseline for remotely monitoring stream restoration and suggests that a minimum 10-year window is likely required to recover a certain level of ecological complexity.

Stream restoration is still a relatively new development in environmental engineering and landscape design, with new approaches being implemented rapidly. This study provides actionable insights for restoration contractors, advocacy groups, residents, and municipal agencies aiming to design projects that balance water quality goals with habitat connectivity, biodiversity, and long-term ecosystem health. Selection and placement of replanting species could be used strategically to restore canopy shading over the stream, accelerating the return of this important riparian ecosystem service. Certain vegetation types may be more effective in restoring canopy cover, especially those that extend over the stream path, these should be preserved when possible or prioritized for rapid recovery. It may be better to leave some patches of established vegetation, rather than clearing a large contiguous swath. Restoration progress can be monitored remotely and could provide an indicator that informs managers when intervention is required, by adding new saplings or helping replanted vegetation to establish.

As technology continues to advance, it would be possible to automate much of this analysis in order to create a dashboard for city managers to continuously monitor restorations and parklands, similar to how transportation departments monitor traffic with cameras and sensors. Integrating citizen science and on-the-ground observations could provide useful context to complement remote sensing data, including information about species presence, plant health, and wildlife activity. Looking forward, evaluating landscape metrics like heterogeneity at a fine scale could provide a measure of ecological resilience and also serve as a useful tool for restoration design. Future work should also examine how restoration affects urban wildlife corridors and movement patterns, not only vegetation metrics.

Data Availability: Supplementary data are available in the attachment and at https://bit.ly/4nyfji8.

Acknowledgment: This study is based upon work supported by the U.S. Geological Survey under Grant/Cooperative Agreement No. G23AP00683 (GY23–GY27). The authors thank Planet Inc. for providing access to their extensive catalog of high-resolution satellite imagery, and Patrick McMahon of Blue Water Baltimore for kindly granting permission to use the stream restoration photo. We are also grateful to Towson

University for access to ArcGIS Pro software, and to Carnegie Science for tuition reimbursement and the Prism software license.

Conflicts of Interest: The authors declare no conflicts of interest. The funders had no role in the design of the study; in the collection, analyses, or interpretation of data; in the writing of the manuscript; or in the decision to publish the results.

References

Abdul, J., & Kang, D. H. (2023). Improving the physical and biological condition of urban stream in the city of Baltimore. In *World Environmental and Water Resources Congress 2023* (pp. 579–586). https://doi.org/10.1061/9780784484852.055

Baltimore City Department of Public Works. (2009). *Urban streams and stream restoration*. https://publicworks.baltimorecity.gov/pw-bureaus/water-wastewater/surface/restoration

Baltimore County, Maryland. (2018). *Special Flood Hazard Area (BCR)*. Baltimore County GIS Open Data. Retrieved April 1, 2025, from https://opendata.baltimorecountymd.gov/datasets/BC-GIS::special-flood-hazard-area-bcr/explore

BWB Communications. (2016). *Jones Falls stream restoration*. Blue Water Baltimore. https://bluewaterbaltimore.org/blog/stream-restoration/

Cadenasso, M. L., Pickett, S. T. A., & Schwarz, K. (2007). Spatial heterogeneity in urban ecosystems: Reconceptualizing land cover and a framework for classification. *Frontiers in Ecology and the Environment*, *5*(2), 80–88. https://hero.epa.gov/hero/index.cfm/reference/details/reference_id/2495746

Claggett, P., Ahmed, L., Buford, E., Czawlytko, J., Macfaden, S., Mccabe, P., Mcdonald, S., O'neill-Dunne, J., Royar, A., Schulze, K., Soobitsky, R., & Walker, K. (2022). *Chesapeake Bay Program's One-meter Resolution Land Use/Land Cover Data: Overview and Production*. U.S. Geological Survey. https://www.usgs.gov/data/chesapeake-bay-land-use-and-land-cover-lulc-database-2022-edition

del Río-Mena, T., Willemen, L., Vrieling, A., & Nelson, A. (2023). How remote sensing choices influence ecosystem services monitoring and evaluation results of ecological restoration interventions. *Ecosystem Services*, *64*, 101565. https://doi.org/10.1016/j.ecoser.2023.101565

Fanelli, R. M., Prestegaard, K. L., & Palmer, M. A. (2019). Urban legacies: Aquatic stressors and low aquatic biodiversity persist despite implementation of regenerative stormwater conveyance systems. *Freshwater Science*, *38*(4), 818–833. https://doi.org/10.1086/706072

Ferreira, V., Albariño, R., Larrañaga, A., LeRoy, C. J., Masese, F. O., & Moretti, M. S. (2023). Ecosystem services provided by small streams: An overview. *Hydrobiologia*, *850*(12–13), 2501–2535. https://doi.org/10.1007/s10750-022-05095-1

Fitts, Y., Tucker, C., Hiernaux, P., Auda, Y., & Kergoat, L. (2025). Using PlanetScope NDVI time series to detect the phenology of individual trees in the Sahel. *Remote Sensing of Environment*, *321*, 114650. https://doi.org/10.1016/j.rse.2025.114650

Friends of Herring Run Parks. (2022). *Lay of the land: Herring Run stream restoration*. Friends of Herring Run. https://www.friendsofherringrun.org/stream-restoration-concerns.html Last access: 28 July 2025.

Iskin, E. P., & Wohl, E. (2023). Quantifying floodplain heterogeneity with field observation, remote sensing, and landscape ecology: Methods and metrics. *River Research and Applications*, *39*(5), 911–929. https://doi.org/10.1002/rra.4109

Kaushal, S. S., & Belt, K. T. (2012). The urban watershed continuum: Evolving spatial and temporal dimensions. *Urban Ecosystems*, *15*(2), 409–435. https://doi.org/10.1007/s11252-012-0226-7

Kenney, M. A., Wilcock, P. R., Hobbs, B. F., Flores, N. E., & Martínez, D. C. (2012). Is urban stream restoration worth it? *Journal of the American Water Resources Association*, *48*(3), 603–615. https://doi.org/10.1111/j.1752-1688.2012.00637.x

Maryland Trout Unlimited (MDTU). (2020). *Jones Falls restoration*. http://www.mdtu.org/jones-falls.html

Murphy, B. M., Russell, K. L., Mould, S., Vietz, G., & Nelson, P. A. (2022). Managing urban riverscapes: An assessment framework to integrate social-ecological values and physical processes. *Journal of Environmental Management*, *322*, 115862. https://doi.org/10.1016/j.jenvman.2022.115862

Morin, E., Herrault, P. A., Guinard, Y., Grandjean, F., & Bech, N. (2022). The promising combination of a Landcover approach and landscape connectivity modelling at a fine scale in urban planning. *Ecological Indicators*, *139*, 108930. https://doi.org/10.1016/j.ecolind.2022.108930

National Oceanic and Atmospheric Administration (NOAA). (2025). *Baltimore County conditions*. Drought.gov. https://www.drought.gov/states/maryland/county/baltimore

Pace, G., Gutiérrez-Cánovas, C., Henriques, R., Carvalho-Santos, C., Cássio, F., & Pascoal, C. (2022). Remote sensing indicators to assess riparian vegetation and river ecosystem health. *Ecological Indicators*, *144*, 109519. https://doi.org/10.1016/j.ecolind.2022.109519

Pennington, D. N., Hansel, J. R., & Gorchov, D. L. (2010). Urbanization and riparian forest woody communities: Diversity, composition, and structure within a metropolitan landscape. *Biological Conservation*, *143*(1), 182–194. https://doi.org/10.1016/j.biocon.2009.10.002

Pickett, S. T. A., Cadenasso, M. L., Baker, M. E., Band, L. E., Boone, C. G., Buckley, G. L., Groffman, P. M., Grove, J. M., Irwin, E. G., Kaushal, S. S., Ladeau, S. L., Miller, A. J., Nilon, C. H., Romolini, M., Rosi, E. J., Swan, C. M., & Szlavecz, K.

(2020). Theoretical perspectives of the Baltimore Ecosystem Study: Conceptual evolution in a social-ecological research project. *BioScience*, *70*(4), 297–314. https://doi.org/10.1093/biosci/biz166

Planet. (2019). *Combined imagery product specifications*. https://assets.planet.com/docs/combined-imagery-product-spec-april-2019.pdf

Planet. (2021). *Planetscope product specifications*. https://assets.planet.com/docs/Planet_PSScene_Imagery_Product_Spec_June_2021.pdf

Rommel, E., Giese, L., Fricke, K., Kathöfer, F., Heuner, M., Mölter, T., Deffert, P., Asgari, M., Näthe, P., Dzunic, F., Rock, G., Bongartz, J., Burkart, A., Quick, I., Schröder, U., & Baschek, B. (2022). Very high-resolution imagery and machine learning for detailed mapping of riparian vegetation and substrate types. *Remote Sensing*, *14*(4), 954. https://doi.org/10.3390/rs14040954

Rusnák, M., Goga, T., Michaleje, L., Michalková, M. Š., Máčka, Z., Bertalan, L., & Kidová, A. (2022). Remote sensing of riparian ecosystems. *Remote Sensing*, *14*(11), 2645. https://doi.org/10.3390/rs14112645

U.S. Department of Agriculture (USDA). (2023). *National Agricultural Imagery Program (NAIP) – 1 meter* [dataset]. https://doi.org/10.5066/F7QN651G

Verma, M., Friedl, M. A., Finzi, A., & Phillips, N. (2016). Multi-criteria evaluation of the suitability of growth functions for modeling remotely sensed phenology. *Ecological Modelling*, *323*, 123–132. https://doi.org/10.1016/j.ecolmodel.2015.11.012

Walsh, C. J., Roy, A. H., Feminella, J. W., Cottingham, P. D., Groffman, P. M., & Morgan, R. P. (2005). The urban stream syndrome: Current knowledge and the search for a cure. *Journal of the North American Benthological Society*, *24*(3), 706–723. https://doi.org/10.1899/04-028.1

Research Article

Satellite Imagery Analyses of Seasonal Shifts of Vegetation Greenness at the Great Smoky Mountains National Park

Alex Larson[1], Jaemo Yang[2,*], Edylson Hernandez[1], Seung Hee Choi[1], and Jeong Chang Seong[1]

[1] School of Field Investigations & Experimental Sciences, Dr. James 'Earl' Perry College of Mathematics, Computing, and Sciences, University of West Georgia, Carrollton, GA 30118, USA; al00320@my.westga.edu; eh00128@my.westga.edu; seunghee@westga.edu; jseong@westga.edu

[2] Department of Geography, Kyung Hee University, Seoul 02447, Republic of Korea; belaw6002@khu.ac.kr

[*] Corresponding Author: belaw6002@khu.ac.kr

Academic Editor: Qi Chen
Received: 28 May 2025
Revised: 29 August 2025; 18 September 2025
Accepted: 22 September 2025
Published: 24 October 2025

Abstract: This study investigates the temporal shifts in seasonal vegetation coloration, focusing on changes in greenness levels (measured by NDVI) from 1982 to 2023, using multiple satellite sources including AVHRR, Landsat, MODIS, and VIIRS. The primary objectives of this research are twofold: (1) to determine whether greenness levels have significantly changed during spring and fall, and (2) to assess whether there are notable differences in NDVI values among the various imaging sensors used. Given the context of global warming, it is plausible that greenness levels would show an increase on the same date in early spring or late fall across multiple years. Our study area consists of the Great Smoky Mountains National Park, where we analyze the timing of seasonal changes, revealing a trend toward earlier springs and longer falls. Our findings indicate significant increases in NDVI values during spring across all datasets, notably from AVHRR and Landsat, while fall data shows less consistent trends, with MODIS and VIIRS revealing minimal changes. The research highlights the importance of sensor selection in NDVI measurements, with non-parametric test results confirming significant variances among the sensors analyzed. This study contributes to understanding the implications of climate change on vegetation dynamics, underscoring the need for continued monitoring as seasonal patterns evolve.

Keywords: shift of greenness, NDVI, Great Smoky Mountains National Park, remote sensing

1. Introduction

Seasonal shifts in vegetation phenology have become increasingly noticeable: springs are arriving earlier and autumn colors emerging later. Multi-decadal analyses document significant alterations in the timing, onset, and duration of seasons, with potential long-term ecological consequences as these changes intensify (Eastman *et al*., 2013; Rozenstein & Adamowski, 2017; Calinger & Curtis, 2023; Hassan *et al*., 2023; Guo *et al*., 2024). Understanding these shifts is especially important for complex, mountainous, and largely protected forests such as the Great Smoky Mountains National Park (GSMNP), where even subtle changes in greenness can ripple through biodiversity, productivity, tourism, and ecosystem dynamics. Especially considering recent unprecedented climate anomalies, such as global warming the analysis of vegetation greenness changes over long time periods is becoming increasingly crucial.

Satellite remote sensing provides a consistent framework for quantifying vegetation greenness via the normalized difference vegetation index (NDVI), a standardized ratio of near-infrared and red reflectance that acts as a robust indicator of photosynthetic activity and ecosystem productivity (Tucker, 1979). NDVI can be computed from any multispectral sensor with visible and near-infrared bands (Huang *et al*., 2020) and is widely used across applications (e.g., Shi *et al*., 2023; Mehmood *et al*., 2024; Tuoku *et al*., 2024; Lu *et al*., 2025). NDVI is calculated by [NDVI = (NIR − Red) / (NIR + Red)], where NIR is the near-infrared band reflectance and Red is the red band reflectance; values range from −1 to +1, with healthy green vegetation typically positive. In practice, multiple sensors have been used to calculate NDVI such as Landsat (medium spatial resolution since 1972), AVHRR (1-km multispectral data across the NOAA series, 1979–2019),

Citation: Larson, A., Yang, J., Hernandez, E., Choi, S. H., & Seong, J. C. (2025). Satellite imagery analyses of seasonal shifts of vegetation greenness at the Great Smoky Mountains National Park. *Journal of Earth Observation and Geospatial Applications, 1*(1), 35–50. DOI: https://doi.org/10.65372/q71k6m39

MODIS (36 spectral bands since 1999), and VIIRS (launched in 2011 to continue and expand Earth observation as MODIS and AVHRR age). Free and open datasets obtained from those sensors, particularly, have made long-term vegetation monitoring easily accessible.

Previous research has consistently linked NDVI variability to climate drivers while documenting widespread greenness increase trends. For example, Yang *et al*. (1997) showed that NDVI changes are closely tied to temperature. Wang *et al*. (2003), using AVHRR, also found a strong relationship between temperature and NDVI at early and late growing seasons in the central Great Plains, U.S.A. At the global scale, Eastman *et al*. (2013) reported that more than half of the Earth's land surface (56.30%) exhibited significant trends, with increasing NDVI values and lengthened growing seasons in many forested areas. At the national level, Nash *et al*. (2017) found that NDVI changed significantly across 48% of the United States over 25 years, with 85% of those changes reflecting increased greenness. However, responses are not uniform: in Russia's tundra biome at the Bovanenkovo region, Lemenkova (2015) documented a decline in NDVI (1988–2011) using three Landsat TM images, attributing it to environmental and anthropogenic factors.

From a methodological perspective, extracting reliable NDVI trends from multi-sensor archives requires close attention to data quality and sensor variability. Effective use of NDVI depends on multispectral data quality and careful interpretation, given atmospheric effects, signal degradation, and sensor characteristics (Huang *et al*., 2020). Furthermore, different datasets might bring unstable consistency at different regions as different AVHRR datasets show inconstancy at Europe, Africa, and the Sahel (Beck *et al*., 2011). Concerns about sensor reliability also remain critical as demonstrated by two different camera sensors onboard unmanned aerial vehicles (Deng *et al*., 2018). Wang *et al*. (2012) also found a 0.001–0.004 yr^{-1} decline of NDVI calculated with the MODIS sensor under a simulated aerosol conditions and surface types. To address these issues, the AVHRR, MODIS, Landsat, and VIIRS datasets have been processed multiple times with new algorithms to make improved scientific time-series datasets. In the case of AVHRR, Version 6 was published in 2023 (Roger *et al*., 2023). Landsat was comprehensively reprocessed to produce Collection 2 (Crawford *et al*., 2023). MODIS datasets were reprocessed to incorporate various calibrations and corrections to produce Version 6.1 products (Vermote, 2021). VIIRS products were also reprocessed to create Version 2 (Vermote *et al*., 2023).

Along with these advances, important gaps remain in analyzing long-term vegetation responses to dynamic climate changes. One is that relatively few studies have used the recently reprocessed products that have incorporated various calibrations and corrections. It is still questionable to check if they endorse significant changes of greenness over time. The other is whether NDVI changes obtained from AVHRR, Landsat, MODIS, and VIIRS are consistent across sensors with known differences and limitations (Huang *et al*., 2020; Beck *et al*., 2011; Wang *et al*., 2012; Deng *et al*., 2018).

To fill these gaps, this study aims at analyzing vegetation greenness characteristics using the recently-reprocessed AVHRR, Landsat, MODIS, and VIIRS products spanning 1982–2023. Specifically, research objectives are (1) evaluating whether NDVI has changed significantly during spring and fall in GSMNP, and (2) assessing the extent of variation in NDVI values among sensors observing the same landscape and dates.

This study offers several key contributions. First, it provides multi-decadal trends in greenness changes with multiple sensors, focusing on a well-preserved, species-rich temperate forest landscape in the United States. Second, by analyzing the same calendar dates in both spring and fall, it directly addresses phenological transitions that are particularly relevant for climate change. Third, through a comparative analysis of newly-reprocessed AVHRR, Landsat, MODIS, and VIIRS data, while considering known data-quality and processing issues (Huang *et al*., 2020; Beck *et al*., 2011; Wang *et al*., 2012; Deng *et al*., 2018), this study highlights how sensor selection affects vegetation greenness analysis.

2. Methodology

2.1. Study Area

The Great Smoky Mountains National Park, covering approximately 2,114 km², was chosen as the study area (Figure 1) because of its rich deciduous tree population and limited human impact from 1982 to 2023. According to Walter *et al*. (2021), the Great Smoky Mountains National Park has a humid, continental climate characterized by a mean annual temperature of 13.3°C. The park receives approximately 1,400 mm of precipitation annually in the low-elevation valleys, while higher elevations receive over 2,200 mm of precipitation each year. Over 95% of the area is forested, with elevations ranging from 270 to 2,025 meters.

At elevations of 1,600 meters and above, the predominant tree species are evergreens, including hemlock (*Tsuga canadensis*), balsam fir (*Abies balsamea*), Fraser fir (*Abies fraseri*), and red spruce (*Picea rubens*). In contrast, lower elevations feature mainly deciduous trees such as tulip tree (*Liriodendron tulipifera*), red maple (*Acer rubrum*), and oak (*Quercus* spp.), alongside dense understories of evergreen shrubs like mountain laurel (*Kalmia latifolia*) and great laurel (*Rhododendron maximum*). The following shows the land cover types of the Great Smoky Mountains National Park when analyzed with the 2025 National Land Cover Dataset from the U.S. Geological Survey (2025) – Water (0.1%), Urban and Built-up (0.6%), Deciduous Forest (43.7%), Evergreen Forest (12.1%), Mixed Forest (42.8%), and Others (0.7%).

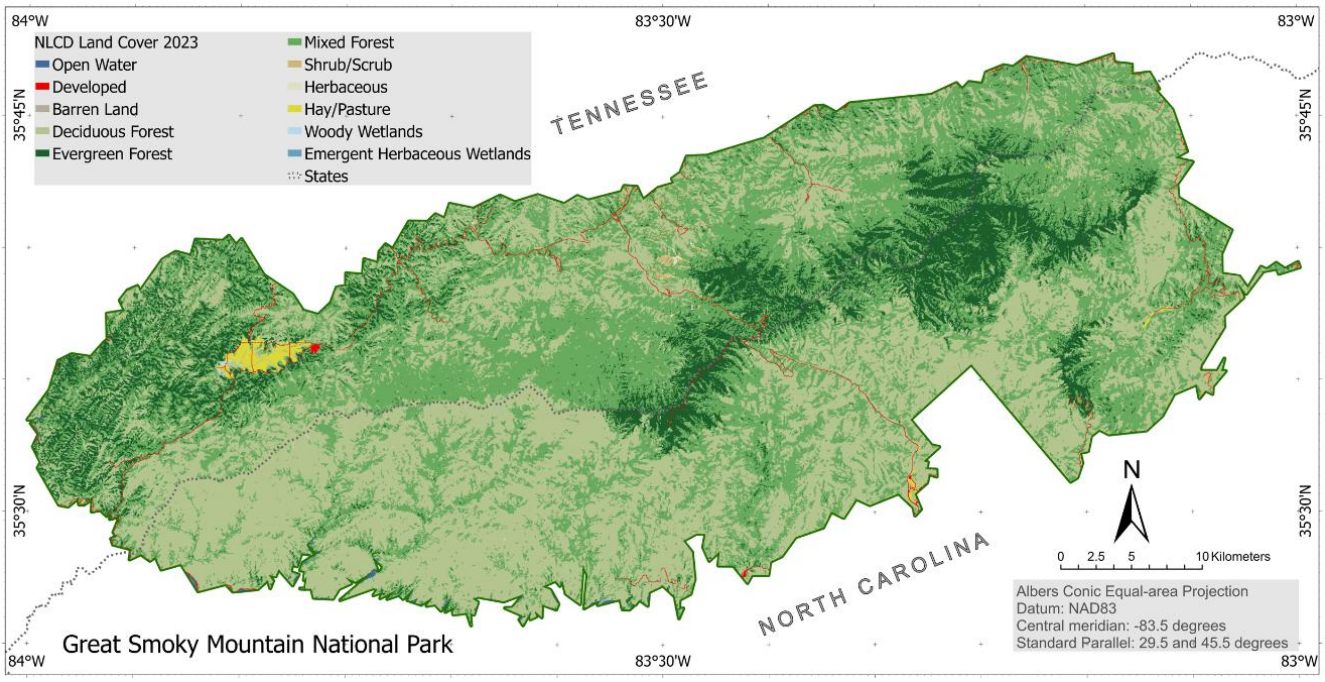

Figure 1. Study area.

2.2. Data Processing

The Google Earth Engine (GEE) and satellite imagery, courtesy of U.S. Geological Survey and NOAA, were utilized to process multi-year time-series datasets. Table 1 lists the datasets processed with GEE, while Table 2 details the specific days of each year that were selected for retrieving satellite imagery. Of the four data sources, the MODIS dataset is unique as it utilizes 8-day images to generate an 8-day composite image based on the best-quality pixels. For Landsat, images from Landsat 4, 5, 7, and 8 were used. Additionally, due to the Landsat's 16-day revisit period (or the 8-day revisit when two Landsat satellites were operational), available images were searched using the 11-day span. Cloud-contaminated pixels and Scan Line Corrector (SLC) error pixels in Landsat 7 were masked using the quality control bands included in each dataset. The average NDVI values and the count of good quality pixels were calculated with the Reducer.mean() and Reducer.count() functions, respectively. If the count of good quality pixels was fewer than 10% of total pixels, that year's dataset was excluded from the analyses. The JavaScript codes used in the GEE Code Editor are available in Appendices 2 through 5.

Table 1. Satellite imagery data sources and their product names in the Google Earth Engine.

Data Source	Dataset Name
AVHRR	NOAA CDR AVHRR: Surface Reflectance, Version 5, 1km.
Landsat	USGS Landsat (Collection 2, Surface Reflectance, Tier 1, Level 2), 30m.
MODIS	MOD09A1.061 Terra Surface Reflectance 8-Day Global 500m.
VIIRS	VNP09GA: VIIRS Surface Reflectance Daily 500m and 1km.

Table 2. The days of each year that were browsed in GEE.

Data Source	Spring Days of Each Year	Fall Days of Each Year
AVHRR	114–116	305–307
Landsat	One day between 111–121	One day between 300–310
MODIS	Composite of 114–121	Composite of 298–305
VIIRS	114–116	305–307

2.3. Statistical Analysis

For AVHRR, Landsat, or VIIRS, if multiple mean values exist for the same season, they were combined to create a grand mean. For example, the mean values of AVHRR for the 114th, 115th, and 116th days in 1982 were averaged to yield the grand mean for spring 1982. The trends in annual mean NDVI changes were then analyzed using the Mann-Kendall test (Mann, 1945; Kendall, 1975; Kenabatho, 2025) to determine if the mean values had significantly increased or decreased. Additionally, simple linear regression analysis was applied to model the trends in NDVI value changes. The use of regression analysis in this study should be viewed as exploratory, given the potential violation of statistical assumptions. Considering the long period of data collection by AVHRR and Landsat, the one-way ANOVA analysis was applied to determine if there were significant differences before and since 2001. The year 2001 was chosen because it divides the study years equally into two groups.

In order to test differences among sensors, the homoscedasticity of variances was tested first. The Brown-Forsythe test (Brown, 1974) was used because of its robustness and less sensitivity to outliers. As shown in Table 3, the Brown and Forsythe test did not detect statistically significant differences in the spring, indicating that variances can be considered equal across sensors. In contrast, it revealed significant differences in the fall, suggesting a violation of the homoscedasticity of variance assumption. The normality was also tested with the Shapiro-Wilk test on each sensor's spring and fall data. As shown in Table 4, the normality assumption is violated by the Landsat spring data and the VIIRS fall data. With the violations of homoscedasticity and normality assumptions, the Kruskal-Wallis test (Kruskal & Wallis, 1952) was performed to test differences among sensors. Furthermore, the Dunn's test (Dunn, 1964) was used to conduct pairwise comparisons.

Table 3. Brown and Forsythe test of the equality of variances.

	df_1	df_2	*F*-statistic	*p*-value
Spring	3	89	1.63	0.187
Fall	3	83	4.72	0.004

Table 4. Shapiro-Wilk normality test results (*W:* test statistic).

	AVHRR		Landsat		MODIS		VIIRS	
	Spring	Fall	Spring	Fall	Spring	Fall	Spring	Fall
Test Statistic *W*	0.960	0.971	0.806	0.985	0.959	0.954	0.959	0.822
p-value	0.283	0.625	0.000	0.972	0.427	0.325	0.753	0.017

3. Results

3.1. Trends of Annual Mean NDVI Changes

Appendix 1 presents annual mean NDVI values categorized by seasons (spring and fall) and imaging sensors (AVHRR, Landsat, MODIS, and VIIRS) from 1982 to 2023. The empty cells in the table indicate no data available due to sensor availability or image quality masks. Rows were shaded for the convenience of reading.

Figure 2 shows scatterplots of the data with linear regression and Mann-Kendall (MK) test results. The AVHRR dataset (2a and 2b) shows a positive trend in NDVI over time, particularly in the spring, where both the linear regression and Mann-Kendall tests indicate strong significance ($p < 0.05$). The fall season (2b) also shows a positive trend, though it is weaker, with a lower R^2 value and a near-significant *p*-value in the MK test. Overall, AVHRR suggests an increase in vegetation greenness over the years, especially during

springtime. The Landsat dataset (2c and 2d) presents a more mixed picture. In the spring (2c), the NDVI has a moderate upward trend, with both the regression and MK tests showing significant results. However, in the fall (2d), the trend is weak and not statistically significant. This suggests that the increase in vegetation greenness might be more prominent during the early growing season, but less so in the later months of the year.

The MODIS (2e and 2f) and VIIRS (2g and 2h) datasets show minimal changes in NDVI trends. MODIS reveals almost no significant trend in both spring and fall, with very low R^2 values and non-significant p-values, suggesting no notable changes in vegetation. VIIRS, on the other hand, shows a slight negative trend in the spring, but a significant positive trend in the fall based on the MK test, indicating potential seasonal differences in vegetation activity in more recent years. Overall, the trends across datasets suggest variability in seasonal vegetation dynamics depending on the data source.

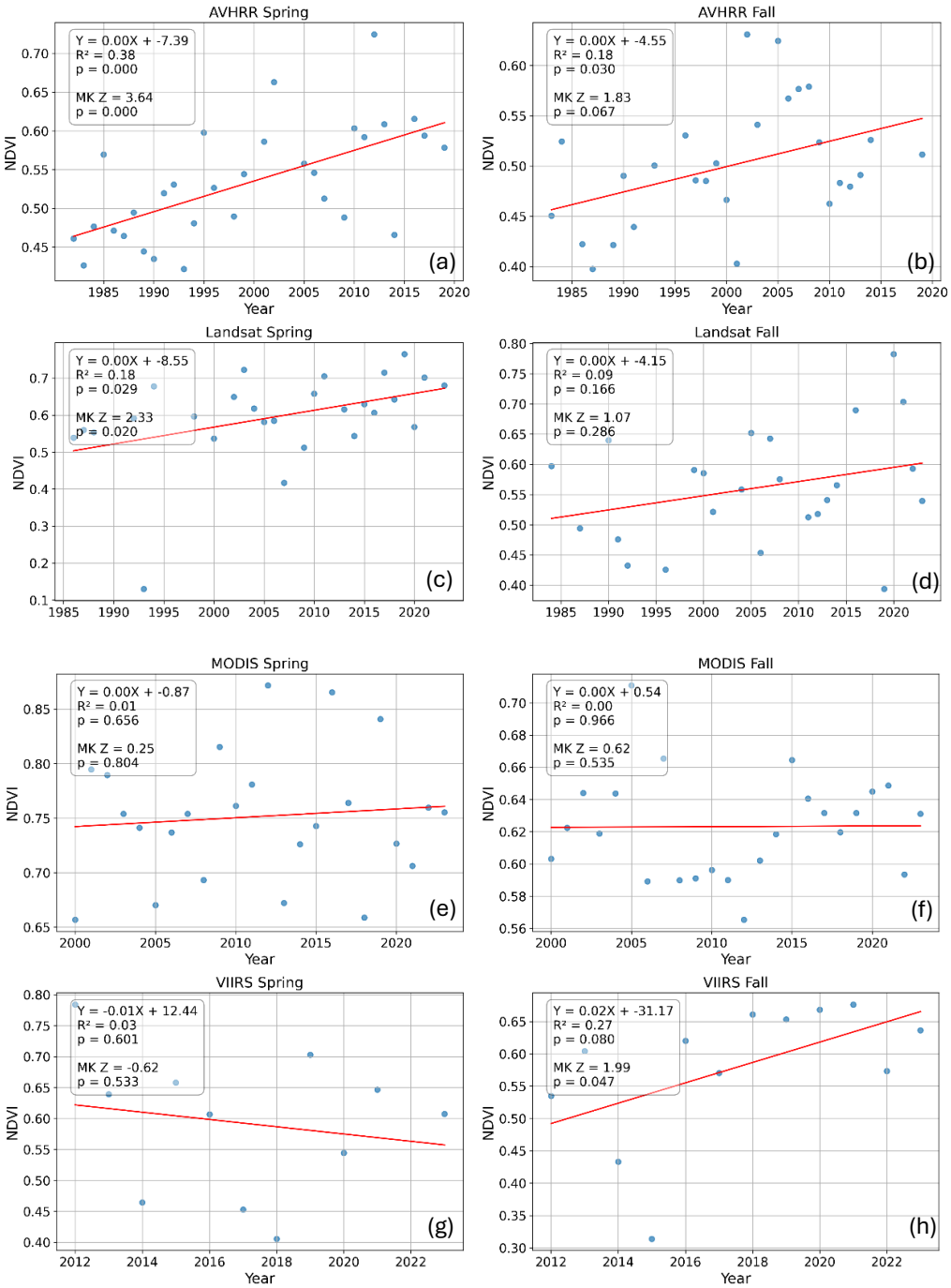

Figure 2. Scatterplots of NDVI annual changes with linear regression and Mann-Kendall tests.

3.2. Comparisons of Before and Since 2001

Table 5 compares NDVI-means before and since 2001 for the AVHRR and Landsat datasets across both spring and fall seasons. Considering the temporal coverage of dataset, AVHRR and Landsat were analyzed as they provide a much longer temporal record compared to MODIS and VIIRS.

For AVHRR Spring dataset, the NDVI mean significantly increased from 0.491 before 2001 to 0.581 since 2001. The *F*-statistic of 18.083 (df1=1, df2=29) and the very low *p*-value ($p = 0.000$) suggest that the observed increase in NDVI is statistically significant, indicating a notable change in vegetation activity in the spring season since 2001. Similarly, AVHRR Fall dataset shows a significant increase in NDVI from 0.471 to 0.529, with an *F*-statistic of 7.745 (df1=1, df2=25) and a *p*-value of 0.010, confirming that the increase in NDVI for fall is also significant, though to a lesser extent than in spring.

For the Landsat Spring dataset, there is a clear upward shift in NDVI, increasing from 0.523 before 2001 to 0.627 since 2001. The *F*-statistic of 4.835 (df1=1, df2=25) and *p*-value of 0.037 indicate that this change is statistically significant, supporting the conclusion that there has been a meaningful increase in spring vegetation as observed by Landsat since 2001. This suggests that, like AVHRR, Landsat also detects an increase in vegetation productivity in the spring season since 2001.

In contrast, the Landsat Fall data demonstrates only marginal NDVI increase from 0.530 to 0.578, which was not statistically significant as indicated by the *F*-statistic of 1.378 (df1=1, df2=22) and a *p*-value of 0.253. This suggests that vegetation activity in the fall did not experience a significant change since 2001 based on the Landsat observations, while the overall results reveal a consistent and statistically significant increase in spring NDVI. Overall, the one-way ANOVA results indicate a stronger trend of NDVI increase in spring than in fall for both datasets.

Table 5. One-way ANOVA analysis.

Dataset	NDVI Mean Before 2001	NDVI Mean Since 2001	*F*-statistic	*p*-value
AVHRR Spring	0.491	0.581	$F_{\{1,29\}} = 18.083$	0.000
AVHRR Fall	0.471	0.529	$F_{\{1,25\}} = 7.745$	0.010
Landsat Spring	0.523	0.627	$F_{\{1,25\}} = 4.835$	0.037
Landsat Fall	0.530	0.578	$F_{\{1,22\}} = 1.378$	0.253

3.3. Comparisons among Imaging Sensors

Non-parametric test methods have fewer assumptions compared to parametric test methods. They do not assume homoscedasticity of variances and normality, which makes them suitable when those assumptions are not met. In addition, non-parametric methods are based on ranks or order statistics. The Kruskal-Wallis test is one of the non-parametric methods used to compare the medians of three or more groups. It is more robust to outliers or extreme values, as it is based on rank. This test is insensitive to variability; it allows us to compare medians without assuming equal variances. The Kruskal-Wallis test result in Table 6 concludes that there are significant differences among the four sensors in both spring and fall seasons, as the *p*-values are less than the significance level 0.05.

Table 6. Kruskal-Wallis test.

		Spring Median	Fall Median
Sensor	AVHRR	0.5264	0.4911
	Landsat	0.6066	0.5621
	MODIS	0.7540	0.6210
	VIIRS	0.6073	0.6120
Kruskal-Wallis Test Results	Kruskal-Wallis *H*-statistic[1]	50.198	31.131
	df	3	3
	p-value	0.000	0.000

[1] The Kruskal-Wallis test statistic approximates a χ^2 distribution.

These results indicate that the median NDVI values measured by the sensors differ significantly, reflecting consistent variability depending on the sensor type. The magnitude of these differences, as observed in the

median ranks, suggests meaningful variations that should be carefully considered when interpreting vegetation index data across different sensors.

3.4. Pairwise Comparisons between Imaging Sensors

The Kruskal-Wallis test result indicates significant variation in the median NDVI values among the four sensors. However, it does not specify where the variation occurs. The next step is to test for pairwise differences of median for each sensor. In the case of differences, a pairwise comparison can provide information as to any statistical differences between median NDVI values for each sensor in relation to each of other sensors. The null hypothesis states that no statistically significant pairwise differences in median NDVI values were found among the four sensors. If the null hypothesis is rejected, we will have information concerning which sensor's mean NDVI values are statistically different from each of the other sensors' mean NDVI value.

The Dunn's test, a nonparametric post hoc test followed by Kruskal-Wallis test, was conducted for pairwise comparisons. It is also based on rank sums to perform multiple comparisons. Two procedures were proposed. One is to use pooled ranking across all groups (Procedure I), and the other is to use separate rankings for each comparison (Procedure II). For our case, a reference sensor is not defined, hence the Procedure I is appropriate. This examines differences across all sensor pairs. The statistic and adjusted *p*-value were computed based on the difference of Column (b) and Column (a) in Table 7, and the test statistic is approximately normal. The Holm method was applied for adjusting *p*-value during the Dunn's test. The Holm method adjusts the *p*-values in a stepwise manner. The Dunn's pairwise comparison in Table 7 shows some notable information. Among the four sensors, MODIS shows the most statistically distinct difference in both seasons. In addition, Landsat and VIIRS consistently show no significant difference, suggesting similar behavior across both seasons.

Table 7. Dunn's pairwise test.

Sensor (a)	Sensor (b)	Spring		Fall	
		Z-statistic	*p*-value[1]	*Z*-statistic	*p*-value[1]
AVHRR	Landsat	2.54	0.017*	2.48*	0.020*
	MODIS	7.02*	0.000*	5.42*	0.000*
	VIIRS	1.63	0.103	3.24*	0.003*
Landsat	AVHRR	−2.54*	0.017*	−2.48*	0.020*
	MODIS	4.42*	0.000*	2.85*	0.009*
	VIIRS	−0.27	0.395	1.22	0.223
MODIS	AVHRR	−7.02*	0.000*	−5.42*	0.000*
	Landsat	−4.42*	0.000*	−2.85*	0.009*
	VIIRS	−3.67*	0.001*	−1.11	0.133
VIIRS	AVHRR	−1.63	0.103	−3.24*	0.003*
	Landsat	0.27	0.395	−1.22	0.223
	MODIS	3.67*	0.001*	1.11	0.133

[1] Reject if $p < \alpha/2$, where $\alpha = 0.05$.

4. Discussion

The study's findings reveal notable trends in vegetation greenness, particularly an increase during spring but mixed patterns in fall. Both linear regression and Mann-Kendall tests consistently indicated similar results in NDVI changes. Specifically, the AVHRR dataset showed a significant positive trend in NDVI over time, especially in the spring ($p < 0.05$), with a weaker but still positive trend in the fall. Similarly, the Landsat dataset presented a moderate upward trend in spring, with significant results from both regression and Mann-Kendall tests. However, Landsat's fall trend was weak and not statistically significant. In contrast, the MODIS dataset showed almost no significant trend in either season, while VIIRS exhibited a slight negative trend in spring but a significant positive trend in fall based on the Mann-Kendall test. Furthermore, one-way ANOVA analyses comparing NDVI means before and since 2001 confirmed significant increases for AVHRR in both

spring (from 0.491 to 0.581, $p = 0.000$) and fall (from 0.471 to 0.529, $p = 0.010$). Landsat also showed a significant upward shift in spring (from 0.523 to 0.627, $p = 0.037$) but not in fall. Overall, these results indicate a stronger trend of NDVI increase in spring than in fall for both AVHRR and Landsat datasets.

Significant differences were observed among the imaging sensors in both spring and fall seasons, as confirmed by the Kruskal-Wallis test ($p < 0.05$). These differences suggest consistent variability in median NDVI values depending on the sensor type. Pairwise comparisons using Dunn's test revealed that MODIS demonstrated the most statistically distinct differences from other sensors in both seasons. Conversely, Landsat and VIIRS showed no significant differences from each other, indicating similar behavior across both seasons. These variations among sensors can be attributed to several factors, including differing correction methods for sensor and atmospheric effects, and the maximum-value compositing technique used, particularly in MODIS. Additionally, sensor characteristics like spatial resolution might play a role; MODIS and VIIRS provide more frequent observations but have lower spatial resolution, which may smooth out greenness trends, while Landsat's higher spatial resolution could capture more variability. The frequency of data collection also varies, with AVHRR capturing data twice per day compared to Landsat's 8 or 16-day revisit period, potentially explaining Landsat's higher standard deviation.

Despite these clear findings, the study acknowledges several limitations that could influence the interpretation of results. Firstly, missing values in some datasets might have affected the consistency of trend detection, especially in the earlier years of the study period. Secondly, the wide range of days used for MODIS (8 days) and Landsat (11 days) to create composite images might introduce instability into statistical analyses, particularly during the dynamic spring and fall transition periods. The spatial resolution of the sensors varies, with MODIS and VIIRS offering more frequent observations but lower spatial resolution, potentially leading to a smoothing of greenness trends. In contrast, Landsat's higher spatial resolution may capture more variability, suggesting that sensor characteristics inherently influence the calculated NDVI means. These suggest that users should be very careful about selecting satellite imagery products for long-term time-series studies.

Lastly, the observed shifts, particularly the notable increases in greenness during spring and mixed patterns in fall, are suggested to stem from vegetation germination processes in spring and circadian rhythms in fall that align with the diurnal cycle. The research hypothesis that annual greenness levels have risen over time, when assessed on the same dates in early spring and late fall, is largely supported for spring. The study, however, underscores the complexity of vegetation dynamics, which are influenced by various factors, including rainfall and temperature. Further ecological research on vegetation is necessary to clarify these findings in greater detail and explore the underlying biological mechanisms contributing to these seasonal shifts.

5. Conclusions

This study aimed to answer two key questions: (1) whether greenness levels have significantly changed during spring and fall since 1982, and (2) whether there are notable differences in NDVI values among the imaging sensors. The results show that NDVI values have significantly increased in spring over the study period, especially in the AVHRR and Landsat datasets. These findings underscore the potential impact of environmental changes on vegetation health, suggesting a positive response during the primary growing season. In contrast, NDVI in fall showed weaker and less consistent trends, indicating that environmental impacts might be less strong towards the end of the growing season.

Regarding sensor comparison, significant differences in NDVI values were observed across the four sensors. MODIS consistently reported higher NDVI values than AVHRR, Landsat, and VIIRS in both seasons, while AVHRR recorded the lowest. These results highlight the importance of sensor selection when analyzing or comparing NDVI data. Overall, the study confirms that both seasonal changes in vegetation and sensor characteristics play important roles in understanding long-term greenness trends.

In summary, this study demonstrates the importance of long-term vegetation monitoring using various remote sensing platforms. The significant post-2001 increase in NDVI, particularly in spring, may indicate a shift in vegetation patterns that deserves further investigation. Future research is necessary to understand the underlying factors driving these changes, including climate and plant phenology. Improved understanding of sensor performance will also support more accurate and consistent vegetation monitoring in future.

Acknowledgment: This material is based upon work partly supported by the U.S. Geological Survey under Grant/Cooperative Agreement No. G18AP00077 (for GY18-GY22) or G23AP00683 (GY23-GY27).

Conflicts of Interest: The authors declare no conflicts of interest. The funders had no role in the design of the study; in the collection, analyses, or interpretation of data; in the writing of the manuscript; or in the decision to publish the results.

References

Beck, H. E., McVicar, T. R., van Dijk, A. I., Schellekens, J., de Jeu, R. A., & Bruijnzeel, L. A. (2011). Global evaluation of four AVHRR–NDVI data sets: Intercomparison and assessment against Landsat imagery. *Remote Sensing of Environment*, 115(10), 2547–2563. https://doi.org/10.1016/j.rse.2011.05.012

Brown, M. B., & Forsythe, A. B. (1974). Robust tests for the equality of variances. *Journal of the American Statistical Association*, 69(346), 364–367. https://doi.org/10.1080/01621459.1974.10482955

Calinger K, Curtis P (2023) A century of climate warming results in growing season extension: Delayed autumn leaf phenology in north central North America. *PLoS ONE* 18(3): e0282635. https://doi.org/10.1371/journal.pone.0282635

Crawford, C. J., Roy, D. P., Arab, S., Barnes, C., Vermote, E., Hulley, G., Gerace, A., Choate, M., Engebretson, C., Micijevic, E., Schmidt, G., Anderson, C., Anderson, M., Bouchard, M., Cook, B., Dittmeier, R., Howard, D., Jenkerson, C., Kim, M., Kleyians, T., Maiersperger, T., Mueller, C., Neigh, C., Owen, L., Page, B., Pahlevan, N., Rengarajan, R., Roger, J.-C., Sayler, K., Scaramuzza, P., Skakun, S., Yan, L., Zhang, H. K., Zhu, Z., & Zahn, S. (2023). The 50-year Landsat collection 2 archive. *Science of Remote Sensing*, 8, 100103. https://doi.org/10.1016/j.srs.2023.100103

Deng, L., Mao, Z., Li, X., Hu, Z., Duan, F., & Yan, Y. (2018). UAV-based multispectral remote sensing for precision agriculture: A comparison between different cameras. *ISPRS Journal of Photogrammetry and Remote Sensing*, 146, 124–136. https://doi.org/10.1016/j.isprsjprs.2018.09.008

Dunn, O. J. (1964). Multiple comparisons using rank sums. *Technometrics*, 6(3), 241–252. https://doi.org/10.1080/00401706.1964.10490181

Eastman, J. R., Sangermano, F., Machado, E. A., Rogan, J., & Anyamba, A. (2013). Global trends in seasonality of normalized difference vegetation index (NDVI), 1982–2011. *Remote Sensing*, 5(10), 4799–4818. https://doi.org/10.3390/rs5104799

Guo, J., Wang, J., Qiao, Y., Huang, X., Smith, N. G., Liu, Z., Zhang, R., Chen, X., Wu, C., Peñuelas, J., & Chen, L. (2024). Greening-induced biophysical impacts lead to earlier spring and autumn phenology in temperate and boreal forests. *Earth's Future*. https://doi.org/10.1029/2024EF004618

Hassan, T., Gulzar, R., Hamid, M., Ahmad, R., Waza, S. A., & Khuroo, A. A. (2024). Plant phenology shifts under climate warming: A systematic review of recent scientific literature. *Environmental Monitoring and Assessment*, 196(36). https://doi.org/10.1007/s10661-023-12190-w

Huang, S., Tang, L., Hupy, J. P., Wang, Y., & Shao, G. (2020). A commentary review on the use of normalized difference vegetation index (NDVI) in the era of popular remote sensing. *Chinese Journal of Plant Ecology, 32*(8), 2711–2729. https://doi.org/10.1007/s11676-020-01155-1

Kenabatho, P. K. (2025). Innovative trend analysis of long-term spatial-temporal rainfall patterns over Botswana: Implications for water resources management. *International Journal of Remote Sensing*, 46(3), Article 102217. https://doi.org/10.1016/j.ejrh.2025.102217

Kendall, M. G. (1975). Rank correlation methods (4th ed.). Charles Griffin.

Kruskal, W. H., & Wallis, W. A. (1952). Use of ranks in one-criterion variance analysis. *Journal of the American Statistical Association*, 47(260), 583–621. https://doi.org/10.2307/2280779

Lemenkova, P. (2015). Analysis of Landsat NDVI time series for detecting degradation of vegetation. In A. N. Petin, P. V. Goleusov, & E. I. Makaseeva (Eds.), *Geoecology and sustainable use of mineral resources. From science to practice. Proceedings of 3rd International Conference of Young Scientists* (pp. 11–13). Belgorod State University. ISBN: 978-5-98242-210-1. Available at SSRN: https://ssrn.com/abstract=3312710.

Lu, Y., Yu, Y., Sun, L., Li, C., He, J., Guo, Z., Duan, L., Zhang, J., & Yu, R. (2025). NDVI-based vegetation dynamics and responses to climate change and human activities at Xinjiang from 2001 to 2020. *Scientific Reports, 15,* 25848. https://doi.org/10.1038/s41598-025-11677-5

Mann, H. B. (1945). Nonparametric tests against trend. *Econometrica*, 13(3), 245–259. https://doi.org/10.2307/1907187

Mehmood, K., Anees, S. A., Muhammad, S., Hussain, K., Shahzad, F., Liu, Q., Ansari, M. J., Alharbi, S. A., & Khan, W. R. (2024). Analyzing vegetation health dynamics across seasons and regions through NDVI and climatic variables. *Scientific Reports*, 14, Article 11775. https://doi.org/10.1038/s41598-024-62464-7

Nash, M. S., Wickham, J., Christensen, J., & Wade, T. (2017). Changes in landscape greenness and climatic factors over 25 years (1989–2013) in the USA. *Remote Sensing*, 9(3), 295. https://doi.org/10.3390/rs9030295

Roger, J. C., Santamaria Artigas, A., Ray, J. P., Villaescusa Nadal, J. L., Vermote, E. F., & Devadiga, S. (2023). *LTDR AVHRR products (Version 6) user guide* (Version 1.2). NASA Goddard Space Flight Center.

Rozenstein, O., & Adamowski, J. (2017). Linking spaceborne and ground observations of autumn foliage senescence in Southern Québec, Canada. *Remote Sensing*, 9(6), 630. https://doi.org/10.3390/rs9060630

Shi, L., Fan, H., Yang, L., Jiang, Y., Sun, Z., & Zhang, Y. (2023). NDVI-based spatial and temporal vegetation trends and their response to precipitation and temperature changes in the Mu Us Desert from 2000 to 2019. *Water Science & Technology, 88*(2), 430–442. https://doi.org/10.2166/wst.2023.212

Tucker, C. J. (1979). Red and photographic infrared linear combinations for monitoring vegetation. *Remote Sensing of Environment*, 8(2), 127–150. https://doi.org/10.1016/0034-4257(79)90013-0

Tuoku, L., Wu, Z., & Men, B. (2024). Impacts of climate factors and human activities on NDVI change in China. *Ecological Informatics, 81,* 102555. https://doi.org/10.1016/j.ecoinf.2024.102555

U.S. Geological Survey (USGS). (2025). *Annual NLCD (National Land Cover Database)—The next generation of land cover mapping: U.S. Geological Survey Fact Sheet 2025–3001* (4 p.). https://doi.org/10.3133/fs20253001. Last access:18 September 2025.

Vermote, E. (2021). MODIS/Terra surface reflectance 8-day L3 global 500m SIN grid V061. NASA Land Processes Distributed Active Archive Center. https://doi.org/10.5067/MODIS/MOD09A1.061. Last access:18 September 2025.

Vermote, E., Franch, B., & Claverie, M. (2023). VIIRS/NPP Surface Reflectance Daily L2G Global 1km and 500m SIN Grid V002. NASA Land Processes Distributed Active Archive Center. https://doi.org/10.5067/VIIRS/VNP09GA.002. Last access: 30 August 2025.

Walter, J. A., Stovall, A. E., & Atkins, J. W. (2021). Vegetation structural complexity and biodiversity in the Great Smoky Mountains. *Ecosphere*, 12(3), e03390. https://doi.org/10.1002/ecs2.3390

Wang, D., Morton, D., Masek, J., Wu, A., Nagol, J., Xiong, X., ... & Wolfe, R. (2012). Impact of sensor degradation on the MODIS NDVI time series. *Remote Sensing of Environment*, 119, 55–61. https://doi.org/10.1016/j.rse.2011.12.001

Wang, J., Rich, P. M., & Price, K. P. (2003). Temporal responses of NDVI to precipitation and temperature in the central Great Plains, USA. *International Journal of Remote Sensing*, 24(11), 2345–2364. https://doi.org/10.1080/01431160210154812

Yang, W., Yang, L., & Merchant, J. W. (1997). An assessment of AVHRR/NDVI-ecoclimatological relations in Nebraska, USA. *International Journal of Remote Sensing*, 18(10), 2161–2180. https://doi.org/10.1080/014311697217819

Appendices

Appendix 1. Annual mean NDVI values by seasons and imaging sensors.

Year	AVHRR Spring	AVHRR Fall	Landsat Spring	Landsat Fall	MODIS Spring	MODIS Fall	VIIRS Spring	VIIRS Fall
1982	0.4611							
1983	0.4265	0.4505						
1984	0.4767	0.5245		0.5971				
1985	0.5695							
1986	0.4714	0.4224	0.5391					
1987	0.4644	0.3975	0.5600	0.4939				
1988	0.4946		0.5534					
1989	0.4445	0.4214						
1990	0.4346	0.4903		0.6399				
1991	0.5195	0.4394		0.4758				
1992	0.5306		0.5917	0.4323				
1993	0.4216	0.5006	0.1303					
1994	0.4809		0.6778					
1995	0.5979							
1996	0.5264	0.5305		0.4257				
1997		0.4858						
1998	0.4897	0.4852	0.5965					
1999	0.5442	0.5027		0.5909				
2000		0.4664	0.5364	0.5853	0.6568	0.6032		
2001	0.5862	0.4028		0.5214	0.7946	0.6225		
2002	0.6631	0.6311	0.6494		0.7895	0.6440		
2003		0.5412	0.7226		0.7540	0.6188		
2004			0.6180	0.5585	0.7411	0.6438		
2005	0.5580	0.6246	0.5813	0.6519	0.6701	0.7108		
2006	0.5460	0.5674	0.5850	0.4533	0.7368	0.5892		
2007	0.5126	0.5767	0.4173	0.6426	0.7540	0.6654		
2008		0.5790		0.5756	0.6931	0.5898		
2009	0.4882	0.5236	0.5121		0.8153	0.5911		
2010	0.6033	0.4626	0.6580		0.7613	0.5963		
2011	0.5919	0.4833	0.7051	0.5124	0.7810	0.5900		
2012	0.7247	0.4796		0.5179	0.8718	0.5654	0.7841	0.5348
2013	0.6086	0.4911	0.6157	0.5409	0.6722	0.6021	0.6392	0.6042
2014	0.4657	0.5261	0.5438	0.5656	0.7261	0.6185	0.4643	0.4331
2015			0.6296		0.7427	0.6645	0.6581	0.3139
2016	0.6156		0.6066	0.6898	0.8656	0.6405	0.6067	0.6199
2017	0.5940		0.7148		0.7639	0.6316	0.4528	0.5703
2018			0.6426		0.6587	0.6196	0.4056	0.6609
2019	0.5785	0.5115	0.7646	0.3936	0.8409	0.6317	0.7031	0.6533
2020			0.5682	0.7824	0.7266	0.6450	0.5443	0.6680
2021			0.7016	0.7034	0.7061	0.6487	0.6466	0.6761
2022				0.5928	0.7597	0.5935		0.5733
2023			0.6803	0.5394	0.7553	0.6311	0.6073	0.6363

Appendix 2. Google Earth Engine Code for AVHRR

```
// Import the boundary of the Great Smoky Mountains National Park
var bnd_generalized = ee.FeatureCollection("projects/ee-geetest20/assets/bnd_generalized");

// The nTH day of year (DOY)
var nThDay = 307; // Use 114, 115, and 116 for spring; and 305, 306, and 307 for fall

// Choose the AVHRR dataset
var collection =
ee.ImageCollection('NOAA/CDR/AVHRR/NDVI/V5').filter(ee.Filter.dayOfYear(nThDay,nThDay));
var timeCollection = collection.select('TIMEOFDAY');
print(collection);

// Function to check image quality
function getQABits(image, start, end, newName) {
var pattern = 0;
  for (var i = start; i <= end; i++) {
    pattern += Math.pow(2, i); }
  return image.select([0], [newName])
  .bitwiseAnd(pattern)
  rightShift(start);
}

// Function for quality mask
function maskQuality(image) {
  var QA = image.select('QA');
  var internalQuality = getQABits(QA,0, 6, 'internal_quality_flag');
  return image.updateMask(internalQuality.eq(0));
}

// Function to choose only the images between 18:30 and 20:00 Zulu time
function timeMask(image) {
  var timeQA = image.select('TIMEOFDAY');
  return image.updateMask(timeQA.gt(1830).lt(2000));
}

// Apply masks
collection = collection.map(maskQuality).map(timeMask);

// Select only the NDVI layer
var ndviCollection = collection.select('NDVI');

// Convert annual NDVI layers to bands in an image
var ndviImage = ndviCollection.toBands();

// Apply a scale factor
ndviImage = ndviImage.multiply(0.0001);

// Calculate NDVI means
var ndviMeans = ndviImage.reduceRegion({
    reducer: ee.Reducer.mean(),
    geometry: bnd_generalized,
    scale: 1000,
    maxPixels: 1e9
  });

// Count the pixels used for calculating means
var ndviCounts = ndviImage.reduceRegion({
    reducer: ee.Reducer.count(),
    geometry: bnd_generalized,
    scale: 1000,
    maxPixels: 1e9
  });

// Print outputs
print('NDVI Means', ndviMeans);
print('NDVI Counts', ndviCounts);
```

Appendix 3. Google Earth Engine Code for Landsat

```
// 1. Define the study area
var bnd_generalized = ee.FeatureCollection("projects/eegeetest20/assets/bnd_generalized")

// 2. Setting Conditions
var start = 111; // Spring. Use 300 for fall.
var end = 121; // Spring. Use 310 for fall.
var scenePath = 19;
var sceneRow = 35;

// 3. Connect to the Landsat Surface Reflectance dataset
var L9col = ee.ImageCollection('LANDSAT/LC09/C02/T1_L2')
```

```
    .filter(ee.Filter.dayOfYear(start,end))
    .filter(ee.Filter.eq('WRS_PATH', scenePath))
    .filter(ee.Filter.eq('WRS_ROW', sceneRow))
    .map(function(image){return image.clip(bnd_generalized)});
var L8col = ee.ImageCollection('LANDSAT/LC08/C02/T1_L2')
    .filter(ee.Filter.dayOfYear(start,end))
    .filter(ee.Filter.eq('WRS_PATH', scenePath))
    .filter(ee.Filter.eq('WRS_ROW', sceneRow))
    .map(function(image){return image.clip(bnd_generalized)});
var L7col = ee.ImageCollection('LANDSAT/LE07/C02/T1_L2')
    .filter(ee.Filter.dayOfYear(start,end))
    .filter(ee.Filter.eq('WRS_PATH', scenePath))
    .filter(ee.Filter.eq('WRS_ROW', sceneRow))
    .map(function(image){return image.clip(bnd_generalized)});
var L5col = ee.ImageCollection('LANDSAT/LT05/C02/T1_L2')
    .filter(ee.Filter.dayOfYear(start,end))
    .filter(ee.Filter.eq('WRS_PATH', scenePath))
    .filter(ee.Filter.eq('WRS_ROW', sceneRow))
    .map(function(image){return image.clip(bnd_generalized)});
var L4col = ee.ImageCollection('LANDSAT/LT04/C02/T1_L2')
    .filter(ee.Filter.dayOfYear(start,end))
    .filter(ee.Filter.eq('WRS_PATH', scenePath))
    .filter(ee.Filter.eq('WRS_ROW', sceneRow))
    .map(function(image){return image.clip(bnd_generalized)});

// 4. Pre-processing
// 4.1. Apply scaling Factors
function applyScaleFactors(image) {
  var opticalBands = image.select('SR_B.').multiply(0.0000275).add(-0.2);
  var thermalBands = image.select('ST_B.*').multiply(0.00341802).add(149.0);
  return image.addBands(opticalBands, null, true)
              .addBands(thermalBands, null, true);
}

L9col = L9col.map(applyScaleFactors);
L8col = L8col.map(applyScaleFactors);
L7col = L7col.map(applyScaleFactors);
L5col = L5col.map(applyScaleFactors);
L4col = L4col.map(applyScaleFactors);

// 4.2. Select bands to be used and Rename
L9col = L9col.select('SR_B5', 'SR_B4', 'QA_PIXEL').map(function(image){return
image.rename(['NIR','RED','QA'])});
L8col = L8col.select('SR_B5', 'SR_B4', 'QA_PIXEL').map(function(image){return
image.rename(['NIR','RED','QA'])});
L7col = L7col.select('SR_B4', 'SR_B3', 'QA_PIXEL').map(function(image){return
image.rename(['NIR','RED','QA'])});
L5col = L5col.select('SR_B4', 'SR_B3', 'QA_PIXEL').map(function(image){return
image.rename(['NIR','RED','QA'])});
L4col = L4col.select('SR_B4', 'SR_B3', 'QA_PIXEL').map(function(image){return
image.rename(['NIR','RED','QA'])});

// 4.3. Merge all selected bands into a collection
var mergedCol = L4col.merge(L5col).merge(L7col).merge(L8col).merge(L9col);
print('mergedCol: ', mergedCol);
Map.addLayer(mergedCol.first().select('NIR'), {min: 0.0, max: 0.3}, 'original');

// 5. QA Bitmask processing function
function qaFunction (image) {
  var qa = image.select('QA').bitwiseAnd(parseInt('0000000000011111', 2)).eq(0);
  return image.updateMask(qa);
}
mergedCol = mergedCol.map(qaFunction);
Map.addLayer(mergedCol.first().select('NIR'), {min: 0.0, max: 0.3}, 'masked');

// 6. NDVI calculation function
var addNDVI = function(image) {
  var ndvi = image.normalizedDifference(['NIR', 'RED']).rename('NDVI');
  return image.addBands(ndvi);
};
mergedCol = mergedCol.map(addNDVI);

var mergedNDVI = mergedCol.select('NDVI');
var ndviImg = mergedNDVI.toBands();

var ndviMeans = ndviImg.reduceRegion({
    reducer: ee.Reducer.mean(),
    geometry: bnd_generalized,
    scale: 30,
    maxPixels: 1e9
});

// Print output
print('NDVI Means: ', ndviMeans);
```

Appendix 4. Google Earth Engine Code for MODIS

```
// 1. Define the study area
var bnd_generalized = ee.FeatureCollection("projects/ee-geetest20/assets/bnd_generalized");

// 2. Connect to the MODIS_500m_8day Surface Reflectance dataset and Set conditions
// 2.1. Connect to dataset and Specify the years and day of year
var collection = ee.ImageCollection('MODIS/061/MOD09A1')
    .filterBounds(bnd_generalized)
  //.filter(ee.Filter.dayOfYear(114,121)); // Landsat Spring : 114 ~ 121
    .filter(ee.Filter.dayOfYear(298,305)); // MODIS Fall : 298 ~ 305
// 2.2. Define lists to store results
var modisBands =
      ['sur_refl_b03','sur_refl_b04','sur_refl_b01','sur_refl_b02','sur_refl_b06','sur_refl_b07'];
var lsBands = ['blue','green','red','nir','swir1','swir2'];

// 3. QA Bitmask processing function
// 3.1. Helper function to extract the QA bits
function getQABits(image, start, end, newName) {
 var pattern = 0;
 for (var i = start; i <= end; i++) {
 pattern += Math.pow(2, i);
 }
 return image.select([0], [newName])
 .bitwiseAnd(pattern)
 .rightShift(start);
}

// 3.2. A function to mask out cloudy pixels.
function maskQuality(image) {
 var QA = image.select('StateQA');
 var internalQuality = getQABits(QA,8, 13, 'internal_quality_flag');
 return image.updateMask(internalQuality.eq(0));
}

// 3.3. Comparison before and after cloud masking
var noCloud = collection.map(maskQuality)
                        .select(modisBands,lsBands);
var Cloud = collection.select(modisBands,lsBands);

var visParams = {bands:['red','green','blue'],min:0,max:3000,gamma:1.3};

// 4. Apply scale factor to the image collection using the map() function
var scaleImage = function (image) {
  return image.multiply(0.0001);
};

noCloud = noCloud.map(scaleImage);

// 5. NDVI calculation function
var addNDVI = function(image) {
  var ndvi = image.normalizedDifference(['nir', 'red']).rename('NDVI');
  return image.addBands(ndvi);
};

noCloud = noCloud.map(addNDVI);

var ndviCollection = noCloud.select('NDVI');
var ndviTimeSeries = ndviCollection.toBands();

// 6. Apply Functions and Filtering
var ndviMeans = ndviTimeSeries.reduceRegion({
    reducer: ee.Reducer.mean(),
    geometry: bnd_generalized.geometry(),
    scale: 500,
    maxPixels: 1e9
});

var ndviCount = ndviTimeSeries.reduceRegion({
    reducer: ee.Reducer.count(),
    geometry: bnd_generalized.geometry(),
    scale: 500,
    maxPixels: 1e9
});

// 7. Visualizae and Print Contents
print("nvdiMeans: ", ndviMeans);
print("nvdiCount:", ndviCount);
```

Appendix 5. Google Earth Engine Code for VIIRS

```
// 1. Define the study area
var bnd_generalized = ee.FeatureCollection("projects/ee-geetest20/assets/bnd_generalized");

// 2. Connect to the VIIRS Surface Reflectance dataset
       var collection = ee.ImageCollection('NOAA/VIIRS/001/VNP09GA').filterBounds(bnd_generalized);

// 3. Setting Conditions
// 3.1. Specify the years and day of year
var startYear = 2012;
var endYear = 2023;
var nThday = 114; // Use 114, 115, and 116 for spring; 305, 306, and 307 for fall.

// 3.2. Define lists to store results
var ndviMeans = [];
var ndviCounts = [];

// 4. QF1 & QF2 Bitmask processing function
// 4.1. Helper function to extract the QA bits
function getQABits(image, start, end, newName) {
  var pattern = 0;
  for (var i = start; i <= end; i++) {
    pattern += Math.pow(2, i);
  }
  return image.select([0], [newName])
    .bitwiseAnd(pattern)
    .rightShift(start);
}

// 4.2. Function to mask out low-quality pixels based on QF1 and QF2
function maskQuality(image) {
  var qf1 = image.select('QF1');
  var qf2 = image.select('QF2');
  var cloudConfidence = getQABits(qf1, 2, 3, 'cloud_confidence');
  var cloudMask = cloudConfidence.eq(0).or(cloudConfidence.eq(1));
  var dayMask = getQABits(qf1, 4, 4, 'day_mask').eq(0);
  var sunGlintMask = getQABits(qf1, 6, 7, 'sun_glint_mask').eq(0);
  var waterMask = getQABits(qf2, 0, 2, 'water_mask').eq(1); // no desert land = 1
  var shadowMask = getQABits(qf2, 3, 3, 'shadow_mask').eq(0);
  var combinedMask = cloudMask.and(dayMask)
                              .and(sunGlintMask)
              .and(waterMask)
              .and(shadowMask)
  return image.updateMask(combinedMask);
}

// 5. NDVI calculation function
var calculateNDVI = function(image) {
  var ndvi = image.normalizedDifference(['I2', 'I1']).rename('NDVI');
  return image.addBands(ndvi);
};

// 6. Apply Functions and Filtering
      // 6.1. Function to filter collection by year and day of year, calculate NDVI, and apply mask
var filterAndCalculateNDVI = function(year, nThday) {
  return collection.filter(ee.Filter.calendarRange(year, year, 'year'))
                   .filter(ee.Filter.dayOfYear(nThday, nThday))
                   .map(calculateNDVI)
                   .map(maskQuality);
};

// 6.2. Function to calculate mean NDVI, count NDVI, and visualize the NDVI
var NDVIStatsAndVisualization = function(year, nThday) {
  var filtered = filterAndCalculateNDVI(year, nThday);
  var meanNdvi = filtered.select('NDVI').mean().reduceRegion({
    reducer: ee.Reducer.mean(),
    geometry: bnd_generalized,
    scale: 500,
    maxPixels: 1e9
  }).get('NDVI');
  var countNdvi = filtered.select('NDVI').count().reduceRegion({
    reducer: ee.Reducer.count(),
    geometry: bnd_generalized,
    scale: 500,
    maxPixels: 1e9
  }).get('NDVI');
  var clippedNdvi = filtered.select('NDVI').mean().clip(bnd_generalized);
  Map.addLayer(clippedNdvi, ndviVisParams, 'NDVI ' + year + ' DOY ' + nThday);
  return {
    'year': year,
    'dayOfYear': nThday,
    'meanNdvi': meanNdvi,
    'countNdvi': countNdvi
```

```
  };
};

// 7. Visualization
// 7.1. NDVI Visualization Function
var ndviVisParams = {
  min: 0,
  max: 1,
  palette: ['blue', 'white', 'green']
};

// 7.2. Loop through the years and collect NDVI stats and visualize
for (var year = startYear; year <= endYear; year++) {
  var stats = NDVIStatsAndVisualization(year, nThday);
  ndviMeans.push(stats.meanNdvi);
  ndviCounts.push(stats.countNdvi);
}

// 7. Print Outputs
print('NDVI Means:', ndviMeans);
print('NDVI Counts:', ndviCounts);
```

Research Article

Urban Heat Island Disparities: A Geospatial Analysis of Household Income and Land Surface Temperatures in Lafayette, Louisiana

Joseph Kolb[1,†], Rodney B. Yantis[2], and Courtney A. Poirier Chicola[3,*]

[1] Regional Application Center & School of Geosciences, University of Louisiana at Lafayette, Lafayette, LA, USA; joseph.kolb1@louisiana.edu

[2] Regional Application Center & School of Geosciences, University of Louisiana at Lafayette, Lafayette, LA, USA; yantis@louisiana.edu

[3] Regional Application Center & School of Geosciences, University of Louisiana at Lafayette, Lafayette, LA, USA; chicola@louisiana.edu

[†] These authors contributed as undergraduate research students.

[*] Corresponding Author: chicola@louisiana.edu; +1-337-852-4731

Academic Editor: Jeong Chang Seong
Received: 30 July 2025
Revised: 25 September 2025
Accepted: 30 September 2025
Published: 24 October 2025

Abstract: The urban heat island (UHI) effect increases heat exposure in cities and disproportionately affects vulnerable groups. This study investigates the relationship between household income, vegetation cover, and land surface temperature (LST) in Lafayette, Louisiana. We used Landsat 8 thermal infrared imagery from July 30, 2023, to measure LST at a 30-m resolution. We then compared these results with 2018 U.S. Census block group income data. We classified land cover into vegetation and non-vegetation classes using 2023 NAIP aerial images, and we validated our classification with an accuracy assessment based on 200 random points. Our results show a negative relationship ($r = -0.38$, $R^2 = 0.14$, $p < 0.05$) between income and surface temperature and a positive relationship ($r = 0.41$, $R^2 = 0.17$, $p < 0.05$) between income and vegetation. Block groups with lower incomes also had less vegetation cover. This suggests that the lack of vegetation contributes to higher LST. We did not find a significant relationship between parcel size and income, which means that land ownership density alone does not explain differences in heat. These findings highlight how socioeconomic and environmental factors work together to create uneven heat burdens. Policymakers may consider targeted tree planting and green infrastructure projects in vulnerable communities to mitigate heat-related risks and reduce energy costs.

Keywords: urban heat island, heat disparities, remote sensing, vegetation cover, land surface temperature

1. Introduction

Urban heat islands (UHIs) are urban areas that experience higher temperatures than nearby suburban and rural areas. UHIs can be classified into surface, canopy, and boundary types, with surface UHIs commonly derived from satellite imagery (Xian & Crane, 2006). In contrast, canopy and boundary UHIs are more difficult to measure because they require complex models based on interpolating weather station data. The UHI effect mainly comes from the heat-retaining qualities of impervious surfaces like asphalt and concrete, reduced vegetation cover, and building designs that restrict airflow. In contrast, areas with vegetation help cool cities by providing shade and releasing moisture through evapotranspiration (Knipling, 1970; Bowler *et al.*, 2010).

UHI effects do not appear evenly throughout cities. Dense development reduces the space available for green infrastructure, such as parks and community gardens. This leads to uneven exposure to heat, which is often called heat disparity or heat inequity. Socioeconomic factors are closely linked to these disparities. Several studies show that low-income and minority groups often live in hotter neighborhoods with less vegetation and more impervious surfaces (Hsu *et al.*, 2021; Jesdale *et al.*, 2013; Nesbitt *et al.*, 2019). These inequities pose a risk to public health, as heat exposure increases the risk of heat exhaustion, heat stroke, and heart problems, particularly for the elderly, young children, and individuals with existing health issues (Anderson & Bell, 2011). Beyond health impacts, UHIs may lead to higher household energy use for cooling,

Citation: Kolb, J., Yantis, R. B., & Poirier Chicola, C. A. (2024). Urban heat island disparities: A geospatial analysis of household income and land surface temperatures in *Lafayette, Louisiana*. *Journal of Earth Observation and Geospatial Applications, 1*(1), 51–63. DOI: https://doi.org/10.65372/48t6d326

with some estimates suggesting that urban heat can raise electricity use by nearly 20% in certain U.S. cities (Li *et al.*, 2019). These effects add to the financial burdens faced by low-income households.

While research has clearly shown UHI disparities in large cities, there are fewer studies focused on medium-sized cities in the southern U.S., where poverty rates may be high and local planning resources may be limited. Lafayette, Louisiana, presents a useful case study because of its hot, humid climate, high poverty rate, and lack of previous UHI research. Understanding local heat disparities is important for guiding future planning and informing mitigation strategies for current conditions.

The purpose of this study is to investigate the presence and causes of UHI disparities in Lafayette, Louisiana. Specifically, this study will aim to answer the following research questions: (1) Do lower-income block groups have higher land surface temperatures than higher-income groups?, (2) How does vegetation cover change with household income, and how much does it influence the relationship between income and heat exposure?, and (3) Does parcel size, which indicates land ownership patterns and development density, relate to household income and surface temperature? By addressing these questions, this study will add to the existing literature on UHI and environmental disparities, filling in the knowledge gaps for this area. It will also provide relevant insights to support equitable climate adaptation and urban planning in Lafayette and similar areas.

2. Study Area and Methods

2.1. Study Area and Data

Lafayette, Louisiana, was chosen as the study area because it is a mid-sized city in the southern United States (U.S.; Figure 1). It has hot, humid summers and socioeconomic differences across the city. These factors make Lafayette a good case study for examining how urban heat island affects vulnerable communities. The city's poverty rates, expanding impervious surfaces, and the lack of previous UHI research emphasize its importance for studying urban heat inequalities.

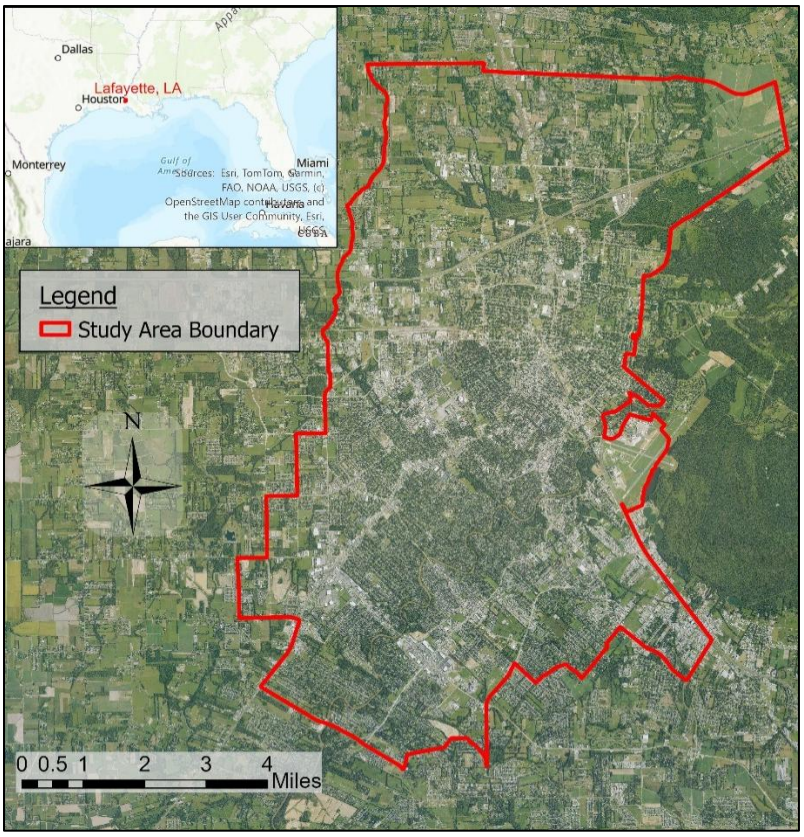

Figure 1. Natural color NAIP image of Lafayette, LA, with its relative location to the Southeast United States.

Census block groups mainly within the city limits were used as the unit of analysis to combine environmental and socioeconomic data. This study used four main datasets: (1) Landsat 8 thermal infrared imagery to calculate land surface temperature (LST), (2) National Agriculture Imagery Program (NAIP) aerial imagery for land cover classification, (3) U.S. Census Bureau block group data for household income and poverty statistics, and (4) local parcel boundaries from the Lafayette Consolidated Government (LCG) to evaluate land ownership density. Table 1 summarizes all datasets, including their sources, formats, and uses.

Table 1. Summary of datasets used in this study.

Dataset	Source	Year/ Date	Format	Resolution/ Scale	Purpose
Landsat 8 Collection 2 Level 2 Surface Temperature (Band 10)	USGS EarthExplorer	July 30, 2023	Raster (TIFF)	30 m	Derivation of land surface temperature
National Agriculture Imagery Program Aerial Mosaic	USDA NRCS Geospatial Data Gateway	2023	Raster (TIFF)	0.3 m (30 cm)	Supervised classification of vegetation vs. non-vegetation
Census Block Groups with Demographics	Esri Demographics Team (ACS 5-year estimates)	2018	Vector (Shapefile/Feature Layer)	Block group	Median household income, poverty statistics
Parcel Boundaries	Lafayette Consolidated Government	2023	Vector (Shapefile)	Parcel	Proxy for land ownership density (average parcel size)
Lafayette City Limits	LCG / ArcGIS Online	2023	Vector (Shapefile)	Municipal boundary	Define the study area extent

2.2. Workflow Overview

We conducted all geospatial analysis in ArcGIS Pro 3.4. The geospatial workflow included four sequential steps: (1) obtain land surface temperature data, (2) perform land cover classification, (3) integrate socioeconomic data, and (4) perform statistical analysis. First, we processed Landsat 8 thermal infrared imagery (Band 10) from July 30, 2023, to derive LST using scaling factors from the USGS, then converted it from Kelvin to degrees Fahrenheit. We then projected the LST raster to NAD 1983 UTM Zone 15N and clipped it to the Lafayette city limits. Figure 2a presents the resulting LST raster where red symbolizes hotter temperatures and blue symbolizes cooler temperatures. Next, we classified land cover from 2023 NAIP color-infrared imagery into vegetation and non-vegetation categories using a supervised maximum likelihood method, with training samples gathered from representative areas such as tree canopies, lawns, impervious surfaces, and rooftops. We evaluated classification accuracy using 200 random points, compared against reference NAIP imagery, and summarized the results in a confusion matrix. We used block group boundaries as the unit of analysis. The block groups used for this study can be viewed in Figure 2b, displayed in a red-to-yellow color scheme based on their 2023 median household income. Red block groups have the lowest median values, while yellow ones have the highest. We applied zonal statistics to calculate average LST and percent vegetation for each block group, while parcel boundaries from the Lafayette Consolidated Government were used to determine mean parcel size. We joined all outputs to socioeconomic attributes using 2018 American Community Survey (ACS) block group income data for statistical comparison in Microsoft Excel. Lastly, we performed Pearson correlation and linear regression to quantify relationships among income, vegetation, parcel size, and LST. This workflow provided a reproducible, multi-scalar method for linking socioeconomic disparities with patterns of heat exposure in Lafayette.

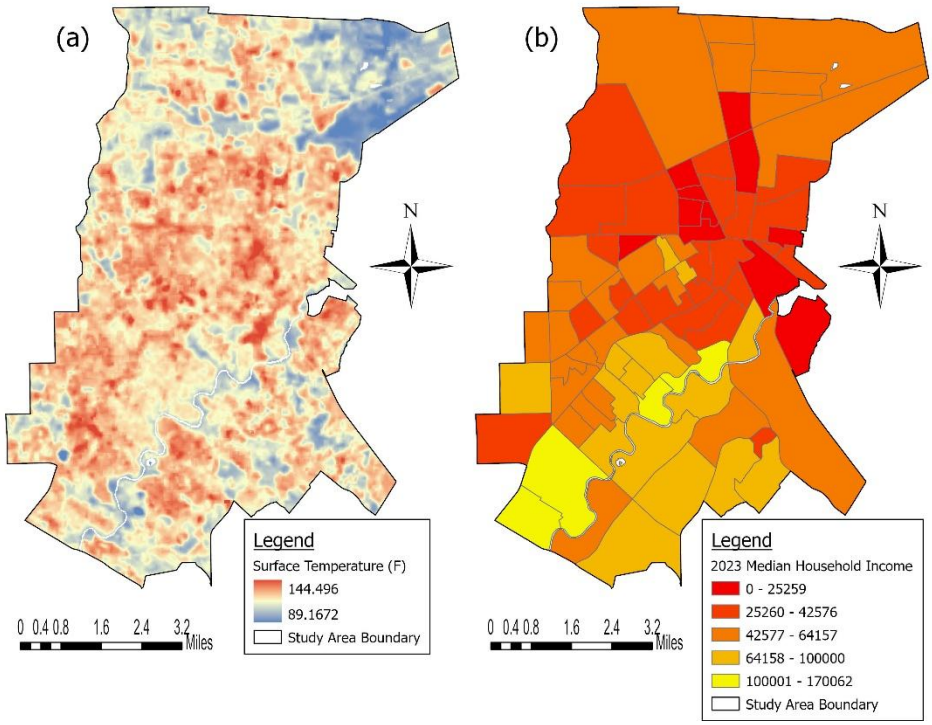

Figure 2. The city of Lafayette study area with (a) land surface temperature and (b) 2023 median income for each block group, where red is the lowest and yellow is the highest.

2.3. Land Surface Temperature Retrieval

This study focused solely on surface temperature disparities due to the complexity of modeling the surface, canopy, and boundary UHIs together. Deriving surface temperatures from raw satellite images can be a complicated process as well. Conveniently, the Landsat U.S. Collection 2 (C2) Analysis Ready Data (ARD) dataset in the USGS EarthExplorer database offers reliable surface temperature products. These products include pre-calculated land surface temperature values generated using numerous factors, including the Level 1 Top of Atmosphere (TOA) reflectance from Band 10 and normalized difference vegetation index (NDVI) values. Therefore, a Landsat Collection 2 Level 2 surface temperature image tile from this dataset was used to create a surface temperature map of Lafayette, LA.

The surface temperature raster layer used for statistical analysis was created from a preprocessed Band 10 (thermal infrared) image tile captured by Landsat 8's Operational Land Imager/Thermal Infrared Sensor (OLI/TIRS). Landsat 8 Collection 2 Level 2 data (Path 23, Row 39) acquired on July 30, 2023, were chosen because of low cloud cover of less than 5% and because they matched peak summer conditions, when UHI intensity is highest.

Thermal band data (Band 10) were changed from digital numbers to at-sensor brightness temperature using the radiometric rescaling coefficients in the metadata (Sayler, 2024). We then calculated surface temperature using the emissivity correction method and converted it from Kelvin to degrees Fahrenheit for easier understanding (Ahmed *et al.*, 2024). The resulting LST raster was reprojected to NAD 1983 UTM Zone 15N and clipped to the Lafayette municipal boundary to define the area for the analysis.

2.4. Land Use/Land Cover Classification

Land use classifications are valuable for quantifying the types of land use within a designated study area (Poirier Chicola, 2021). This method was particularly useful for generating land use statistics that were subsequently compared with income statistics provided by the U.S. Census Bureau. An aerial image of Lafayette, collected by the National Agriculture Imagery Program (NAIP) in 2023, was used for land use

classification due to its high spatial resolution of 30 cm. A color-infrared county mosaic for Lafayette Parish was obtained from the Natural Resource Conservation Service (NRCS) Geospatial Data Gateway.

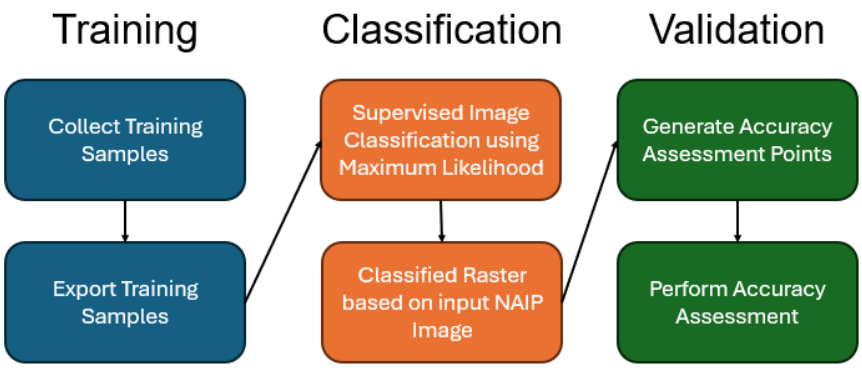

Figure 3. The general land use classification workflow used in this study. Training data was used to classify the NAIP aerial imagery of the city of Lafayette. An accuracy assessment was used to determine the effectiveness of the classification method (Congalton & Green, 1999).

The color-infrared NAIP imagery was classified into two categories: vegetation (tree canopy, grass, lawns) and non-vegetation (impervious surfaces, rooftops, bare soil). This classification used a supervised maximum likelihood classification (MLC) approach. MLC was chosen for its strong performance in binary vegetation classification tasks and its fit with NAIP's spectral characteristics (Aziz & Alwan, 2021).

Color-infrared imagery consists of near-infrared, red, and green spectral bands in that order. This color-infrared band combination was selected instead of natural color to better distinguish between vegetation and developed land. Plant leaves reflect high amounts of near-infrared light (Knipling, 1970), allowing color-infrared imagery to effectively highlight the presence of vegetation and facilitate identification during image classification. Training data included 37 manually digitized polygons (17 for vegetation and 20 for non-vegetation) spread across the study area to capture spectral variability among different land cover types. We assessed classification accuracy with 200 stratified random points validated against unclassified NAIP imagery. A confusion matrix was created to calculate overall accuracy, user's accuracy, producer's accuracy, and the kappa coefficient. Although the kappa statistics have limitations as a reliability metric (Foody, 2020), it was included for consistency with earlier UHI classification studies.

2.5. Socioeconomic and Parcel Data

Socioeconomic data, such as median household income and the number of households living in poverty, came from the 2018 American Community Survey 5-year estimates. This data is the latest demographic information available at the block group level. Although the ACS data is older than the 2023 satellite imagery, we recognize this timing issue as a limitation, but it does not significantly impact the spatial patterns of income distribution.

We obtained parcel boundary data from the Lafayette Consolidated Government to calculate the average parcel size for each block group. We included parcel size as a way to measure land ownership density and development intensity. This allows us to explore whether patterns of parcelization affect heat exposure.

2.6. Statistical Analysis

All spatial analyses were done in ArcGIS Pro 3.4. Zonal statistics calculated block group averages for land surface temperature and vegetation cover. We determined percent vegetation cover as the ratio of classified vegetation pixels within each block group polygon. The average parcel size was found by dividing the total parcel area by the number of parcels in each block group.

We calculated Pearson correlation coefficients to examine relationships among variables, reporting significance testing (*p*-values). Linear regression models estimated the strength of associations, and R^2 values described explanatory power.

3. Results

3.1. Land Cover Classification Accuracy

The supervised classification of 2023 NAIP imagery reached an overall accuracy of 85% and a kappa coefficient of 0.79. This shows a strong agreement between classified and reference data. User accuracy was 89% for vegetation and 82% for non-vegetation. Producer accuracy was 87% and 84%, respectively. Full results of this accuracy assessment are listed in the confusion matrix generated during the assessment, which is displayed as Table 2. Misclassifications occurred most often in shaded vegetation and senescent grass areas, where spectral signatures overlapped with non-vegetated surfaces. The kappa coefficient value from the 200-point assessment was lower, yet a kappa coefficient of 0.79 still suggests substantial agreement between user and producer values, as noted by Geymen (2016), thus validating the classification method. A kappa coefficient of 0.79 indicates substantial agreement between classified and ground-truth values, as defined by Landis & Koch (1977).

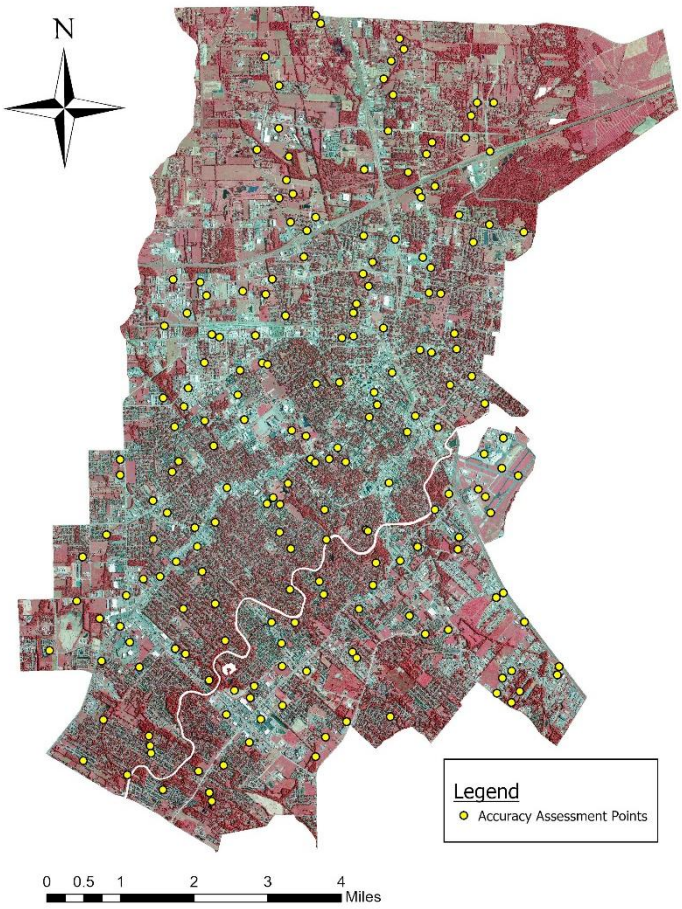

Figure 4. Distribution of 200 points generated for accuracy assessment overlayed on 2023 Color Infrared NAIP imagery used for supervised image classification. Accuracy assessment points are displayed in yellow.

Table 2. Accuracy assessment of the classified image using 200 random points.

		Reference Image		User Accuracy
		Non-Vegetation	**Vegetation**	
Classified Image	**Non-Vegetation**	**95**	5	0.95
	Vegetation	16	**84**	0.84
Producer's Accuracy		0.86	0.94	**0.90**
Kappa		**0.79**		

Certain surfaces and their features led to more significant errors in classification than others. For instance, shaded vegetation was frequently misidentified as non-vegetation. Thick layers of hay also resulted in incorrect classifications. Large grass fields that should have appeared as solid areas were often marked by random spots or splotches of non-vegetation, which were indicated by lighter shades of pink on the color-infrared NAIP image. After visiting some of these sites, it was confirmed that these lighter colors were indeed caused by the presence of hay. This issue mainly occurred due to the decomposition of chlorophyll in the grass, which hindered the reflection of near-infrared light.

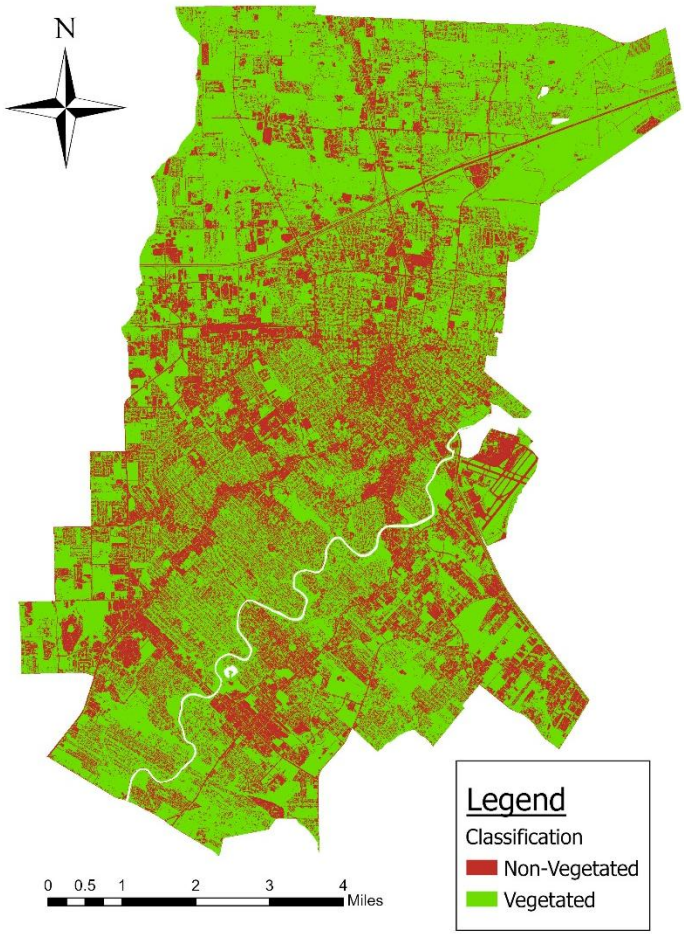

Figure 5. Classified image produced by the maximum likelihood image classification method using the 2023 Color Infrared NAIP image. Green represents areas classified as vegetation, whereas red/brown represents non-vegetated areas.

3.2. Mean Income Relationships

3.2.1. Income and Surface Temperature

Average land surface temperatures in block groups ranged from 110°F to 129°F, with standard deviations between 1.6°F and 8.5°F. Regression analysis showed a significant negative relationship between median household income and average land surface temperature ($r = –0.38$, $R^2 = 0.14$, $p < 0.05$), meaning that lower-income block groups generally had higher surface temperatures than higher-income areas (Figure 6).

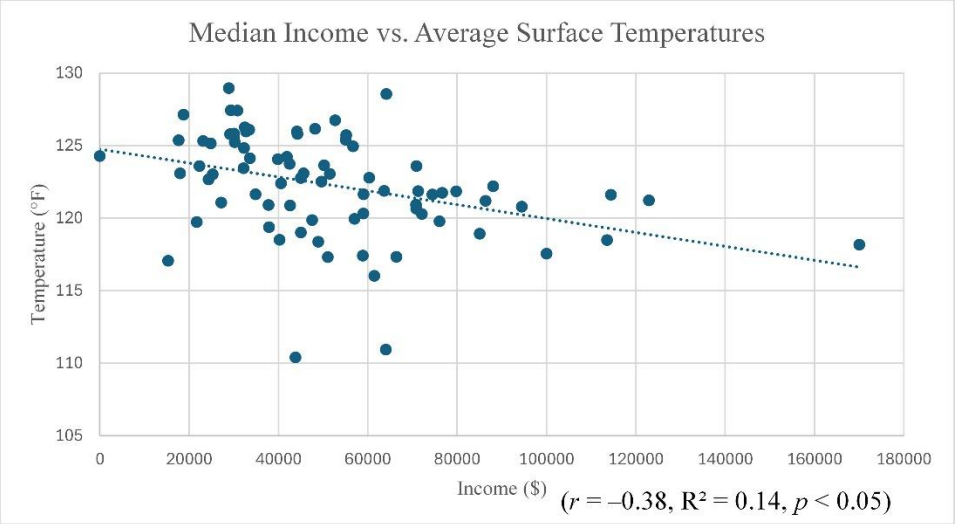

Figure 6. 2023 block group median household income relationship with average surface temperatures.

Block groups with more varied land cover had larger standard deviations in surface temperature. This indicates that local climate differences are affected by the uneven distribution of vegetation. Poverty metrics showed a similar trend: areas with more households living below the poverty line had significantly higher average surface temperatures (Figure 7).

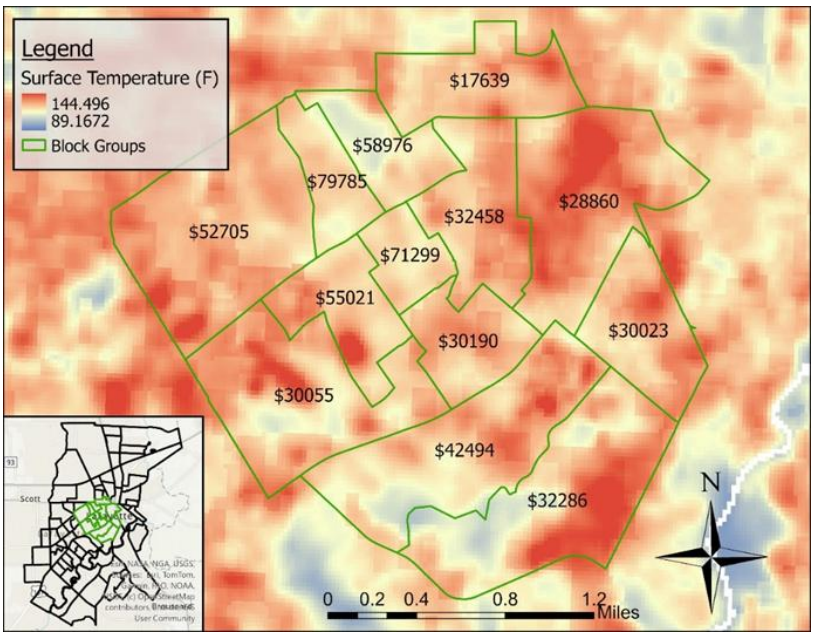

Figure 7. Block groups located in the center of the study area, with the corresponding 2023 median income superimposed on the surface temperature map. Red shades represent hotter temperatures, where yellows and blues are cooler.

3.2.2. Income and Vegetation Cover

Vegetation cover had a positive relationship with median household income ($r = 0.41$, $R^2 = 0.17$, $p < 0.05$). This means that higher-income neighborhoods had significantly more vegetation than lower-income ones (Figure 8). This connection implies that vegetation is important in creating heat differences. Wealthier neighborhoods benefit from more tree cover and green spaces, which help lower surface temperatures through shading and evapotranspiration.

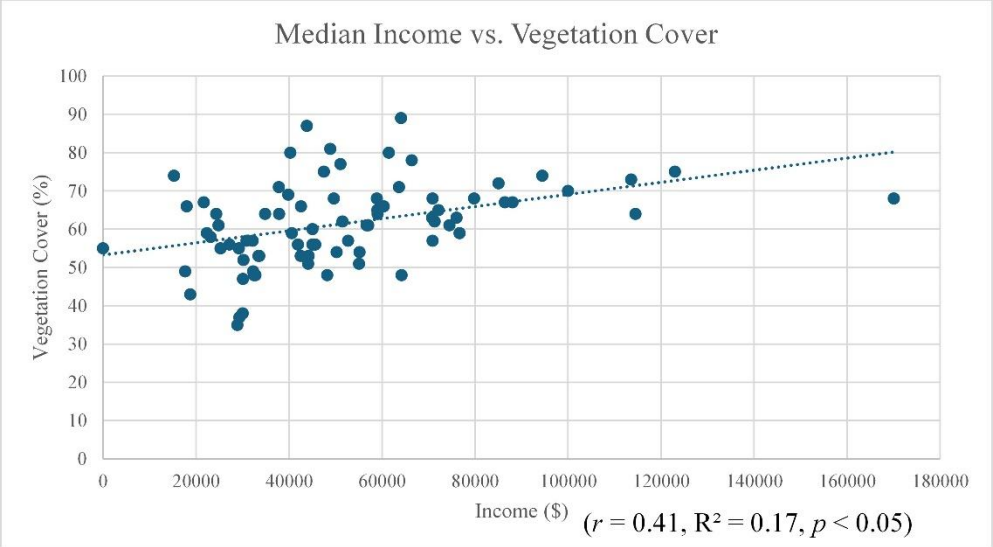

Figure 8. 2023 block group median household income relationship with vegetation cover.

A comparison shows this gap clearly: a high-income block group with 68% vegetation cover had an average land surface temperature of 106.3°F, while a low-income block group with 43% vegetation cover had an average land surface temperature of 127.1°F (Figure 9).

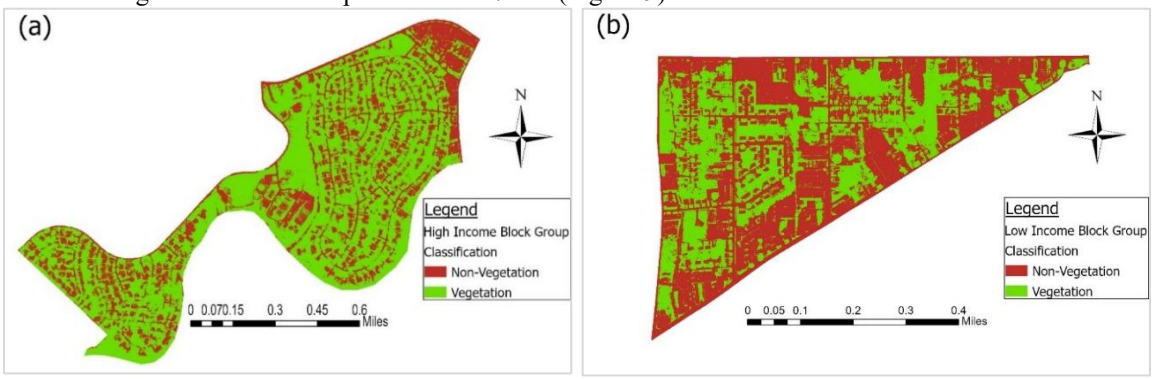

Figure 9. Comparison of vegetation cover in high- and low-income block groups using a classified NAIP image of Lafayette. (a) A higher income block group with a median income of $170,062, 68% vegetation coverage, and 106.3 °F average surface temperature compared to (b) a lower income block group with a median income of $18,747, 43% vegetation coverage, and 127.1 °F average surface temperature.

3.2.3. Income and Parcel Size

There was no significant relationship between parcel size and median household income ($r \approx 0.0$). This suggests that the patterns of land ownership and parcel size do not explain the heat differences seen (Figure 10). These findings indicate that vegetation cover is the key factor affecting spatial differences in heat exposure across Lafayette, not parcel size.

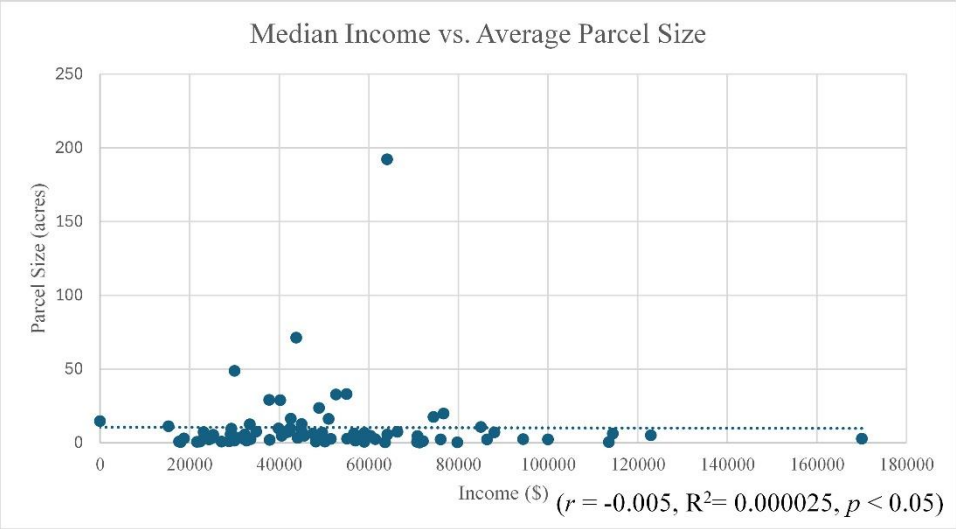

Figure 10. The 2023 block group median household income relationship with the average parcel size.

4. Discussion

This study shows that heat disparities exist across Lafayette, Louisiana. Lower-income neighborhoods face higher land surface temperatures and have less vegetation. These findings are aligned with nationwide studies that have found greater exposure to UHIs in low-income and minority areas (Hsu *et al.*, 2021; Jesdale *et al.*, 2013). By focusing on Lafayette, a medium-sized city in the southern U.S., this study expands environmental justice studies beyond the larger cities that often dominate the UHI literature.

4.1. Vegetation as a Mediating Factor

The negative correlation observed between income and temperature, along with the positive correlation between income and vegetation cover, highlights the role of vegetation in mitigating UHI. Vegetation lowers surface temperatures through shading and evapotranspiration (Bowler *et al.*, 2010). In Lafayette, lower-income areas have fewer trees and less green space, with limited changes for large-scale greening due to denser buildings and smaller lots. Similar issues with vegetation distribution have been found in other U.S. cities, where people in wealthier neighborhoods have more access to trees and parks (Nesbitt *et al.*, 2019).

4.2. Implications for Public Health

Heat disparities lead to health inequities. Higher surface temperatures increase the risk of heat exhaustion, heat stroke, and cardiovascular stress, especially for vulnerable groups like the elderly, children, and individuals with pre-existing conditions (Anderson & Bell, 2011). In Lafayette, where poverty rates are higher than the national averages, the energy and health burdens of UHI disproportionately impact those with fewer resources to cope, raising risks during extreme heat events.

4.3. Energy Use and Economic Burden

Higher surface temperatures boost household energy needs for cooling, driving up utility bills. Previous studies have shown that UHIs can lead to a nearly 20% rise in urban energy use (Li *et al.*, 2019). In Lafayette's low-income areas, the increased demand for cooling adds financial strain to already tight household budgets. This "energy-poverty-heat" connection highlights the need for policies that tackle environmental justice, climate resilience, and affordable housing.

4.4. Adaptation and Policy Relevance

Several strategies emerge from these findings. Increasing tree canopy cover through targeted planting in heat-vulnerable neighborhoods could greatly lower surface temperatures and improve comfort. Low-cost actions, like planting shade trees along residential streets or turning vacant lots into community green spaces,

have successfully reduced local UHI intensity (Fadhil *et al.*, 2023). These strategies also contribute to goals of lowering peak electricity use and reducing health risks associated with heat exposure. For Lafayette, including equity-focused heat mitigation in city planning and zoning could ensure that investments in green infrastructure benefit underserved neighborhoods and future neighborhood development.

4.5. Contributions and Limitations

This study provides the first spatial analysis of UHI disparities in Lafayette, Louisiana. What started off as an undergraduate semester research project for a class turned into a study that can add to the limited research on UHI in smaller U.S. cities. It shows how open-source Earth observation data can be used with socioeconomic information to uncover heat exposure inequalities. However, there are some limitations to note. First, the income data from 2018 and LST imagery from 2023 do not match in time, due to data availability; this does not invalidate the correlations found, but does lower temporal accuracy. Second, only surface temperature was examined; canopy and boundary-layer UHIs, which might impact human thermal comfort more directly, were not considered. Also, while NAIP imagery provided finer resolution for small-scale land use-land cover classification, the use of the National Land Cover Dataset (NLCD) may improve standardization and reproducibility across larger study areas. This research study was part of an undergraduate semester course project where students were required to download their own imagery and perform their own land use-land cover classification based on training samples they created. Future studies should use multi-seasonal and multi-year imagery, include health outcome data, and explore different classification methods beyond maximum likelihood, which was the required classification method for the class research project, to strengthen vegetation analysis.

4.6. Broader Significance

Urban heat inequities are not limited to large cities but are also evident in smaller cities such as Lafayette, Louisiana. By documenting these differences, this study provides local policymakers and community members with information to support climate resilience projects. More broadly, it emphasizes the importance of including environmental justice factors in UHI research and resilience planning, ensuring that climate adaptation strategies protect the most vulnerable groups and help inform future infrastructure development.

5. Conclusions

The results of this study suggest that lower-income neighborhoods in Lafayette, Louisiana, have higher land surface temperatures and less vegetation cover. The negative correlation between household income and land surface temperature, along with the positive connection between income and vegetation cover, highlights how green spaces can impact urban heat differences. While parcel size did not relate significantly to income or temperature, the results point to vegetation loss as a main component contributing to unequal heat exposure.

The study adds to the understanding of UHI and environmental justice by looking at a medium-sized city in the southern U.S., which has not been explored in previous studies. The findings make it clear that heat inequity is not just a problem in large metropolitan areas, but it also affects smaller cities, especially those with high poverty levels.

From a policy perspective, the results stress the need for focused interventions that promote better public health. Programs that incorporate tree planting, turn vacant lots into green spaces, and prioritize greening efforts in low-income neighborhoods can help lower local temperatures, ease energy costs, and improve public health. Including these strategies in urban planning will be essential for building future infrastructure and helping combat rising temperatures in Lafayette and similar communities.

Future research is needed to address data and methodological limitations by incorporating multi-season analyses, studying canopy and boundary-layer UHIs, and adding health outcomes data. These efforts will increase understanding of the connections between socioeconomic factors, land cover, and urban heat, and support evidence-based adaptation strategies.

Funding: This research was funded by the University of Louisiana at Lafayette Sustainable Research Award, sponsored by the Office of the Vice President for Research, Innovation and Economic Development, and the Dwight W. Andrus, Jr. / BoRSF Eminent Scholar Endowed Chair for Finance, the University of Louisiana at

Lafayette Regional Application Center applied research program, and the National Science Foundation (NSF Award No. 2120015) in support of undergraduate research activities that were used in the summer workshop programs under the direction, mentorship and guidance of the Regional Application Center.

Data Availability Statement: Data are available at their respective open-source locations: High-resolution aerial imagery for Lafayette Parish was sourced from the USDA's 2023 NAIP mosaic, available via https://nrcs.app.box.com/v/naip/file/1442308681697. Demographic data, including population and socioeconomic variables from 2018, were accessed through Esri's ArcGIS REST service (https://services.arcgis.com/P3ePLMYs2RVChkJx/arcgis/rest/services/AGOL_Base_2018_Final/FeatureServer). U.S. Census Bureau Block Groups with Demographic Attributes (ACS 5-Year Estimates) were obtained from ArcGIS Online. Local administrative boundaries, including parish and city delineations, were obtained from the Lafayette Consolidated Government's BaseLayers dataset (https://www.arcgis.com/home/item.html?id=4744e86e1607481aab7b42e03941ddeb). To assess land surface temperature, we utilized the Landsat Collection 2 ARD Tile Surface Temperature Bundle, downloadable through the USGS EarthExplorer platform (earthexplorer.usgs.gov). These combined resources enabled a multi-scalar analysis of urban heat island effects across geospatial, demographic, and thermal dimensions.

Acknowledgment: The authors thank the Louisiana Research Collaborative at the University of Louisiana at Lafayette for its support and encouragement of undergraduate research through the Sustainable Development Research Awards Program. This initiative promotes student-led investigations into critical environmental and societal challenges and has been instrumental in making this collaborative project possible. We also acknowledge the U.S. Geological Survey (USGS) and the Landsat satellite program for providing open-access Earth observation data through the EarthExplorer database. This platform has been essential for enabling long-term monitoring of landscape change and supporting applied research in environmental challenges such as urban heat island (UHI) studies. The availability of these high-quality datasets empowers science-based decision-making and fosters transparency and reproducibility in geospatial analysis. Finally, we gratefully acknowledge LouisianaView and AmericaView, whose geospatial resources, collaborative networks, and commitment to advancing remote sensing research and education have further supported the development and broader impact of this work. This material is based upon work partly supported by the U.S. Geological Survey under Grant/Cooperative Agreement No. G18AP00077 (for GY18-GY22) or G23AP00683 (GY23-GY27).

Conflicts of Interest: The authors declare no conflicts of interest. The funders had no role in the design of the study; in the collection, analyses, or interpretation of data; in the writing of the manuscript; or in the decision to publish the results.

References

Ahmed, A. Y., Ali, A. M., & Ahmed, N. (2024). Temporal dynamics of leaf area index and land surface temperature correlation using Sentinel-2 and Landsat OLI data. *Environmental Systems Research, 13*(43). https://doi.org/10.1186/s40068-024-00371-6

Anderson, G. B., & Bell, M. L. (2011). Heat waves in the United States: Mortality risk during heat waves and effect modification by heat wave characteristics in 43 U.S. communities. *Environmental Health Perspectives, 119*(2), 210–218. https://doi.org/10.1289/ehp.1002313

Aziz, N. A., & Alwan, I. A. (2021). An accuracy analysis comparison of supervised classification methods for mapping land cover using Sentinel-2 images in the Al-Hawizeh Marsh Area, Southern Iraq. *Geomatics and Environmental Engineering, 15*(1), 5–21. https://doi.org/10.7494/geom.2021.15.1.5

Bowler, D. E., Buyung-Ali, L., Knight, T. M., & Pullin, A. S. (2010). Urban greening to cool towns and cities: A systematic review of the empirical evidence. *Landscape and Urban Planning, 97*(3), 147–155. https://doi.org/10.1016/j.landurbplan.2010.05.006

Congalton, R. G., & Green, K. (1999). *Assessing the accuracy of remotely sensed data: Principles and practices*. Lewis Publishers.

Earth Resources Observation and Science (EROS) Center. (2020). *Landsat 8-9 Operational Land Imager / Thermal Infrared Sensor Level-2, Collection 2* [Dataset]. U.S. Geological Survey. https://doi.org/10.5066/P9OGBGM6

Esri. (2024). *ArcGIS Pro* (Version 3.4.0) [Computer software]. Esri Inc. https://www.esri.com/en-us/arcgis/products/arcgis-pro/overview

Fadhil, M., Hamoodi, M. N., & Ziboon, A. R. T. (2023). Mitigating urban heat island effects in urban environments: strategies and tools. *IOP Conference Series: Earth and Environmental Science, 1129,* 012025. https://doi.org/10.1088/1755-1315/1129/1/012025

Foody, G. M. (2020). Explaining the unsuitability of the kappa coefficient in the assessment and comparison of the accuracy of thematic maps obtained by image classification. *Remote Sensing of Environment, 239,* 111630. https://doi.org/10.1016/j.rse.2019.111630

Geymen, A. (2016). Determination of the impacts of land use change on water basin using remote sensing and geographical information system. *Anadolu University Journal of Science and Technology A - Applied Sciences and Engineering, 17*(3), 484–496. https://doi.org/10.18038/btda.84861

Hsu, A., Sheriff, G., Chakraborty, T., & Manya, D. (2021). Disproportionate exposure to vegetation intensity across major U.S. cities. *Nature Communications, 12,* 2721. https://doi.org/10.1038/s41467-021-22799-5

Jesdale, B. M., Morello-Frosch, R., & Cushing, L. (2013). The racial/ethnic distribution of heat risk-related land cover in relation to residential segregation. *Environmental Health Perspectives, 121*(7), 811–817. https://doi.org/10.1289/ehp.1205919

Knipling, E. B. (1970). Physical and physiological basis for the reflectance of visible and near-infrared radiation from vegetation. *Remote Sensing of Environment, 1*(3), 155–159. https://doi.org/10.1016/S0034-4257(70)80021-9

Landis, J. R., & Koch, G. G. (1977). An application of hierarchical kappa-type statistics in the assessment of majority agreement among multiple observers. *Biometrics, 33*(2), 363–374. https://doi.org/10.2307/2529786

Li, X., Zhou, Y., Yu, S., Jia, G., Li, H., & Li, W. (2019). Urban heat island impacts on building energy consumption: A review of approaches and findings. *Energy, 174,* 407–419. https://doi.org/10.1016/j.energy.2019.02.183

Nesbitt, L., Meitner, M. J., Girling, C., Sheppard, S. R. J., & Lu, Y. (2019). Who has access to urban vegetation? A spatial analysis of distributional green equity in 10 U.S. cities. *Landscape and Urban Planning, 181,* 51–79. https://doi.org/10.1016/j.landurbplan.2018.08.007

Poirier Chicola, C. A. (2021). *Effect of land use change on river network and channel morphology of four tributaries in the Vermilion Watershed in South Louisiana* (Master's thesis, University of Louisiana at Lafayette). ProQuest.

Sayler, K. (2024). *Landsat 8–9 Level 2 Science Product (L2SP) guide* (Version 6, May 2024). U.S. Geological Survey.

Xian, G., & Crane, M. (2006). An analysis of urban thermal characteristics and associated land cover in Tampa Bay and Las Vegas using Landsat satellite data. *Remote Sensing of Environment, 104*(2), 147–156. https://doi.org/10.1016/j.rse.2005.09.023

Research Article

Three Decades of Changes in the Urban Heat Island Effect in Denver, Colorado, Revealed by Landsat

Sadia Islam Ritu[1] and Bruce Millett[2,*]

[1] Department of Geography and Environmental Studies, Texas State University, San Marcos, Texas, USA; ghw31@txstate.edu

[2] Department of Geography and Geospatial Sciences, South Dakota State University, Brookings, South Dakota, USA; bruce.millett@sdstate.edu

[*] Corresponding Author: bruce.millett@sdstate.edu; +1-605-688-4833.

Abstract: Rapid urbanization has imposed negative environmental impacts and contributed to global climate change on multiple scales. The urban heat island (UHI) is directly caused by urban expansion, dramatically increasing land surface temperature (LST). Despite the growing concern about the UHI in Denver, Colorado, few studies among the existing literature have addressed this issue. This study used United States Geological Survey (USGS) Landsat 5, 7, and 8 analysis-ready data (ARD) to characterize land cover changes and UHI in Denver for three decades (e.g., 1990, 2000, 2010, and 2020). Land surface temperature was derived from USGS Landsat Collection 2 ARD for twelve dates across summer, fall, and winter seasons in 1990, 2000, 2010, and 2020, and analyzed on both seasonal and annual scales. Land cover change (LCC) analysis detected a 13% increase in developed land cover and a 12% decrease in cropland and grass/shrubs from 1990 to 2020. The relationship between land cover and LST was modeled using ordinary least squares (OLS) and geographically weighted regression (GWR) analysis between land cover indices—e.g., the normalized difference vegetation index (NDVI), two-band enhanced vegetation index (EVI2), urban index (UI), and LST. The results from the regression models showed seasonal variability, spatiotemporal variations, and other underlying factors affecting the bivariate correlations. Finally, the seasonal and annual distribution and variation of UHI intensity were measured, and it was identified that the mean annual UHI intensity in 2020 was 1°C higher than that recorded in 1990, which illustrated a consistent spatial distribution throughout downtown Denver and the central areas of the city, while the intensity of UHI represented a more scattered distribution in the non-urban areas. The methods applied in this study can serve as a model for future research on other cities, and the findings can be used to inform sustainable urban planning and to mitigate the effects of UHI in Denver.

Keywords: land surface temperature, urban heat island, surface reflectance, ordinary least squares, geographically weighted regression

Academic Editor: Mohamed Aly
Received: 1 July 2025
Revised: 24 September 2025; 6 October 2025
Accepted: 10 October 2025
Published: 24 October 2025

Citation: Ritu, S. I., & Millett, B. (2025). Three decades of changes in the urban heat island effect in Denver, Colorado, revealed by Landsat. *Journal of Earth Observation and Geospatial Applications*, *1*(1), 64–82. DOI: https://doi.org/10.65372/e3fq4y36

1. Introduction

Rapid urbanization has profoundly transformed landscapes worldwide over the past few decades (UN, 2018). Currently, more than 50% of the global population resides in cities, a proportion projected to exceed 60% by 2030 (Keyvan *et al*., 2021). Urban growth alters land cover and surface energy balances through the expansion of impervious and built-up surfaces, fundamentally reshaping the urban environment. These processes are central to land cover change (LCC) studies, as urban expansion is closely linked to increasing imperviousness.

One of the most significant consequences of urban land use/land cover (LULC) change is the modification of land surface temperature (LST), which is also influenced by urban heat balance and climate change (Yuvaraj, 2020). LST reflects energy fluxes between the atmosphere and the land surface and provides an important measure of atmosphere–surface interactions (Zhengming & Dozier, 1996; Liu & Weng, 2009). Consequently, the spatial and temporal patterns of LST reveal variations in climate, land surface properties,

and urban development (Yuvaraj, 2020). Understanding the urban thermal environment therefore requires examining key factors such as LST, land cover, and solar radiation (Aguiar & Gonçalves, 2002; Liu & Weng, 2009).

The urban heat island (UHI) effect—defined as the increase of surface temperatures in urban areas relative to surrounding rural zones—arises from reduced albedo, limited evapotranspiration, and intensified anthropogenic heat emissions (Voogt & Oke, 2003). LST differences between urban and rural areas are used to quantify UHI intensity (George *et al*., 2022). Advances in thermal remote sensing have enabled extensive research on surface urban heat islands (SUHI), providing spatially and temporally consistent observations of LST (Voogt & Oke, 2003). For example, comparative analyses of metropolitan regions such as Atlanta and Minneapolis demonstrated that variations in LST between urban and adjacent non-urban areas reflect differences in UHI intensity and landscape thermal properties (George *et al*., 2022).

Currently, satellite-based thermal infrared remote sensing provides the most effective means of investigating spatial and temporal variations in LST (Yuvaraj, 2020). This technology is indispensable for understanding the complexities of urban thermal environments and surface–atmosphere energy exchanges, due to its ability to provide synoptic, consistent, and long-term records (George *et al*., 2022).

Spatiotemporal modeling of the UHI effect using Landsat TM and ETM+ imagery has shown that early studies primarily focused on the relationship between land cover composition, particularly vegetation abundance, and LST (Buyantuyev *et al*., 2010; Frey *et al.,* 2007; Weng *et al*., 2006). Because ground station data are sparse and unevenly distributed, they are insufficient for characterizing the spatial patterns of UHIs in a large area (George *et al*., 2022). Recent studies have moved beyond quantifying total vegetation cover to examine the influence of vegetation patch size, distribution, and configuration on LST (Cao *et al.,*2010; Peng *et al*., 2018; Yue *et al.,* 2007). Additional research has also investigated the relationship between landscape heterogeneity and variations in LST zones (Liu & Weng, 2009).

UHI intensity (UHII) is commonly measured as the LST difference between urban pixels and surrounding non-urban reference areas (Voogt & Oke, 2003; Xian, 2008; Imhoff *et al*., 2010; Clinton & Gong, 2013), with remote sensing providing the most effective means for capturing these differences (Streutker, 2002). Assessments of surface UHI typically focus on mapping UHII and its spatial distribution at a given time using remote sensing data integrated with land cover information (George *et al*., 2022). Urban footprints are often defined based on contiguous built-up areas, beginning with the central business district (CBD) and expanding outward (Harald *et al*., 2020; Richard *et al*., 2022). For example, Richard *et al*. (2022) used 8-day MODIS Aqua MYD11A2 composites (1 km resolution) to quantify UHI trends from 2003 to 2019, applying a 10 km buffer around urban boundaries to compare urban and surrounding non-urban LST. Their analysis further examined diurnal and nocturnal annual mean LST trends in six climate-diverse cities—continental (Beijing), temperate (Mexico City and Santiago), and arid (Cairo, Hyderabad, and Riyadh) using 1 km MODIS data (2003–2019). These methods highlight how thermal remote sensing can identify urban hotspots and support the design of targeted heat mitigation strategies (George *et al*., 2022).

Denver consistently ranks among the U.S. cities with the most intense UHI effects, placing third out of 60 cities in one national assessment (Kenward *et al*., 2014). Over the past decade, the city has exhibited an average urban–rural temperature difference of approximately 2.5 °C (4.9 °F), with more than 26 days each year exceeding 32 °C (90 °F). Rapid urbanization, population growth, and declining vegetation cover have intensified these effects. High-rise buildings, dark roofing, and impervious pavements exacerbate heat retention by reducing nighttime cooling and enhancing radiative and turbulent heat transfer (Davis, 2021). Despite these severe conditions, Denver has not been extensively studied using long-term remote sensing approaches, leaving gaps in understanding the role of land cover change in shaping UHI intensity.

This study addresses this gap by examining three decades (1990–2020) of satellite-derived data to investigate the relationship between LCC, LST, and UHI intensity in Denver. Using Landsat Analysis Ready Data (ARD), we quantified changes in land cover composition and assessed the spatial and temporal dynamics of LST. UHI intensity was evaluated by comparing urban pixel temperatures with the mean LST of non-urban buffer zones (5 km and 10 km). The analysis reveals extensive urban expansion over the study period and demonstrates its direct influence on surface temperature patterns. The study highlights the broader significance of understanding how long-term land cover dynamics contribute to UHI intensity in Denver. By integrating remote sensing with spatial analysis, this study provides valuable insights into how urban growth, loss of vegetation, and rising surface temperatures are connected. These findings provide an important foundation for guiding sustainable urban planning, promoting green infrastructure, and developing climate adaptation strategies to help reduce UHI impacts in rapidly growing cities.

2. Study Area and Data

2.1. Study Area

Denver is situated between the Rocky Mountains to the west and the High Plains to the east, at 39.74°N latitude and 104.99°W longitude (Figure 1). The city lies at an elevation of approximately 1,609 m above sea level, earning it the title "Mile High City." This elevation, combined with its mid-latitude location, produces a semi-arid climate characterized by mild winters, dry summers, and low relative humidity. These conditions not only shape local thermal dynamics but also amplify the UHI effect by reducing evaporative cooling potential and intensifying heat retention in built-up areas.

Denver is one of the fastest-growing metropolitan regions in the United States, with a population of 2.9 million that has expanded more rapidly than the national average (World Report, 2019). Rapid urbanization, coupled with the city's unique geographic and climatic context, makes Denver especially vulnerable to UHI effects. Between 2001 and 2016, the city underwent a net land cover change of 32.3 km², with substantial increases in medium and high-intensity development (MRLC, 2016). According to the National Land Cover Database, urban land is classified by imperviousness: high intensity (80–100%), medium intensity (50–79%), low intensity (20–49%), and open space (<20%) (Homer *et al*., 2020). Over this period, Denver County experienced an 8.05% change in land cover, including a gain of 16.9 km² in developed land and 11.91 km² in impervious surfaces. Grassland and cropland were the primary land cover types lost, converted into urban development.

Together, Denver's high elevation, semi-arid climate, and rapid urban expansion provide a unique setting for investigating UHI intensity and its drivers. These characteristics not only distinguish Denver from other U.S. cities but also highlight the need for long-term monitoring of land cover and temperature dynamics to better understand and mitigate the city's urban heat risks.

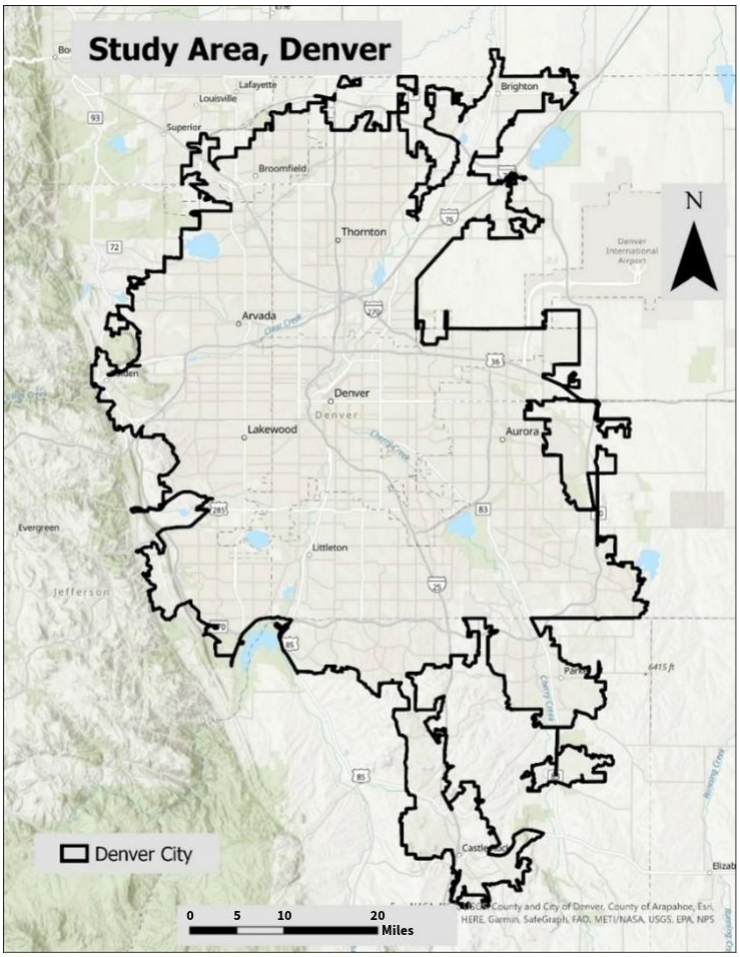

Figure 1. Map of the study area, Denver (Reprojected to NAD 1983 UTM Zone 13N).

2.2. Land Cover Data

Land cover change from 1990 to 2020 was examined using the Land Change Monitoring, Assessment, and Projection (LCMAP) dataset, obtained from the USGS Earth Explorer platform (Table 1). LCMAP provides annual land cover maps of the conterminous United States, classified into eight categories: Developed, Cropland, Grass/Shrub, Tree Cover, Wetland, Water, Ice/Snow, and Barren. These classes are based primarily on the Anderson Level I classification scheme (Anderson *et al*., 1976). For this study, land cover maps from the USGS LCMAP Collection 1 products were used directly for analysis, with a subset of the Denver metropolitan area. The permanent ice/snow class was excluded because it is not found in the study area; instead, seven of the eight land cover classes were used. The LCMAP product has an overall accuracy of 82.5%, validated through 25,000 randomly distributed reference samples annotated using Google Earth (Stephen *et al*., 2021).

Table 1. Necessary data for the study. Data source: U.S. Geological Survey (USGS). Projection: NAD 1983 UTM Zone 13N.

Data/ Product	Data Source	Years	Version	Resolution
Shapefile	TIGER Data Product			
LCMAP	USGS	1990	CCDC V 1.3	30 x 30 m
		2000		
		2010		
		2020		
Surface Reflectance (SR)	USGS	1990	Landsat C2 U.S. (ARD)	30 x 30 m
		2000	Landsat 5, 7 and 8	
		2010		
		2020		
Surface Temperature (ST)	USGS	1990	Landsat C2 U.S. (ARD)	30 x 30 m
		2000	(Landsat 5,7 and 8)	
		2010		
		2020		

2.3. Surface Reflectance Data

To minimize atmospheric influences on spectral measurements, Landsat surface reflectance products were employed. These products incorporate corrections for atmospheric aerosols, gases, and water vapor, thereby providing consistent geophysical and biophysical parameters across sensors and time periods (Dwyer *et al*., 2018). The use of surface reflectance data ensures the comparability of multi-temporal analyses of vegetation indices and land cover.

2.4. Land Surface Temperature Data

Land surface temperature was derived from the thermal bands of Landsat sensors. For historical observations, LST was extracted from band 6 of the Landsat 5 Thematic Mapper (TM). For recent years, LST was retrieved from band 10 of the Thermal Infrared Sensor (TIRS) onboard Landsat 8. These datasets enabled consistent estimation of spatial and temporal variations in LST over the 30-year study period.

3. Methods

This study followed a prototype workflow adapted from Xian *et al*. (2021). Land cover maps were generated from LCMAP data using ArcGIS Pro. Vegetation and urban indices, including the enhanced vegetation index 2 (EVI2), normalized difference vegetation index (NDVI), and urban index (UI), were derived from Landsat surface reflectance products. These indices were calculated using the Map Algebra function in the Spatial Analyst extension of ArcGIS Pro.

LST was calculated through raster-based map algebra operations using the Raster Calculator. To support statistical analysis, 800 sample points were generated through random sampling in ArcGIS Pro, and values of EVI2, NDVI, UI, and LST were extracted from the corresponding raster layers.

Ordinary least squares (OLS) regression and geographically weighted regression (GWR) were applied to assess spatial and temporal relationships between land cover indices and LST. Non-urban reference buffers were delineated using the Proximity Analysis tool, and zonal statistics were used to summarize mean conditions within these buffers. Urban heat island intensity was then computed as the difference between mean non-urban buffer temperatures and urban pixel temperatures, derived using Map Algebra in ArcGIS Pro (Figure 2).

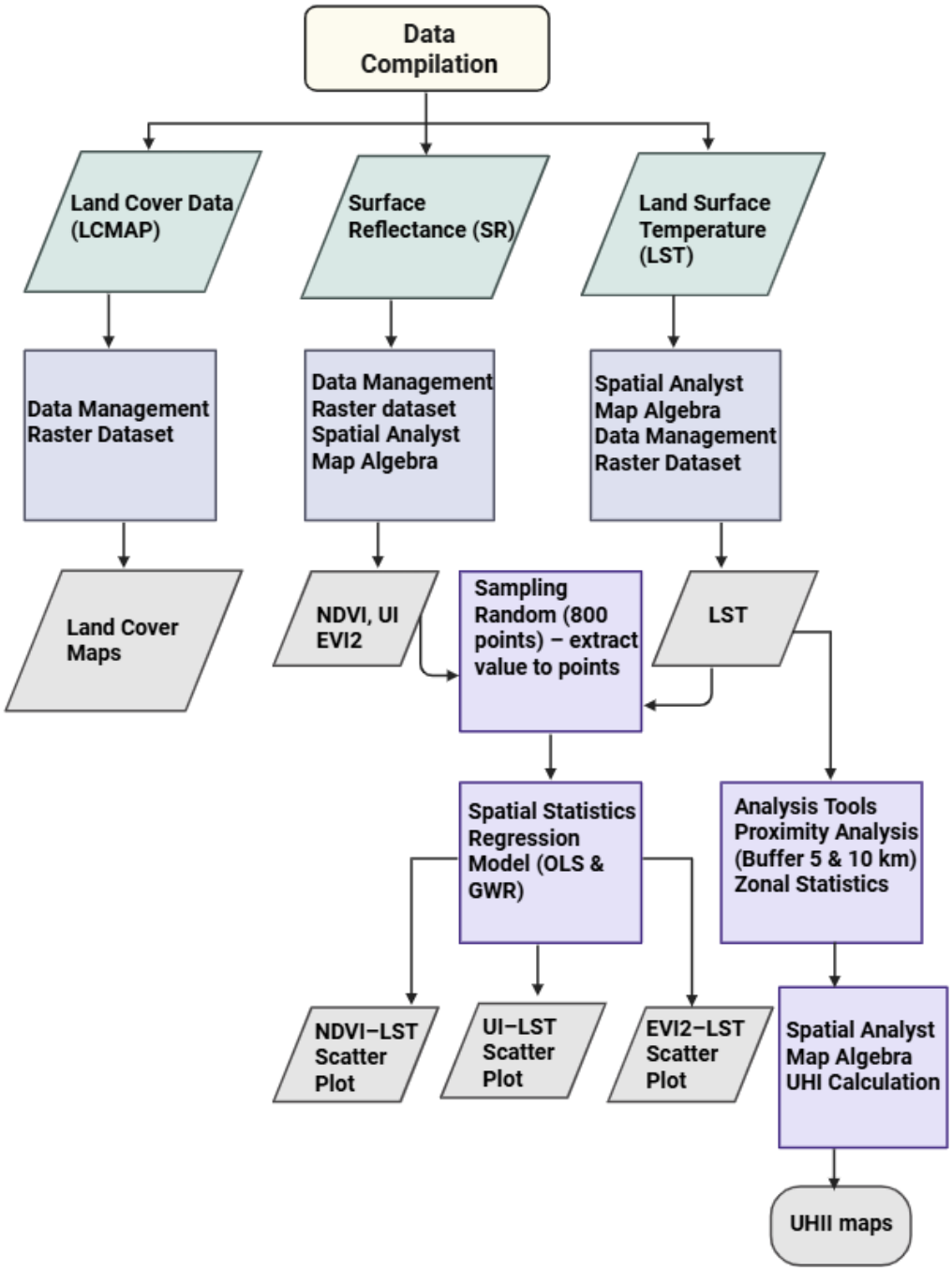

Figure 2. Workflow diagram.

3.1. Land Cover Change Analysis

The urban land cover map was derived from the LCMAP, which has eight primary land cover classes. LCMAPs from different years examined the changes in land cover over 30 years (e.g., from agricultural and rural land cover to developed impervious surfaces).

3.2. Land Cover Indices and LST Comparison

This study examined the relationship between land cover indices, urban index and LST. Surface reflectance (SR) and surface temperature (ST) data were used for analysis. Landsat LST measures the Earth's temperature in Kelvin. LST was converted to degrees Celsius using the Map Algebra toolset of Spatial Analyst Tools in ArcGIS Pro. The formula in Equation (1) applied for the conversion of LST from Kelvin to degrees Celsius is the following:

$$\begin{aligned} T(℃) &= T(\mathrm{K}) - 273.15 \\ &= LST \times 0.00341802 + 149 - 273.15 \end{aligned} \tag{1}$$

where T (°C) and T (K) are the LST in degrees Celsius and Kelvin, respectively. LST is the stored ST values in the Landsat Collection-2 data derived from band 6 for Landsat 5 and 7 and band 10 for Landsat 8, respectively. The 0.00341802 and 149 are the two linear coefficients used to convert the stored values to ST in Kelvin (K) (Christopher *et al*., 2023).

SR data were used to derive spectral indices. NDVI measures the reflectance of incoming solar radiation from the Earth's surface to the Landsat sensor. It is widely used to extract information about vegetation density, predict crop production, monitor drought, and measure surface temperature. In addition, NDVI measures vegetation abundance and is frequently used to indicate land surface characteristics in studies related to UHI.

The formula in Equation (2) used for NDVI index calculation of different wavelengths of the Landsat data is the following:

$$\begin{aligned} NDVI &= \frac{(NIR - Red)}{(NIR + Red)} \\ NDVI(Landsat\ 4,5\ \&\ 7) &= \frac{(Band\ 4 - Band\ 3)}{(Band\ 4 + Band\ 3)} \\ NDVI\ (Landsat\ 8\ \&\ 9) &= \frac{(Band\ 5 - Band\ 4)}{(Band\ 5 + Band\ 4)} \end{aligned} \tag{2}$$

where NDVI value always ranges from −1 to + 1.

NIR is the near-infrared waveband (band 4), and Red is the visible band (band 3). The NDVI value for green vegetation ranges from 0.1 to 0.7, so higher values indicate healthy and dense vegetation cover.

The two-band enhanced vegetation index (EVI2) was derived using the following formula in Equation (3):

$$EVI2 = \frac{2.5 * (NIR - Red)}{(NIR + Red + 1.0)} \tag{3}$$

where EVI2 value ranges from −1 to + 1.

UI was derived using the following formula, explained in Equation (4):

$$UI = \frac{(SWIR - NIR)}{(SWIR + NIR)} \tag{4}$$

where UI value ranges from −1 to + 1.

To evaluate the influence of land cover characteristics on land surface temperature, vegetation indices (NDVI, EVI2), UI, and LST were compared across multiple years. NDVI, EVI2, and UI were treated as

independent variables, while LST served as the dependent variable (Figure 6). Regression analysis was employed to quantify the bivariate relationships between LST and each land cover index.

Ordinary least squares and geographically weighted regression were used to estimate regression slopes and assess the strength of these relationships. OLS provided global estimates of the correlation, while GWR captured local variations in regression coefficients across the study area.

For statistical analysis, raster datasets of LST and land cover indices were converted into point features. A total of 800 random points were generated across the study area, and values of NDVI, EVI2, UI, and LST were extracted at these locations using the Extract by Mask tool in the Spatial Analyst extension of ArcGIS Pro. This approach ensured representative sampling of both urban and non-urban environments.

Scatterplot diagrams were generated from both OLS and GWR outputs to examine the bivariate correlations between land cover indices and LST for 1990, 2000, 2010, and 2020. While the OLS scatterplots reflected overall global trends rather than detailed spatial variation, the GWR scatterplots provided precise detail by capturing local differences and temporal changes in the strength of these relationships. Therefore, only the GWR scatterplots were presented in the paper (Figure 6), as they more effectively illustrate the spatial heterogeneity in the associations between vegetation indices, urban index, and LST. In the scatterplot, LST values illustrated the surface temperature gradient, NDVI, EVI2, and UI values reflected temporal variation in vegetation cover and urban development across the study area.

3.3. Quantifying UHI Intensity

The first step in calculating urban heat island intensity was to delineate the urban boundary. Urban areas identified in 2017 within the administrative boundary of Denver were defined as the extent of the urban core, based on the land cover dataset. To establish reference conditions, non-urban buffers extending 10 km beyond the urban boundary were generated. More than 99% of these buffer zones were classified as non-urban land cover types.

UHI intensity was then quantified as the temperature difference between urban and non-urban areas from 1990 to 2020. Specifically, LST values for each urban pixel (30 m resolution) were compared with the mean LST of surrounding non-urban buffer pixels. This approach allowed estimation of both temporal trends and spatial variation in UHI intensity across the study area. The calculation of UHI intensity followed the method outlined by Xian *et al*. (2021). The following formula has been used (see Equation (5)).

$$UHII\ (i) = Tu(i) - \overline{T}\,r(i) \tag{5}$$

Here, $UHII\ (i)$ is the UHI intensity for an urban pixel i, $Tu(i)$ is the temperature of the urban pixel i, and $\overline{T}\,r(i)$ is the mean LST of a surrounding non-urban buffer pixel i (Xian *et al*., 2021). The UHI intensities associated with different land cover types have been quantified, and new urban growth regions have been identified (Xian *et al*., 2021).

The Landsat-derived annual mean LST was used to quantify UHI intensity while minimizing the influence of short-term daily fluctuations. The annual mean LST was calculated following the algorithm developed by the USGS Earth Resources Observation and Science (EROS) center for UHI studies (Xian *et al*., 2021). This algorithm removes pixels contaminated by clouds, shadows, and snow/ice using the Landsat surface reflectance quality assessment (QA) and surface temperature quality assessment (STQA) bands. Clear-sky pixels with surface temperatures above 0 °C were averaged from March through November to reduce the influence of snow, ice, and cloud contamination (Xian *et al*., 2021). In this study, we adopted this approach by using pixels with effective seasonal records to compute annual mean LST values, which were then applied to analyze temporal changes in Denver's LST (1990–2020) and to generate UHI intensity maps.

4. Results and Discussion

4.1. Urban Land Cover Change Analysis

Seven of the eight land cover classes defined in the Land Change Monitoring, Assessment, and Projection (LCMAP) dataset were considered in this study; the permanent ice/snow class was excluded, as it is not present in the Denver metropolitan region. LCMAP was used to generate land cover maps for 1990, 2000, 2010, and 2020 (Figures 3a & 3d), allowing assessment of spatial patterns and temporal changes in land

cover over the 30 years. These maps were directly obtained from pre-classified LCMAP products, which are generated by the USGS using Landsat observations through an established processing and validation framework. For this study, the LCMAP data were subset to the Denver region, and the relevant classes were selected and visualized in ArcGIS Pro.

In 1990, grassland and shrubland dominated the southern and northwestern portions of the study area, while cropland was concentrated in the northeast. Urban development was largely confined to the central city (Figure 3a). By 2000, developed land cover had increased by approximately 7% relative to 1990, primarily through the conversion of grassland and cropland (Figure 3b). Expansion occurred to the north and south, with additional but more limited growth to the east and northwest. While some cropland persisted in the northeast, much of the grassland and shrubland in the south had already been converted to urban use (Figure 3b). By 2020, a substantial proportion of the cropland and grass/shrubland present in 1990 and 2000 had been replaced by developed land, reflecting extensive urban expansion across the study area (Figure 3d).

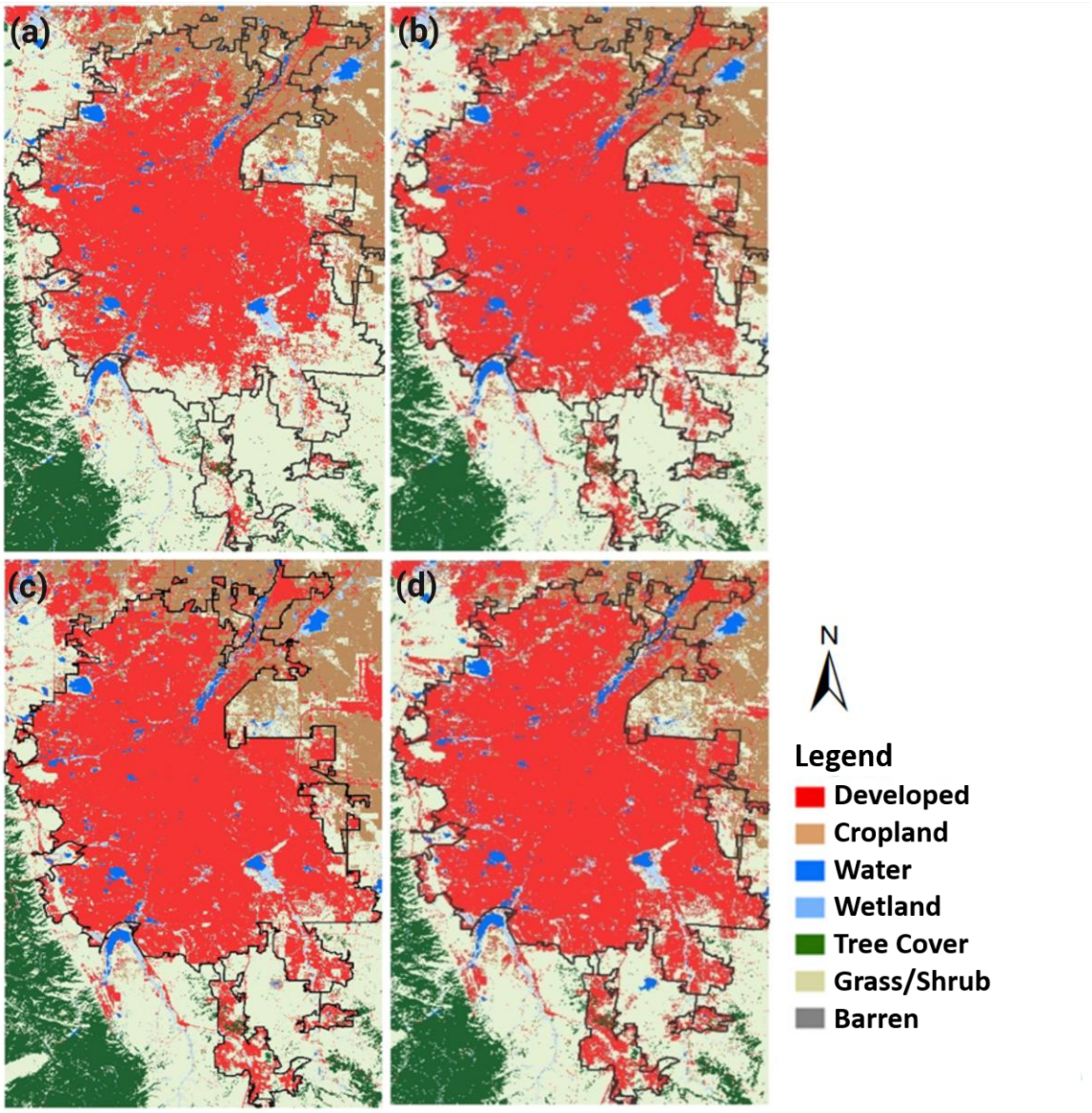

Figure 3. Land cover patterns and changes in Denver city in 1990 (a), 2000 (b), 2010 (c), and 2020 (d) with seven land cover classes.

4.2. Seasonal NDVI

NDVI values provide information about vegetation cover, abundance, and type across the landscape. Using Landsat reflectance data, NDVI maps were created for multiple years and three different seasons (Figures 4a–f). To highlight long-term trends, the comparison between 1990 and 2020 is emphasized, since it best illustrates landscape changes over three decades. Summer results were the most reliable, though fall and winter patterns were also considered. In urban areas, NDVI values were consistently low, reflecting limited vegetation and a high proportion of impervious surfaces. The lowest values were concentrated in the city center and commercial districts with dense development, while suburban areas retained slightly higher values. In contrast, the northeast and north-central parts of the city generally showed higher NDVI values across all years. In the city center, NDVI values during summer (June–August) ranged from 0.01 to 0.10 (Figures 4a & 4b). In fall (September–November), values ranged from 0.02 to 0.18 (Figures 4c & 4d), and in winter (December–February) from 0.001 to 0.10 in both 1990 and 2020 (Figures 4e & 4f). These values highlight the sharp contrast between heavily built-up urban zones and greener suburban or undeveloped areas.

Denver International Airport, located in the northeast of the city, had the lowest NDVI value (0.002), reflecting very little vegetation. In contrast, the western part of Denver, which includes mountain areas, showed much higher NDVI values due to dense vegetation. Figures 4a–d illustrate that the city center consistently had low NDVI values in both summer and fall, since this highly urbanized core is dominated by built-up surfaces. The western side of Denver changed very little between 1990 and 2020 because the mountains limited development. Instead, most urban expansion occurred in the northeast, while the southern part of the city experienced only minor changes. NDVI patterns outside the city were uneven, especially in winter, when NDVI is less reliable as an indicator of vegetation cover.

4.3. Seasonal LST

LST maps were created from Landsat data, with all values shown in degrees Celsius (Figures 5a−f). To show long-term change, we focus on 1990 and 2020 across summer, fall, and winter. Although data were also available for 2000 and 2010, the 1990–2020 comparison best captures the overall warming trend, and summer results were the most consistent across years.

Over the past 30 years, mean seasonal LST values rose sharply, especially in the urban core where new developments added more heat-absorbing surfaces. In 1990, seasonal mean LSTs were estimated at 7.8 °C in summer, 19.0 °C in fall, and −19.4 °C in winter in the Denver metropolitan area. By 2020, these values had increased substantially to 47.6 °C in summer, 34.9 °C in fall, and 11.4 °C in winter. This shows overall warming and a smaller seasonal gap compared to earlier decades. The unusually low winter average in 1990 and the relatively warm summer average in the same year are likely caused by residual effects of snow cover, incomplete masking of water surfaces, or atmospheric contamination in the remote sensing imagery, rather than by actual surface conditions.

Figure 5 depicts LST using a color gradient, where dark blue represents cooler areas and red indicates hotter areas. A comparison of the summer maps between 1990 and 2020 reveals a distinct shift in the central city from yellow to deep red, reflecting a substantial rise in surface temperatures. The steady increase in all seasons and a reduction of the seasonal difference evident that Denver has seen substantial surface warming, driven by land cover change and rapid urbanization. This increase corresponds to the expansion of impervious, built-up surfaces, which intensified the UHI effect.

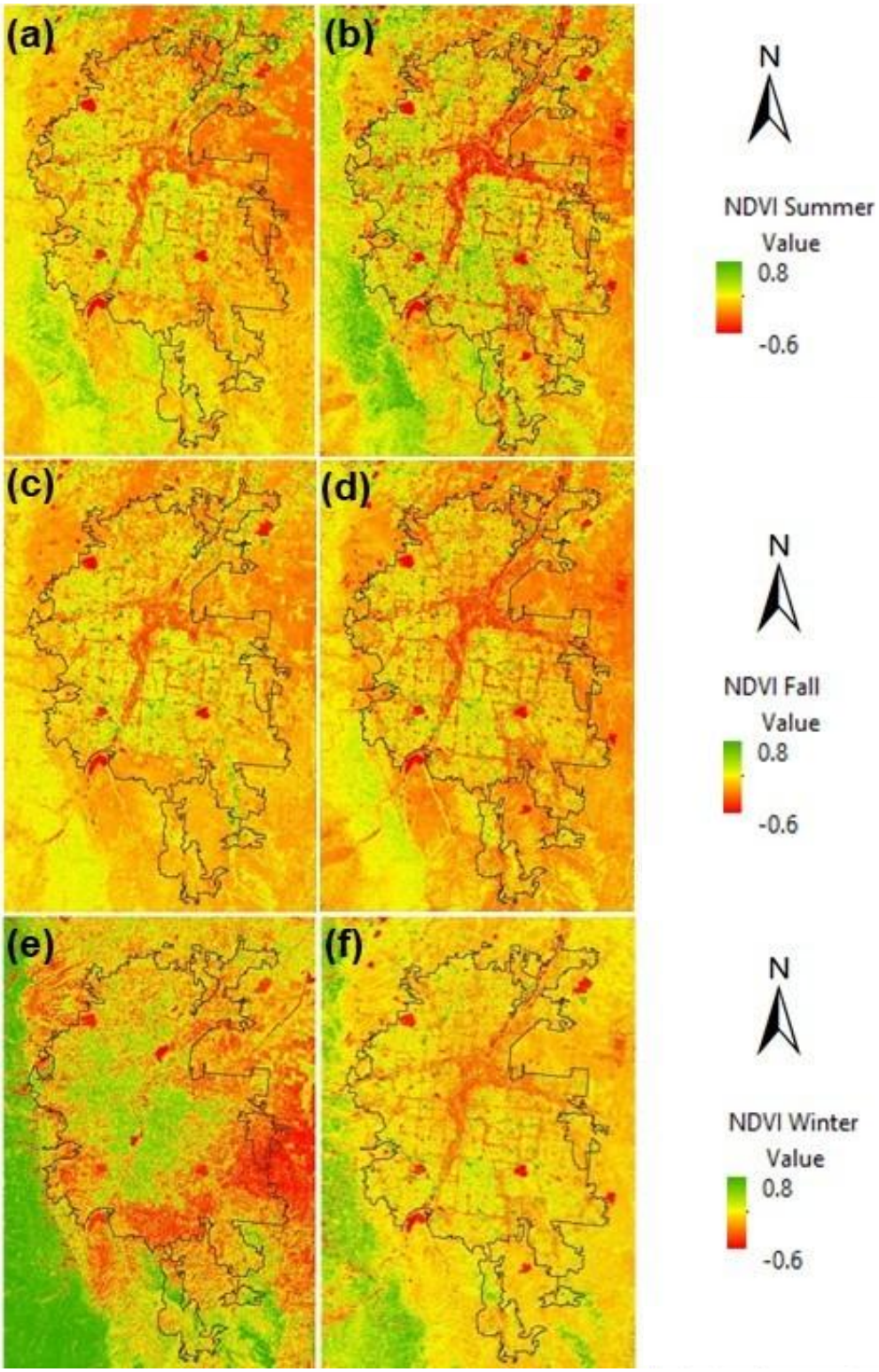

Figure 4. Spatial and temporal distribution of NDVI in the Denver urban area across three seasons, summer (a, b), fall (c, d), and winter (e, f)—for the years 1990 (a, c, e), and 2020 (b, d, f).

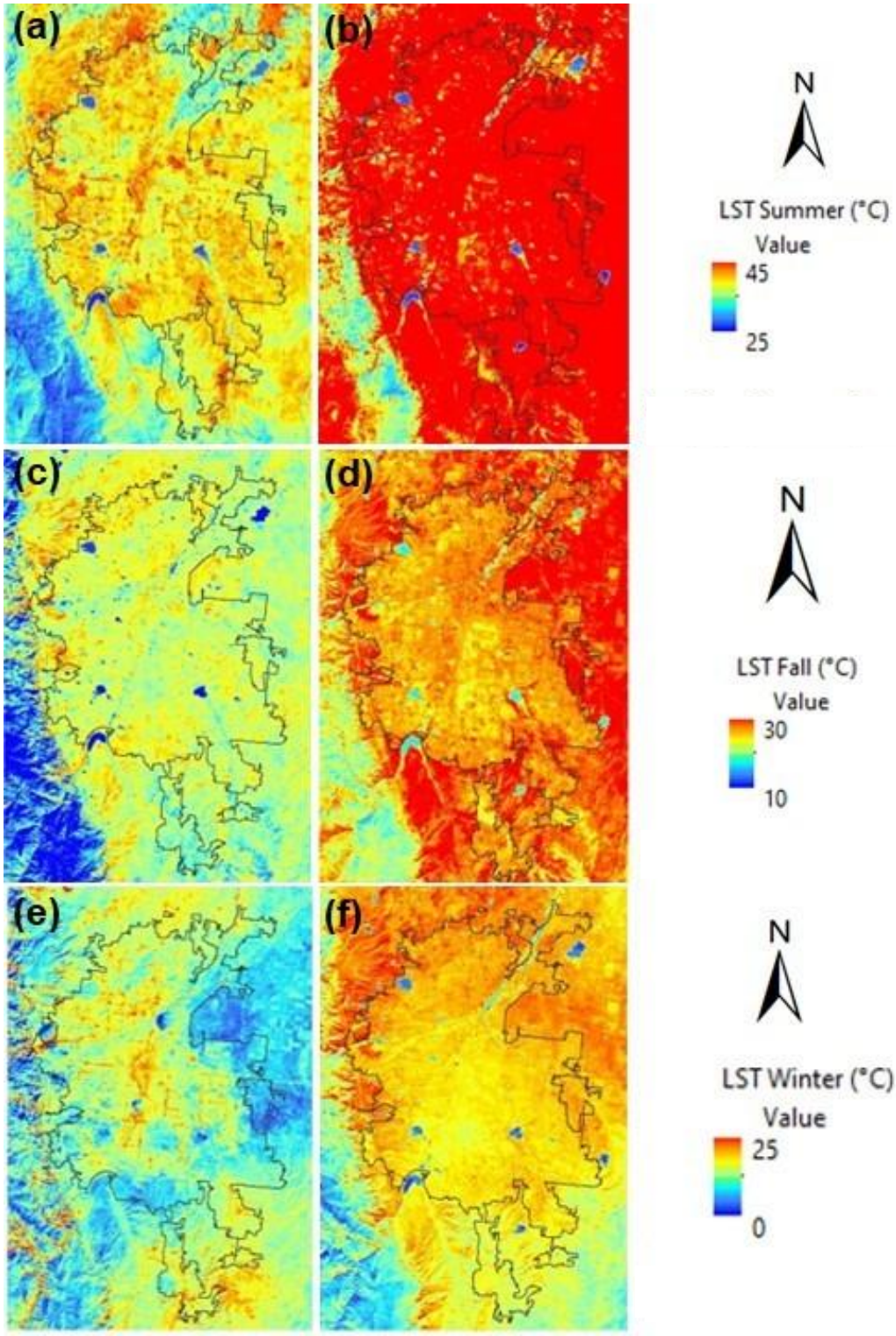

Figure 5. Spatial and temporal distribution of LST (°C) across three seasons—summer (a, b), fall (c, d), and winter (e, f)—for two reference years: 1990 (a, c, e), and 2020 (b, d, f) in the Denver urban area.

4.4. Relationship between Land Cover Indices and LST

The relationship between vegetation indices (NDVI, EVI2), the UI, and LST was analyzed using regression models. OLS regression provided the slope of these relationships, showing whether the correlation was negative (e.g., more vegetation linked to cooler temperatures) or positive (e.g., more built-up land linked to hotter temperatures). Figure 6 includes scatter plots from the GWR model, which illustrates how well the predicted values match the observed data.

To measure the strength of these relationships, we used the R^2 statistic. This value, which ranges from 0 to 1 (or 0% to 100%), indicates how much of the variation in LST can be explained by the independent variables (NDVI, EVI2, and UI). An R^2 of 1.0 means a perfect fit, while a value near 0 means the variables do not explain LST well.

However, relying solely on R^2 for interpretation can be misleading. A low R^2 does not necessarily mean the model is poor, nor does a high R^2 always mean it is ideal. Scatter plots may reveal biases or mismatches between data points and model predictions. Thus, R^2 is best seen as one indicator of how well the model captures the relationship between land cover indices and LST (Kutner *et al*., 2004)

The OLS regression analysis showed how strongly land cover and urban indices (NDVI, EVI2, and UI) were related to LST in Denver for 1990, 2000, 2010, and 2020. For the UI, the adjusted R^2 was 3% in 1990, indicating a weak relationship with LST. By 2000, the relationship strengthened considerably (42%) but then declined in 2010 (14%) before rising again in 2020 (32%). For the EVI2, the adjusted R^2 was 8% in 1990, increased to 25% in 2000, dropped slightly to 15% in 2010, and settled at 18% in 2020. These results suggest that the influence of built-up areas and vegetation on LST varied over time, with the strongest relationships occurring around 2000, followed by weaker correlations in 2010, and increasing again by 2020.

The OLS model did not represent the spatial heterogeneity within the study area, although it offered a helpful global summary of these associations. To overcome these limitations, GWR was then applied to examine how NDVI, EVI2, and UI related to LST in Denver for 1990, 2000, 2010, and 2020. The results showed relatively low adjusted R^2 values in 1990, meaning the land cover indices explained only a small portion of the variation in LST at that time. Nevertheless, the analysis confirmed that NDVI, EVI2, and UI influence LST. While these indices are not the only factors affecting surface temperature, they also contribute to its changes. This supports the study's goal of identifying how land cover characteristics are linked to variations in LST.

Figure 6 presents scatter plots from the GWR model, showing how NDVI, EVI2, and UI explained variations in land surface temperature across four time periods. For NDVI, the adjusted R^2 was 8% in 1990, increased to 25% in 2000, then declined to 15% in 2010, and rose slightly to 18% in 2020. The urban index showed the lowest value in 1990 at 3%, but it climbed sharply to 43% in 2000 before dropping to 14% in 2010 and recovering to 32% in 2020. For EVI2, the adjusted R^2 was 8% in 1990, rose to 26% in 2000, fell sharply to 3% in 2010, and improved to 19% in 2020. According to the literature, adjusted R^2 values between 10% and 50% are generally acceptable when statistically significant (Fricker *et al*., 2015). The results of this study fall within that range, confirming that vegetation and urban indices had a meaningful, though varying, influence on LST across the three decades. Overall, UI generally showed the strongest influence on surface temperature, while NDVI and EVI2 played smaller but more consistent roles.

The correlation between vegetation indices and LST follows a consistent trend: as NDVI and EVI2 increase, LST decreases, and vice versa. Increased vegetation cover is associated with a reduction in the slope of temperature change, whereas vegetation loss corresponds to an increase in that slope. In contrast, the expansion of developed and built-up land cover contributes to substantial increases in temperature. The relationships among NDVI, EVI2, the urban index, and LST are influenced by seasonal variation, diurnal cycles, and data accuracy. The negative correlation between NDVI/EVI2 and LST is largely attributable to vegetation density and the topographic characteristics of the study area. Overall, these relationships remain consistent across all years examined. Previous research has demonstrated that the NDVI–LST relationship is particularly pronounced and reliable during summer months. In this study, linear regression analysis was applied using NDVI, EVI2, and UI as explanatory variables to quantify their bivariate correlations with LST.

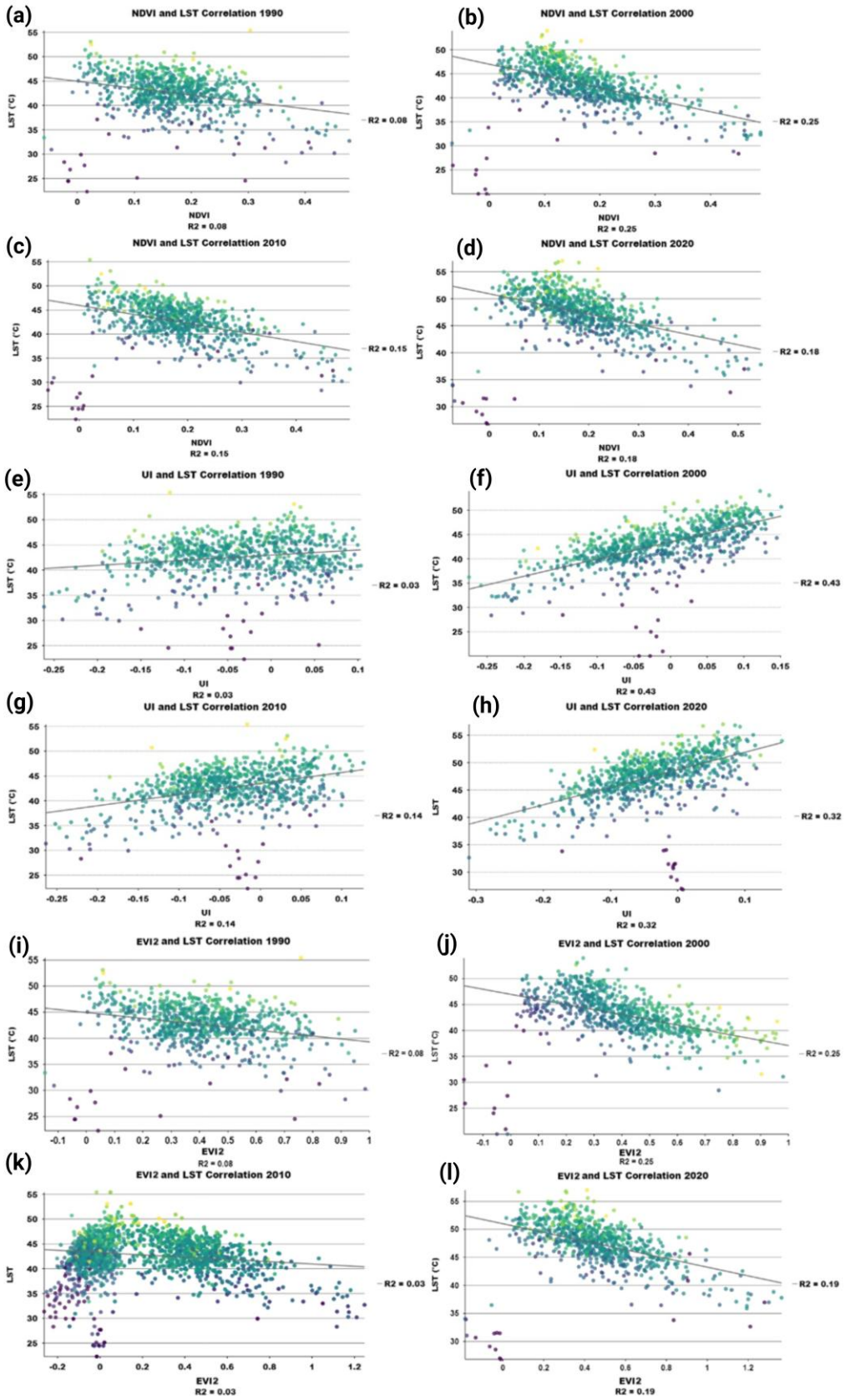

Figure 6. Geographically weighted regression analysis between NDVI, EVI2, UI, and LST (°C) in the Denver urban area in four different years (1990, 2000, 2010, and 2020) depicts the trend of correlation between land cover and LST.

4.5. UHI Intensity

4.5.1. Mean Annual LST

Figure 7 shows the annual mean LST, highlighting the spatial distribution of surface temperatures across Denver and its surrounding 5 km and 10 km non-urban buffers. The results reveal a pronounced urban–rural temperature gradient, with consistently higher LST values in urban areas relative to adjacent non-urban zones between 1990 and 2020. By 2020, LSTs were substantially elevated within Denver, particularly in the northeastern sector of the 5 km buffer, where urban expansion contributed to localized warming (Figure 7c). The most pronounced hotspots were located in downtown Denver, the central business district, major commercial zones, and the airport area in the northeast.

In 1990, the mean LST in Denver was 23 °C (Figure 7a), with increased temperatures concentrated in the northeastern areas, particularly in built-up areas such as the airport and commercial zones. By 2000, the mean LST had increased to 24 °C, with higher values observed across the northern, northeastern, southern, and southeastern parts of the city (Figure 7b). These patterns indicate that urban development was closely associated with localized warming. In 2010, the mean LST rose further to 26 °C (Figure 7c), and by 2020, the mean LST had reached 28 °C (Figure 7d), reflecting a significant increase relative to 1990 and 2000 (Figure 7d). Overall, the results highlight a steady rise in LST over three decades, with rapid changes occurring in the most recent decade. These patterns strongly suggest that Denver has undergone pronounced surface warming, linked to rapid urban expansion and associated land cover transformations. Furthermore, the gradual increase in annual mean LST from 23 °C in 1990 to 28 °C in 2020 supports the warming trend while reducing the influence of seasonal anomalies.

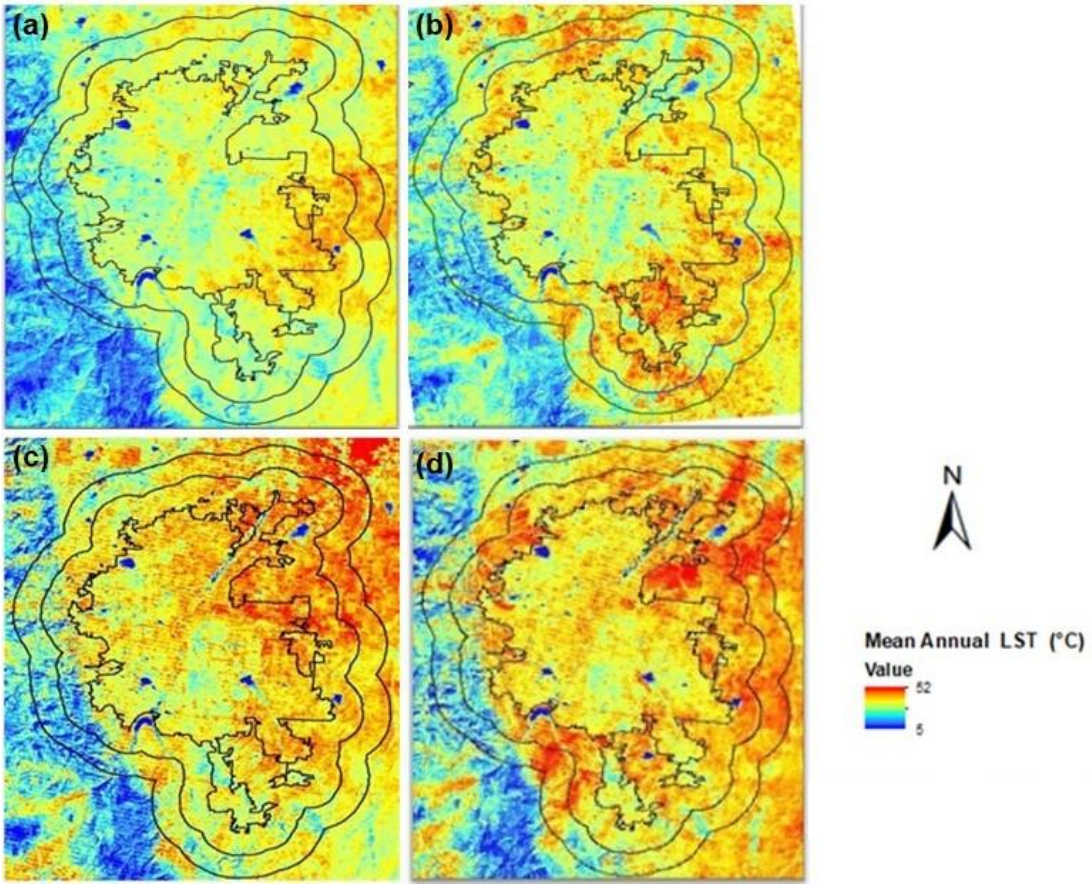

Figure 7. Mean annual LST (°C) in Denver in 1990 (a), 2000 (b), 2010 (c), and 2020 (d).

The spatial distribution of LST is characterized by elevated values in urbanized areas, including industrial zones, downtown districts, and the airport. However, beginning in 2003, the Landsat 7 Scan Line Corrector (SLC) malfunction introduced data gaps that produced artificial striping in the imagery, leading to

anomalously low LST estimates in both urban and rural areas (Xian *et al*., 2021). These artifacts are evident in the mean LST maps for 2010 and 2020 (Figures 7c & 7d), where stripes of lower temperature values appear across the study area. Consequently, the estimation of mean LST for these years may be partially affected by SLC-related errors, as reflected in the striping patterns observed in the LST difference maps (Xian *et al*., 2021).

4.5.2. Annual UHI Intensity

Urban heat island intensity in Denver was quantified by comparing the land surface temperature of urban pixels with the mean LST of surrounding non-urban buffer zones extending 10 km from the city boundary. Specifically, UHI intensity was calculated as the difference between the LST of each urban pixel and the mean LST of the corresponding 10 km non-urban buffer. Mean annual LST values from 1990, 2000, 2010, and 2020 were used to assess temporal and spatial trends in UHI intensity (Figures 8a–d).

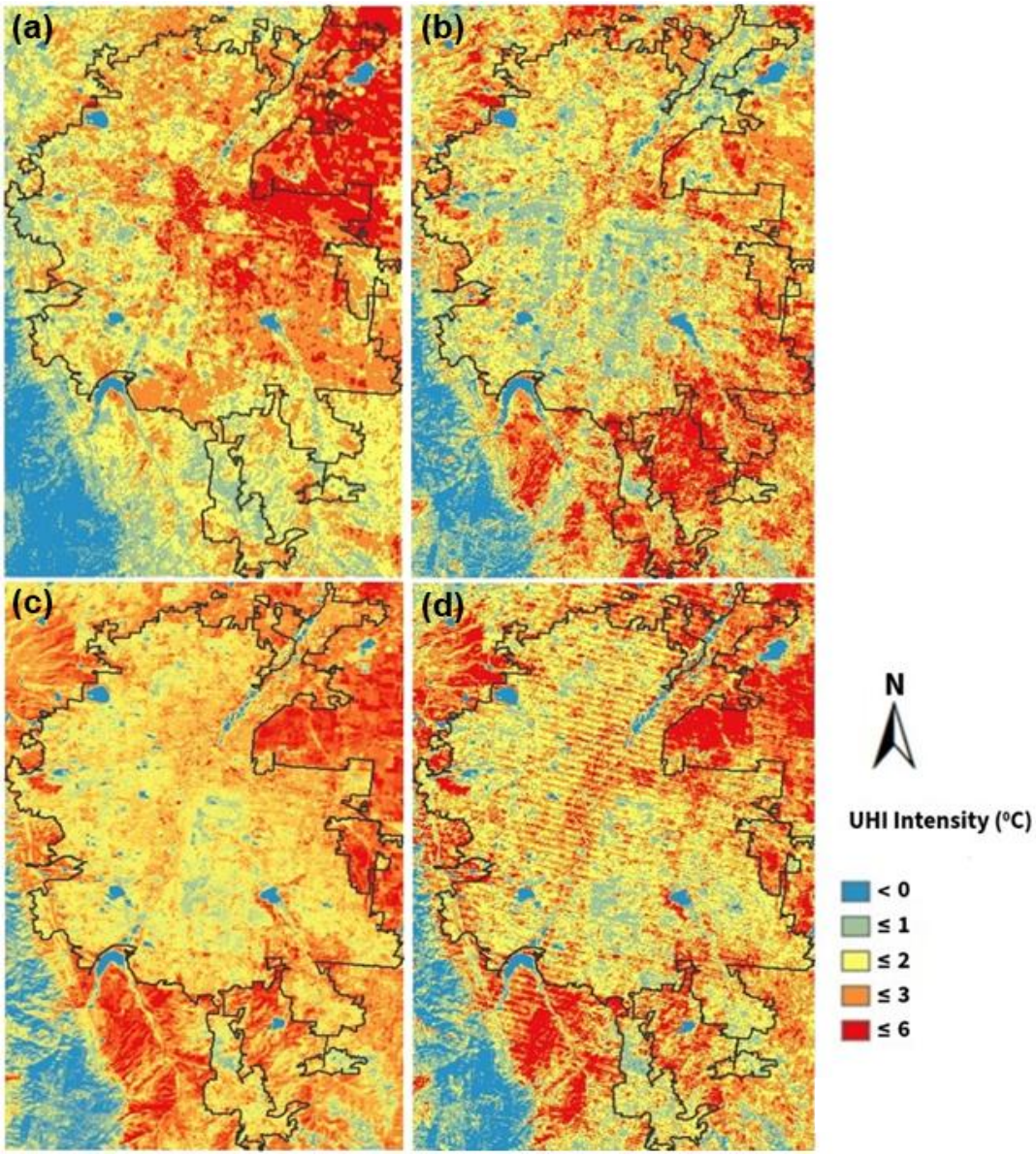

Figure 8. Spatial and temporal distribution of annual UHII (Degree Celsius) in 1990 (a), 2000 (b), 2010 (c), and 2020 (d), and temporal trends of change in UHII from 1990 to 2020.

In 1990, the mean annual UHI intensity was –1.5 °C (Figure 8a). Spatial patterns revealed higher UHI intensity in the northeastern portion of the city, moderate intensity in the southeastern and south-central areas,

and relatively low intensity in the southwest. These results highlight the heterogeneous nature of UHI intensity across Denver's urban landscape.

In 2000, the mean annual UHI intensity was –0.89 °C (Figure 8b), reflecting a shift in spatial distribution compared to 1990 (Figure 8a). The highest UHI intensity values were concentrated in the southeastern and southwestern parts of Denver, while moderate values appeared in the northern, northeastern, and northwestern portions of the city. These patterns suggest that by 2000, UHI effects had become more spatially dispersed across both urban and adjacent rural areas within the 10 km buffer.

By 2020, the mean annual UHI intensity had increased to 1 °C (Figure 8d). The UHI map indicates substantial changes in the northeastern sector of Denver relative to 2000, coinciding with continued urban expansion. Similar to 2000, higher to moderate UHI intensity values persisted in the southeastern portion of the study area (Figures 8c & 8d). These results highlight both the intensification and redistribution of UHI effects over time, with notable growth in magnitude and spatial extent between 2000 and 2020.

The UHI intensity maps (Figures 8a–d) illustrate the spatial distribution and temporal evolution of UHI intensity in Denver over the past three decades. The results derived from mean annual LST indicate that changes in UHI intensity were not uniform across time but showed a general increasing trend. Spatial patterns varied, with some areas exhibiting scattered distributions of UHI intensity, while others displayed more concentrated hotspots within and beyond the urban boundary. Shifts in land cover and modifications to the thermal environment strongly influenced these patterns. For instance, large-scale developments such as the expansion of Denver International Airport and the growth of Commerce City likely contributed to localized increases and redistribution of UHI intensity.

5. Future Work and Limitations

A primary limitation of this study lies in the method used to estimate UHI intensity, which was calculated as the difference between the temperature of urban pixels and the mean LST of non-urban buffer zones. The choice of buffer distance directly influences UHI estimates, as demonstrated in previous research. Xian *et al*. (2021) noted that UHI intensity depends on the spatial extent of selected urban and rural zones as well as the landscape characteristics of the study region. Similarly, Li *et al*. (2019) found that the size of the surrounding non-urban area strongly affects UHI estimation. Jiameng *et al*. (2018) reported that most remote-sensing-based studies use buffer widths ranging from 1 to 50 km to delineate non-urban extents. Although Xian *et al*. (2021) observed similar temporal trends in UHI intensity when using 5 km and 10 km buffers, there is currently no consistent standard for defining non-urban reference areas.

The results of this study further demonstrate the complexity of UHI estimation in Denver. For example, some areas outside the city exhibited higher UHI intensity than the urban core (Figure 8). This pattern reflects Denver's unique geographic and climatic context, including its semi-arid environment. On the eastern side of the city, sparse shrubland and bare soils—characterized by low heat absorption capacity—heat rapidly during the daytime, producing localized cooling contrasts that complicate UHI interpretation. Additionally, highly impervious zones such as Denver International Airport, located northeast of the city, generated higher LST than many urbanized portions of Denver itself. These examples underscore the localized nature of UHI, which varies with geographic setting, climate, land cover, and the composition of built-up surfaces. Consequently, UHI intensity should be analyzed with explicit consideration of local landscape characteristics, and future studies must account for the unique climatic and geographic conditions of each study area.

Future work should also incorporate additional biophysical and land cover variables to refine UHI estimation. Vegetation indices such as NDVI and EVI, while widely used, have notable limitations: NDVI saturates in high-biomass regions and is sensitive to background brightness in sparsely vegetated areas, whereas EVI is more stable across biomes but influenced by topographic factors (Huete *et al*., 2002; Matsushita *et al*., 2007; Reygadas *et al.,* 2020). The leaf area index (LAI) has been suggested as a complementary metric to overcome these shortcomings (Reygadas *et al.,* 2020). Similarly, tree canopy percentage is a strong predictor of LST, particularly from spring through fall (Decheng *et al*., 2014). Incorporating variables such as LAI, canopy cover, and impervious surface fraction into multivariate regression models can improve explanatory power by capturing more of the complex relationships driving LST variation. High-resolution land cover data would further enhance this capacity. For example, differentiating impervious surfaces into pavement and buildings, or separating vegetation into tree and grass classes, could yield more accurate predictions of LST.

Finally, future studies should explore the temporal dynamics of urban cooling in Denver, examining when and under what conditions cooling effects occur. Such analyses would help clarify the role of vegetation, land

cover, and microclimatic factors in shaping UHI patterns, and would contribute to more effective urban planning and climate adaptation strategies.

6. Conclusions

This study examined the relationships between land cover change, land surface temperature, and the spatial and temporal dynamics of urban heat island intensity in Denver using Landsat data from 1990 to 2020. The results highlight the significant impacts of rapid urbanization on surface thermal patterns and UHI intensity. Key findings include:

(1) Land cover change: Between 1990 and 2020, Denver experienced a 13% increase in developed land, primarily at the expense of cropland and grass/shrub cover, particularly in the southern and northeastern regions. These changes reflect substantial urban expansion over the study period.
(2) LST–land cover relationships: Linear and geographically weighted regression analyses revealed a consistent inverse relationship between vegetation indices (NDVI and EVI2) and LST, while the urban index exhibited a positive correlation. Adjusted R^2 values ranged from 0.03 to 0.43 across the study period, indicating variable explanatory power depending on year and spatial context.
(3) Temperature trends: The mean annual LST in Denver increased from 23 °C in 1990 to 28 °C in 2020. Higher temperatures were consistently concentrated in built-up areas, including downtown, commercial districts, and Denver International Airport.
(4) UHI intensity: Annual UHI intensity increased from –1.5 °C in 1990 to 1 °C in 2020. Spatial patterns revealed the emergence of concentrated hotspots in the northeastern and southeastern sectors of the city, as well as around the airport, coinciding with urban expansion.
(5) Methodological considerations: While NDVI, EVI2, and UI were significantly correlated with LST, other biophysical and atmospheric factors likely influence surface temperature. Incorporating additional metrics, such as the leaf area index (LAI) or detailed measures of impervious and vegetation cover, could enhance the explanatory capacity of future models.

Overall, this study demonstrates that urbanization has intensified LST and UHI effects in Denver over the past three decades. Findings underscore the strong link between rapid land cover transformation and intensification of UHI effects in the Denver metropolitan region. These findings provide a scientific basis for understanding UHI processes in rapidly growing cities and can inform urban planning and environmental management strategies aimed at mitigating heat-related impacts and enhancing urban sustainability.

Funding: This research received no specific grant from any funding agency in the public, commercial, or not-for-profit sectors.

Acknowledgment: We gratefully acknowledge their ongoing efforts to promote the use of remote sensing and geospatial technologies in scientific research and education. We would like to extend our gratitude to Dr. Hankui Zhang for his technical support and help with data acquisition, to Dr. Maitiniyazi Maimaitijiang and Dr. Kimberly Johnson Maier for their writing assistance, and to Dr. Hua Shi, Research Scientist at USGS EROS, for supplying the mean annual LST data used in this study.

Conflicts of Interest: The authors declare no conflicts of interest. The funders had no role in the study's design, the collection, analyses, or interpretation of data, the writing of the manuscript, or the decision to publish the results.

References

Aguiar, R.O.M., Gonçalves, H. (2002). Climate change impacts on the thermal performance of Portuguese buildings: Results of the SIAM study. *Building Services Engineering Research and Technology*, 23, 223–231. https://doi.org/10.1191/0143624402bt045oa

Anderson, J., Hardy, E., Roach, J., Witmer, R. (1976). A land use and land cover classification system for use with remote sensing data. *U.S. Geological Survey Professional Paper*, 964.

Buyantuyev, Alexander, & Wu, J. (2010). Urban heat islands and landscape heterogeneity: linking spatiotemporal variations in surface temperatures to land-cover and socioeconomic patterns. *Landscape Ecology*, 17-33. https://doi.org/10.1007/s10980-009-9402-4

Cao, Xin, Akio, O., Jin, C., & Hidefumi, I. (2010). Quantifying the cool island intensity of urban parks using ASTER and IKONOS data. *Landscape and Urban Planning* , 224-231.

Clinton, N., & Gong, P. (2013). MODIS detected surface urban heat islands and sinks: Global locations and controls. *Remote Sensing of Environment*(134), 294-304. https://doi.org/10.1016/j.rse.2013.03.008

Christopher, J. C., David, P. R., Saeed, A., Christopher, B., Eric, V., Glynn, H., Aaron, G., Mike, C., Christopher, E., Esad, M., Gail, S., Cody, A., Martha, A., Michelle, B., Bruce, C., Ray, D., Danny, H., Calli, J., Steve, Z. (2023). The 50-year Landsat Collection 2 archive. *Science of Remote Sensing*, 8, 100103. https://doi.org/10.1016/j.srs.2023.100103

Davis, R., 2021. Climate report: Denver's 'heat island' could get hotter and harder for homeless. *The Denver VOICE*, August 29, 2021. https://www.denvervoice.org/archive/2021/8/30/climate-report-denvers-heat-island-could-get-hotter-and-harder-for-homeless Last access: 30 June 2025.

Decheng, Z., Shuqing, Z., Shuguang, L., Liangxia, Z., Chao, Z. (2014). Surface urban heat island in China's 32 major cities: Spatial patterns and drivers. *Remote Sensing of Environment*, 152, 51–61. https://doi.org/10.1016/j.rse.2014.05.017

Dwyer, J.L., Roy, D.P., Sauer, B., Jenkerson, C.B., Zhang, H.K., Lymburner, L. (2018). Analysis Ready Data: Enabling analysis of the Landsat archive. *Remote Sensing*, 10, 1363. https://doi.org/10.3390/rs10091363

Frey, C. M., Rigo, G., & Parlow, E. (2007). Urban radiation balance of two coastal cities in a hot and dry environment. *International Journal of Remote Sensing*, 2695-2712. https://doi.org/10.1080/01431160600993389

Fricker, G.A., Wolf, J.A., Saatchi, S.S., Gillespie, T.W. (2015). Predicting spatial variations of tree species richness in tropical forests from high-resolution remote sensing. Ecological Applications, 25, 1776–1789. https://doi.org/10.1890/14-1593.1

George, X., Hua, S., Qiang, Z., Roger, A., Kevin, G., Zhuoting, W., Michael, K. (2022). Monitoring and characterizing multi-decadal variations of urban thermal condition using time-series thermal remote sensing and dynamic land cover data. *Remote Sensing of Environment*, 269, 112803. https://doi.org/10.1016/j.rse.2021.112803

Harald, Z., Ludwig, G., Luis, I. (2020). And the winner is? Comparing urban green space provision and accessibility in eight European metropolitan areas using a spatially explicit approach. *Urban Forestry & Urban Greening*, 49, 126603. https://doi.org/10.1016/j.ufug.2019.126603

Homer, C., Dewitz, J., Jin, S., Xian, G., Costello, C., Danielson, P., Gass, L., Funk, M., Wickham, J., Stehman, S., Auch, R., Riitters, K. (2020). Conterminous United States land cover change patterns 2001–2016 from the 2016 National Land Cover Database. *ISPRS Journal of Photogrammetry and Remote Sensing*, 162, 184–199.

Huete, A., Didan, K., Miura, T., Rodriguez, E.P., Gao, X., Ferreira, L.G. (2002). Overview of the radiometric and biophysical performance of the MODIS vegetation indices. *Remote Sensing of Environment*, 83, 195–213. https://doi.org/10.1016/S0034-4257(02)00096-2

Imhoff, L, M., Zhang, P., E, R., Wolfe, & Bounouaa, L. (2010). Remote sensing of the urban heat island effect across biomes in the continental USA. *Remote Sensing of Environment*, 504-513. https://doi.org/10.1016/j.rse.2009.10.008

Jiameng, L., Wenfeng, Z., Fan, H., James, V., Benjamin, B., Michael, A., Shushi, P., Falu, H., Yongxue, L., Peijun, D. (2018). Identification of typical diurnal patterns for clear-sky climatology of surface urban heat islands. *Remote Sensing of Environment*, 217, 203–220. https://doi.org/10.1016/j.rse.2018.08.031

Kenward, A., Yawitz, D., Sanford, T., Wang, R. (2014). *Summer in the city: Hot and getting hotter*. Climate Central Report.

Keyvan, E., Manouchehr, C., Mohsen, A., Ali Akbar, M. (2021). Spatiotemporal analysis of land surface temperature using multi-temporal and multi-sensor image fusion techniques. *Sustainable Cities and Society*, 64, 102508. https://doi.org/10.1016/j.scs.2020.102508

Kutner, M.H., Nachtsheim, C.J., Neter, J., 2004. *Applied Linear Regression Models*, 4th ed. McGraw-Hill/Irwin, New York.

Li, K., Chen, Y., Wang, M., Gong, A. (2019). Spatial–temporal variations of surface urban heat island intensity induced by different definitions of rural extents in China. *Science of the Total Environment*, 669, 229–247. https://doi.org/10.1016/j.scitotenv.2019.02.408

Liu, H., Weng, Q. (2009). Scaling effect on the relationship between landscape pattern and land surface temperature: A case study of Indianapolis, United States. *Photogrammetric Engineering and Remote Sensing*, 75, 291–304.

Matsushita, B., Yang, W., Chen, J., Onda, Y., Qiu, G. (2007). Sensitivity of the Enhanced Vegetation Index (EVI) and Normalized Difference Vegetation Index (NDVI) to topographic effects: A case study in high-density cypress forest. *Sensors*, 7, 2636–2651. https://doi.org/10.3390/s7112636

MRLC. (2016). MRLC Evaluation Report. https://www.mrlc.gov/ Last access: 20 June 2025.

Peng, J., Jia, J., Liu, Y., Li, H., & Wu, J. (2018). Seasonal contrast of the dominant factors for spatial distribution of land surface temperature in urban areas. *Remote Sensing of Environment, 215*, 255–267. https://doi.org/10.1016/j.rse.2018.06.010

Reygadas, Y., Jensen, J. L., Moisen, G. G., Currit, N., & Chow, E. T. (2020). Assessing the relationship between vegetation greenness and surface temperature through Granger causality and impulse-response coefficients: A case study in Mexico.

International Journal of Remote Sensing, 41, 3761–3783. https://doi.org/10.1080/01431161.2019.1711241

Richard, L.-R., Luis, I., Harald, Z. (2022). Intraurban heterogeneity of space–time land surface temperature trends in six climate-diverse cities. *Science of the Total Environment*, 804, 150037. https://doi.org/10.1016/j.scitotenv.2021.150037

Stephen, V.S., Bruce, W.P., Josephine, A.H., Danika, F.W. (2021). Validation of the U.S. Geological Survey's Land Change Monitoring, Assessment and Projection (LCMAP) Collection 1.0 annual land cover products 1985–2017. *Remote Sensing of Environment*, 265, 112646. https://doi.org/10.1016/j.rse.2021.112646

Streutker, D.R. (2002). A remote sensing study of the urban heat island of Houston, Texas. *International Journal of Remote Sensing*, 23, 2595–2608. https://doi.org/10.1080/01431160110115023

United Nations. (2018). *World Urbanization Prospects: The 2018 Revision*. UN Department of Economic and Social Affairs, New York.

Voogt, J.A., Oke, T.R. (2003). Thermal remote sensing of urban climates. *Remote Sensing of Environment*, 86, 370–384. https://doi.org/10.1016/S0034-4257(03)00079-8

Weng, Q., Lu, D., Liang, B. (2006). Urban surface biophysical descriptors and land surface temperature variations. *Photogrammetric Engineering & Remote Sensing*, 72, 1275–1286. https://doi.org/10.14358/PERS.72.11.1275

World Report. (2019). *World Report.* Retrieved from https://www.hrw.org/world-report/2019

Xian, G. (2008). Satellite Remotely-sensed Land Surface Parameters and Their Climatic Effects for Three Metropolitan Regions. *Advances in Space Research*(41), 1861-1869. https://doi.org/10.1016/j.asr.2007.11.004

Xian, G., Shi, H., Auch, R., Gallo, K., Zhou, Q., Wu, Z. (2021). The effects of urban land cover dynamics on urban heat island intensity and temporal trends. *GIScience & Remote Sensing*, 58, 501–515. https://doi.org/10.1080/15481603.2021.1903282

Yue, W., Xu, J., Tan, W., & Xu, L. (2007). The relationship between land surface temperature and NDVI with remote sensing: application to Shanghai Landsat 7 ETM+ data. International Journal of Remote Sensing, 28(15), 3205–3226. https://doi.org/10.1080/01431160500306906

Yuvaraj, R.M. (2020). Extents of predictors for land surface temperature using multiple regression model. *The Scientific World Journal*, 2020, 3958589. https://doi.org/10.1155/2020/3958589

Zhengming, W., Dozier, J. (1996). A generalized split-window algorithm for retrieving land-surface temperature from space. *IEEE Transactions on Geoscience and Remote Sensing*, 34, 892–905. https://doi.org/10.1109/36.508406

Research Article

Mapping Fluvial Terraces Using Geospatial Analysis: A Case Study on the Piedmont of Georgia, USA

Ana C. dos Santos[1,*] and Andrew H. Ivester[1]

[1] School of Field Investigations & Experimental Sciences, Dr. James 'Earl' Perry College of Mathematics, Computing, and Sciences, University of West Georgia, Carrollton, GA 30118, USA; aivester@westga.edu (AHI)

[*] Corresponding Author: adossan1@westga.edu (ACdS)

Academic Editor: Jeong C. Seong
Received: 12 August 2025
Revised: 26 September 2025
Accepted: 30 September 2025
Published: 24 October 2025

Abstract: Mapping of alluvial soils and geomorphic units can be useful for purposes as varied as land management, cultural resource planning, flood risk assessment, and modeling stream system response to environmental change. This research project develops a method that combines USDA-NRCS soil map units with a geospatial workflow processing 1-m LiDAR imagery to delineate stream terraces in the Upper Little Tallapoosa basin of western Georgia (USA). Existing soil surveys distinguish between high and low terrace alluvium by different soil series. "Old alluvium" is represented by the Masada (map unit abbreviations MoB, MpB, MpC2), Augusta (Asl), and Worsham (Wsl) series. These are further distinguished as low vs. high terraces: Masada is typically found in high terraces, and Augusta and Worsham in lower terraces. We use various geospatial tools to de-trend a LiDAR-based DEM in order to optimize for identifying stream terrace surfaces. This approach results in planimetric terrace surface polygons that differ somewhat from the soil survey map units. We then create gradient profiles to identify any correlated terrace surfaces along the stream valley. Hypsometric curves and histograms of select stream reaches are used to visualize elevation distributions and to identify any terrace surfaces. Field checks at several sites, based on backhoe trenches and hand augered cores, indicate that our new integrated approach is an effective method for mapping terraces.

Keywords: geomorphometrics, fluvial hypsometry, DEM analysis, stream terraces

1. Introduction

1.1. Background

Fluvial terraces are geomorphic features that represent remnants of former floodplains abandoned as a result of stream incision. They can occur as bench- or step-like features along a stream valley and often have distinctive soil properties, less clayey than upland and better-drained than floodplain soils. Despite lacking the attention and legal protections offered to wetlands, terraces also contribute important ecological benefits, occupying an intermediate position in the landscape, a transition zone with special properties. Terraces contribute as ecological corridors for animal movements, oriented both perpendicular to the stream valley, linking upland with wetland, and parallel to the stream valley as along-stream corridors. Humans have long appreciated these many unique characteristics and, in prehistory, have preferred terraces as sites for occupation and other activities, making stream terraces rich repositories of cultural and archaeological information. The hydrological importance of terraces is as a buffer between wetlands and uplands, helping to filter water before entering the stream system. They can help reduce flooding by storing runoff or allowing for the accommodation of higher floodwaters.

Ecosystems in the southeastern U.S. Piedmont are under tremendous pressure due to urban expansion and development, as the region continues to grow. Stream systems and wetlands are especially affected as the demand for water continues to increase. Land management and conservation groups, local and regional governments, and other groups can greatly benefit from more detailed and accurate maps of river systems and their associated geomorphic units. Such maps could be used for modeling the distribution of archaeological sites and for strategically planning construction and development in order to preserve cultural

Citation: dos Santos, A. C., & Ivester, A. H. (2025). Mapping fluvial terraces using geospatial analysis: A case study on the Piedmont of Georgia, USA. *Journal of Earth Observation and Geospatial Applications, 1*(1), 83–93. DOI: https://doi.org/10.65372/471gz108

resources. As fluvial geomorphology can be used for reconstructing past climate, environmental, and tectonic histories of a basin, mapping terraces and terrace heights can be an important first step in documenting the history of a basin and how agriculture and human activities have affected the system. Fluvial terraces are a great tool for better understanding and quantifying river aggradation and incision, and their possible causes.

Mapping terraces and other alluvial geomorphic units is seldom straightforward. Fluvial features can sometimes be identified based on topography alone as they often retain a flat, low-slope surface (tread) and can be bounded by a steep scarp (riser). In other cases, erosional modification has obscured their topographic expression; field assessment may be required to define terraces, based on soil profiles that reveal their distinctive soil properties or based on coring to define their internal stratigraphy. Lateral migration might also result in discontinuous, sparse preservation of terrace remnants. With few terraces remaining, recognizing and correlating them might be made more difficult.

Previous studies have taken various approaches to automating the delineation of stream geomorphic features, revealing many challenges (Clubb *et al*., 2017, Clubb *et al*., 2022; Hopkins & Snyder, 2016; Stout & Belmont, 2013; Iacobucci *et al*., 2022). Fluvial geomorphic features occur on an along-stream elevation gradient across the stream basin, making it difficult to group them on an unprocessed DEM with true elevations. Thus, a detrended model that normalizes elevations to the nearby stream channel or some other surface that follows the trend of the drainage is more easily used to visualize and identify terraces. Even a detrended DEM might have issues, however, given that terraces and stream characteristics in general are not consistent along the entire stream system, but can vary greatly by stream reach. Higher resolution DEMs allow for sharper visualization of smaller terrace units, although 1-m DEMs may not be available for all areas. Where available, the large file sizes involved can be an issue for disk storage and processing time. Natural fluvial features can be obscured by human impacts associated with urbanization, impoundment, and channelization. Incision or aggradation in response to human impacts can affect terrace identification; for example, along streams with legacy sediment accumulation, low terraces that might be similar in height to the active floodplain. Finally, even when a terrace map is produced, evaluation of the resulting map units is a challenge, requiring field mapping and field checks to determine the accuracy of the map.

1.2. Aim

This research project aims to create a map of floodplains and terraces in the Upper Little Tallapoosa basin and to compare LiDAR-derived alluvial map units with USDA-NRCS (United States Department of Agriculture, Natural Resources Conservation Service) soil map units. We develop a workflow that integrates soil survey data and LiDAR-based DEMs in order to identify terraces, to determine terrace elevations, and to construct stream and terrace gradient profiles. We then make interpretations of the resulting maps to identify possible terrace heights and to assess whether and what height terrace surfaces can be correlated along the gradient.

1.3. Study Area

This project focuses on the Upper Little Tallapoosa basin in western Georgia, an 826.8 km^2 watershed that lies mainly within Carroll and Haralson Counties. The decision to limit the area to Georgia ensures consistent soil map unit interpretations from a single soil survey publication (Brooks, 1971), excluding map units based on different criteria across the state line. We define the basin based on a “pour point” (or catchment delineation point) placed near the state line, immediately downstream of the confluence with Indian Creek. The point also happens to coincide with a transition in other stream system characteristics; in Alabama, the Little Tallapoosa is more sinuous compared to reaches upstream in Georgia. Within our defined basin area, the Little Tallapoosa River is a 5th-order stream (Strahler, 1957), with other major tributaries including Buffalo Creek and Wolf Creek. The total length of streams in the basin area is 1,282.5 km, with a drainage density of 1.55 km/km^2. The study area contains two USGS stream gauges, one located upstream from the state line and another near Carrollton, GA (USGS WaterWatch, 2025).

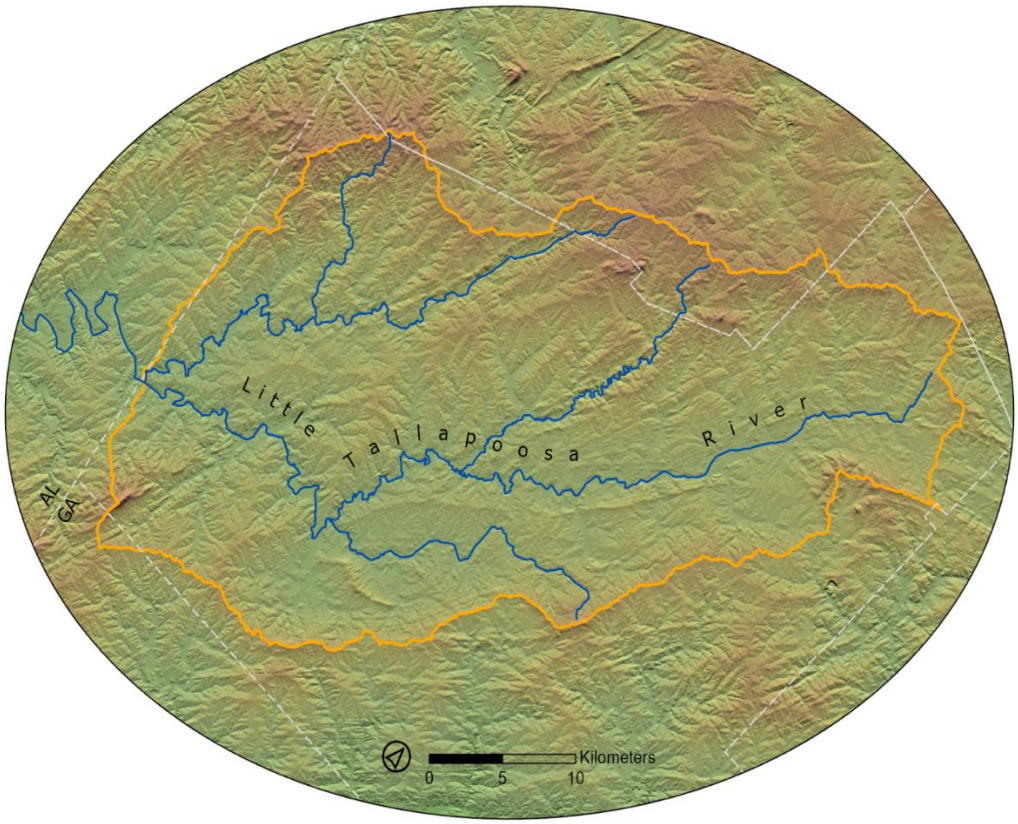

Figure 1. The Little Tallapoosa River basin study area, in the Upper Piedmont of western Georgia. This study focuses on mapping stream deposits in a 2.4-km-wide buffer zone along the main channel of the Little Tallapoosa, from the Alabama/Georgia line across Carroll County, GA. Note that the map is oriented with north toward the upper right. The orange line marks the basin boundary; dashed gray lines indicate county or state boundaries.

2. Methods

2.1. Overview

This project is based on integrating existing NRCS alluvial soil data with our newly developed GIS workflow that we applied to create a final interpretational synthesis of floodplain and terrace map units. We developed a method for the visualization and identification of terrace heights and their possible connection to surfaces along the whole basin. Once the planimetric polygons of alluvial geomorphic units were decided upon, these were used to define terrace surface heights and to correlate terraces along the stream profile.

2.2. NRCS Soil Survey Map Units

A useful source of information for an initial assessment of terrace distribution comes from NRCS Soil Surveys, available for download online through the Web Soil Survey (Soil Survey Staff, 2025). Brooks (1971) classified alluvial soils in the study area as eight phases across six series, where three of the soil series are recent alluvium and three are old alluvium (Table 1). Congaree (Cng), Buncombe (Bfs), and Chewacla (Cfs) series soils are formed in "recent" alluvium, while Masada (MoB, MpB, MpC2), Augusta (Asl), and Worsham (Wsl) series are formed in "old" alluvium. These series were used to help identify high and low terraces, as the Masada series is intended to map soils found on higher terraces, while Augusta and Worsham series indicate soils of lower terraces. An additional phase, *Augusta sandy loam,* 2 to 6 percent slopes, was excluded from our maps as it is found at the heads of drainageways in a zone that might be considered colluvial (slope deposits) rather than alluvial. The digital soil map units form a "first pass" map of alluvial geomorphic units in the study area.

Table 1. Alluvial soil map unit heights, determined using USDA soil survey map units across the entire Upper Little Tallapoosa basin, based on the detrended DEM.

Soil Phase	Soil Map Unit Symbol	Flood Frequency	Area (ha)[1]	Mean Height Above Channel (m)[2]	Median Height Above Channel (m)[2]
Floodplain soils:					
Chewacla soils, 0-2% slopes	Cfs	< 1 year	10,100	3.3 ± 3.7	2.3
Congaree soils, 0-2% slopes	Cng	1-5 years	2,630	4.5 ± 5.0	2.7
Buncombe loamy sand, 0-4% slopes	Bfs	1-5 years	400	2.9 ± 1.7	2.6
Low terrace soils:					
Worsham silt loam, 0-2% slopes	Wsl	< 1 year	360	2.9 ± 2.5	1.8
Augusta loam, 0-2% slopes	Asl	1-5 years	350	2.9 ± 2.3	2.1
High terrace soils:					
Masada fine sandy loam, 2-6% slopes	MoB	none	1,070	6.2 ± 4.0	5.3
Masada gravelly sandy loam, 2-6% slopes	MpB	none	690	11.2 ± 5.6	11.0
Masada gravelly sandy loam, 6-10% slopes	MpC2	none	410	11.6 ± 6.3	10.4

[1] Total area of each soil map unit within Carroll County, GA (Brooks, 1971).

[2] Mean and median values within buffer zone around the main channel of the Little Tallapoosa River, calculated using the Zonal Statistics tool in ArcGIS Pro and the detrended 1-m DEM as input (This study).

2.3. Geospatial Workflow

A geospatial workflow model (Figure 2) was developed to produce a preliminary map of terraces based solely on their topographic expression. We primarily used tools available in ArcGIS Pro 3.3.1, although similar functions and tools are available in other GIS software, such as QGIS. The starting point for mapping terraces was to obtain a 1-m LiDAR-derived DEM for the area of interest (USGS, 2025) and then to create a hillshade for better visualization. Available channel vectors (Georgia DOT, 1997) differed enough from the DEM that they didn't exactly follow the actual channel center line, due to very recent meander cutoffs, channel shifts, or due to other errors that resulted in the vector crossing the channel bank in places over the natural levee and onto the floodplain. Therefore, we used the DEM as a basis for manually tracing the channel center line.

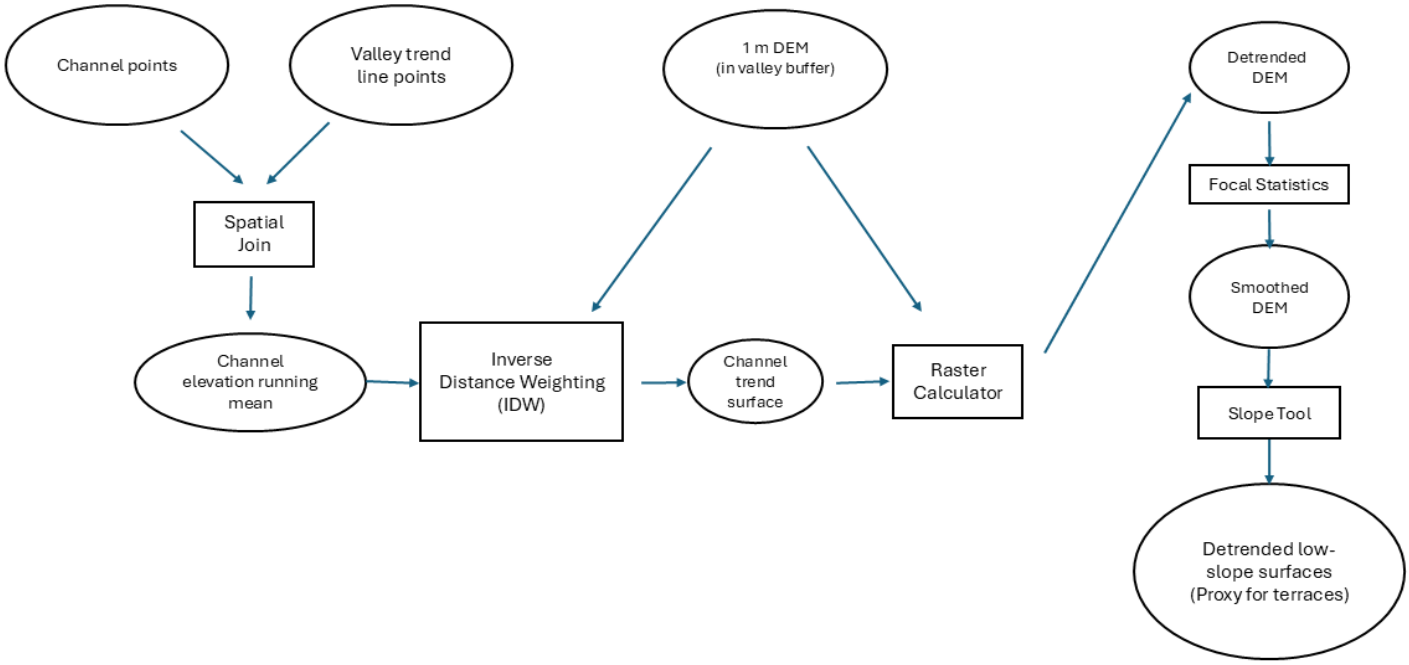

Figure 2. Workflow model for producing a map of possible terrace surfaces.

We constructed a generalized valley trend line and created a series of points along that line at every 10 m, assigning each point an elevation from the DEM. A buffer was created 1.2 km from the valley trend line (on both sides) to include possible terraces and the DEM was clipped to the buffer for a better focus on the main stream valley. Using the Spatial Join tool, we extracted the mean elevation value for the channel within 1.2 km of each point on the valley trend line (Figure 3). Using the valley trend line (channel elevation running mean) and the buffered DEM, we applied the Inverse Distance Weighting (IDW) tool to create a channel trend surface. The intention of this surface is to smoothly fit the modern stream channel elevations. The Raster Calculator tool was then used to subtract this trend surface from the DEM, resulting in a detrended DEM, with all raster values now expressed as heights above the mean channel elevation in the vicinity. We used the Focal Statistics tool to smooth the surface of the DEM, and applied the Slope tool to generate a layer of slopes so that low slopes could be demarcated. A new layer was then created to filter out areas that were not flat (slope > 3%) or had elevations higher than 20 m, so we could get a proxy for terrace surfaces. Finally, the slope layer was blended with the detrended DEM for the best visualization of the flat and sloped areas. This resulted in a "semi-automated" map of possible terraces based solely on objective criteria.

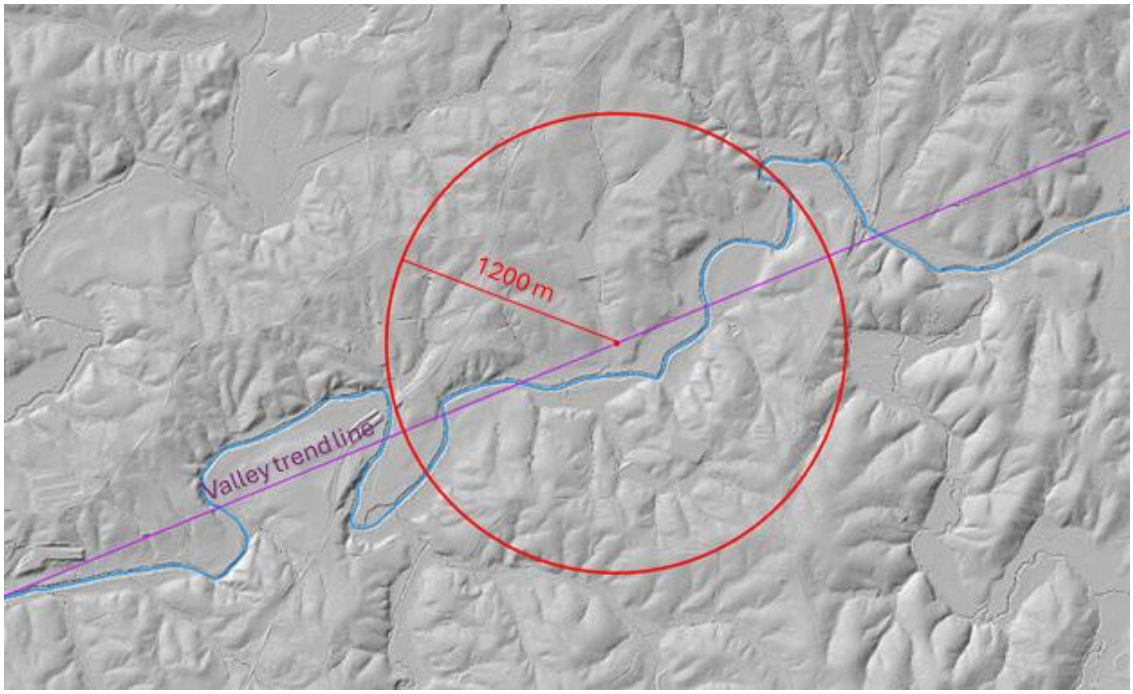

Figure 3. Schematic of how the Spatial Join tool was used to fit a running mean of channel elevation along a valley trend line. Each point on the trend line (at 10 m intervals) is assigned a value equal to the mean channel elevation for channel points within a 1200 m radius. Trend line elevations were then extended laterally to fill a buffer zone within 1.2 km, resulting in a smooth surface that represents a best-fit surface to the channel. This surface was used to detrend the DEM.

2.4. Synthesis and Interpreted Terrace Planimetry

A synthesized interpretation of terrace map units was manually determined by examining the soil survey map units and terrace locations suggested by the geospatial processing algorithm. Terraces were then delineated manually with reference to the soil map units and the final detrended, low-slope surfaces, with frequent reference to the detrended DEM (displayed with an appropriate hillshade and stretched color scale). This final step in terrace mapping is subjective. In most cases, a geomorphic unit was mapped as a terrace if it was suggested by multiple sources. In certain cases, what looked visibly like a clear terrace on the detrended DEM was mapped as such, even if missing on the soil survey. Terrace boundaries in many cases extend to the edge of the landform tread, even if slightly beyond the boundary of the area mapped as a detrended flat surface. As such, this final synthesis was a holistic, subjective effort that resulted in a best estimate of terrace planimetry.

2.5. Terrace Height Determinations

The methodologies described thus far for this study (Sections 2.2–2.4) have focused on determining the planimetric extent of terraces. A separate problem is that of identifying the heights of terraces and their correlation up and down the valley. Being able to distinguish and correlate traceable terrace surfaces along the stream, accompanied by dating evidence, can be useful in determining the history of stream processes and drivers such as paleoenvironmental and paleotectonic changes.

The terrace height determinations were estimated in three different ways. First, we determined mean and modal heights from the detrended DEM across soil phases using the Zonal Statistics as Table tool in ArcGIS Pro. A second method was to use the Raster Terrain Analysis plugin, which has a Hypsometric Curve tool, in QGIS. This tool extracted height values from the detrended DEM, which were then processed further for graphing in Excel. A final method for determining terrace heights was to manually determine elevations of clearly expressed terraces (on the DEM) and to plot them directly on a graph with stream profile gradient elevations.

3. Results

3.1. Planimetric Mapping Results

Our integrated workflow resulted in a detrended DEM of the river corridor that made it easier to identify terraces along the valley (Figure 4). Using this detrended DEM and referring to the soil map units and map of low slope areas, we were able to produce a final feature class of 422 interpreted terrace tread polygons along the main trunk stream of the Little Tallapoosa River that we consider to mark terraces with a high degree of confidence. A representative stream segment (Figure 5) illustrates the relationship between soil map units, the detrended flat zones that resulted from the geospatial workflow, and our final interpretation of terrace treads.

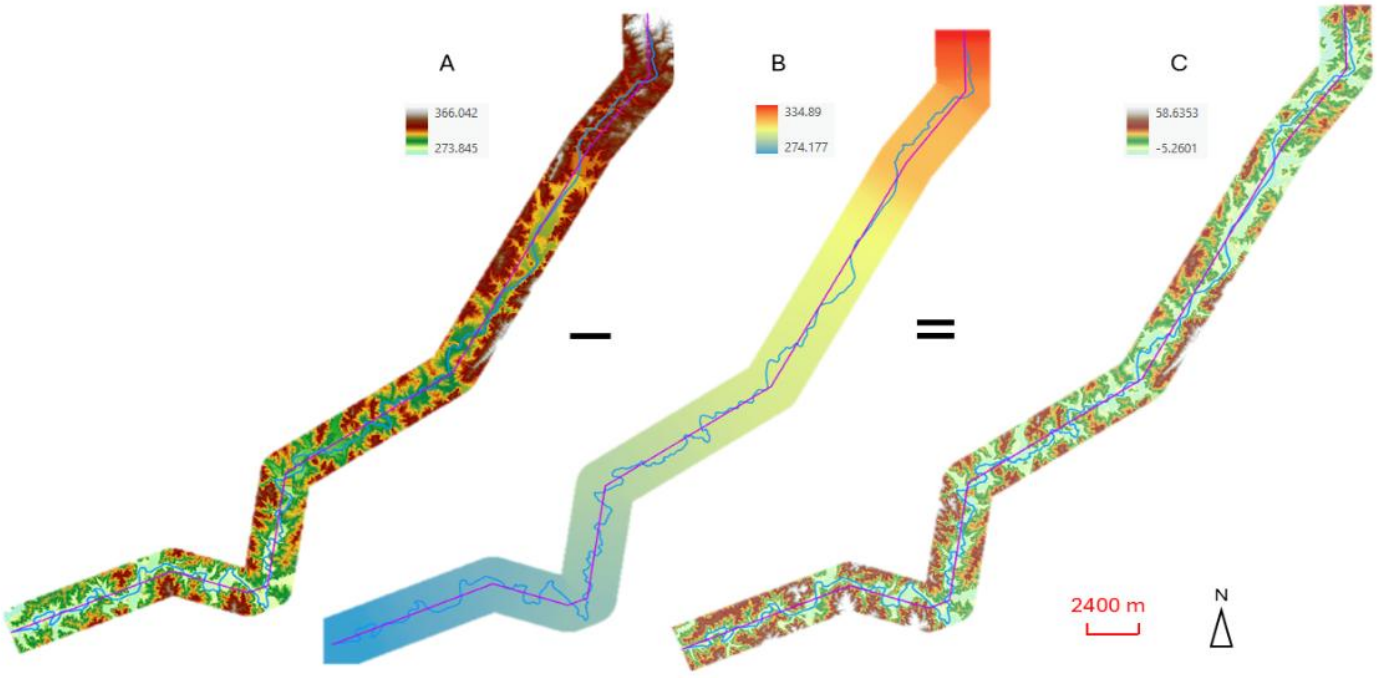

Figure 4. Creation of a detrended DEM for the buffer zone around the main trunk stream using raster math. (A) Original 1-m DEM. (B) Trend surface created to fit to the running mean channel elevation. (C) Detrended (flattened) DEM with elevations as heights above the local channel. The detrended DEM shows land surface heights measured relative to the mean channel elevation at that point along the stream valley. Elevation and height scales are in meters. Note that the detrended DEM has a few pixels with negative heights; These represent localized channel entrenchment.

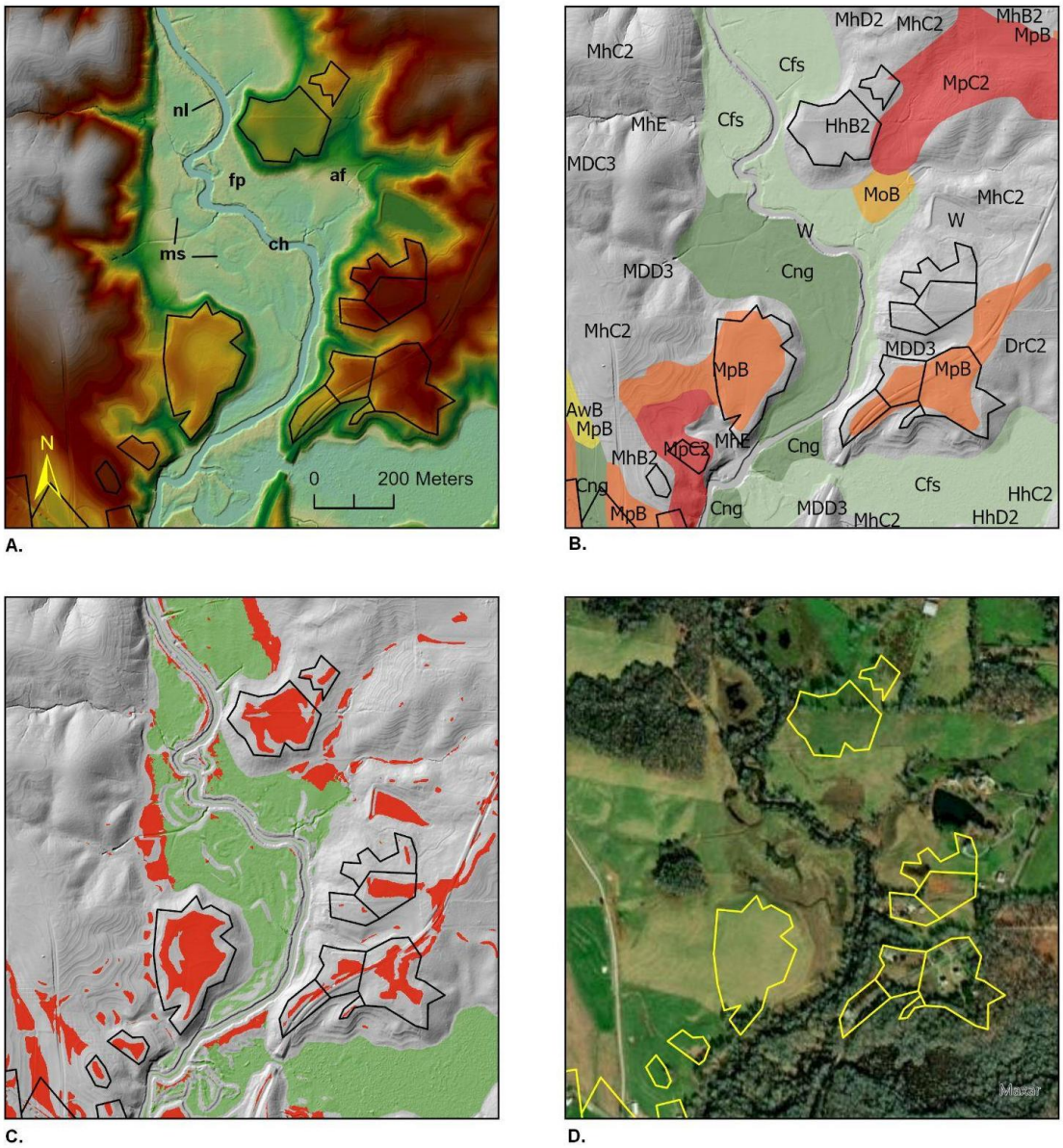

Figure 5. Representative stream segment illustrating terrace map unit determinations. (A) Detrended 1-m DEM. Geomorphic features indicated: af = alluvial fan, ch = channel, fp = floodplain, ms = meander scars, nl = natural levee. Final terrace determinations are indicated by solid line polygons. (B) Soil Survey map units (see Table 1 for explanation of map unit abbreviations). (C) Detrended flats of < 3% slope. Green = floodplain, Red = terrace. (D) True color aerial imagery (Esri, 2025).

3.2. Estimates of Terrace Heights

Terrace and floodplain heights above the nearby channel, based on NRCS soil map units, are shown in Table 1. Values measured from the detrended DEM indicate that floodplain and low terrace soils are both mapped for areas about 2 m above the channel and are indistinguishable, given the variation about the mean. “High” terraces, on the other hand, mapped as Masada series soils, occur significantly higher, at 5–12 m above the stream channel. This gives a preliminary idea of the range of terrace heights that might be expected in the study area. Hypsometric curves of elevations were constructed for select segments of the AOI (Area of Interest) buffer and examined to check for indications of terraces and, in some cases, were effective for more clearly identifying terrace heights (Figure 6). Our third method for identifying terrace heights along the channel, plotting spot elevations of our final terrace determinations (Figure 7), suggests possible terrace surfaces at 4, 6, 9, 12, and 16 m above the channel.

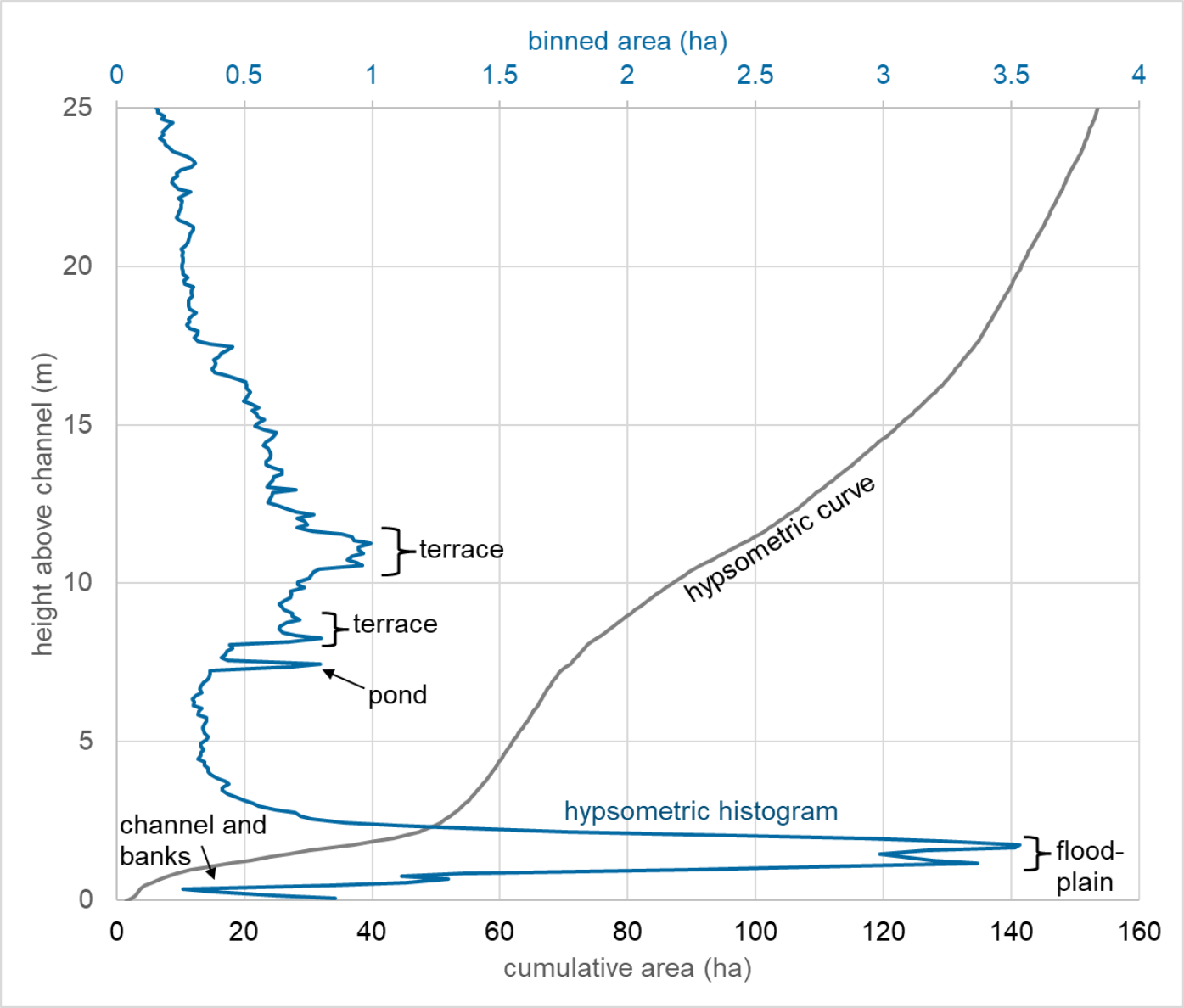

Figure 6. Stream profile gradient and interpreted terrace surfaces for the area of interest mapped in Figure 5. Note that the hypsometric histogram is more effective at showing details of surface heights than the more commonly used hypsometric curve. The bimodal height distribution of the floodplain might reflect distinct floodplain and low terrace surfaces.

4. Discussion

This project has produced a workflow useful for terrace mapping based on an integrated approach that combines multiple data sources processed using both semi-automated, objective criteria and manual, subjective interpretation. The resulting terrace map units are more reliable than those based on either automated determinations or soil survey maps alone. The increased reliability of our final terrace polygon layer is illustrated by examining a representative stream reach (Figure 5), where two visually obvious terrace remnants are preserved, one of which was missed by the soil survey (mapped as an upland soil with designation HhB2). This terrace is clearly visible on the detrended DEM and is included in our detrended, low-slope raster (Figures 5A & 5B). Another area that is likely mis-mapped by the soil survey as a high

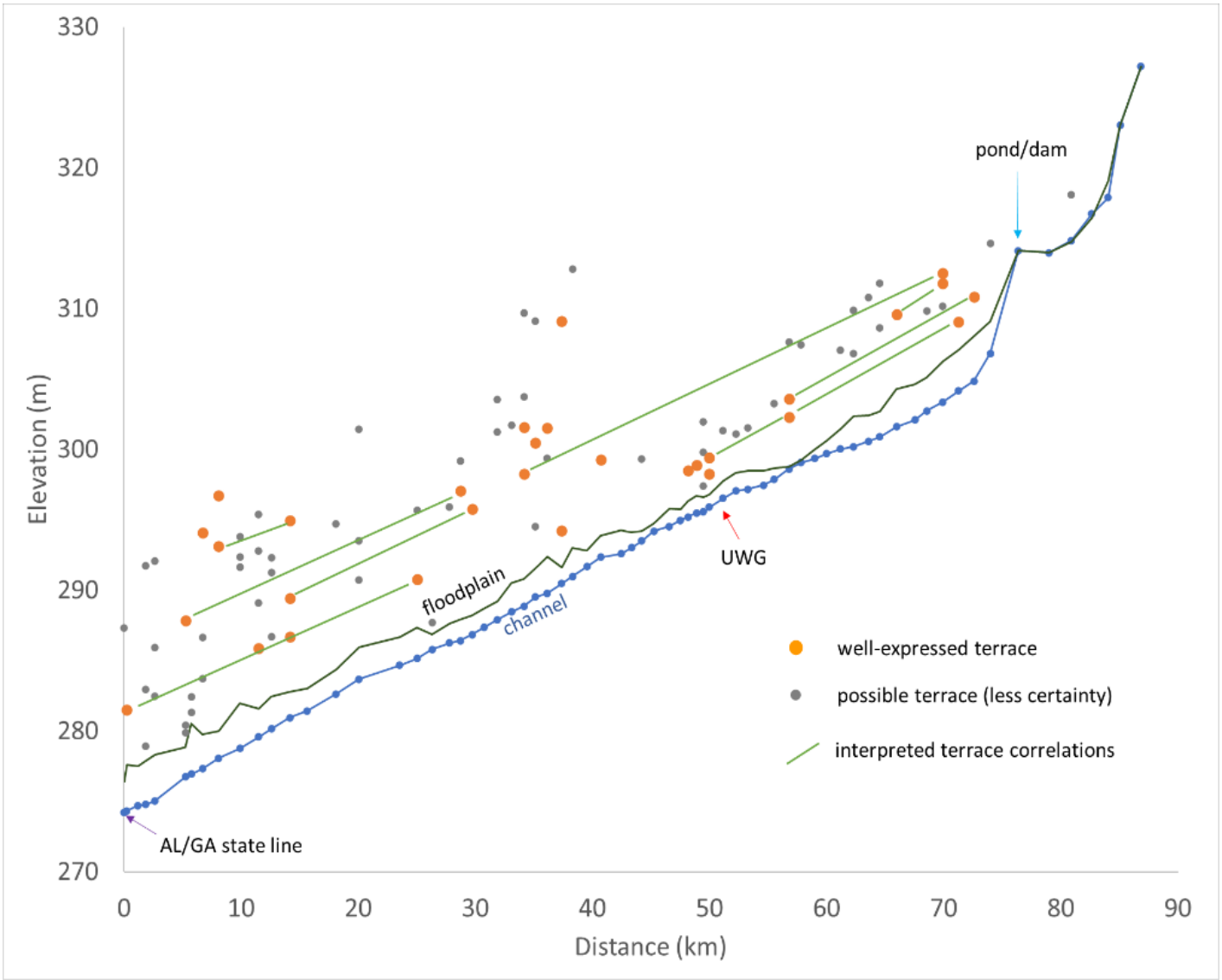

Figure 7. Stream profile gradient and interpreted terrace surfaces of the Little Tallapoosa's main trunk stream in the study basin. Note the channel incision just downstream of the dam. Four or five distinct terrace surfaces are suggested.

terrace (MoB) is seen topographically to actually be an alluvial fan, at the outlet of a first-order drainage. Our final total of 330 ha of terrace treads in the buffer AOI, suggests that the soil survey slightly overestimates terrace tread areas (378 ha). The same stream reach also illustrates how an approach based solely on automated topographic algorithms tends to underestimate the extent of terrace treads (Figure 5C) and how terraces are not always obvious on true-color aerial imagery (Figure 5D).

Although the final map product seems to have good reliability, its imperfections reflect the many challenges involved in terrace mapping (see Section 1.1.), requiring that final map units be checked in the field. Existing soil surveys are a useful tool to guide where to look for terraces along the stream, but they should not be taken as definitive. In many cases, the soil survey overestimates the size of a terrace, or doesn't map as a terrace a very obvious surface. Many areas of the terraces are mapped on alluvial fans where no terrace is visible. The change in technologies from 54 years ago to today clearly results in different interpretations. The soil survey is based on air photo interpretation with limited field testing, as it is not feasible to soil test at every meter. The DEM reveals topography in great detail, even underneath vegetation. However, it does not automatically give soil information on the region and terrace identification based on this information alone is difficult. Accuracy of topography does not automatically translate to accurate identification of geomorphological features. Field checking is essential for mapping stream features. The

floodplain and low terrace soils have similar values in Table 1 because valley aggradation may be masking the low terrace topography. They would have similar elevation but drastically distinct characteristics and ages.

The QGIS Geomorphon tool has been used for terrace mapping purposes (Iacobucci *et al*., 2022). When adjusting the slope of the area to 6, both the Geomorphon and our process have comparable results. Our process is particularly useful for finding potential paired terraces by coloring the different classifications of terrace heights with distinct colors. The method presented in this paper allows more freedom when manipulating the potential terraces layer (detrended low slope DEM), so deeper analysis is conducted, such as calculating area, median and mean elevation, and generating hypsometric curves.

Analysis of the heights of our final terrace polygons suggests modes at 4, 6, 9, 12, and 16 m above the channel. These surfaces are semi-traceable along the valley, but not necessarily along the entire stretch of our study area. In shorter stream reaches (of 10–15 km), it's possible to find multiple surfaces at roughly the same elevation (within a meter or so). But tracing a surface further is not always easy or obvious. Stream lateral migration seems to have eliminated all but a few scattered remnants of previous floodplains. Stable stream states, punctuated by rapid incision, might produce more distinct (separated) terrace surfaces. This is not the case for the study area. Our final map of terrace treads totals only 330 ha of area along approximately 60 km of the main trunk stream. Such discontinuous landforms would be difficult to correlate, even if they were initially discrete, continuous floodplain surfaces.

5. Conclusions

Mapping river terraces in the Little Tallapoosa River involved the use of USDA soil survey, LiDAR-based DEMs, and GIS processing algorithms. Our integrated workflow is a useful method for identifying, outlining, and visualizing terraces in detail along the whole stream. The method can be used as a preliminary tool for analyzing the topography before field testing.

Existing NRCS soil surveys are useful as a "first pass" method for identifying alluvial soil–geomorphic relationships and give a good indication of where fluvial terraces might occur in the landscape. However, as is acknowledged by NRCS, map unit boundaries should not be interpreted as precise delineations of individual fluvial geomorphic features. This study found examples where both false positive and false negative classifications occur along the study area. Likewise, existing GIS terrain analysis tools can give an initial indication of where terraces might occur, but cannot be used to fully automate the generation of reliable terrace maps. An integrated workflow that includes manual, subjective interpretation and combines both soil survey and GIS tools can, however, produce a more reliable map of terraces. Even this must be field tested for final assessment.

In testing our workflow, it became very clear that the detrended 1-m DEM, properly displayed with appropriate hillshading and, especially blending with the slope map, made terrace visualization much easier. The detrended DEM was also critical in determining terrace heights. However, we found that fluvial geomorphic properties vary enough along the entire stream that it's best to analyze terrace heights along particular stream reaches. Terraces along the Upper Tallapoosa River are semi-continuous and might not be traceable along the entire study area.

The terrace surfaces identified are dependent on subjective analysis and field testing. Most of the surfaces are ambiguous enough and too different along the stream to have only one set of standard characteristics for terraces. Many of the smaller and lower terraces were underestimated or not picked up at all from the filters applied to the DEM, making field testing even more crucial in this case. The alluvial fans along the valley and high flat uplands that fall within the buffer are often classified within the terraces filter standard, so further refining of the procedure is needed.

This project produced maps useful for urban planning, archeology, and flood planning for a rapidly developing part of the Atlanta greater metropolitan area. According to its latest comprehensive plan update (Carroll County Department of Community Development, 2023), Carroll County has shown interest in maintaining a GIS-based inventory of historic, archeological, and cultural resources. In addition, the plan also lists water supply, watersheds, wetlands, rivers, streams, and lakes as topics requiring special attention. As development pressures continue to affect the region, geospatial workflows such as the one presented here will help enable strategic, responsible stewardship of the region's natural resources.

Acknowledgment: This research was funded in part by the University of West Georgia (UWG) Dr. James 'Earl' Perry CMCS fund, the UWG School of Field Investigations and Experimental Sciences department fund, and The GeorgiaView Consortium. This material is based upon work supported partly by the U.S. Geological Survey under Grant/Cooperative Agreement No. G18AP00077 (for GY18-GY22) or G23AP00683 (GY23-GY27).

Conflicts of Interest: The authors declare no conflicts of interest. The funders had no role in the design of the study; in the collection, analyses, or interpretation of data; in the writing of the manuscript; or in the decision to publish the results.

References

Brooks, J. F. (1971). *Soil Survey, Carroll and Haralson Counties, Georgia* (Vol. 9). US Soil Conservation Service.

Carroll County Department of Community Development, (2023). *Comprehensive Plan Update 2023*, Carroll County, GA. https://www.carrollcountyga.gov/618/Comprehensive-Plan Last access: 2 October 2025.

Clubb, F. J., Mudd, S. M., Milodowski, D. T., Valters, D. A., Slater, L. J., Hurst, M. D., & Limaye, A. B. (2017). Geomorphometric delineation of floodplains and terraces from objectively defined topographic thresholds. *Earth Surface Dynamics*, *5*(3), 369-385. https://doi.org/10.5194/esurf-5-369-2017

Clubb, F. J., Weir, E. F., & Mudd, S. M. (2022). Continuous measurements of valley floor width in mountainous landscapes. *Earth Surface Dynamics,* 10(3), 437–456. https://doi.org/10.5194/esurf-10-437-2022

Esri. (2025, July 7). *World Imagery* [basemap]. Scale 1:591M–1:288k. http://www.arcgis.com/home/item.html?id=30e5fe3149c34df1ba922e6f5bbf808f Last access: 7 July 2025.

Georgia Department of Transportation. (1997). *Georgia DLG-F Linear Hydrographic Features*, Georgia GIS Data Clearinghouse, https://data.georgiaspatial.org/ Last access: 2 October 2025

Hopkins, A. J., & Snyder, N. P. (2016). Performance evaluation of three DEM-based fluvial terrace mapping methods. *Earth Surface Processes and Landforms,* 41(8), 1144–1152. https://doi.org/10.1002/esp.3922

Iacobucci, G., Piacentini, D., & Troiani, F. (2022). Enhancing the Identification and Mapping of Fluvial Terraces Combining Geomorphological Field Survey with Land-Surface Quantitative Analysis. *Geosciences*, 12(11), 425. https://doi.org/10.3390/geosciences12110425

Soil Survey Staff, Natural Resources Conservation Service, United States Department of Agriculture. (n.d.). *Web Soil Survey*. http://websoilsurvey.sc.egov.usda.gov/. Last access: 23 July 2025.

Stout, J. C., & Belmont, P. (2013). TerEx Toolbox for semi-automated selection of fluvial terrace and floodplain features from lidar. *Earth Surface Processes and Landforms*, 39(5), 569–580. https://doi.org/10.1002/esp.3464

Strahler, A. N. (1957). Quantitative analysis of watershed geomorphology. *Transactions American Geophysical Union*, *38*(6), 913–920. https://doi.org/10.1029/tr038i006p00913

The National Map. (2025). USGS. https://www.usgs.gov/programs/national-geospatial-program/national-map Last access: 2 October 2025.

U.S. Geological Survey. (2025). 3D Elevation Program 1-Meter Resolution Digital Elevation Model (published 2020-2023). https://www.usgs.gov/the-national-map-data-delivery Last access: 2 October 2025.

USGS WaterWatch – Streamflow conditions. (2025). https://waterwatch.usgs.gov/?m=real&r=ga&w=map Last access: 2 October 2025.

Research Article

Estimating North Texas Urban Tree Above-Ground Biomass Based on Terrestrial LiDAR and Optimized Quantitative Structure Models

Elizabeth Elkins[1] and Kashif Mahmud[2,*]

[1] Kimbell School of Geosciences, Midwestern State University, Wichita Falls TX 76308, lizcelkins10@gmail.com
[2] Kimbell School of Geosciences, Midwestern State University, Wichita Falls TX 76308, kashif.mahmud@msutexas.edu
[*] Corresponding Author: kashif.mahmud@msutexas.edu; +1-940-397-4475

Abstract: Several studies have revealed that terrestrial light detection and ranging (LiDAR) remote-sensing technology can be an alternative, more accurate approach to estimate tree above-ground biomass (AGB). A set of algorithms has been developed to create a volume reconstruction of tree point clouds, which can be converted to an AGB estimate. These calculate AGB non-destructively and more accurately compared to current forestry practices, which use generic allometric equations. LiDAR scans of trees within Midwestern State University's campus were collected and analyzed with a tree segmentation/modeling algorithm. The validation method was based on comparing the estimated above-ground attributes to actual field measurements. Optimized PD1 and PD2Max increase as the tree size increases, whereas PD2Min remains relatively the same for different tree sizes. Quantitative structure modeling (QSM) produces accurate diameter at breast height (DBH) estimates, however it fails to calculate it precisely when there are low branches or dense leaves within the canopy. These occlusions commonly occur with certain tree species, such as *Pinus echinata* and *Juniperus virginiana*. Our result suggests good agreement of QSM-derived AGB estimates for larger trees but overestimated AGB for smaller trees. This is due to the limitations in LiDAR technology, struggling to accurately scan fine branches and twigs of small trees, leading to errors in point cloud data and subsequent overestimation of their volume in the QSM. While the study provides valuable insights, the small sample size due to the complexity of destructive tree harvesting in urban ecosystems might limit the generalizability of the results.

Keywords: LiDAR, QSM, urban, trees, AGB

Academic Editor: Jeong Chang Seong
Received: 5 May 2025
Revised: 9 July 2025; 5 August 2025
Accepted: 16 August 2025
Published: 24 October 2025

Citation: Elkins, E., & Mahmud, K. (2025). Estimating North Texas Urban Tree Above-Ground Biomass Based on Terrestrial LiDAR and Optimized Quantitative Structure Models. *Journal of Earth Observation and Geospatial Applications*, *1*(1), 94–107. DOI: https://doi.org/10.65372/8w66ep09

1. Introduction

Urban green spaces serve to increase mental health and wellbeing (e.g., Lee *et al.*, 2015), increase air quality (Wolf *et al.*, 2020), reduce heat island effects and provide comfort (e.g., Aram *et al.*, 2019; Rahman *et al.*, 2020), ultimately reducing the energy consumption of buildings (McDonald *et al.*, 2019). Urban vegetation, particularly on university campuses, is a good way to promote stewardship of the environment (e.g., trash pickups, tree planting and adoption, wildlife awareness) and foster community-based events (Schick *et al.*, 2023). Improving the knowledge of tree carbon storage will help better understand climate change, both locally and globally (Nowak & Crane, 2002).

Furthermore, such plantings manage and store carbon, and doing so in urban spaces is one of the most important ways to offset building carbon emissions (Jo & McPherson, 2001) and combat climate change (Tavasoli *et al.*, 2019). Quantifying above-ground biomass (AGB) permits urban planners to assess carbon storage and other ecosystem functions and design more effective strategies in building carbon sinks (Tigges *et al.*, 2016). Improving the overall net carbon budget starts with gathering information about the study site, which could only be feasible with better tree AGB estimates (Nowak & Crane, 2002). The current rate of urbanization causes urban forests to increase in size as a fraction of the total land cover (Hutyra *et al.*, 2014). And as trees account for up to 97% of urban AGB (Davies *et al.*, 2011), it is of great importance to have an accurate prediction of AGB. In traditional forestry practices, allometric relationships are used to convert

diameter at breast height (DBH, measured 1.3 m above the ground) into tree AGB. These methods were developed through destructive harvesting. Many allometric equations have significant uncertainties, particularly for larger trees that can be attributed to (1) limited harvest data, (2) extrapolating the allometric relationship without considering the environment, and (3) measurement errors of tree dimensions (Mascaro *et al.*, 2011; Duncanson *et al.*, 2015). When species-specific allometries are applied, an approximately 35 % underestimation was found for large trees (Calders *et al.*, 2014). The relationship can lead to errors when estimating biomass or volume growth because it is based on limited observation. Extensive destructive sampling is required for accurate species- and ecosystem-specific allometric equations (Roxburgh *et al.*, 2015). Harvesting trees on a large scale may be practical in forested areas; however, it is often not feasible or too costly in urban settings. Conversely, the allometric equations established for forest trees may not apply to urban trees due to variations in the ecosystem (McHale *et al.*, 2009).

Light detection and ranging (LiDAR) sensors have received significant attention for assessing three-dimensional (3D) tree structure and AGB in various ecosystem types. Recent advancements in terrestrial LiDAR offer fine-scale 3D tree point clouds by recording the reflected signal of millions of laser trajectories produced by the instrument. Although LiDAR has been used in forestry for about two decades, recent advances in remote sensing technology and computational power have made it a commonplace tool in the field. Tree attributes can be assessed without any destructive harvesting (Calders *et al.*, 2014). An individual tree point cloud can be separated from the entire LiDAR point cloud, and tree attributes can be estimated using the quantitative structure modeling (QSM) (Raumonen *et al.*, 2013). The method fits cylinders to the 3D point cloud to construct a tree model for each tree, providing detailed information on volume and structure. QSM has been successfully used in different forest ecosystems (Calders *et al.*, 2014; Tanago *et al.*, 2017; Torresan *et al.*, 2018). The method can estimate AGB within 10 % of values determined by destructive harvesting (Calders *et al.*, 2014). The quality of such volumetric tree models is highly dependent on the complexity of the trees, scan acquisition geometry, pattern and settings, and meteorological conditions during the LiDAR scans. Moreover, a set of QSM parameters controls the overall fit of cylinders and the accuracy of the 3D model. Jiang *et al.* (2020) optimized QSM parameters using 160 Australian eucalyptus trees to calculate AGB for plot-scale carbon budget estimation.

This study aimed to apply QSM on terrestrial LiDAR evaluations of a small population of trees within a North Texas urban setting (the campus of Midwestern State University). The trees in this study were modeled and separated into size groups, allowing an evaluation of tree-size influence on model parameters. The accuracy of high-resolution LiDAR data and state-of-the-art tree segmentation algorithms to quantify above-ground volume to estimate AGB of urban trees was evaluated. Analysis explores ways to improve the post-processing computer algorithms based on the fine-scale ground-truth field data. More importantly, the unprecedented details from LiDAR measurements propagate useful tools for forest structure and growth data, with implications on larger scales, such as using satellite-derived data for local/regional forests. This technique provides a non-destructive approach for estimating tree AGB and has real-world impacts on local stakeholders by informing them of the potential of LiDAR technology and data-based practical recommendations for terrestrial carbon stock and sustainable forestry management strategies.

2. Study Area and Data Collection

2.1. Study Area

This study characterized twenty-four individual trees of varying sizes (DBH = 8.2 – 77 cm) and heights (2.5 – 13.5 m) across the Midwestern State University's (MSU Texas) campus, including distributions at Bolin Science Hall in Figure 1a, Sikes Lake in Figure 1b, and Killingsworth Hall in Figure 1c). All trees were scanned using a Leica BLK360 terrestrial laser scanner. An example of LiDAR tree point clouds on the south side of the Bolin Science Hall can be seen in Figure 2. Most of the trees are species native to the Rolling Plains physiographic province or to the larger North Texas region. The study includes one well-adapted

ornamental species, *Acer truncatum*. All the tree species were identified and listed in Table 1 with corresponding densities (x 10^{-3} kg/cm³) gathered from Appendix 11 of Nowak (2024). Scans were completed during the summer of 2023.

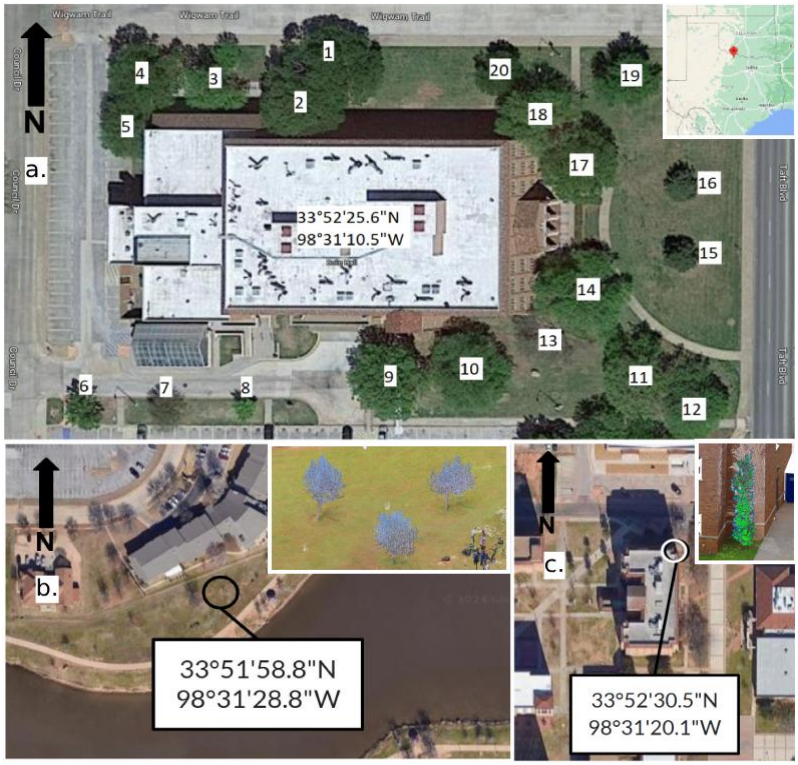

Figure 1. Aerial view of Bolin Science Hall (a), Sikes Lake (b), and Killingsworth Hall (c) with approximate locations (Google Maps). Bolin Science Hall has 20 trees. Sikes Lake has three small trees within the circle, and Killingsworth Hall has one tree within the circle. There are a total of 24 trees. The inset figure in (a) shows the location of MSU Texas' campus. The inset figures in the top right corners (in b & c) show the tree point clouds from LiDAR scans.

Figure 2. Sample LiDAR scan showing tree point clouds on the south side of Bolin Science Hall.

2.2. Data Collection

Field data such as circumference at 1.3 m above ground, LiDAR point clouds, and species were collected for each tree. AGB was measured for four trees, three small (SL1, SL2, SL3) and one large (BO5) (Table 1). The circumference of each tree was measured at the top of a 1.3 m tall wood post reference. The post was

standing upright next to the tree, and the circumference of the trunk was measured using a measuring tape reel. The circumference was converted to diameter (DBH) for each tree. The large tree (BO5, *Ulmus crassifolia*) was weighed on a commercial truck scale. We used Shadman *et al.* (2022) green weight to dry weight equation to obtain the dry weight. The small trees (SL1, SL2, SL3, *Acer truncatum*) were weighed using a standard, hand-held luggage scale. Two trees (SL1 and SL3) were sufficiently small to be weighed intact; the other (SL2) was cut into pieces, where each piece was weighed, and all the weights were summed for the total. All small trees had died prior to harvest, resulting in a dry weight. Species were identified for all 24 trees. LiDAR scans were taken using a Leica BLK360 terrestrial laser scanner at its finest spatial resolution (~3 cm). Capturing a single tree requires multiple scans from different angles. Over 50 scans were captured to survey the entire study area. Every angle of the trees needs to be scanned to have enough data points for accurate modeling. A minimum of four scans per individual tree was obtained. However, the proximity of the trees allows each tree to share multiple scans with the neighboring tree due to the LiDAR scanning in a full 360° rotation. These scans are positioned in the corners of a square around the tree, with the tree in the center.

Table 1. List of the trees considered in this study with their species, common names, density, and size.

Tree ID	Species	Common Name	Density (x 10 kg/cm³)	Tree Size
BO1	*Ulmus crassifolia*	Cedar Elm	0.59	Large
BO2	*Ulmus crassifolia*	Cedar Elm	0.59	Medium
BO3	*Ulmus crassifolia*	Cedar Elm	0.59	Medium
BO4	*Ulmus crassifolia*	Cedar Elm	0.59	Large
BO5	*Ulmus crassifolia*	Cedar Elm	0.59	Large
BO6	*Quercus buckleyi*	Texas Red Oak	0.62	Small
BO7	*Quercus virginiana*	Live Oak	0.8	Medium
BO8	*Quercus buckleyi*	Texas Red Oak	0.62	Small
BO9	*Quercus macrocarpa*	Bur Oak	0.58	Large
BO10	*Ulmus crassifolia*	Cedar Elm	0.59	Medium
BO11	*Quercus buckleyi*	Texas Red Oak	0.62	Large
BO12	*Ulmus crassifolia*	Cedar Elm	0.59	Large
BO13	*Ulmus crassifolia*	Cedar Elm	0.59	Medium
BO14	*Ulmus crassifolia*	Cedar Elm	0.59	Large
BO15	*Pinus echinata*	Shortleaf Pine	0.47	Small
BO16	*Pinus echinata*	Shortleaf Pine	0.47	Medium
BO17	*Ulmus crassifolia*	Cedar Elm	0.59	Large
BO18	*Ulmus crassifolia*	Cedar Elm	0.59	Large
BO19	*Ulmus crassifolia*	Cedar Elm	0.59	Medium
BO20	*Ulmus crassifolia*	Cedar Elm	0.59	Small
SL1	*Acer truncatum*	Shantung Maple	0.59	Small
SL2	*Acer truncatum*	Shantung Maple	0.59	Small
SL3	*Acer truncatum*	Shantung Maple	0.59	Small
KH1	*Juniperus virginiana*	Red Juniper	0.44	Medium

3. Methods

3.1. QSM Derived Tree Attribute

After the LiDAR survey, all individual scans were downloaded using the software Cyclone Register 360 associated with the BLK360 scanner and assembled into a single point cloud. Any unnecessary portions (e.g., buildings, cars, ground) were removed, and each tree point cloud was separated using CloudCompare, a 3D point cloud processing software.

Volume reconstructions of tree point clouds were made using QSM of Raumonen *et al.* (2013). A brief summary of the algorithm is provided below; readers are directed to the source for further details. QSM uses cylinders as basic building blocks to reconstruct the tree model from a point cloud, which is usually produced by a terrestrial laser scanner and must contain only one tree. The tree model is defined based on three parameters (PD1, PD2Min, PD2Max), and optimization of these parameters is imperative for a better representation of the tree. Initial processing of QSM filters the point cloud by creating spheres around the data points and then rejecting those points that contain too few data points within the sphere. This effectively removes noise, reducing the data to the surface of the tree. Next, the cover sets create connected surface patches, defining the surface topology and shape of the tree. The cover sets connect together via neighbor-relation, group data points based on their common point. The number of neighbors typically varies. Once grouped, the algorithm characterizes the cover sets geometrically. Trunk and branches tend to be locally cylindrical, such that the algorithm works best for trees. The branches are separated using the branching relations of the child and parent branches. Finally, the algorithm estimates DBH, surface area, volume, and other geometric attributes. DBH was estimated by taking the diameter of the cylinder at 1.3 m from the ground. Volume measurements were estimated by calculating and summing the volume of the corresponding cylinders.

Jiang *et al.* (2020) used QSM with a set of optimum parameters (PD1 = 0.09, PD2Min = 0.02, and PD2Max = 0.08) based on Australian eucalyptus trees. PD1, PD2Min, and PD2Max control the overall fit of cylinders and the accuracy of QSM. The initial QSM analysis in this study used the Jiang *et al.* (2020) parameters. In subsequent analyses, the parameters were further optimized by comparing field observations of tree weight and DBH within our study area. Different sets of parameters were compared using the Mean Squared Error (MSE) of DBH and harvest AGB. The automated optimization technique within the QSM was first implemented to find the optimum parameters, however it didn't perform well for the trees in this study. Hence, we tried an iterative optimization technique with trial and error and cross-validation. The parameters were composed of numbers ranging from 0.001 to 0.2 for PD1, PD2Min, and PD2Max. Each combination was run on test trees for each size group. The test trees were SL1 and SL2 for the small group; BO2, BO7, and BO19 for the medium trees; and BO5 for the large trees. Test trees for the small and large groups were chosen because their DBH and AGB were known. The medium test trees were chosen at random since there was no known AGB data for this group. The species-specific wood densities from Nowak (2024) were used in this study and are listed in Table 1. QSM-derived volume estimate was multiplied by the wood density to convert to AGB. The model-derived DBH and AGB estimates were compared to the measured DBH and destructively harvested AGB respectively, by calculating error percentage (*((QSM-derived estimate − Field measurement) / Field measurement * 100*) and root mean square errors (RMSE) to assess QSM's performance. Figure 3 compares the LiDAR point cloud and the QSM 3D model with optimum parameters for two (BO11 and BO8) of the Texas Red Oaks from the study area.

3.2. Allometry-based AGB Estimation

The allometry-based AGB was estimated using the equation (Equation 1) from Jenkins *et al.* (2004), where bm = total AGB (kg) for trees with 2.5 cm and larger DBH, DBH = diameter at breast height (cm), β_0 and β_1 are coefficients.

$$bm = \mathrm{Exp}(\beta_0 + \beta_1 \ln(DBH)) \quad (1)$$

The coefficients β_0 and β_1 vary with tree species. This equation is based on compiling published diameter-based allometric regression equations for estimating dry weight AGB (e.g., Gholz *et al.*, 1979; Binkley, 1983) and modifying them using meta-analysis to create a consistent AGB regression equation (Jenkins *et al.*, 2003). Table 2 shows selected parameters. Jenkins *et al.* (2004) suggests using the mixed hardwoods coefficients for Cedar Elm (*Ulmus crassifolia*, the hard maple coefficients for Live Oak (*Quercus virginiana*), the hard maple coefficients for Bur Oak (*Quercus macrocarpa*), the pine coefficients for Shortleaf Pine (*Pinus echinata*), and the cedar coefficients for Eastern Red Cedar (*Juniperus virginiana*). For Texas Red Oak (*Quercus buckleyi*), Jenkins *et al.* (2004) did not directly state which parameters to use. Shumard Oaks (*Quercus shumardii*) are similar to Texas Red Oaks (Greene *et al.*, 2008); therefore, the hard maple parameters are used. Jenkins *et al.* (2004) did not directly state which parameters to use with the Shantung Maple (*Acer truncatum*), but given that the species is a hard maple, those parameters seemed most suitable.

Table 2. The parameters (β_0 and β_1) for the allometry-based estimate for the groups of trees at the study sites (Modified from Jenkins *et al.*, 2004).

Species Group	β_0	β_1	Max DBH (cm)	R^2
Mixed Hardwood	−2.4800	2.4835	56	0.980
Hard Maple	−2.0127	2.4342	73	0.988
Cedar	−2.0336	2.2592	250	0.981
Pine	−2.5356	2.4349	180	0.987

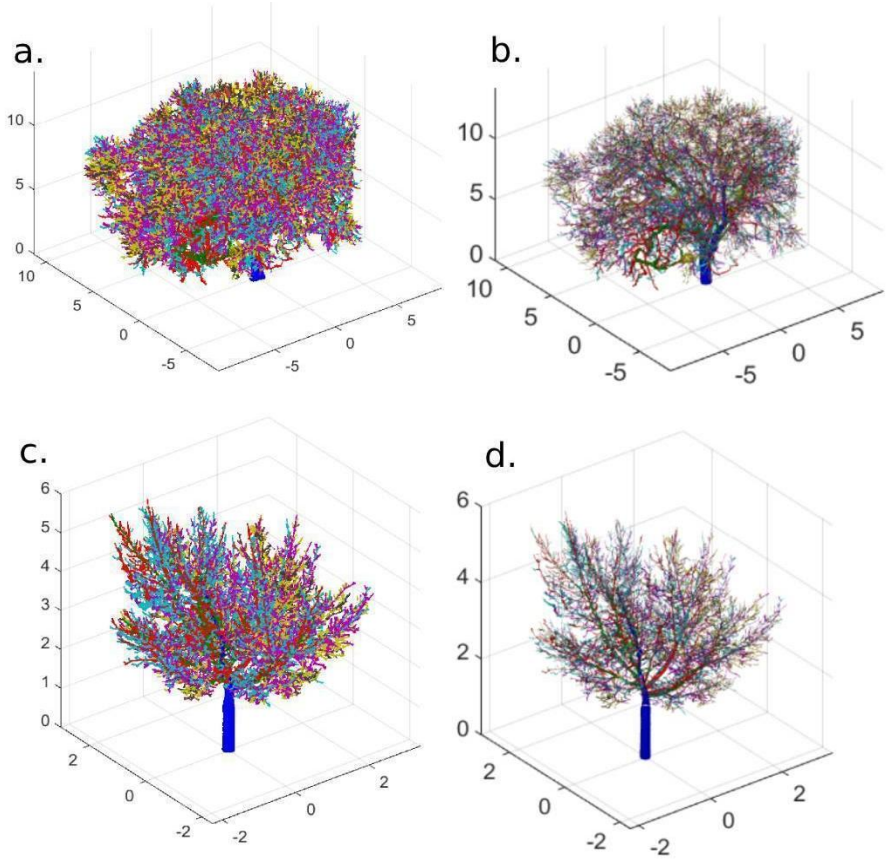

Figure 3. The left column shows BO11 (a) and BO8 (c) point clouds. The right column shows the 3D model generated by QSM for BO11 (b) and BO8 (d). BO11 is located on the southeast side of Bolin Science Hall, and BO8 is located on the southwest side of Bolin Science Hall.

4. Results

4.1. Parameter Optimization

Figure 4 shows the MSE of DBH and harvest biomass (depending on tree groups) for the parameter tests for each parameter (PD1, PD2Min, and PD2Max) and size group (small: DBH < 36 cm, medium: DBH 36 - 55 cm, large: DBH > 55 cm). We used harvested biomass to optimize parameters for both small and large trees, hence the reported MSE values are for biomass and greater than the medium-sized trees. DBH is used for medium-sized trees due to a lack of harvest data. Therefore, the MSE values are for DBH. The small group was optimized using the trunk volume of SL1 and SL2 due to the high error percentage of QSM's total volume estimates. The medium group was optimized using DBH from BO2, BO7, and BO19. These trees were picked because their field DBH measurements were close to the maximum, minimum, and mean of the medium trees' DBH. The large group was optimized using BO5 because we had harvested above-ground mass to compare to QSM's AGB. The figure also plots the computational time required for the corresponding tests. The lowest observed MSE values largely correspond with smaller parameters, and the fastest run times usually occur for larger parameters. There is a trade-off between these two variables in terms of choosing the optimum set of parameters.

For the small trees, the lowest MSE occurred when PD1 = 0.02 with a run time of about 5 minutes. A reduced run time can be achieved, but at the expense of a lower MSE. For PD2Min, the lowest MSE was when PD2Min = 0.01 with a run time of about 13 minutes. For PD2Max, the lowest MSE was at PD2Max = 0.01, having a run time of about 17 minutes. For the medium trees, the parameters do not largely affect the DBH outputs as seen by the relatively consistent MSE values. PD1 was 0.05 with the lowest run time of about 30 hours. For the PD2Min, the lowest MSE was when PD2Min = 0.01 with a run time of about 35 hours while the best run time was when PD2Min = 0.05 at 3 hours. When PD2Min was 0.02, the MSE was slightly higher than PD2Min at 0.01; the slightly higher run time at PD2Min = 0.05 suggested that PD2Min = 0.02 was a better choice. PD2Max = 0.01 produced the lowest MSE for the medium trees for a run time of about 120 hours. The lowest run time was about 15 hours when PD2Max = 0.09. The optimum was when PD2Max = 0.05 because the MSE was similar to the lowest and the run time was about 25 hours. For the large tree, the PD1 = 0.11 yielded the lowest MSE and a lower run time, making it preferable. When PD2Min = 0.01, the MSE was lowest and had a decent run time. PD2Min = 0.03 could be chosen if a shorter run time was preferred. The lowest MSE for PD2Max had a run time of about one hour. However, the shorter run times had increases in MSE. We chose the optimum values for PD2Max to be 0.17 for the large trees.

To summarize, the optimum parameters are listed in Table 3 for three different tree size groups. PD1 and PD2Max increase as the tree size increases, whereas PD2Min remains relatively the same for different tree sizes (Table 3).

Table 3. The optimized parameters for each tree size group.

	Small Group	Medium Group	Large Group
PD1	0.02	0.05	0.11
PD2Min	0.01	0.02	0.01
PD2Max	0.01	0.05	0.17

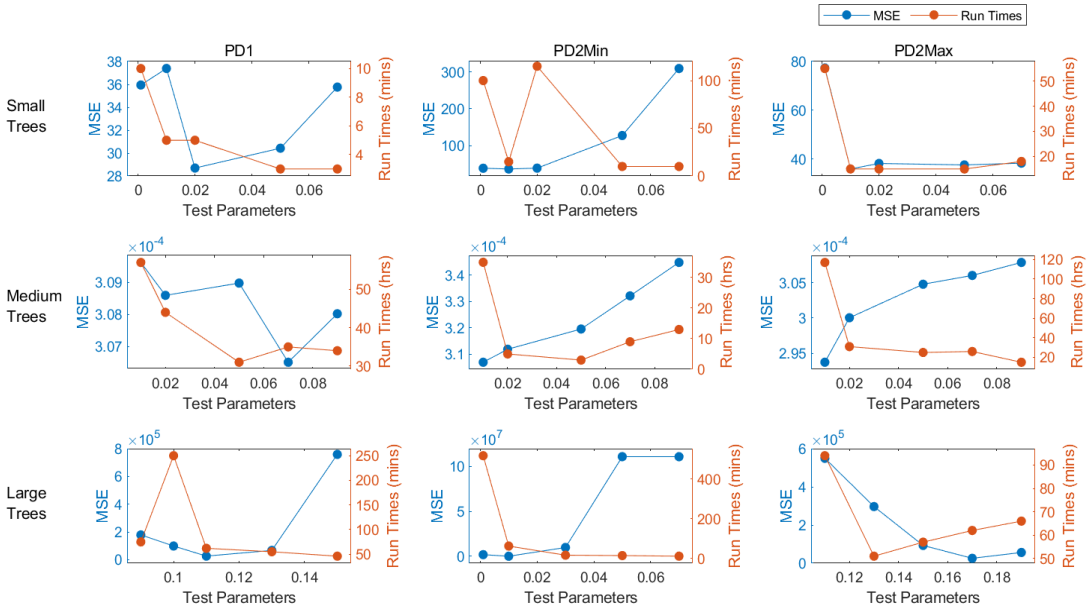

Figure 4. MSE of DBH and harvest biomass for the parameter tests for each parameter (PD1, PD2Min and PD2Max) and size group (small: DBH < 35 cm, medium: DBH 36 – 55 cm, large: DBH > 55 cm) are shown in blue colors. The run times for the corresponding tests are shown in orange colors.

4.2. Evaluation of Tree DBH and AGB

Using the optimized parameters, we calculated the DBH, above-ground volume, and other attributes for all tree point clouds. Table 4 compares measured DBH and AGB versus QSM derived DBH and AGB with the error percentage. The table also lists allometry-based AGB and the difference between the two AGB estimates (QSM-derived vs allometry-based AGB). It also has the total AGB and the total carbon stored in all 24 trees calculated by both methods (QSM-derived and allometry-based). We used half of the dry weight as total carbon storage in these trees (Shadman *et al.*, 2022). QSM and allometry-based AGB error percentages are all positive for smaller trees (SL1, SL2 and SL3) with the exception of the large tree (BO5) having the allometry-based AGB underestimated (Table 4). On the contrary, most of the QSM-derived DBH errors are negative (Table 4), indicating an overall underestimation of DBH prediction. Moreover, the QSM-derived AGB is larger compared to allometry-based AGB estimates (Table 4). For the smaller trees (SL1, SL2, and SL3), the allometry-based AGB had a smaller error percentage compared to the QSM-based AGB (Table 4). For the large tree (BO5), the QSM-derived AGB had a smaller error percentage than the allometry-based AGB (Table 4). The R-squared value of field DBH compared to QSM-derived DBH is 0.95 (Figure 5). The linear regression line has a close match with the 1:1 (major diagonal) line, representing a good agreement between QSM-derived DBH and field DBH. The QSM performed well in calculating the DBH with an overall underestimation and a couple of exceptions (Figure 5). However, the QSM-derived AGB was overestimated significantly (Figure 5) for at least two small trees, with an error of more than 250% (Table 4).

Separate box plots were constructed showing the QSM-derived DBH error percentages for tree size and tree species (Figure 6). The small trees performed well with QSM-derived DBH error ranging from −14.5 to +9.3%, with an RMSE of 3.03 cm, but the medium and large trees had slightly higher error percentages with the medium tree group having the largest variation in the DBH estimates (Figure 6). However, the large tree group had the best match for QSM-derived DBH with the lowest RMSE of only 1.48 cm. When the trees are grouped by species, the cedar elms have an RMSE of 2.77 cm while the oaks have an RMSE of 1.42 cm. The

RMSE on pines was 5.88 cm, and the juniper was 20.92 cm, larger than those for cedar elms and oaks. Overall, the QSM-derived DBH consistently underestimated DBH.

Figure 7 illustrates the differences between the traditional method (allometry-based AGB) and QSM-derived AGB for tree size and tree species. When the AGB difference is grouped by tree genus, most of the QSM-derived AGB estimates for each species group were larger than the corresponding traditional estimates based on allometric equations (Figure 7). The cedar elms have a 75% difference. The oaks and pines both have a 60% difference. However, the juniper (KH1) provided a larger allometry-based AGB than the QSM-derived estimate (460% difference). The average percentage difference between QSM and allometric AGB estimates was 50% when excluding KH1 and 70% when including KH1. These substantial variations between the two techniques indicate the importance of further research, particularly with more harvest data for urban trees.

Table 4. Field measurements, QSM attributes, DBH error, AGB error, and AGB differences between QSM and allometry-based estimates.

Tree ID	Field DBH (cm)	QSM DBH (cm)	DBH Error (%)	Field AGB (kg)	QSM-derived AGB (kg)	AGB Error (%)	Allo. based AGB (kg)	Allo. & QSM based AGB Difference (%)
BO1	74.49	72.00	−3.34	–	5332.64	–	3734.71	−29.97
BO2	50.61	48.06	−5.04	–	3998.37	–	1430.47	−64.22
BO3	45.52	43.31	−4.86	–	2704.14	–	1099.23	−59.35
BO4	58.89	56.00	−4.91	–	4481.68	–	2083.68	−53.51
BO5	61.12	55.00	−10.01	4269	4307.65	0.9	2285.01	−46.95
BO6	30.88	29.00	−6.09	–	527.50	–	564.89	7.09
BO7	37.24	35.55	−4.54	–	5455.75	–	891.54	−83.66
BO8	23.56	23.00	−2.38	–	253.35	–	292.31	15.38
BO9	71.3	70.00	−1.82	–	4868.78	–	4332.50	−11.01
BO10	49.98	47.99	−3.98	–	5153.82	–	1386.20	−73.10
BO11	77.03	75.00	−2.64	–	6290.44	–	5229.35	−16.87
BO12	52.52	51.00	−2.89	–	6413.59	–	1568.31	−75.55
BO13	35.65	35.13	−1.46	–	2731.63	–	599.16	−78.07
BO14	64.94	62.00	−4.53	–	7827.43	–	2656.30	−66.06
BO15	32.79	32.00	−2.41	–	666.78	–	388.49	−41.74
BO16	35.65	27.37	−23.23	–	1290.62	–	476.39	−63.09
BO17	53.16	52.00	−2.18	–	3650.66	–	1615.94	−55.74
BO18	58.57	55.00	−6.10	–	4258.72	–	2055.82	−51.73
BO19	44.88	45.14	0.58	–	5308.29	–	1061.44	−80.00
BO20	29.29	32.00	9.25	–	1766.71	–	367.60	−79.19
SL1	8.19	7.00	−14.53	15.17	56.96	275.45	22.34	−60.78
SL2	9.71	10.00	2.99	30	37.67	25.57	33.81	−10.25
SL3	9.29	8.00	−13.89	16.1	77.27	379.95	30.36	−60.71
KH1	46	25.08	−45.48	–	133.32	–	747.00	460.29
Total AGB (kg):					77593.77		34952.85	
Total Carbon Storage (kg):					38796.89		17476.43	

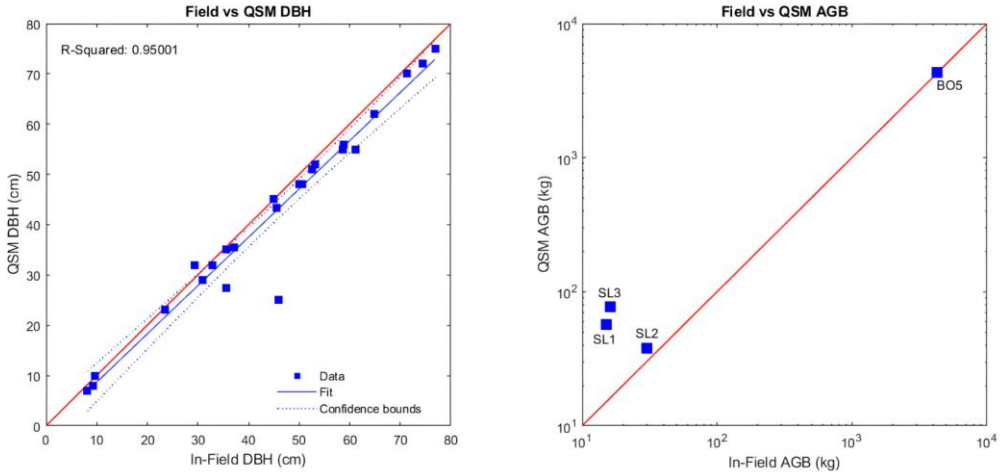

Figure 5. Comparison between field measurements and QSM-derived measurements for both DBH and AGB. We only have four of the trees (BO5, SL1, SL2 and SL3) harvested, hence only four points for the AGB plot. The red line is the 1:1 line. The R-squared and the linear regression line are also shown for the DBH plot.

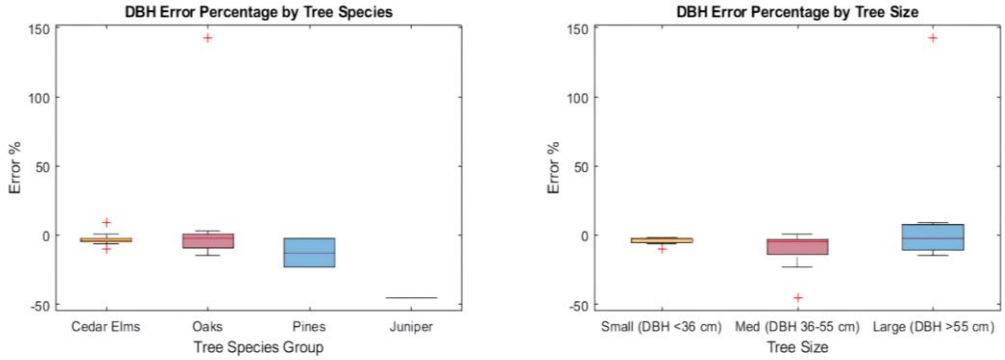

Figure 6. Box plots showing the error percentage for QSM-derived DBH grouped by tree species and size. There are 13 cedar elms, 8 oaks, two pines, and one juniper.

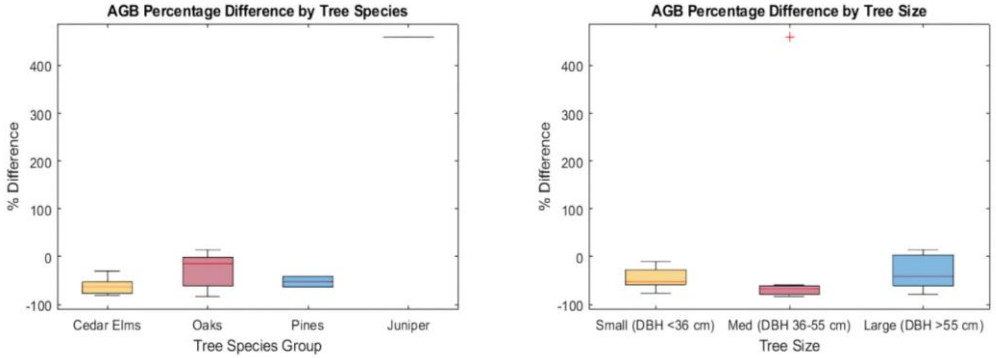

Figure 7. Box plots showing the percentage difference for AGB estimated by two methods (QSM and allometry-based) grouped by tree species and size. There are 13 cedar elms, 8 oaks, two pines, and one juniper.

5. Discussion

5.1. Overview

Generally, QSM is accurate when calculating DBH; it tends to poorly calculate DBH when there are low branches or many leaves. Two trees (BO16 and KH1) had low branches and many leaves, deteriorating the QSM model and DBH estimates. One of the pine trees (BO16, *Pinus echinata*) has many occlusions caused by shadowing due to its low branches and many leaves along the branches. The Juniper tree (KH1, *Juniperus virginiana*) presented issues as well. This tree was in the corner of a building, leading to an insufficient LiDAR scan angle between the building and the tree. KH1 is a tall tree with a narrow shape, and dense branches and leaves distribution. Since the point density in the LiDAR scan was low, QSM had challenges, particularly in reconstructing the stem and branches of the Juniper. Moreover, measuring DBH over bark can lead to significant errors, particularly in younger trees where bark is a larger proportion of the stem, and also in older trees where bark thickness is often variable around the stem. We believe this caused an overestimation of our field DBH measurements, hence the QSM-derived DBH underestimation is expected for these urban trees having irregular bark.

Unfortunately, we have a limited sample size and harvest AGB data, but we found similar results in AGB estimates as previous studies applying QSM (Calders *et al.*, 2014; Tanago *et al.*, 2017; Kükenbrink *et al.*, 2021). Among the four trees with field AGB data, the large tree's (BO5) QSM-derived AGB (4308 kg) was very close to the harvest biomass (4269 kg). However, the traditional allometry-based AGB underestimated the tree by 47%. Allometry-based tree AGB estimation, while a useful tool, can be inaccurate due to several factors. These include the application of equations developed for one species or location to different species or environments, the variability in tree growth patterns influenced by factors like site productivity, and the difficulty in capturing the complexity of tree architecture with simple models. Additionally, small sample sizes in some allometric equations can lead to bias and measurement errors. Hence, QSM offers a non-destructive approach to estimating AGB more accurately than the traditional allometric method, particularly for large trees. We emphasize that accurately estimating the AGB for large trees is vital because of their crucial role in carbon storage within urban forests. They store significantly more carbon than smaller trees, and their size allows them to absorb carbon more efficiently. Large trees accumulate substantial amounts of carbon annually. Protecting and allowing large trees to continue growing is vital for climate mitigation, as they can store carbon within the urban environment for centuries. The accurate prediction of large urban tree biomass directly impacts the estimation of how much carbon is stored and how much is being sequestered annually. Therefore, combining remote sensing techniques with QSM provides an efficient tool for the accurate prediction of carbon storage for urban ecosystems.

QSM-derived AGB overestimated all three smaller trees (SL1, SL2, and SL3) estimates. These overestimations in smaller tree AGB are particularly caused by the tiny branches and twigs, due to limitations in LiDAR technology. Specifically, LiDAR struggles to accurately scan fine branches and twigs, leading to errors in point cloud data and subsequent overestimation of their volume in the QSM, hence the tree AGB. This could also be due to errors within the point clouds, such as occlusions caused by shadowing, movement of the tree during scanning, non-circular branches, non-wooden material, or segmentation and structure errors in the QSM cylinder model (Krooks *et al.*, 2014). For example, one of the small trees (SL1) harvested AGB was 15.17 kg while the QSM estimate was 56.99 kg with an error of 275%. However, the harvest weight of the small trees was measured using a standard luggage scale, which possibly introduced human measurement errors, causing higher error percentages for the small trees. On the contrary, the traditional method performed well in estimating the urban small tree AGB, indicating these equations are derived with adequate field data representing the tree species. However, that is certainly not the case for the large urban tree due to limited harvest data.

This project defined the nature of tree-carbon storage in urban environments. Due to having four AGB ground truth data, more harvest data needs to be collected. This is the starting point for collecting carbon storage data using LiDAR and QSM at MSU Texas campus and for the entirety of the surrounding city,

representing the North Texas urban ecosystem. However, QSM using tree LiDAR point clouds looks promising with better AGB estimation for large urban trees, which is crucial for accurately estimating their role in carbon uptake and storage within cities.

5.2. Future Work

Our work is limited to four samples due to the complexity we faced with destructive tree harvesting in urban ecosystems. It is more common to harvest large forest trees for timber production and forest management for wildlife and ecosystem health, rather than in urban areas. Hence, we chose our campus for the project having the collaboration of the facilities services, informing us before harvesting any campus tree. Due to the small sample size, future work will focus on scanning and harvesting more trees. This will provide more harvest AGB for better parameter optimization for different sizes and species of urban trees. Collecting more harvest data is the most important strategy for creating an accurate estimation of urban carbon storage. Future projects could then include the use of airborne and/or satellite LiDAR to expand the spatial coverage of the study area. QSM can also be used to test allometric equations, particularly for larger trees, which are underrepresented in allometric equations because of limited harvest data (Tanago *et al.*, 2017).

QSM has been further modified recently, with the segmentation process becoming automated. Therefore, modeling has improved with add-ons such as TLS2Trees (Wilkes *et al.*, 2023) and Real Twig (Morales & MacFarlane, 2024). TLS2Trees automatically separates individual tree point clouds. This reduces time spent manually separating trees. Real Twig uses branch measurements to correct QSM models by fixing the volume overestimation commonly found in QSM estimates due to small branches. Using these in future work could greatly improve the accuracy of QSM, especially for the smaller trees and the estimation of total carbon storage in urban ecosystems.

6. Conclusions

Allometric equations are the traditional method to estimate AGB, but they are generalized and based on destructive harvest data. With the advancement of LiDAR technology, assessing 3D tree structure is a feasible method to estimate AGB in various ecosystems including urban environments. The aim of the project was to apply QSM using terrestrial LiDAR data on a small population of trees within a North Texas urban setting. We optimized QSM's parameters (PD1, PD2min, and PD2max) by comparing field data and estimated the total carbon stored in the study site. These optimized parameters vary with tree size. PD1 and PD2max increased as DBH increased, however PD2min stayed the same. Overall, QSM underestimates DBH within 10% when excluding BO16 and KH1. This underestimation is partly due to a possible overestimation in our field measurements due to irregular tree bark. It is evident that the traditional allometry-based equation underestimates the large urban tree AGB by 50%, whereas the QSM-derived AGB has an accurate match with the harvest data (Table 4). Therefore, LiDAR could possibly provide a reasonable evaluation of AGB for urban trees, especially for the large trees, but more data is needed to fully validate this method. The QSM approach is an accurate, most importantly, a non-destructive process to estimate large urban tree AGB and other attributes. Effectively modeling tree characteristics allows for more information about green spaces to be readily available and practically utilized.

Data Availability Statement: Individual tree point clouds, field data, and QSM code can be accessed at https://github.com/liz-elkins/MSUTX-TreeQSM.

Acknowledgment: The authors thank Midwestern State University and AmericaView for supporting this research. This research was funded by Midwestern State University and AmericaView. This material is based upon work supported by the U.S. Geological Survey under Grant/Cooperative Agreement No. G18AP00077 (for GY18-GY22) or G23AP00683 (GY23-GY27). We also thank Dr. Jonathan D. Price and Dr. Steven Rosscoe for their valuable suggestions and Dr. Timothy Pegg for his help with identifying tree species.

Special thanks to Kathryn Brown and Rowann Remie for their help in the field.

Conflicts of Interest: The authors declare no conflicts of interest. The funders had no role in the design of the study; in the collection, analyses, or interpretation of data; in the writing of the manuscript; or in the decision to publish the results.

References

Aram, F., Higueras García, E., Solgi, E., & Mansournia, S. (2019). Urban green space cooling effect in cities. *Heliyon, 5*(4), e01339. https://doi.org/10.1016/j.heliyon.2019.e01339

Binkley, D. (1983). Ecosystem production in Douglas-fir plantations: Interaction of red alder and site fertility. *Forest Ecology and Management, 5*(3), 215–227. https://doi.org/10.1016/0378-1127(83)90073-7

Calders, K., Newnham, G., Burt, A., Murphy, S., Raumonen, P., Herold, M., Culvenor, D., Avitabile, V., Disney, M., Armston, J., & Kaasalainen, M. (2014). Nondestructive estimates of above-ground biomass using terrestrial laser scanning. *Methods in Ecology and Evolution, 6*(2), 198–208. https://doi.org/10.1111/2041-210X.12301

Davies, Z. G., Edmondson, J. L., Heinemeyer, A., Leake, J. R., & Gaston, K. J. (2011). Mapping an urban ecosystem service: Quantifying above-ground carbon storage at a city-wide scale. *Journal of Applied Ecology, 48*(5), 1125–1134. https://doi.org/10.1111/j.1365-2664.2011.02021.x

Duncanson, L., Rourke, O., & Dubayah, R. (2015). Small sample sizes yield biased allometric equations in temperate forests. *Scientific Reports, 5*(1), 17153. https://doi.org/10.1038/srep17153

Gholz, H. L., Grier, C. C., Campbell, A. G., & Brown, A. T. (1979, April). *Equations for estimating biomass and leaf area of plants in the Pacific Northwest*. Oregon State University. https://ir.library.oregonstate.edu/concern/technical_reports/bn999796n?locale=en

Greene, T. A., Reemts, C. M., & Appel, D. N. (2008). Efficacy of basal girdling to control oak wilt fungal mat production in Texas Red Oak (*Quercus buckleyi*) in Central Texas. *Southern Journal of Applied Forestry, 32*(4), 168–172. https://doi.org/10.1093/sjaf/32.4.168

Hutyra, L. R., Duren, R., Gurney, K. R., Grimm, N., Kort, E. A., Larson, E., & Shrestha, G. (2014). Urbanization and the carbon cycle: Current capabilities and research outlook from the natural sciences perspective. *Earth's Future, 2*(10), 473–495. https://doi.org/10.1002/2014EF000255

Jenkins, J. C., Chojnacky, D. C., Heath, L. S., & Birdsey, R. A. (2004). *Comprehensive database of diameter-based biomass regressions for North American tree species* (General Technical Report NE-319). U.S. Department of Agriculture, Forest Service. https://doi.org/10.2737/NE-GTR-319

Jenkins, J., Chojnacky, D., Heath, L., & Birdsey, R. (2003). National scale biomass estimators for United States tree species. *Forest Science, 49*(1), 12–35. https://doi.org/10.1093/forestscience/49.1.12

Jiang, M., Medlyn, B. E., Drake, J. E., Duursma, R. A., Anderson, I. C., Barton, C. V. M., Boer, M. M., Carrillo, Y., Castañeda-Gómez, L., Collins, L., Crous, K. Y., De Kauwe, M. G., dos Santos, B. M., Emmerson, K. M., Facey, S. L., Gherlenda, A. N., Gimeno, T. E., Hasegawa, S., Johnson, S. N., & Känaste, A. (2020). The fate of carbon in a mature forest under carbon dioxide enrichment. *Nature, 580*(7802), 227–231. https://doi.org/10.1038/s41586-020-2128-9

Jo, H.-K., & McPherson, E. G. (2001). Indirect carbon reduction by residential vegetation and planting strategies in Chicago, USA. *Journal of Environmental Management, 61*(2), 165–177. https://doi.org/10.1006/jema.2000.0393

Krooks, A., Kaasalainen, S., Kankare, V., Joensuu, M., Raumonen, P., & Kaasalainen, M. (2014). Predicting tree structure from tree height using terrestrial laser scanning and quantitative structure models. *Silva Fennica, 48*(2), 1125. https://www.silvafennica.fi/article/1125

Kükenbrink, D., Gardi, O., Morsdorf, F., Thürig, E., Schellenberger, A., & Mathys, L. (2021). Above-ground biomass references for urban trees from terrestrial laser scanning data. *Annals of Botany, 128*(6), 709–724. https://doi.org/10.1093/aob/mcab002

Lee, A., Jordan, H., & Horsley, J. (2015). Value of urban green spaces in promoting healthy living and wellbeing: Prospects for planning. *Risk Management and Healthcare Policy, 8*, 131–137. https://doi.org/10.2147/RMHP.S61654

Mascaro, J., Litton, C. M., Hughes, R. F., Uowolo, A., & Schnitzer, S. A. (2011). Minimizing bias in biomass allometry: Model selection and log-transformation of data. *Biotropica, 43*(6), 649–653. https://doi.org/10.1111/j.1744-7429.2011.00798.x

McDonald, R. I., Kroeger, T., Zhang, P., & Hamel, P. (2019). The value of US urban tree cover for reducing heat-related health impacts and electricity consumption. *Ecosystems, 23*(1), 137–150. https://doi.org/10.1007/s10021-019-00395-5

McHale, M. R., Burke, I. C., Lefsky, M. A., Peper, P. J., & McPherson, E. G. (2009). Urban forest biomass estimates: Is it important to use allometric relationships developed specifically for urban trees? *Urban Ecosystems, 12*(1), 95–113. https://doi.org/10.1007/s11252-009-0081-3

Morales, A., & MacFarlane, D. W. (2024). Reducing tree volume overestimation in quantitative structure models using modeled branch topology and direct twig measurements. *Forestry: An International Journal of Forest Research.* Advance online publication. https://doi.org/10.1093/forestry/cpae046

Nowak, D. J. (2024). *Understanding i-Tree: 2023 summary of programs and methods* (General Technical Report NRS-200-2023). U.S. Department of Agriculture, Forest Service. https://doi.org/10.2737/NRS-GTR-200-2023

Nowak, D. J., & Crane, D. E. (2002). Carbon storage and sequestration by urban trees in the USA. *Environmental Pollution, 116*(3), 381–389. https://doi.org/10.1016/S0269-7491(01)00214-7

Rahman, M. A., Stratopoulos, L. M. F., Moser-Reischl, A., Zölch, T., Häberle, K.-H., Rötzer, T., Pretzsch, H., & Pauleit, S. (2020). Traits of trees for cooling urban heat islands: A meta-analysis. *Building and Environment, 170*, 106606. https://doi.org/10.1016/j.buildenv.2019.106606

Raumonen, P., Kaasalainen, M., Åkerblom, M., Kaasalainen, S., Kaartinen, H., Vastaranta, M., Holopainen, M., Disney, M., & Lewis, P. (2013). Fast automatic precision tree models from terrestrial laser scanner data. *Remote Sensing, 5*(2), 491–520. https://doi.org/10.3390/rs5020491

Roxburgh, S. H., Paul, K. I., Clifford, D., England, J. R., & Raison, R. J. (2015). Guidelines for constructing allometric models for the prediction of woody biomass: How many individuals to harvest? *Ecosphere, 6*(3), Article 38. https://doi.org/10.1890/ES14-00251.1

Schick, M., Griffin, R., Cherrington, E., & Sever, T. (2023). Utilizing LiDAR to quantify aboveground tree biomass within an urban university. *Urban Forestry & Urban Greening, 89*, 128098. https://doi.org/10.1016/j.ufug.2023.128098

Shadman, S., Ahanaf Khalid, P., Hanafiah, M. M., Koyande, A. K., Islam, M. A., Bhuiyan, S. A., Kok, S. W., & Show, P.-L. (2022). The carbon sequestration potential of urban public parks of densely populated cities to improve environmental sustainability. *Sustainable Energy Technologies and Assessments, 52*, 102064. https://doi.org/10.1016/j.seta.2022.102064

Tanago, J. G. de, Lau, A., Bartholomeus, H., Herold, M., Avitabile, V., Raumonen, P., Martius, C., Goodman, R. C., Disney, M., Manuri, S., Burt, A., & Calders, K. (2017). Estimation of above-ground biomass of large tropical trees with terrestrial LiDAR. *Methods in Ecology and Evolution, 9*(2), 223–234. https://doi.org/10.1111/2041-210X.12904

Tavasoli, N., Arefi, H., Samiei-Esfahany, S., & Ronoud, Q. (2019). Modelling the amount of carbon stock using remote sensing in urban forest and its relationship with land use change. *The International Archives of the Photogrammetry, Remote Sensing and Spatial Information Sciences, XLII-4/W18*, 1051–1058. https://doi.org/10.5194/isprs-archives-XLII-4-W18-1051-2019

Tigges, J., Churkina, G., & Lakes, T. (2016). Modeling above-ground carbon storage: A remote sensing approach to derive individual tree species information in urban settings. *Urban Ecosystems, 20*(1), 97–111. https://doi.org/10.1007/s11252-016-0585-6

Torresan, C., Chiavetta, U., & Hackenberg, J. (2018). Applying quantitative structure models to plot-based terrestrial laser data to assess dendrometric parameters in dense mixed forests. *Forest Systems, 27*(1), e004. https://doi.org/10.5424/fs/2018271-12658

Wilkes, P., Disney, M., Armston, J., Bartholomeus, H., Bentley, L., Brede, B., Burt, A., Calders, K., Chavana-Bryant, C., Clewley, D., Duncanson, L., Forbes, B., Krisanski, S., Malhi, Y., Moffat, D., Origo, N., Shenkin, A., & Yang, W. (2023). TLS2trees: A scalable tree segmentation pipeline for TLS data. *Methods in Ecology and Evolution, 14*(12), 3083–3099. https://doi.org/10.1111/2041-210X.14233

Wolf, K. L., Lam, S. T., McKeen, J. K., Richardson, G. R. A., van den Bosch, M., & Bardekjian, A. C. (2020). Urban trees and human health: A scoping review. *International Journal of Environmental Research and Public Health, 17*(12), 4371. https://doi.org/10.3390/ijerph17124371

Research Article

Spatial and Temporal Assessment of Meteorological Drought Using the Standardized Precipitation Index (SPI) and Its Effect on Crop Yield Over the Corn Belt Region of the United States from 2000 to 2023

Victor Araya[1], Mbongowo Mbuh[1,*], Gregory Vandeberg[1] and Jeffrey VanLooy[2]

[1] Department of Geography and Geographic Information Science, University of North Dakota, Grand Forks, USA;
[2] Earth System Science and Policy, University of North Dakota, Grand Forks, USA
* Corresponding author: mbongowo.mbuh@und.edu ; +1-701-777-4587

Abstract: Climate change and global warming have contributed to extreme weather events and patterns, including severe flooding, earthquakes, wildfires, and drought. Drought happens to be the deadliest catastrophic event around the world. Drought's impact on ecosystems and local communities has been increasing in many parts of the world, including the United States and, most importantly, the Corn Belt, which also happens to be the country's food basket. Drought prediction and mitigation can be investigated through drought indices. The standardized precipitation index (SPI) is considered the most reliable in this study. The index is the most reliable as it serves as one of the most fundamental. It is used in this study to present the critical identifier for diagnosing the intensity, duration, and frequency of drought severity. Additionally, SPI is a key identifier in extreme precipitation events. It is comparable to various landscapes across a region and is simple to use concerning its calculation process. This study focuses on the Midwest Corn Belt Region of the United States, between the climate record from 2000–2023. This study is designed to understand precipitation regimes and their impact on cropland cover and yield (condition monitoring and crop progress) over the climate record. Results of the study showed drought affecting portions of the region, especially during the first half of the period, with 2012 indicating peak severity plaguing both corn belts. Generally, pre-2012 and post-2012 indicated the wettest conditions, especially in 2010, 2014, and 2016. While cropland cover highlighted the widespread distribution of corn and soybean cover in both Corn Belts, crop condition and progress corresponded and responded well to low yields during the intense drought years and high yields during the wettest years. Our analysis shows that climate change has undoubtedly resulted in a temperature rise, exacerbating the frequency and severity of heat waves and extreme precipitation events impacting parts of the United States, including the Corn Belt.

Keywords: meteorological drought, Corn Belt region, drought indices, standardized precipitation index (SPI), climate change

Academic Editor: Jeong Chang Seong
Received: 15 August 2025
Revised: 22 September 2025
Accepted: 30 September 2025
Published: 24 October 2025

Citation: To be added by editorial staff during production.

1. Introduction

Studies worldwide have indicated that the global climate has resulted in changes in temperature and rainfall patterns, with many areas experiencing increasing global air temperatures. These projections are expected to continue to increase over the next 90 years in many parts of the world, as evidenced by global climate projection models (GCMs) (de Oliveira-Júnior *et al.*, 2025; Liu *et al.*, 2013; Sakellariou *et al.*, 2024; Shrestha *et al.*, 2020) This could result in a lower reduction of water supplies from increased evaporation rates, as evidenced by rising temperatures (Liu *et al.*, 2013; Sakellariou *et al.*, 2024). In addition, ocean-atmosphere projections predict that wetter regions will become wetter and drier regions will become drier (Shrestha *et al.*, 2020). Research on multiple climate processes has theoretically become socially and economically valuable. Drought is a continuous and temporary state of precipitation deficit, leading to a

Citation: Araya, V., Mbuh, M., Vandeberg, G., & VanLooy, J. (2025). Spatial and temporal assessment of meteorological drought using the standardized precipitation index (SPI) and its effect on crop yield over the Corn Belt region of the United States from 2000 to 2023. *Journal of Earth Observation and Geospatial Applications, 1*(1), 108–128. DOI: https://doi.org/10.65372/8h4pbf47

reduction in water supplies, encompassing a larger area and extended period over time (Tsiros *et al.*, 2020). Drought has drawn the attention of environmentalists, meteorologists, hydrologists, geologists, and agricultural scientists, as it is recognized as an environmental hazard (Mishra & Singh, 2010). As the climate changes, drought will challenge and amplify societal demands due to water stress, food insecurity, and, most critically, impacting national economies. In population growth, industry, energy, and agriculture sectors, water availability has often exceeded demand in many regions worldwide (Liu *et al.*, 2013; Mishra & Singh, 2010). Drought affects each of these sectors globally. The impacts of drought are highly synchronized across society, the environment, and the economy (Meresa *et al.*, 2023; Tsiros *et al.*, 2020). As a result, research indicates that climate variability will likely increase hydrological and meteorological droughts shortly *(*Meresa *et al.*, 2023). Moreover, climate change has influenced drought and precipitation events, leading to demands in agriculture, livestock practices, and excessive runoff, which is likely to occur in the future. As the severity and frequency of droughts increase, mitigation and adaptation strategies will be essential to support economic stability by ensuring adequate water supply during future droughts (Shiru *et al.*, 2019).

The frequency and severity of drought have increased across many regions worldwide (Sharafati *et al.*, 2020). Severe drought strongly influences the carbon cycle over lush climates such as tropical rainforests. For example, if the Amazon climate experiences more severe droughts under the influence of warming temperatures, it would potentially shift the Amazon climate into a new climate phase. Many portions of southeast Amazonia could be replaced by Savanna-like climates, influencing drier and warmer climates. Furthermore, some models suggest that there may be an increase in air temperature, which may influence increased carbon emissions, further accelerate forest degradation, and result in significant losses of carbon stocks (Duffy *et al.*, 2015). Further north, in the United States, there has been an increase in the severity and frequency of drought, particularly in the southwest United States, at the start of the 21st century. States impacted include Arizona, California, Colorado, New Mexico, and Utah. In spring 2022, Lake Mead and Lake Powell experienced their lowest levels. These impacts have led to landscape and ecosystem aridification. Furthermore, (Wahl *et al.*, 2022) presented that climate simulations have projected wetter climates in the northern latitudes, while southern latitudes in the subtropical regions will become drier (i.e., American Southwest). However, the exact locality for areas receiving more or less precipitation is uncertain.

Between 2000 and 2018, the United States experienced growing demand for agricultural output including both crop yields and livestock production, which has been accompanied by a decline in overall agricultural losses. These agricultural losses are related to a loss in crop production and profitability, especially in drought stricken regions like the southwest and Midwest. In the United States, the first 18 years of the 21st century have witnessed crop yield demand and livestock leading to reduced agricultural losses. This assessment shows crop loss has yielded over a billion dollars, with an adjusted average loss of 6.97 billion dollars and 26 heat-related deaths yearly (Leeper *et al.*, 2022). From 1989–2009, the loss contributed to 17.33 billion dollars worldwide, while the average annual loss experienced an increase of 23.125 billion dollars, far exceeding the costliest disaster of any other meteorological disaster (Wang *et al.*, 2022). From these projections, droughts are expected to become more prolonged, frequent, and severe (Li *et al.*, 2020; Shrestha *et al.*, 2020). Understanding drought characteristics is essential as it provides key information for forecasting and identifying drought. Strategies and procedures are developed to allow policy makers and stakeholders to adapt practices for resilience. This has further aided the community to learn practices to further building preparedness and response efforts to climate change. (Li *et al.*, 2020). Successful mitigation strategies and planning can be organized through best practices of interactions and coordination between local, state, regional, and national stakeholders. Specifically, these entities can provide mitigation and adaptation strategies based on historical drought (Leeper *et al.*, 2022). A drought is a non-preventable hazard, but drought resilience strategies can be implemented in response to drought hazards. The spatial and temporal characteristics are crucial for managing drought impacts and risks. Drought is a spatio-temporal process commonly characterized by its duration, intensity, and spatial extent on a regional scale (Hosseini *et al.*, 2021). Communities can practice resilience and preparedness by understanding a drought's origin, evolution, and behavior, which influence a community's economic development and well-being. Drought is linked to the deficit and decline in rainfall in a given time sequence of a season or year, and can occur in both low or high-rainfall regions (Mishra & Singh, 2010; Wilhite & Glantz, 1985). Drought is a widespread climatic event that can negatively impact agriculture productivity (cropland and rangeland) and ecological biodiversity which can lead to food insecurity by reduced surface and ground water supply used for hydropower and irrigation (Meresa *et al.*, 2023). Reduced water supply also interferes recreational water use affecting many economic and social activities (Mishra & Singh, 2010). The impacts of drought are most significant in water-stressed communities. Drought's implications regarding water quality, human health, and

critical infrastructure are less understood, which can result in indirect societal effects such as loss of electricity or industrial cooling. These communities are likely to become more vulnerable as populations in water-scarce environments grow, and the demand for water from agriculture, energy, and industry rises (Leeper *et al.*, 2022).

The Midwest is home to an agriculturally intense region that is home to one of the most essential crop commodities in the world, corn. Drought has been increasing over many parts of the world, including the United States. Understanding drought impacts on a region, such as the Corn Belt, is essential as it identifies the spatial and temporal assessment of drought, allowing this research to fill in the gap for understanding drought and its influence on crop yield. Drought is difficult to quantify, which can lead to uncertainty. Furthermore, drought is highly complex and may vary from region to region. And while one area within the region may be experiencing drought, another area may not experience drought at all. Even so, many communities have their own holistic approach for identifying drought impacts related to the demand of resources and its impact on the economy. Numerous drought indices have been developed to account for this uncertainty using rainfall, snowpack, streamflow, and other water supply indicators to provide comprehensive picture (Liu *et al.*, 2013). For example, the standardized precipitation index (SPI) and the standardized precipitation evapotranspiration index (SPEI) are excellent indices for identifying meteorological drought. (Acharki *et al.*, 2023; Li *et al.*, 2020; Stagge *et al.*, 2015). In addition, there are other remote sensing derived indices including enhanced vegetation index (EVI), evaporative stress index (ESI), normalized difference vegetation index (NDVI), vegetation condition index (VCI), temperature condition index (TCI), vegetation drought response index (VegDRI), vegetation health index (VHI), normalized difference water index (NDWI), land surface water index (LSWI), as well as soil adjusted vegetation index (SAVI), Palmer drought severity index (PDSI), standardized anomaly index (SAI), soil moisture anomaly (SMA), Palmer Z Index, aridity index (AI), and combined drought indicator (CDI) (Acharki *et al.*, 2023; Ayugi *et al.*, 2022). Monitoring meteorological drought has also been done using the PDSI , SPI, and SPEI (Sharafati *et al.*, 2020; Sun *et al.*, 2023). Some indices present unique strategies over other indices. In this study, we evaluate the processes of precipitation regimes and drought severity using the Standardized Precipitation Index of the Midwest Corn Belt Region, USA. This index can help us understand the effects of wet and dry regimes across different climate zones within a region. This index can also help us understand how these drought conditions impact one of the world's most populous crops (corn and soybeans) by presenting patterns and trends related explicitly to crop yield and production within the corn belt region, as will be assessed by this index. The study will also aid us in understanding the relevance of these impacts from the beginning of the 21st century to the most recent period of the climate record. Together, this research can aid in developing mitigation and adaptation plans designed for these agricultural communities in preparation for future drought impacts.

2. Study Area and Methods

2.1. Study Area

The Midwest Corn Belt is located along the heartland of the United States, extending from the central and northern Great Plains into the Upper Midwest (Ort & Long, 2014; Panagopoulos *et al.*, 2015; Suyker & Verma, 2012) (Figure 1). This region can be described through the five different physiographic regions from west to east: the Great Plains, Central Lowlands, the Ozark, and the Driftless Area. The Corn Belt is defined as the region from the Great Plains stretching eastward towards the Central Lowlands that intersects the Ozark to the south and Driftless Areas to the north. The remainder of the provinces to the east are along the southern and eastern portions of the region, making up the northern portions of the Ohio River Valley: Ozark Plateaus, Coastal Plain, Interior Low Plateaus, and Appalachian Plateaus (Fenneman, 1917). Ten states define the Midwest Corn Belt. These include the states of North Dakota, South Dakota, Nebraska, Iowa, Minnesota, Wisconsin, Illinois, Indiana, Michigan, and Ohio. The study area can be divided into two sub-regions: the Eastern Corn Belt and the Western Corn Belt. The Eastern Corn Belt comprises Wisconsin, Illinois, Indiana, Michigan, and Ohio (Auch *et al.*, 2013). The Western Corn Belt comprises North Dakota, South Dakota, Nebraska, Iowa, and Minnesota. Two major river systems divide the region, tangent to one another, known as the Mississippi River and the Ohio River. The headwaters of the Mississippi River are located in Minnesota, and the Illinois flows southward towards Iowa and Illinois. Further south, the Ohio River meets the Mississippi River in Illinois and flows eastward towards southern Ohio. Interestingly, this region is native to the provinces that make up the valley of the Ohio River in the Eastern Corn Belt (Figure 1).

In the Western Corn Belt, the climate of the Great Plains is assessed by its geographic position within North America. Precipitation decreases drastically from southeast to northwest. Annual precipitation ranges from more than 32 inches in southeast Iowa to less than 16 inches in western portions of North Dakota. Annual temperature extremes show the January average temperature ranges from −5 degrees Fahrenheit in Northwest Dakota to 15 degrees Fahrenheit in southeast Nebraska and southern Iowa. Normal daily maximum temperatures in July range from values more than 90 degrees Fahrenheit in southern portions of Nebraska to around 70 degrees Fahrenheit in northeast Minnesota (Rosenberg, 1987). In the Eastern Corn Belt, the climate is maintained by factors including latitude, continental location, large-scale circulation, and the presence of the Great Lakes. Average annual temperatures from 1980–2010 range from 40 degrees Fahrenheit in the North Shore and Upper Peninsula to 55 degrees Fahrenheit in southern Illinois and Indiana. Average winter temperatures from DJF range from 10 degrees Fahrenheit in northern Wisconsin to 30 degrees Fahrenheit in southern Illinois, Indiana, and Ohio. DJF refers to climatological season winter months of December, January, February (Chen *et al.*, 2024). Total annual precipitation ranges from 25 inches in the north of Michigan to as much as 45 inches in the southern portions of Illinois, Indiana, and Ohio. Summertime precipitation in JJA has annual maximum rainfall from the western portions of Wisconsin and minimum precipitation along Michigan's upper peninsula. Refer to Figure 1 below.

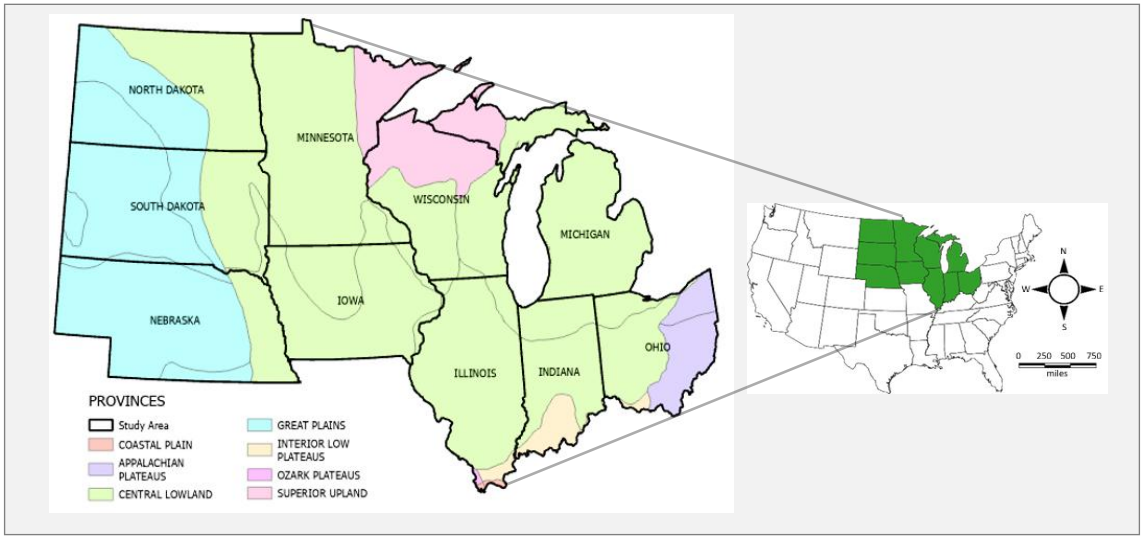

Figure 1. Study area. Corn Belt Region Provinces. The map shows provinces from west to east along the Western and Eastern Corn Belt; Great Plains, Coastal Lowland, Superior Upland, Ozark Plateau, Coastal Plain, Interior Low Plateaus, and Appalachian Plateaus. Credit by Esri.

2.2. Data

The data used for this study include CHIRPS (Climate Hazards Group InfraRed Precipitation with Station Data) which provides precipitation data from 1981 such as UCSB-CHG/CHIRPS/DAILY (or monthly), GridMET Drought dataset, cropland cover data, yield data, and crop condition/progress monitoring datasets (Funk *et al.*, 2015). The CHIRPS dataset was adopted by the U.S. Geological Survey (USGS) and the University of California at Santa Barbara to provide global precipitation at high spatial resolutions. These were set at resolutions of 0.05 degrees and 0.25 degrees, providing precipitation data from 1981 to the present (de Oliveira-Júnior *et al.*, 2021; Du *et al.*, 2024; López-Bermeo *et al.*, 2022). Cropland cover data was used to analyze and create the maps for cropland cover for the years in the climate record (Han *et al.*, 2012). Yield data from USDA NASS crop statistics were used to aid in calculating cropland cover for the crop types designed to quantify measured crop types in Bushels per hectare over the entire region. Crop condition/progress was used to create a condition progress table to indicate the percentage of crop cover compared to drought/wetness years (Boryan *et al.*, 2011). All the data used for this research were accessible via Google Earth Engine.

2.3. Methods

The standardized precipitation index is widely used to assess meteorological drought on various timescales. This precipitation data is typically distributed as a Pearson Type III or gamma distribution and is lastly categorized into a normal distribution as this is demonstrated in Eqs 7&8 (Schneider *et al.*, 2013). We demonstrate how the SPI equation works in the following paragraph.

The first step in presenting the calculation of the SPI is to assess a probability density function that describes the long-term series of observations (Eq. 1–4). Second, the cumulative probability of an observed precipitation amount is computed once the distribution is examined. The inverse normal (Gaussian function) is then processed to the likelihood, which defines the SPI. The values of SPI are positive (negative) for greater (less) than the median precipitation. The departure from zero results in a probability of the severity of wetness or aridity that can be used for risk assessment. Following these steps from (Guttman, 1998; Guttman, 1999), the gamma distribution as in (Eq.1) (defined by (Angelidis *et al.*, 2012; Bouaziz *et al.*, 2021; Liu *et al.*, 2021; Lloyd-Hughes & Saunders, 2002; Sönmez *et al.*, 2005) can be described as follows:

$$g(x) = \frac{1}{\beta^{\alpha}\Gamma(\alpha)} x^{\alpha-1} e^{-x/\beta} \tag{1}$$

$\alpha > 0$	α	is a shape parameter.
$\beta > 0$	β	is a scale parameter.
$x > 0$	x	is the precipitation amount.
$\Gamma(\alpha) = \lim_{n\to\infty} \prod_{v=0}^{n-1} \frac{n! n^{y-1}}{y+v} \equiv \int_0^{\infty} y^{\alpha-1} e^{-y}\, dy$	$\Gamma(\alpha)$	is the gamma function.

where $G(x)$ It is the average likelihood of the data series being converted into an incomplete gamma distribution. According to (Lloyd-Hughes & Saunders, 2002), $\Gamma(\alpha)$ It is a unique arithmetic approach that expands on the implication leading to the final equation.. To fit the distribution, the parameters of α and β need to be estimated. Therefore, these parameters are calculated for each station, for each time scale of interest (3 months, 12 months, 48 months, etc.), and for each month of the year. This process can be examined as follows:

$$\alpha = \frac{1}{4A}\left(1 + \sqrt{1 + \frac{4A}{3}}\right) \tag{2}$$

$$\beta = \frac{\bar{x}}{\widehat{\alpha}} \tag{3}$$

For n observations, we have

$$A = \ln(\bar{x}) - \frac{\sum \ln(x)}{n}. \tag{4}$$

Integrating the probability distribution function (Eq 5) concerning x and inserting the estimates of α and β gives an expression for the cumulative probability G(x) for an observed amount of precipitation occurring for a given month and time scale.

$$G(x) = \int_0^x g(x)\, dx = \frac{1}{\widehat{\beta}^{\widehat{\alpha}}\Gamma(\widehat{\alpha})} \int_0^x x^{\widehat{\alpha}} e^{-x/\widehat{\beta}}\, dx \tag{5}$$

which can be expressed as the incomplete Gamma function. As the gamma function is undefined at x = 0 and a precipitation distribution may contain zeros, the cumulative probability becomes:

$$H(x) = q + (1 - q)G(x) \tag{6}$$

Statistically, $q = P(x = 0) > 0$ where $P(x = 0)$ It is the probability of zero precipitation (Eq 6). The cumulative probability distribution is converted into the standard normal distribution to yield the SPI (Eqs 9-11). Moreover, it can be transformed into the standard normal random variable Z with mean zero and variance

of one, which is the value of the SPI. The Z or SPI value in Eq 7&8 is more easily obtained computationally using an approximation designed by (Bouaziz *et al.*, 2021; Lloyd-Hughes & Saunders, 2002), which converts the cumulative probability to a standard normal random variable Z as follows:

$$Z = SPI = -(t - \frac{t - C_0 + C_1 t + C_2 t^2}{1 + d_1 t + d_2 t^2 + d_3 t^3}) \quad \text{for } 0 < H(x) \leq 0.5 \tag{7}$$

$$Z = SPI = +(t - \frac{t - C_0 + C_1 t + C_2 t^2}{1 + d_1 t + d_2 t^2 + d_3 t^3}) \quad \text{for } 0.5 < H(x) < 1 \tag{8}$$

Where t is given as

$$t = \sqrt{\ln\left[\frac{1}{(H(x))^2}\right]} \quad \text{for } 0 < H(x) \leq 0.5 \tag{9}$$

$$t = \sqrt{\ln\left[\frac{1}{(1 - H(x))^2}\right]} \quad \text{for } 0.5 < H(x) < 1 \tag{10}$$

$$C_0 = 2.515517 \qquad C_1 = 0.802853 \qquad C_2 = 0.010328 \tag{11}$$

$$d_1 = 1.432788 \qquad d_2 = 0.189269 \qquad d_3 = 0.001308$$

For crop yield, the data was calculated to represent bushels of total production as the first method for the analysis. First, the raster layer is 30 meters by 30 meters in spatial resolution. The total area in resolution is 900 m^2. To find the location in acres, square meters were converted to acres to get the total area in acres. Lastly, the total area (acres) and crop yield data were converted to bushels per acre to get the overall production in bushels per acre using the equation below. These calculation steps were applied for Corn and soybean crops individually, and then all crop types combined. The resolution of the dataset was 30 m. The total area of the dataset was 900 m. The total length of the pixel was given in meters (m). The total resolution area was multiplied by the pixel length to get the total area in acres.

- Resolution = 30 m
- Area
  - 30 m * 30 m = 900 m^2
  - Count * 900 m^2

Next, the total area is converted from m^2 to acres as follows:

- Area (Ac)
  - Area m^2 * 0.000247 $\frac{Ac}{m^2}$
- Total production (BU)
  - Area (Ac) * Yield * ($\frac{BU}{Ac}$) = Total Production (BU)

The first step introduces the resolution of the dataset that is represented in m^2. The second calculation process represented three different quantities of crops. While the above equation indicates the calculation for total production (BU), the analysis was conducted in a modified format. The first and second crop types in this research are corn and soybeans. The last quantity is the sum of all crop types, in addition to corn and soybeans, that make up the entire Corn Belt. The overall production was represented in finalized units. m^2. Corn, soybeans, and all crops were categorized accordingly, placing each in a pie chart for each year to represent these quantities. Crop condition and crop progress were the second methods used for the analysis. Even though this step is part of the calculation process, it will not be treated as the calculation. In this procedure, there are three rows. The first graph shows good, excellent crop progress and conditions (Figure 2 on next page). The second graph represents the percentage or type in each condition category (excellent, good, fair, poor and very poor). The third graph represents the progress percentage (planted, emerged, silking, dented, matured, etc.). For this research, we will stick to the first row. The condition progress is recorded for each type of crop. The colored line represents the time series for the first five years. The lines run from April to October. At the end of each line, the crop progress is processed in a table. On the right side is a list of all

crops grown from January to December. As observed, all crops are harvested from May to September, as denoted in Figure 2b. The first part of the figure is the crop time series. The second part is seasonal crops (Figure 2).

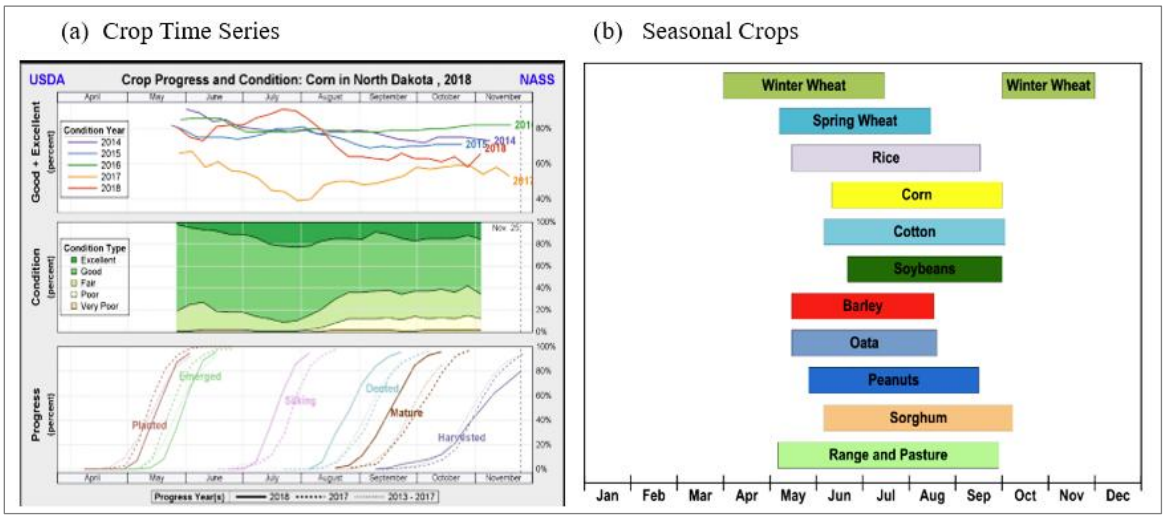

Figure 2. (a) Crop progress and condition grown in ND, 2018, of condition year (1st graph), percent by condition type (2nd graph), and average. Plant growth stage across the growing period (3rd graph) and (b) Seasonal crops of annual variation of crop types grown in the U.S. Credit by USDA.

3. Results and Discussion

This study provides a detailed assessment of drought variability across the Corn Belt, examining its spatial and temporal patterns over more than twenty years. Using the standardized precipitation index, clear distinctions are made between periods of extreme, severe, moderate, and non-significant drought. These classifications reveal how dry and wet conditions shift over time and also show how drought severity directly affected crop yields for corn and soybeans throughout the region. The analysis shows that drought years often led to significant drops in crop productivity, while years without drought generally resulted in higher-than-average yields. The results are discussed in two parts. Section one discusses the relationship between wet and dry conditions over the region using the SPI index (Mishra & Singh, 2010; Wilhite & Glantz, 1985). Section two discusses the wet and dry conditions and their influence on crop yield (Green *et al.*, 2018; Mishra & Singh, 2010; Wilhite & Glantz, 1985). The results can be discussed using the drought classification: extreme, severe, moderate and no significant drought. All five of these classes are distributed through the years over the entire climate record. The second section discusses these classifications using the cropland cover and crop quantities (crop yield assessment) and crop harvest and progress affected directly by these drought classifications. For assessing crop yield impacted by drought, values from crop progress and condition (Figure 2a) were interpolated onto a table represented in 3.2 of this chapter. Threshold levels were used to assess each crop yield class impacted by each classification of drought. The following thresholds are defined as follows: extreme drought (35 percent or less), severe drought (40 percent or less), and moderate drought (45 percent or less). Non-significant drought differs. It is used to describe much of the region, including all states, that was under an area that indicated no drought. Therefore, to make the classification more specific and consistent with the results, threshold levels were defined as above average (60–79 percent) and well above average (80 percent or greater). These two thresholds were defined as productive (above average) or extremely productive (well above average) thresholds. These thresholds were used based on the statistical probability at which these values corresponded to on each drought classification.

3.1. Relationships Between Wet and Dry Conditions Over the Corn Belt Region Over 20 Years

In 2012, major drought coverage extended in the Eastern and Western Corn Belt regions. Widespread

extreme dry conditions extended from Nebraska and South Dakota, spreading eastward to Ohio and Michigan (Figure 3a). Widespread extreme conditions dominated most of these states, with Nebraska and South Dakota representing a much larger area of widespread extreme dryness (Shrestha *et al.*, 2020). In the East Corn Belt, widespread extremely dry conditions were observed in Wisconsin, Indiana, and portions of Ohio (Auch *et al.*, 2013; Mishra & Singh, 2010; Wilhite & Glantz, 1985). Portions of Illinois and Michigan also indicated extreme conditions, but these conditions were not as widespread as in these other states (Figure 3).

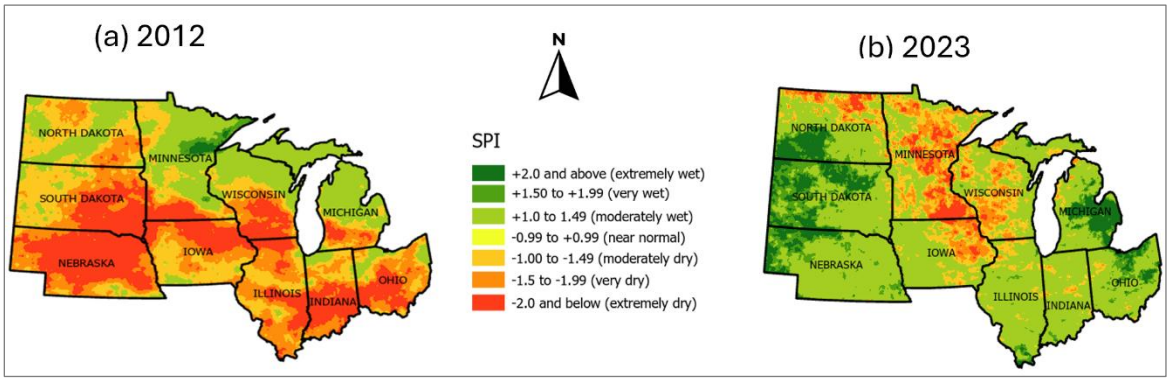

Figure 3. Extreme dryness (−2.0 and below) over the entire corn belt; (a) 2012; (b) 2023. Figure representing the region that represented extreme dryness during the years of extreme drought. Displayed using the SPI index.

In 2023, numerous pockets of severe to extreme dryness were observed along a diagonal extending from North Dakota into sections of Iowa and Wisconsin (Ort & Long, 2014; Panagopoulos *et al.*, 2015; Suyker & Verma, 2012) (Figure 3b). Many states indicated frequent pockets of these drought episodes, especially in Minnesota, where severe to extreme dry pockets were present in numerous places across the region (Meresa *et al.*, 2023).

The intensity and coverage of severe droughts were the greatest, especially in 2002 and 2006, along the Western Corn Belt. Despite severe conditions in the eastern states in 2011, 2002, and 2006 experienced numerous and widespread impacts. Impacts were mainly along the west and east corn belt in 2002, with 2006 indicating severe impacts along the Dakotas and into Minnesota.

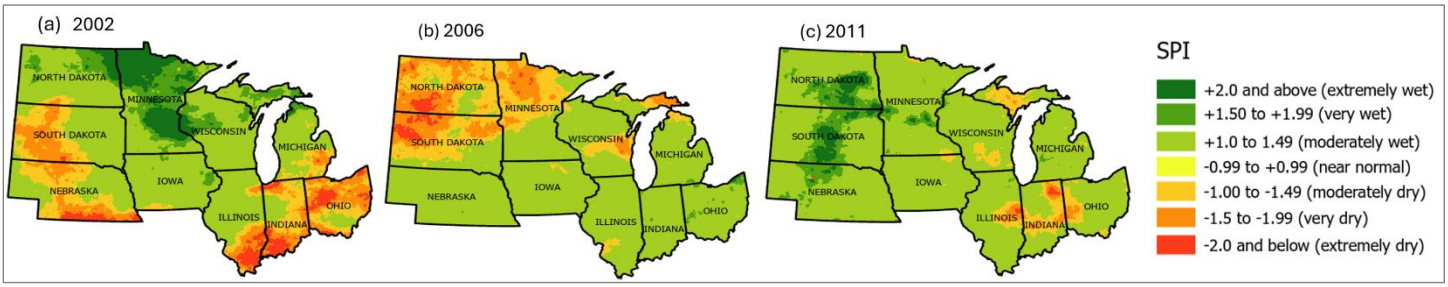

Figure 4. Severe dryness (−1.5 to −1.99) over the entire corn belt; (a) 2002, (b) 2006, (c) 2011. Figure representing the region that represented severe dryness during the years of severe drought. Displayed using the SPI index.

In 2002, drought conditions were observed from the North Dakota border and into South Dakota, stretching southward towards Nebraska (Figure 4a). Moderately arid conditions were along the northern portion of this boundary, especially in South Dakota (Meresa *et al.*, 2023; Mishra & Singh, 2010). Going southward, conditions worsened from severe to extreme, especially along the Nebraska border (Shrestha *et al.,* 2020).

In 2006, severe to extreme dryness was observed, especially along the western portions of the Dakotas, extending into Minnesota along the northern portion of the state (Figure 4b). Coverage was widespread along this region of the west belt, especially along the western sections of the Dakotas. Here, severe dryness was numerous with some sections indicating extreme dryness. In moderate drought years, 2013 and 2021 experienced numerous and widespread coverage of severe drought throughout most of the region *(*Meresa *et*

al., 2023; Mishra & Singh, 2010; Wilhite & Glantz, 1985). While 2013 was the greatest drought year recovering from the 2012 major drought, impacts were still widespread in coverage and intensity throughout the entire region, especially along the southern corn states (Auch *et al.*, 2013; Meresa *et al.*, 2023). Drought coverage extended from Nebraska and stretched into Indiana (Figure 5b). Conditions of severe dryness, with some pockets of extreme dryness, were observed, especially in Illinois (Figure 5).

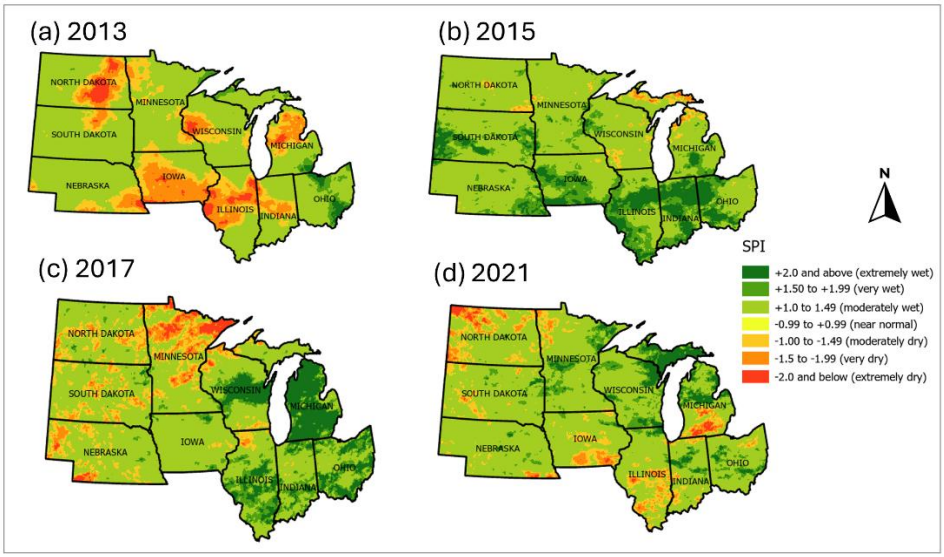

Figure 5. Moderate dryness (−1.00 to −1.49) over the entire corn belt. (a)2013, (b) 2015, (c) 2017, (d) 2021 Figure representing the region that represented moderate dryness during the years of moderate drought. Displayed using the SPI index.

The year 2021 indicated drought impacts mainly along the west corn belt, but in numerous pockets, with drought increasing northeastward towards the Superior Northland, sustaining the most significant impacts (Leeper *et al.*, 2022; Mishra & Singh, 2010; Sakellariou *et al.*, 2024). Moreover, while the Eastern Corn Belt indicated wetness, the Western Corn Belt showed significant dryness impacts (Figure 5d). Much of the Great Plains extending northeast to northland shore regions encompassed a greater expanse of dryness, especially near the northland shore, where more widespread dryness was observed (Shrestha *et al.*, 2020). The Great Plains experienced pockets of dryness from Nebraska to North Dakota (Ort & Long, 2014; Panagopoulos *et al.*, 2015; Suyker & Verma, 2012). Pockets were scattered throughout these states, especially towards the west. Specifically, the southwest border of Nebraska experienced patches of intense and severe impacts along this subregion of the Western Corn Belt (Auch *et al.*, 2013). Regionally, dryness increased from southwest to northeast, where much of Minnesota's north shore had the most significant impacts along the northeast corner of Lake Superior and into the border of Canada. While 2015 and 2017 indicated impacts from drought, they were not as extreme as the other years described. In 2003, much of the Western and Eastern Corn Belt exhibited moderately wet conditions despite spotty sections of drought in western sections of the Dakotas and eastern Nebraska (Figure 6a). In 2004, moderate wetness was much more widespread than in the previous year, and it was prominent in both Corn Belts (Figure 6b). Drought remained in northern sections of the region (Figure 6).

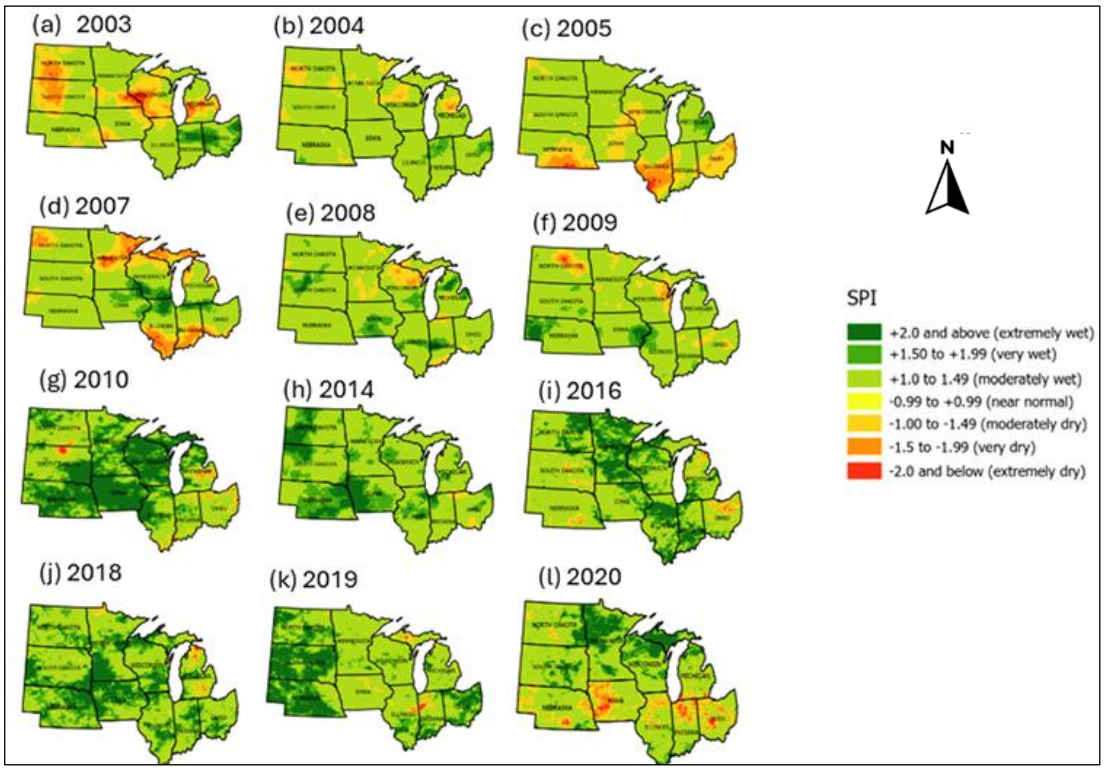

Figure 6. No significant drought. Near normal (–0.99 to +0.99), moderately wet (+1.0 to 1.49), very wet (+1.50 to +1.99), and extremely wet (+2.0 and above). (a) 2003; (b) 2004, (c) 2005; (d) 2007; (e) 2008; (f) 2009; (g) 2010; (h) 2014; (i) 2016; (j) 2018; (k) 2019; (l) 2020. Figure representing the region that represented near-normal to extreme wetness during the years of non-drought. Displayed using the SPI index.

In 2005, widespread moderate wetness conditions were observed along the northern half of both corn belts. Very wet conditions can be observed over eastern Michigan while southern sections of the region remained in drought (Liu *et al.*, 2013; Sakellariou *et al.*, 2024; Shrestha *et al.*, 2020). In 2007, widespread drought-free conditions were observed in the region's interior, with excessive wetness increasing towards the middle (Figure 7d). Here, a section of excessive wetness can be observed overlapping the Western and Eastern Corn Belt Regions, extending towards the eastern states of the Eastern Corn Belt Region (Auch *et al.*, 2013). In 2008, widespread drought-free conditions were observed throughout the region, especially towards the west, where drought improved along Lake Superior's northland region and the Ohio Valley (Figure 6e). Widespread wet conditions were observed along the Western Corn Belt, especially in the western states of the Great Plains. Much of the region experienced moderate to severe wet conditions along the Eastern Corn Belt. Severe wetness was along sections of southeast Wisconsin, southern sections of Illinois and Indiana, and northern Michigan. While drought conditions have shown significant improvement along Northland Superior and the Ohio Valley, widespread moderate wetness was dominant throughout the region. Overall, pockets of severe to excessive wetness were scattered throughout the region (Leeper *et al.*, 2022; Meresa *et al.*, 2023). In 2009, moderate wetness conditions dominated much of the landscape, especially the Western Corn Belt Region, where severe to extreme wetness was present along the panhandle of Nebraska and southeast sections of Iowa (Figure 6f). Drought conditions improved along the northern Great Lakes. In 2010, much of the region experienced widespread extreme wetness conditions, making it the wettest year in this drought-free group, especially along the Western Corn Belt (Meresa *et al.*, 2023; Mishra & Singh, 2010; Ort & Long, 2014; Panagopoulos *et al.*, 2015; Suyker & Verma, 2012). This pattern was extended from the southern Great Plains into the northern Great Lakes Region, putting a significant dent in the drought in this area. While the Eastern Corn Belt exhibited wet conditions, especially in the western states, this region was not as intense. Moderate wetness was the main culprit along the eastern portions of the area. While 2014 and 2016 experienced widespread wetness intensity, they were not as widespread as 2010. In 2014, much of the region experienced a drought-free year, with many areas indicating moderate wetness (Wilhite & Glantz, 1985). Severe to extreme wetness was noted along the western portion of the Dakotas and southern sections of the Western Corn Belt (Nebraska and Iowa). In 2016, both belts also experienced moderate wetness (Figure

6i). A boundary of extreme wetness was observed dividing this line, which could be extended from the Ohio Valley and into the northern Prairie Pothole region states (Ort & Long, 2014; Panagopoulos *et al.*, 2015; Suyker & Verma, 2012). This was a diagonal of intense wetness covering most of the region, which extending from North Dakota, stretching southeastward towards Illinois and Indiana. Similar to 2016, 2018, and 2019 experienced widespread moderate wetness with excessive wetness along the Great Plains into much of the Prairie Pothole states and sections of Indiana and Ohio (Auch *et al.*, 2013). Conditions were not as intense as receding years, but still indicated pockets of severe to extreme wetness along these areas (Figures 6j & 6k).

3.2. Impact of Drought Conditions on Crop Yield in the Region

In the extreme drought years, corn and soybeans represented widespread distribution throughout the region, originating from North Dakota down into Nebraska and extending eastward towards Illinois, Indiana and Ohio (Brandes *et al.*, 2016; Green *et al.*, 2018; Ort & Long, 2014; Panagopoulos *et al.*, 2015; Peña-Gallardo *et al.*, 2019; Prince *et al.*, 2001; Suyker & Verma, 2012; Wilson *et al.*, 2022)(Figures 7a & 7b).

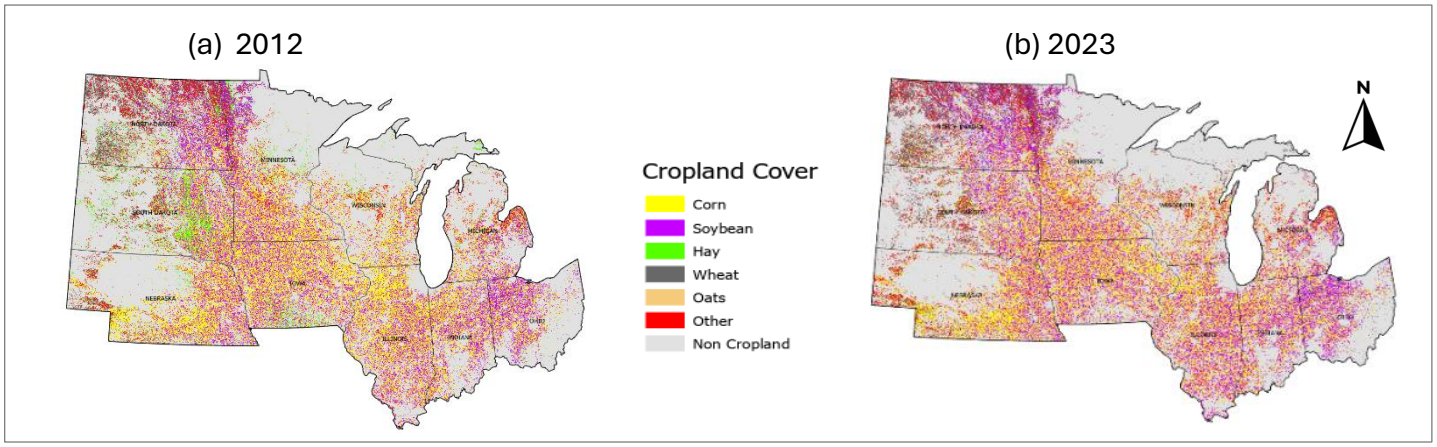

Figure 7. Cropland cover of extreme drought years. Figure describing corn, soybean, hay, wheat, oats, and other cropland over the Corn Belt Region. (a) 2012 crop cover, (b) 2023 crop cover. Crop cover is not a measure of drought impacts but of crop rotation, plantations, and depletion.

Regarding the drought impacts, crop yield experienced very low levels for both crops, especially for corn yield. These threshold levels as defined in introduction of this chapter most impacted the Eastern Corn Belt. Crop production and harvest of corn were low for the following states: Nebraska, Iowa, South Dakota, Illinois, Wisconsin, Indiana, Michigan, and Ohio (Green *et al.*, 2018; Liu *et al.*, 2013). Corn was exceptionally low, and the lowest crop progress was 30% or less in some states over other years, especially for Iowa, South Dakota, Illinois, Indiana, Michigan, and Ohio, with Illinois representing the lowest production and harvest (Fadhli *et al.*, 2020; Green *et al.*, 2018). As for soybeans, threshold levels were not as low, but some states indicated below threshold levels (Prince *et al.*, 2001). These states included Nebraska, South Dakota, Wisconsin, and Illinois. Nebraska represented the lowest threshold level. (Table 1). Corn and soybean quantities were less in the year, 2023 (Figure 8). While these quantities were less for this year corn still indicated a greater quantity than soybeans (Green *et al.*, 2018; Leeper *et al.*, 2022). In 2023, corn and soybean quantities were larger than in the preceding year.

Table 1. Crop production thresholds of extreme drought. Table 1 describes the impacts of corn and soybeans for the years impacted by extreme drought in the Corn Belt Region. The table demonstrates the impacts of drought on crop yield.

Year	Nebraska	Iowa	South Dakota	North Dakota	Minnesota	Illinois	Wisconsin	Indiana	Michigan	Ohio
Corn										
2012	32	20	25	57	59	7	36	12	27	16
2023	51	51	48	57	40	55	53	68	47	87
Soybean										
2012	23	32	27	-	60	40	26	27	39	36
2023	40	51	45	-	44	48	60	67	48	81

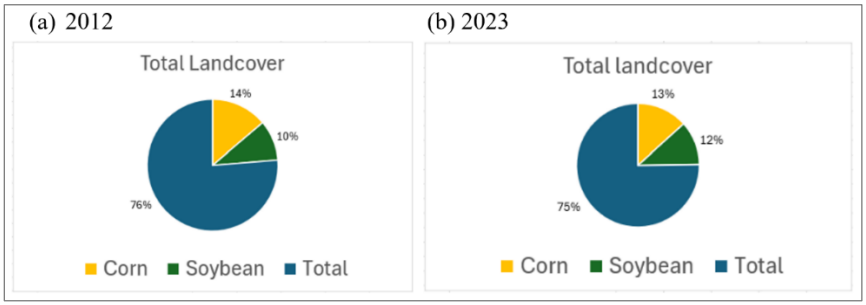

Figure 8. Total landcover distribution of extreme drought years. Crop quantities of corn (orange), soybean (green), and total overall crop distribution of the Corn Belt Region. Not a reflection of drought impacts. Credit by CropScape.

During the severe drought years, corn and soybeans were distributed throughout the southern states (Green *et al.*, 2018). The prevalence of crop diversity (other crops) blended in, especially during the earlier periods (2002 and 2006), but then decreased towards 2011. Oats were also introduced, especially during the beginning period (2002), and have since risen throughout the period (2006 and 2011). Soybean concentrations were also prevalent, especially in the eastern states. Crop cover is not a measure of drought impacts but of crop rotation, plantation, and depletion. (Figure 9). For drought impacts, 2011 indicated minimal impacts. And 2002 experienced the lowest yields for both crops, especially in the Eastern Corn Belt, with soybean indicating the lowest yield in Ohio of around 12%. While soybeans were also impacted, low corn yield was much more frequent for these states (Indiana and Ohio). These quantities ranged from 13–35% harvest. While 2006 and 2011 experienced low levels, they were less impactful than 2002 (Table 2).

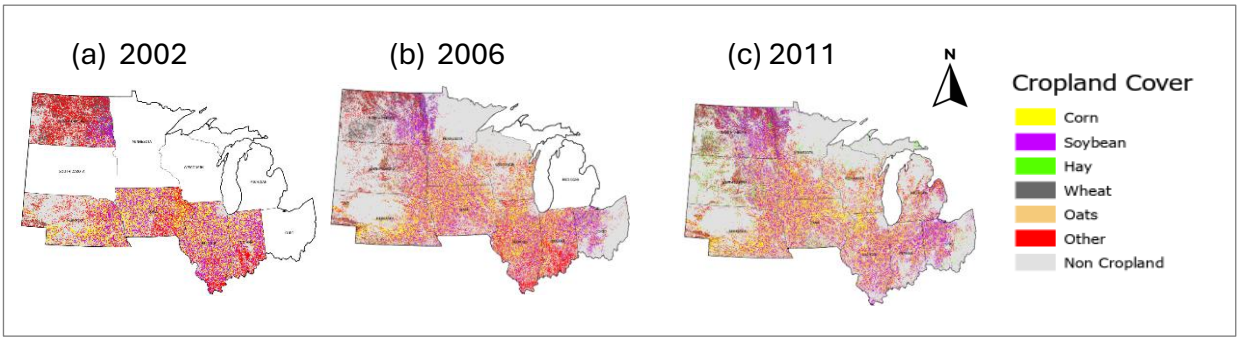

Figure 9. Cropland cover of severe drought years showing corn, soybean, hay, wheat, oats, and other cropland over the Corn Belt Region. (a) 2002 crop cover, (b) 2006 crop cover, and (c) 2011 crop cover.

Table 2. Crop production thresholds of severe drought. Table 2 describes the impacts of corn and soybeans for the years impacted by extreme drought in the Corn Belt Region. The table demonstrates the impacts of drought on crop yield in the region.

Year	Nebraska	Iowa	South Dakota	North Dakota	Minnesota	Illinois	Wisconsin	Indiana	Michigan	Ohio
Corn										
2002	33	71	42	59	73	35	65	26	44	13
2006	57	73	32	36	68	73	62	72	71	72
2011	79	59	72	57	57	45	79	36	64	59
Soybean										
2002	23	65	43	-	72	39	67	32	53	12
2006	62	75	50	-	66	73	65	74	73	67
2011	77	65	64	-	55	51	75	43	68	64

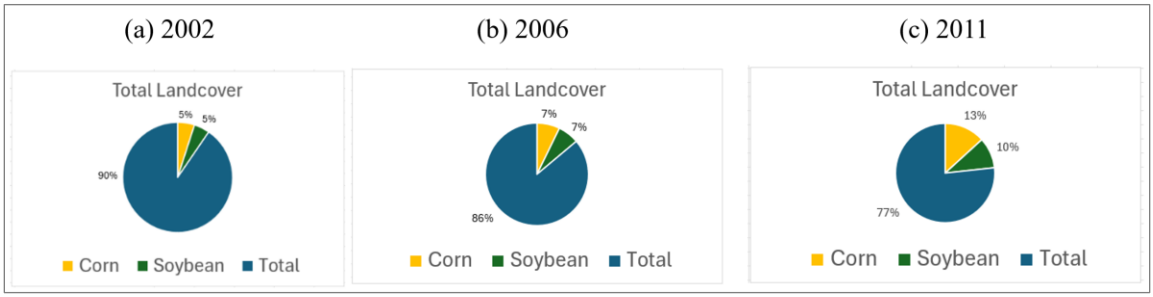

Figure 10. Total landcover distribution of severe drought years. Crop quantities of corn (orange), soybean (green), and total overall crop distribution of the Corn Belt Region. Not a reflection of drought impacts. Credit by CropScape.

Low crop quantities were indicative of missing data on cropland cover for these years (Figure 10). While missing data returned to normal levels, this indicated an increased production of tremendous quantities of one-quarter of the overall distribution for both crops. Overall crop cover distribution is the largest in 2002, of around seven-eighths, but then decreased to three-quarters of the distribution in 2011. In moderate drought years, corn and soybean concentrations increased throughout the severe drought years (2002, 2006, and 2011). Crop patterns remained stagnant and consistent throughout the period, with little to no change. (Figure 11).

Table 3. Crop production thresholds of severe drought. Table 3 describes the impacts of corn and soybeans for the years impacted by severe drought in the Corn Belt Region. Table demonstrates the impacts of drought on crop yield in the region.

Year	Nebraska	Iowa	South Dakota	North Dakota	Minnesota	Illinois	Wisconsin	Indiana	Michigan	Ohio
Corn										
2013	68	49	65	51	59	67	47	73	68	84
2015	76	84	80	71	88	56	79	48	72	52
2017	64	66	48	54	82	63	71	59	56	69
2021	71	62	21	16	37	70	72	70	73	79
Soybean										
2013	69	42	54	-	55	63	43	68	58	72
2015	74	77	78	-	83	60	80	51	66	53
2017	64	64	53	-	69	60	74	58	43	58
2021	74	63	24	-	36	72	73	69	63	67

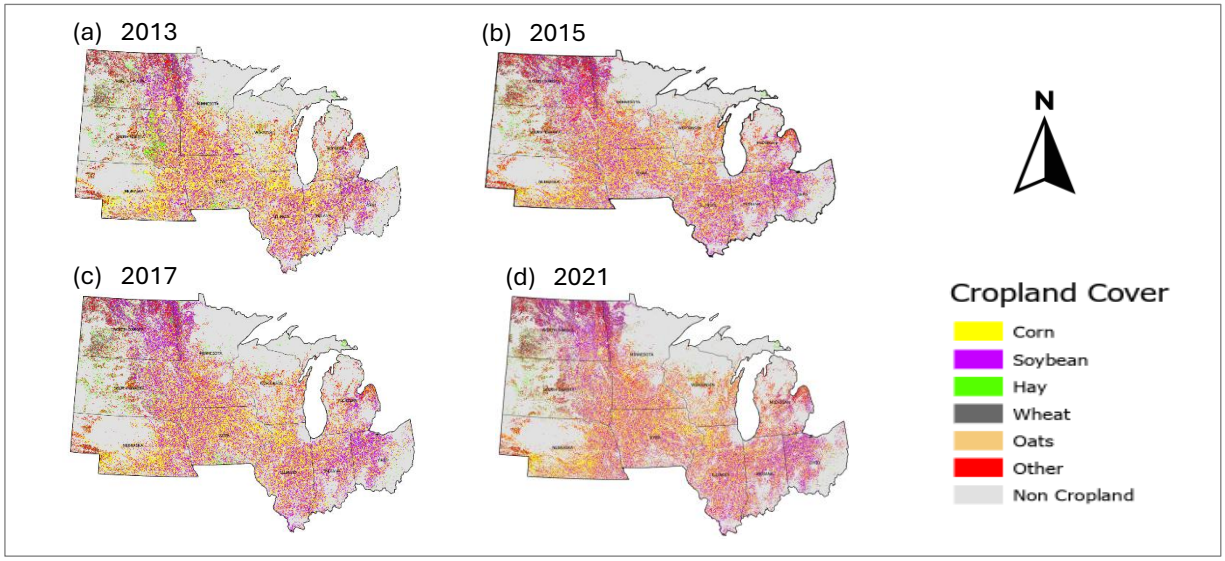

Figure 11. Cropland cover of moderate drought years. Figure describing corn, soybean, hay, wheat, oats, and other cropland over the Corn Belt Region. (a) 2012 crop cover, (b) 2023 crop cover. Crop cover is not a measure of drought impacts but of crop rotation, plantations, and depletion.

For drought impacts, 2021 indicated the most impactful crop yield impacts for both crops along the Western Corn Belt, with both crops severely impacted. Moreover, the Western Corn Belt was most impacted. The threshold level fell within severe limits for corn yield, especially in the west. Severe threshold levels were reported for South Dakota, North Dakota, and Minnesota. North Dakota indicated the lowest threshold levels. For soybeans, impacts were not as low but still within severe limits, with South Dakota indicating the lowest level. While earlier years exhibited drought conditions throughout the region, they did not experience severe threshold levels and instead witnessed unusually productive levels, especially in 2015 (Table 4). Crop quantities showed that in 2013 and 2015, less than one-quarter of the distribution was displayed as corn and soybean cover. The years 2017 and 2021 indicated a gradual increase in corn and soybean quantities. Overall crop distribution remained consistent with little to no change in distribution throughout the period. (Figure 12).

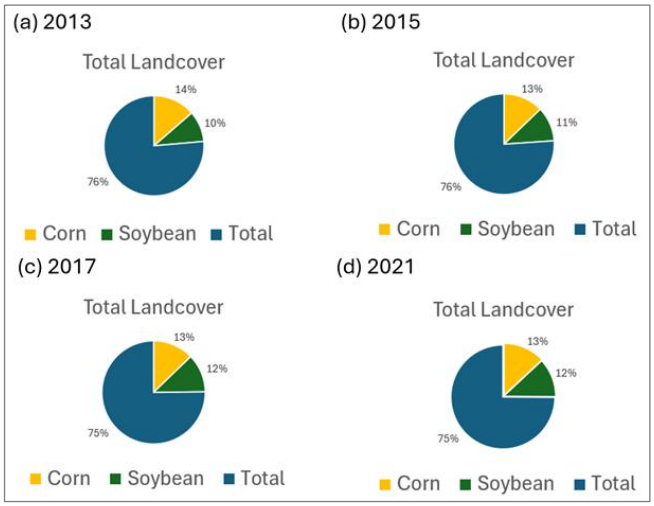

Figure 12. Total landcover distribution of moderate drought year. Crop quantities of corn (orange), soybean (green), and total overall crop distribution of the Corn Belt Region. Not a reflection of drought impacts.

During non-drought years, corn and soybeans started with an early period (2003–2005) of crop diversity blended with corn and soybean distribution but then decreased with more cropland cover of corn and soybean

concentrations after 2007. Crop diversity was prevalent but was more observable in the southern sections of Illinois and Indiana, along with Wisconsin and Michigan. (Figure 13). In 2009 and 2010, much of the landscape was unchanged (Figures 13f & 13g). New plantations of hay were added to sections of eastern South Dakota in 2010. From here, the crop was a dominant practice along the corn/soybean belt areas. It spread to other locations, such as North Dakota, Iowa, and Nebraska. Corn and soybean distribution was distributed from the Western Corn Belt from North Dakota down into Nebraska, extending eastward towards the east belt states, presenting permanent land cover practices throughout the period (Auch *et al.*, 2013). While crop rotations became prominent in this region, crop diversity decreased (after 2005), preserving more corn and soybean concentrations (after 2007) and blending other crops such as hay and oats (after 2010). In terms of non-drought impacts, above to well above average threshold levels were indicated, especially during the middle period, where numerous conditions indicated the wealthiest production. Both 2010 and 2016 experienced the highest productivity of these conditions, where numerous reports indicated well above average production throughout the region (Leeper *et al.*, 2022; Meresa *et al.*, 2023; Mishra & Singh, 2010). For both crops, Nebraska, North Dakota, Minnesota, and Wisconsin all experienced maximum thresholds. Minnesota indicated the most significant levels of production. Above to well-above-average conditions were represented throughout the region, especially corn yield, which indicated numerous maximums in 2010. Iowa, North Dakota, Minnesota, and Wisconsin were among the wealthiest productive states for both crops in 2016. While both crops were among their maximum and most productive harvest of any other year, corn yield indicated the greatest productivity, making it one of the most valuable crops harvested in the region (Green *et al.*, 2018; Ort & Long, 2014; Panagopoulos *et al.*, 2015; Suyker & Verma, 2012) (Table 4).

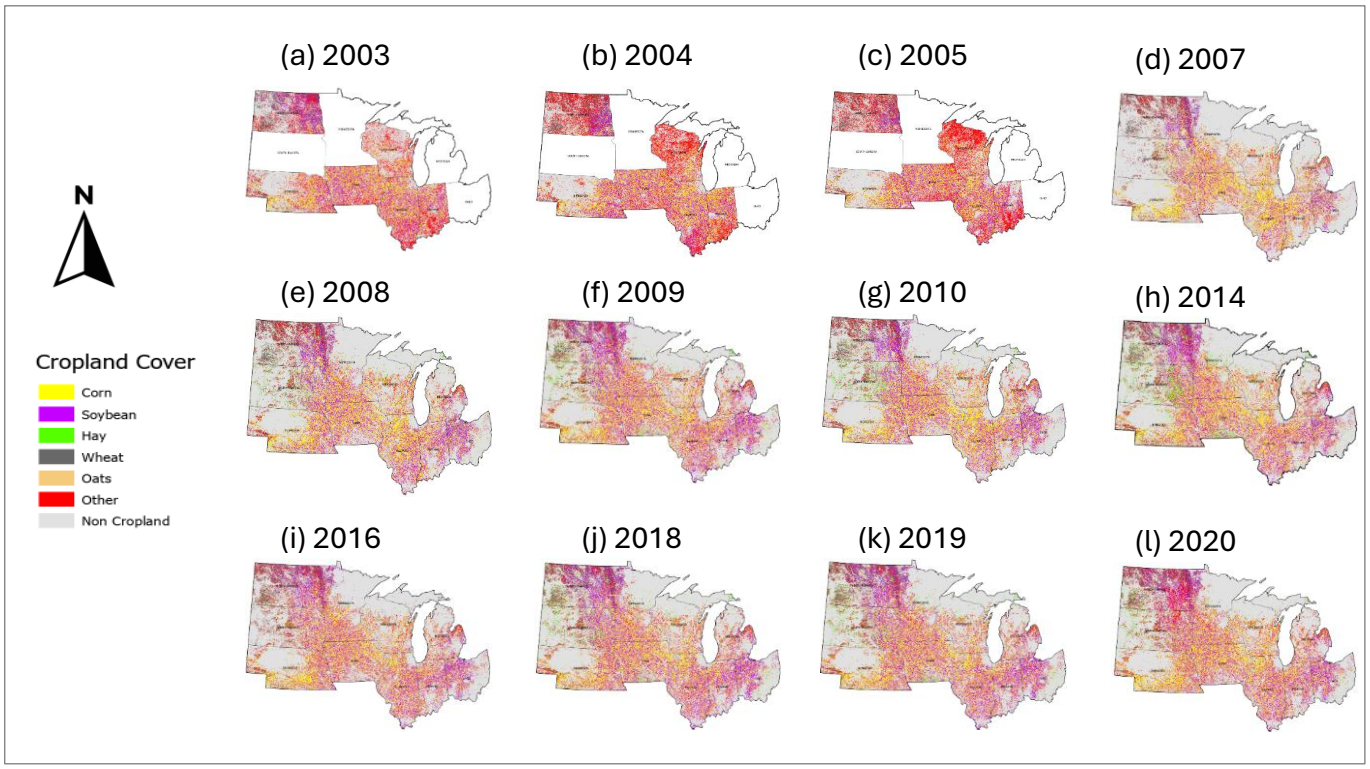

Figure 13. Cropland cover of no significant drought years. Figure describing corn, soybean, hay, wheat, oats and other cropland over Corn Belt Region. (a) 2003, (b) 2004, (c) 2005, (d) 2007, (e) 2008, (f) 2009, (g) 2010, (h) 2014, (i) 2016, (j) 2018, (k) 2019, (l) 2020 crop cover years. Crop cover is not a measure of drought impacts but of crop rotation, plantations, and depletion.

In crop quantities, the overall distribution of crop cover showed more cropland cover of overall distribution, displaying more than seven-eighths of the overall distribution as evidenced by missing data (2003–2005), but then started to decrease from 2007–2015 (Green *et al.*, 2018). High quantities of corn and soybeans were dominant in 2016 and 2018, showing exactly one-quarter of the distribution, but decreased slightly to less than one-quarter in 2019 and 2020. (Figure 14).

Table 4. Crop production thresholds of no significant drought. Table 4 describes the impacts of corn and soybeans for the years impacted by non-significant drought in the Corn Belt Region. The table demonstrates crop productivity as a result of non-drought to considerable wetness in the region.

Year	Nebraska	Iowa	South Dakota	North Dakota	Minnesota	Illinois	Wisconsin	Indiana	Michigan	Ohio
Corn										
2003	51	43	56	41	53	67	33	65	60	74
2004	80	76	74	36	63	84	57	84	55	73
2005	67	77	62	70	75	22	65	54	66	47
2007	82	73	73	74	46	77	46	52	31	51
2008	77	65	78	70	67	72	61	59	54	38
2009	80	69	71	62	49	62	62	56	71	76
2010	81	70	74	84	87	53	84	56	74	63
2014	76	76	74	73	66	84	72	77	72	78
2016	73	83	57	83	87	83	86	70	67	47
2018	79	69	72	66	76	80	68	70	56	82
2019	73	67	65	52	57	55	67	36	42	37
2020	59	47	78	59	80	66	81	62	65	51
Soybean										
2003	27	16	47	-	21	46	16	45	37	57
2004	63	73	65	-	47	76	58	78	54	68
2005	61	77	63	-	73	34	56	57	56	59
2007	80	76	73	-	56	77	61	43	38	54
2008	70	62	66	-	56	72	46	49	37	28
2009	80	69	71	-	62	62	49	62	56	71
2010	78	73	67	-	84	53	83	54	70	59
2014	75	73	77	-	67	80	71	75	60	75
2016	77	81	65	-	83	82	85	77	72	63
2018	79	66	61	-	72	81	72	71	73	78
2019	71	66	57	-	54	49	64	33	44	35
2020	66	49	68	-	78	67	82	63	67	57

4. Conclusions

This research was designed to investigate the effects of precipitation regimes on drought severity and their influence on crop yield and production (Sun *et al.*, 2023). This research demonstrated the need to assess the parameters of wetness and dryness regimes given by the index of SPI. In this research, the focus of this paper was on the climate and weather effects dedicated to drought assessment and its impact on crop production and yield from 2000 to 2023, as categorized through the four classification groups. While the three classifications were under drought, one class was under non-significant drought.

This research indicated a clear picture of widespread coverage and intensity, followed by numerous pockets of drought conditions throughout the region. Drought coverage and severity were widespread and numerous throughout both regions, mainly for extreme, severe, and moderate drought categories (Hosseini *et al.*, 2021; Li *et al.*, 2020; Shrestha *et al.*, 2020). In extreme cases, 2002, 2006, 2012, and 2013

Figure 14. Total landcover distribution of no significant drought years. Crop quantities of corn (orange), soybean (green), and total overall crop distribution of the Corn Belt Region. Not a reflection of drought impacts.

experienced widespread impacts, especially in 2012, where most of the region was under widespread extreme dryness. For non-drought, a persistent wet pattern started to plague the region, especially during the last two-thirds of the period, especially in 2010, 2014, and 2016. These years indicated perhaps the most significant patterns of wetness, especially along the Western Corn Belt of the western Great Plains and the northern Great Lakes Region (Auch *et al.*, 2013; Green *et al.*, 2018; Ort & Long, 2014; Panagopoulos *et al.*, 2015; Suyker & Verma, 2012). This analysis concluded that the research results support the evidence of drought severity and its influence on crop production. Specifically, climate change can alter weather patterns, leading to drought stress among plants such as corn and soybeans (Fadhli *et al.*, 2020; Green *et al.*, 2018; Sakellariou *et al.*, 2024). In this research, the four classifications correlated well with the results in terms of crop production. As crop production varied between the crop types, results revealed similar patterns in terms of the different regimes of these classes. Specifically, the corn and soybean yields were plentiful throughout the

period (S. Li *et al.*, 2021; Peña-Gallardo *et al.*, 2019; Prince *et al.*, 2001). While missing data affected the overall results, heavy concentrations of crop diversity were widespread, especially during the early decadal period of some of the drought classes, especially in the corn and soybean distribution cover. Overall, corn and soybeans mixed with oats (later in the period) were distributed along the southern corn belt states. The analysis showed that these widespread and intense drought episodes impacted crop production. While drought conditions were numerous, crop yields were severely affected in the region throughout these drought periods, especially in 2002, 2012, and 2021 (Aghelpour *et al.*, 2021; Peña-Gallardo *et al.*, 2019; Prince *et al.*, 2001; Yoon *et al.*, 2020). The most significant impacts were between 2002 and 2012 and 2021, indicating the lowest yields of both crops compared to any other year. Non-drought years indicated numerous above to well above average levels of wealthy crop production for both crops. Crop production indicated wealthier conditions throughout the period, with 2010 and 2016 indicating the most significant levels than any other year, especially along the northern Great Lakes states from North Dakota and Minnesota stretching southeastward towards Illinois (Green *et al.*, 2018; Ort & Long, 2014; Panagopoulos *et al.*, 2015; Suyker & Verma, 2012).

Overall, this research supported the need to understand the four drought types. It also demonstrated the hypothesis that meteorological drought is the leading drought type influencing the economic, environmental, and social sectors. Therefore, extreme climate events such as drought and extreme precipitation have been on the rise in other countries and other sections of the western hemisphere (Gattoni *et al.*, 2025; McGranahan & Wonkka, 2024; Weaver & Bruner, 1948). This research supports the evidence that there has been an increase in drought conditions and that the severity and intensity of drought has increased, especially in the concentrated corn and soybean belts, with an uptick in wet conditions along the Great Plains to the northern Great Lakes (L. Li *et al.*, 2020; Shrestha *et al.*, 2020; Wahl *et al.*, 2022). This research has also demonstrated the need to understand further drought and its impacts on crop yield, allowing communities to provide adaptation measures for resiliency and mitigation responses for future occurrences of drought in the future (Leeper *et al.*, 2022; L. Li *et al.*, 2020; Shiru *et al.*, 2019; Shrestha *et al.*, 2020).

Data Availability Statement: Data, climate, cropland cover, and yield are available online for open-access use at https://climatedataguide.ucar.edu/climate-data/chirps-climate-hazards-infrared-precipitation-station-data-version-2, crop cover data - https://nassgeodata.gmu.edu/, and yield data - https://www.nass.usda.gov/Data_and_Statistics/index.php, and crop yield data https://www.nass.usda.gov/Research_and_Science/Cropland/SARS1a.php for data-ready access.

Acknowledgment: Funded by the University of North Dakota and North DakotaView. This material is based upon work supported partly by the U.S. Geological Survey under Grant/Cooperative Agreement No. G18AP00077 (for GY18-GY22) or G23AP00683 (GY23-GY27).

Conflicts of Interest: The authors declare no conflicts of interest. The funders had no role in the design of the study; in the collection, analyses, or interpretation of data; in the writing of the manuscript; or in the decision to publish the results.

References

Acharki, S., Singh, S. K., do Couto, E. V., Arjdal, Y., & Elbeltagi, A. (2023). Spatio-temporal distribution and prediction of agricultural and meteorological drought in a Mediterranean coastal watershed via GIS and machine learning. *Physics and Chemistry of the Earth, Parts A/B/C*, *131*, 103425. https://doi.org/10.1016/j.pce.2023.103425

Aghelpour, P., Mohammadi, B., Mehdizadeh, S., Bahrami-Pichaghchi, H., & Duan, Z. (2021). A novel hybrid dragonfly optimization algorithm for agricultural drought prediction. *Stochastic Environmental Research and Risk Assessment*, *35*(12), 2459–2477. https://doi.org/10.1007/s00477-021-02011-2

Angelidis, P., Maris, F., Kotsovinos, N., & Hrissanthou, V. (2012). Computation of drought index SPI with alternative distribution functions. *Water Resources Management*, *26*(9), 2453–2473. https://doi.org/10.1007/s11269-012-0026-0

Auch, R. F., Laingen, C., Drummond, M. A., Sayler, K. L., Reker, R. R., Bouchard, M. A., & Danielson, J. J. (2013). Land-use and land-cover change in three Corn Belt ecoregions: Similarities and differences. *Focus on Geography*, *56*(4), 135–143. https://doi.org/10.1111/foge.12022

Ayugi, B., Eresanya, E. O., Onyango, A. O., Ogou, F. K., Okoro, E. C., Okoye, C. O., Anoruo, C. M., Dike, V. N., Ashiru, O. R., Daramola, M. T., Mumo, R., & Ongoma, V. (2022). Review of meteorological drought in Africa: Historical trends, impacts,

mitigation measures, and prospects. *Pure and Applied Geophysics*, *179*(4), 1365–1386. https://doi.org/10.1007/s00024-022-02988-z

Boryan, C., Yang, Z., Mueller, R., & Craig, M. (2011). Monitoring US agriculture: The US Department of Agriculture, National Agricultural Statistics Service, Cropland Data Layer Program. *Geocarto International*, *26*(5), 341–358. https://doi.org/10.1080/10106049.2011.562309

Bouaziz, M., Medhioub, E., & Csaplovisc, E. (2021). A machine learning model for drought tracking and forecasting using remote precipitation data and a standardized precipitation index from arid regions. *Journal of Arid Environments*, *189*, 104478. https://doi.org/10.1016/j.jaridenv.2021.104478

Brandes, E., McNunn, G. S., Schulte, L. A., Bonner, I. J., Muth, D. J., Babcock, B. A., Sharma, B., & Heaton, E. A. (2016). Subfield profitability analysis reveals an economic case for cropland diversification. *Environmental Research Letters*, *11*(1), 014009. https://doi.org/10.1088/1748-9326/11/1/014009

Chen, M., Kumar, A., L'Heureux, M., Peng, P., Zhang, T., Hoerling, M. P., & Diaz, H. F. (2024). Why do DJF 2023/24 upper-level 200-hPa geopotential height forecasts look different from the expected El Niño response? *Geophysical Research Letters*, *51*(14), e2024GL108946. https://doi.org/10.1029/2024GL108946

de Oliveira-Júnior, J. F., da Silva Junior, C. A., Teodoro, P. E., Rossi, F. S., Blanco, C. J. C., Lima, M., de Gois, G., Correia Filho, W. L. F., de Barros Santiago, D., & dos Santos Vanderley, M. H. G. (2021). Confronting CHIRPS dataset and in situ stations in the detection of wet and drought conditions in the Brazilian Midwest. *International Journal of Climatology*, *41*(9), 4478–4493. https://doi.org/10.1002/joc.7080

de Oliveira-Júnior, J. F., Mendes, D., Porto, H. D., Cardoso, K. R. A., Neto, J. A. F., da Silva, E. B. C., de Aquino Pereira, M., Mendes, M. C. D., Baracho, B. B. D., & Jamjareegulgarn, P. (2025). Analysis of drought and extreme precipitation events in Thailand: Trends, climate modeling, and implications for climate change adaptation. *Scientific Reports*, *15*(1), 4501. https://doi.org/10.1038/s41598-025-86826-x

Du, H., Tan, M. L., Zhang, F., Chun, K. P., Li, L., & Kabir, M. H. (2024). Evaluating the effectiveness of CHIRPS data for hydroclimatic studies. *Theoretical and Applied Climatology*, *155*(3), 1519–1539. https://doi.org/10.1007/s00704-023-04721-9

Duffy, P. B., Brando, P., Asner, G. P., & Field, C. B. (2015). Projections of future meteorological drought and wet periods in the Amazon. *Proceedings of the National Academy of Sciences*, *112*(43), 13172–13177. https://doi.org/10.1073/pnas.1421010112

Fadhli, N., Farid, Muh., Rafiuddin, Effendi, R., Azrai, M., & Anshori, M. F. (2020). Multivariate analysis to determine secondary characters in selecting adaptive hybrid corn lines under drought stress. *Biodiversitas Journal of Biological Diversity*, *21*(8). https://doi.org/10.13057/biodiv/d210826

Fenneman, N. M. (1917). Physiographic subdivision of the United States. *Proceedings of the National Academy of Sciences*, *3*(1), 17–22. https://doi.org/10.1073/pnas.3.1.17

Funk, C., Peterson, P., Landsfeld, M., Pedreros, D., Verdin, J., Shukla, S., Husak, G., Rowland, J., Harrison, L., Hoell, A., & Michaelsen, J. (2015). The climate hazards infrared precipitation with stations—A new environmental record for monitoring extremes. *Scientific Data*, *2*(1), 150066. https://doi.org/10.1038/sdata.2015.66

Gattoni, K., Gendron, E. M. S., McQueen, J. P., Powers, K., Powers, T. O., Harner, M. J., Corman, J. R., & Porazinska, D. L. (2025). The nature of microbial diversity and assembly in the Nebraska Sandhills depends on organismal identity and habitat type. *Community Ecology*, *26*(1), 1–14. https://doi.org/10.1007/s42974-024-00206-5

Green, T. R., Kipka, H., David, O., & McMaster, G. S. (2018). Where is the USA Corn Belt, and how is it changing? *Science of The Total Environment*, *618*, 1613–1618. https://doi.org/10.1016/j.scitotenv.2017.09.325

Guttman, N. B. (1998). Comparing the Palmer drought index and the standardized precipitation index 1. *JAWRA Journal of the American Water Resources Association*, *34*(1), 113–121. https://doi.org/10.1111/j.1752-1688.1998.tb05964.x

Guttman, N. B. (1999). Accepting the standardized precipitation index: A calculation algorithm 1. *JAWRA Journal of the American Water Resources Association*, *35*(2), 311–322. https://doi.org/10.1111/j.1752-1688.1999.tb03592.x

Han, W., Yang, Z., Di, L., & Mueller, R. (2012). CropScape: A Web service based application for exploring and disseminating US conterminous geospatial cropland data products for decision support. *Computers and Electronics in Agriculture*, *84*, 111–123. https://doi.org/10.1016/j.compag.2012.03.005

Hosseini, A., Ghavidel, Y., Mohammad Khorshiddoust, A., & Farajzadeh, M. (2021). Spatio-temporal analysis of dry and wet periods in Iran by using Global Precipitation Climatology Center-Drought Index (GPCC-DI). *Theoretical and Applied Climatology*, *143*(3–4), 1035–1045. https://doi.org/10.1007/s00704-020-03463-2

Leeper, R. D., Bilotta, R., Petersen, B., Stiles, C. J., Heim, R., Fuchs, B., Prat, O. P., Palecki, M., & Ansari, S. (2022). Characterizing U.S. drought over the past 20 years using the U.S. drought monitor. *International Journal of Climatology*, *42*(12), 6616–6630. https://doi.org/10.1002/joc.7653

Li, L., She, D., Zheng, H., Lin, P., & Yang, Z.-L. (2020). Elucidating diverse drought characteristics from two meteorological drought indices (SPI and SPEI) in China. *Journal of Hydrometeorology*, *21*(7), 1513–1530. https://doi.org/10.1175/JHM-D-19-0290.1

Li, S., Thompson, M., Moussavi, S., & Dvorak, B. (2021). Life cycle and economic assessment of corn production practices in the western US Corn Belt. *Sustainable Production and Consumption*, *27*, 1762–1774. https://doi.org/10.1016/j.spc.2021.04.021

Liu, C., Yang, C., Yang, Q., & Wang, J. (2021). Spatiotemporal drought analysis by the standardized precipitation index (SPI) and standardized precipitation evapotranspiration index (SPEI) in Sichuan Province, China. *Scientific Reports*, *11*(1), 1280. https://doi.org/10.1038/s41598-020-80527-3

Liu, L., Hong, Y., Looper, J., Riley, R., Yong, B., Zhang, Z., Hocker, J., & Shafer, M. (2013). Climatological drought analyses and projection using SPI and PDSI: Case study of the Arkansas Red River Basin. *Journal of Hydrologic Engineering*, *18*(7), 809–816. https://doi.org/10.1061/(ASCE)HE.1943-5584.0000619

Lloyd-Hughes, B., & Saunders, M. A. (2002). A drought climatology for Europe. *International Journal of Climatology*, *22*(13), 1571–1592. https://doi.org/10.1002/joc.846

López-Bermeo, C., Montoya, R. D., Caro-Lopera, F. J., & Díaz-García, J. A. (2022). Validation of the accuracy of the CHIRPS precipitation dataset at representing climate variability in a tropical mountainous region of South America. *Physics and Chemistry of the Earth, Parts A/B/C*, *127*, 103184. https://doi.org/10.1016/j.pce.2022.103184

McGranahan, D. A., & Wonkka, C. L. (2024). Pyrogeography of the Western Great Plains: A 40-year history of fire in semi-arid rangelands. *Fire*, *7*(1), Article 1. https://doi.org/10.3390/fire7010032

Meresa, H., Zhang, Y., Tian, J., & Abrar Faiz, M. (2023). Understanding the role of catchment and climate characteristics in the propagation of meteorological to hydrological drought. *Journal of Hydrology*, *617*, 128967. https://doi.org/10.1016/j.jhydrol.2022.128967

Mishra, A. K., & Singh, V. P. (2010). A review of drought concepts. *Journal of Hydrology*, *391*(1), 202–216. https://doi.org/10.1016/j.jhydrol.2010.07.012

Ort, D. R., & Long, S. P. (2014). Limits on yields in the Corn Belt. *Science*, *344*(6183), 484–485. https://doi.org/10.1126/science.1253884

Panagopoulos, Y., Gassman, P. W., Jha, M. K., Kling, C. L., Campbell, T., Srinivasan, R., White, M., & Arnold, J. G. (2015). A refined regional modeling approach for the Corn Belt – Experiences and recommendations for large-scale integrated modeling. *Journal of Hydrology*, *524*, 348–366. https://doi.org/10.1016/j.jhydrol.2015.02.039

Peña-Gallardo, M., Vicente-Serrano, S. M., Quiring, S., Svoboda, M., Hannaford, J., Tomas-Burguera, M., Martín-Hernández, N., Domínguez-Castro, F., & El Kenawy, A. (2019). Response of crop yield to different time-scales of drought in the United States: Spatio-temporal patterns and climatic and environmental drivers. *Agricultural and Forest Meteorology*, *264*, 40–55. https://doi.org/10.1016/j.agrformet.2018.09.019

Prince, S. D., Haskett, J., Steininger, M., Strand, H., & Wright, R. (2001). Net primary production of U.S. Midwest croplands from agricultural harvest yield data. *Ecological Applications*, *11*(4), 1194–1205. https://doi.org/10.1890/1051-0761(2001)011[1194:NPPOUS]2.0.CO;2

Rosenberg, N. J. (1987). Climate of the Great Plains Region of the United States. *Great Plains Quarterly*, *7*(1), 22–32.

Sakellariou, S., Spiliotopoulos, M., Alpanakis, N., Faraslis, I., Sidiropoulos, P., Tziatzios, G. A., Karoutsos, G., Dalezios, N. R., & Dercas, N. (2024). Spatiotemporal drought assessment based on gridded Standardized Precipitation Index (SPI) in vulnerable agroecosystems. *Sustainability*, *16*(3), 1240. https://doi.org/10.3390/su16031240

Schneider, D. P., Deser, C., Fasullo, J., & Trenberth, K. E. (2013). Climate Data Guide spurs discovery and understanding. *Eos, Transactions American Geophysical Union*, *94*(13), 121–122. https://doi.org/10.1002/2013EO130001

Sharafati, A., Nabaei, S., & Shahid, S. (2020). Spatial assessment of meteorological drought features over different climate regions in Iran. *International Journal of Climatology*, *40*(3), 1864–1884. https://doi.org/10.1002/joc.6307

Shiru, M. S., Shahid, S., Chung, E.-S., & Alias, N. (2019). Changing characteristics of meteorological droughts in Nigeria during 1901–2010. *Atmospheric Research*, *223*, 60–73. https://doi.org/10.1016/j.atmosres.2019.03.010

Shrestha, A., Rahaman, M. M., Kalra, A., Jogineedi, R., & Maheshwari, P. (2020). Climatological drought forecasting using bias corrected CMIP6 climate data: A case study for India. *Forecasting*, *2*(2), 59–84. https://doi.org/10.3390/forecast2020004

Sönmez, F. Kemal., Kömüscü, A. Ü., Erkan, A., & Turgu, E. (2005). An analysis of spatial and temporal dimension of drought vulnerability in Turkey using the Standardized Precipitation Index. *Natural Hazards*, *35*(2), 243–264. https://doi.org/10.1007/s11069-004-5704-7

Stagge, J. H., Tallaksen, L. M., Gudmundsson, L., Van Loon, A. F., & Stahl, K. (2015). Candidate distributions for climatological drought indices (SPI and SPEI). *International Journal of Climatology*, *35*(13), 4027–4040. https://doi.org/10.1002/joc.4267

Sun, P., Liu, R., Yao, R., Shen, H., & Bian, Y. (2023). Responses of agricultural drought to meteorological drought under different climatic zones and vegetation types. *Journal of Hydrology*, *619*, 129305. https://doi.org/10.1016/j.jhydrol.2023.129305

Suyker, A. E., & Verma, S. B. (2012). Gross primary production and ecosystem respiration of irrigated and rainfed maize–soybean cropping systems over 8 years. *Agricultural and Forest Meteorology*, *165*, 12–24. https://doi.org/10.1016/j.agrformet.2012.05.021

Tsiros, I. X., Nastos, P., Proutsos, N. D., & Tsaousidis, A. (2020). Variability of the aridity index and related drought parameters in Greece using climatological data over the last century (1900–1997). *Atmospheric Research*, *240*, 104914. https://doi.org/10.1016/j.atmosres.2020.104914

Wahl, E. R., Zorita, E., Diaz, H. F., & Hoell, A. (2022). Southwestern United States drought of the 21st century presages drier conditions into the future. *Communications Earth & Environment*, *3*(1), 202. https://doi.org/10.1038/s43247-022-00532-4

Wang, F., Lai, H., Li, Y., Feng, K., Zhang, Z., Tian, Q., Zhu, X., & Yang, H. (2022). Dynamic variation of meteorological drought and its relationships with agricultural drought across China. *Agricultural Water Management*, *261*, 107301. https://doi.org/10.1016/j.agwat.2021.107301

Weaver, J. E., & Bruner, W. E. (1948). Prairies and pastures of the dissected loess plains of central Nebraska. *Ecological Monographs*, *18*(4), 507–549. https://doi.org/10.2307/1948587

Wilhite, D. A., & Glantz, M. H. (1985). Understanding the drought phenomenon: The role of definitions. *Water International*, *10*(3), 111–120. https://doi.org/10.1080/02508068508686328

Wilson, A. B., Avila-Diaz, A., Oliveira, L. F., Zuluaga, C. F., & Mark, B. (2022). Climate extremes and their impacts on agriculture across the Eastern Corn Belt Region of the U.S. *Weather and Climate Extremes*, *37*, 100467. https://doi.org/10.1016/j.wace.2022.100467

Yoon, D.-H., Nam, W.-H., Lee, H.-J., Hong, E.-M., Feng, S., Wardlow, B. D., Tadesse, T., Svoboda, M. D., Hayes, M. J., & Kim, D.-E. (2020). Agricultural drought assessment in East Asia using satellite-based indices. *Remote Sensing*, *12*(3), Article 3. https://doi.org/10.3390/rs12030444

Best Practice

Addressing Challenges and Exploring Solutions to Enhance Earth Observation Applications for Emergency Management

Patrick Kerwin[1,*], Jordan Bell[2], John Cooney[3], Timothy Lahmers[4], Alexander Melancon[5], Julia Milton[6], Kristen Okorn[7], Julie Rolla[8], Rachel Vershel[9], Joshua Barnes[10], Lauren Childs-Gleason[11], Katie Picchione[12], and Patrick Rea[13]

1 Analytical Mechanics Associates; patrick.m.kerwin@nasa.gov
2 NASA Marshall Space Flight Center; jordan.r.bell@nasa.gov
3 NASA Langley Research Center; john.w.cooney@nasa.gov
4 NASA Goddard Space Flight Center; timothy.lahmers@nasa.gov
5 University of Alabama Huntsville; alexander.melancon@nasa.gov
6 Jet Propulsion Laboratory; julia.milton@jpl.nasa.gov
7 NASA Ames Research Center; kristen.e.okorn@nasa.gov
8 Jet Propulsion Laboratory; julie.a.rolla@jpl.nasa.gov
9 Science Systems and Applications Inc; rachel.vershel@nasa.gov
10 NASA Langley Research Center; joshua.j.barnes@nasa.gov
11 NASA Langley Research Center; lauren.m.childs@nasa.gov
12 NASA Langley Research Center; katie.picchione@nasa.gov
13 Analytical Mechanics Associates; patrick.r.rea@nasa.gov
* Corresponding Author: patrick.m.kerwin@nasa.gov, +1-757-864-4204.

JOURNAL OF EARTH OBSERVATION & GEOSPATIAL APPLICATIONS

Academic Editor: Jeong C. Seong
Received: 11 August 2025
Revised: 11 September 2025
Accepted: 23 September 2025
Published: 24 September 2025

Abstract: Earth observations (EO) and remote sensing technology provide essential data for understanding natural hazards and their effect on the environment and society. Emergency management relies on data-driven decision making to address disruptive and damaging events, increasingly using remote sensing to improve situational awareness. Unfortunately, gaps between the cutting edge of remote sensing science and application in emergency management diminish the value of data before use. Challenges include: the trade-offs in temporal resolution, spatial resolution, and area coverage; geographic nuances affecting asset utility; complexity in the tasking, collection, processing, exploitation, and dissemination process; expectations for analysis and interpretation; data accessibility; and the rapid advancement of remote sensing and space technology. The NASA Disasters Program's Disasters Response Coordination System (DRCS) launched in June 2024 to improve the application of NASA science for disaster response. This paper shares challenges the DRCS experienced throughout its first year and discusses best practices to improve the effectiveness of remote sensing support of emergency management activities. To bridge the gap, the DRCS proposes better curation and communication of product catalogues, tailored and varied approaches to capacity building, and enhanced coordination and collaboration.

Keywords: remote sensing, Earth observation, emergency management, disaster response

1. Introduction

Researchers routinely harness Earth observations (EO) and remote sensing data to monitor natural hazards and improve our understanding of their consequences on the environment and society (Kirschbaum *et al*., 2017). Remote sensing technology has developed rapidly for scientific, civil, and commercial applications, elevating its potential utility across fields, including emergency management (Denis *et al*., 2016). When coordinating a response, emergency managers require timely, relevant data to inform decisions and increasingly look to EO to fill gaps in field reporting (Cova, 1999; Drabek and Hoetmer, 1991). But despite emerging technology, novel applications, and an emergency management (EM) community eager to maximize its impact, remote sensing often fails to meet emergency managers' expectations.

Citation: Kerwin, P., Bell, J., Cooney, J., Lahmers, T., Melancon, A., Milton, J., Okorn, K., Rolla, J., Vershel, R., Barnes, J., Childs-Gleason, L., Picchione, K., & Rea, P. (2025). Addressing challenges and exploring solutions to enhance Earth observation applications for emergency management. *Journal of Earth Observation and Geospatial Applications, 1*(1), 129–143. DOI: https://doi.org/10.65372/x7e2t216

This paper describes persistent challenges limiting the use of remote sensing to support disaster response and shares lessons learned from the first year of the NASA Disasters Response Coordination System (DRCS). The DRCS launched in June 2024 to better connect NASA's remote sensing capabilities with the emergency management community. Through 18 activations since its launch supporting federal, state, international, and non-governmental organizations, the DRCS observed a disconnect between the scientific and disaster response communities. Emergency managers can at times struggle to effectively request and utilize products derived from EO, while scientists and technologists lack understanding of emergency managers' informational needs or how best to provide decision-ready data. Although this problem is not new, sparse literature reveals the nature of this disconnect and solutions.

The DRCS asserts that bridging the gap between data providers and emergency managers is feasible. Here the authors highlight six challenges separating remote sensing science from practical applications in disaster response and emergency management. These challenges include: trade-offs in temporal resolution, spatial resolution, and area coverage; geographic nuances affecting asset utility; complexity in the tasking, collection, processing, exploitation, and dissemination process; expectations for analysis and interpretation; data accessibility; and the rapid advancement of remote sensing and space technology. The authors propose several best practices for improving outcomes, including better curation and communication of product catalogues, tailored and varied approaches to capacity building, and enhanced collaboration. This paper is intended for scientists and engineers hoping to support disaster response and for emergency managers seeking to understand how remote sensing might better meet their needs.

2. Background

2.1. Remote Sensing in Disaster Response

In April 1906, a devastating earthquake (retroactively estimated as 7.9 on the Richter scale) shook San Francisco, California. The initial tremor destroyed 5,000 homes and subsequent damage to stoves and gas lines caused a major fire that destroyed 28,000 buildings throughout the city (Strupp, 2006; Canton, 2006). In the aftermath, photographer George R. Lawrence used a creative system of kites to hoist a camera into the sky to document the damage from above. These images are considered the first use of imagery for assessing disaster damage and inspired subsequent use of remote sensing to understand the effects of disasters (Kerle *et al*., 2019).

Lawrence's ingenuity represents a larger trend in remote sensing and its application for disaster response. Although incredibly valuable for disaster response, the best available remote sensing technology is often not designed specifically for that application and therefore carries various limitations. Today, instruments mounted on overhead platforms such as satellites, unmanned aerial vehicles (UAV), or aircraft, passively or actively measure energy across the electromagnetic spectrum to provide data about features on the ground or in the atmosphere (Kirschbaum *et al*., 2017; Picchione *et al*., 2024). Emergency managers commonly leverage remote sensing products during disasters today, including multispectral imagery, hyperspectral imagery, panchromatic imagery, optical imagery, light detection and ranging (LiDAR), and synthetic aperture radar (SAR) (Hodgson *et al*., 2013; Picchione *et al*., 2024).

2.2. Emergency Management Remote Sensing End Users

The value of remote sensing products for disaster response is largely determined by those actively using it during a crisis. End users of remote sensing data include first responders, survivors, and emergency managers (Picchione *et al*., 2024). First responders such as firefighters, paramedics, and search and rescue teams can use remote sensing to gain insights into damage, inaccessible and dangerous areas, impacted structures, and validate other reports and data sources (Hodgson *et al*., 2013). Disaster survivors are becoming more engaged with geospatial data aided by an increase in public-facing data platforms including mobile navigation apps, weather apps, news outlets that frequently publish public overhead imagery during disasters, such as NASA Worldview, and others (McCormick, 2012). However, the primary end users of remote sensing and geospatial data are typically emergency managers. Responsible for coordinating response activities in affected areas, emergency managers constantly collect and share information, identify priorities, and align response operations across many independent organizations. Timely, accurate data help emergency managers make informed decisions, increase situational awareness, validate ground reports, and allocate resources.

2.3. Geospatial Needs of Emergency Management End Users

Emergency managers need data within a reasonable timeline, with an adequate level of detail, and covering the entire area of interest (AOI). Data that satisfy these needs contribute to understanding response capabilities, community conditions, and incident conditions (FEMA, 2018). Timeliness is crucial. Once a disaster happens, information from overhead imagery is most valuable to emergency managers within the first 24–72 hours (Hodgson *et al*., 2013; Battersby *et al*., 2012). After this period, the impact of the imagery diminishes as other data become available and situational awareness increases. Hodgson *et al*. (2013) found in a survey of emergency managers that 90% of state EM offices needed information on damage to structures within 72 hours of the incident.

Identifying damage to structures, as well as addressing other common asks such as determining the status of roads, estimating damage to infrastructure, and identifying the extent and boundaries of hazards depend on sufficient spatial resolution, or detail, of imagery. Battersby *et al*. (2012) found that imagery with a resolution greater than 1.5 m created limitations. Different remote sensing instruments offer different advantages and disadvantages. Understanding the limitations and trade-offs of each clarifies how remote sensing can address EM end user needs.

2.4. Response Coordination Case Studies

The DRCS only activates when end users directly request support that NASA data and expertise can help address. Requestors can include federal, state, tribal, territorial, or local government units, and private or non-profit organizations operating at national or international levels. End users request DRCS support by contacting the team and sharing details such as the area of interest, desired products or expertise, response needs remote sensing products are expected to address, and the timeframe needed to support decision making. The DRCS then enters a screening process to ensure that it has the capacity and scope to satisfy the request, that NASA products can add novel perspective and value, and that the team has the available resources to meet the need. This section illustrates four disasters where the DRCS responded to requests from partners for operational support. Each case reveals challenges and best practices discussed further in the following sections.

2.4.1. Hurricane Helene

Hurricane Helene made landfall in Florida as a category 4 hurricane on September 26, 2024. It caused extensive flooding, power outages, landslides, and severe wind damage to areas across six states and resulted in over 200 deaths and $78 billion in economic losses (Amorim *et al*., 2025; NCEI, 2025). The geographical scale and severity of the storm and its protracted impacts across the region delayed ground-based reports, rendering EO data critical to building situational awareness. The DRCS activated on September 24, 2024, supporting numerous state, federal, and non-governmental partners.

Table 1. Selected products from the DRCS response to Hurricane Helene.

Request	Product Highlights
Power Outage Awareness	An experimental power outage assessment created with Black Marble nighttime lights daily blue-yellow composite imagery visualized locations experiencing extended power outages, particularly in rural communities.
Locations of Flooding and Damage	Normalized difference vegetation index (NDVI) is an analysis used to assess vegetation health (Huang et al., 2021). To help identify areas damaged by the hurricane's water and wind impacts, the DRCS created an experimental NDVI binary change detection product that highlights areas that experienced change of any kind since before the event.
Locations of Landslides	The DRCS collaborated with the USGS Landslide Assessments, Situational Awareness, and Event Response Research (LASER) team in an interagency effort that utilized optical imagery from Sentinel-2 and other higher-resolution data to map the landslides on the ground (Macias et al., 2024).

Initial requests focused on nighttime lights data and coordination around flood mapping, but a need for information on landslides developed as well. The DRCS provided a wide array of products to support requestors' needs (Table 1) and developed new products to bring additional insights to responders (Figure 1). Feedback from partners highlighted an overabundance of SAR-derived flood products made it difficult to know which one best addressed their needs. This incident also highlighted the need during large-scale incidents for clear strategies that minimize processing and publication bottlenecks often associated with the computer systems that analyze and display geospatial data, also known as Geographic Information Systems (GIS) (USGS, 2025).

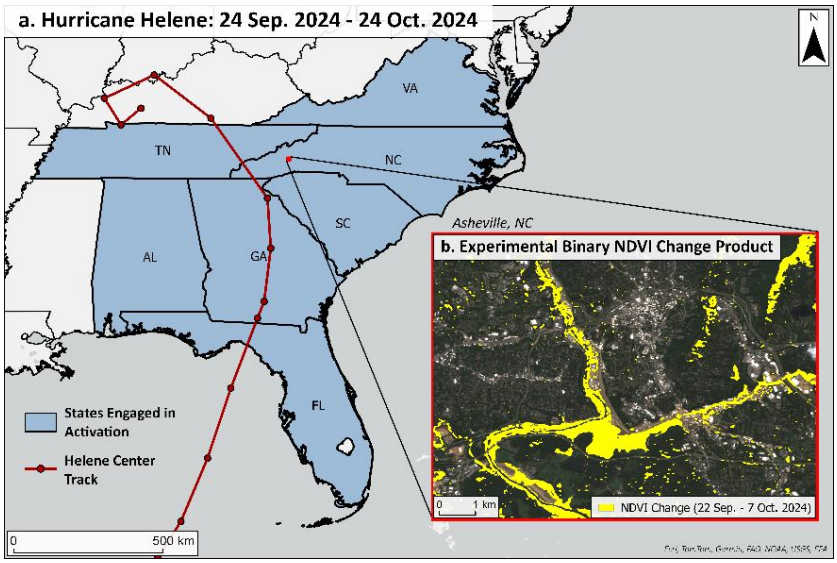

Figure 1. NDVI binary change detection product for Hurricane Helene. (a) A visualization of Hurricane Helene's storm track over the southeastern U.S. with states involved in the DRCS activation from 24 September to 24 October 2024 shaded in blue; (b) A subset of the experimental binary NDVI change product over Asheville, NC generated using ESA Sentinel-2 imagery from 22 September 2024 (pre-incident) and 7 October 2024 (post-incident) which highlights areas of change potentially associated with storm damage (yellow). Contains modified Copernicus Sentinel data processed by ESA, 2024.

2.4.2. Houston Derecho and Extreme Heat Incident

On May 16, 2024, a derecho, or convectively generated windstorm, unleashed tornadoes and destructive winds across Central Texas and Houston, causing extensive damage and knocking out power for over one million homes and businesses (Ashley *et al*., 2005, CenterPoint Energy, 2024). In the days following, extreme heat exacerbated the risk of power outages. Federal partners requested that the DRCS use EO data to identify rural communities and vulnerable neighborhoods without power to help delineate areas to prioritize aid. The DRCS provided nighttime light imagery created by the NASA Black Marble science team with data from the Visible Infrared Imaging Radiometer Suite (VIIRS) sensor (Table 2).

In addition to imagery for situational awareness and clear visualization of outages, the DRCS created experimental value-added products, or products intended to be more immediately useful to end users, that integrate sociodemographic information with EO to identify vulnerable communities (Figure 2). Through this activation and the subsequent response to Hurricane Beryl in July 2024, the DRCS expanded its knowledge of the Black Marble nighttime light data and identified the optimal data products and pipelines to create power loss proxy maps for future incidents.

Table 2. Selected products from the DRCS response to the Houston derecho and extreme heat incident.

Request	Product Highlights
Vulnerable Populations with Power Loss	The DRCS provided nighttime light imagery maps created by the NASA Black Marble science team with data from the Visible Infrared Imaging Radiometer Suite (VIIRS) sensor on the NASA–NOAA Suomi NPP satellite.

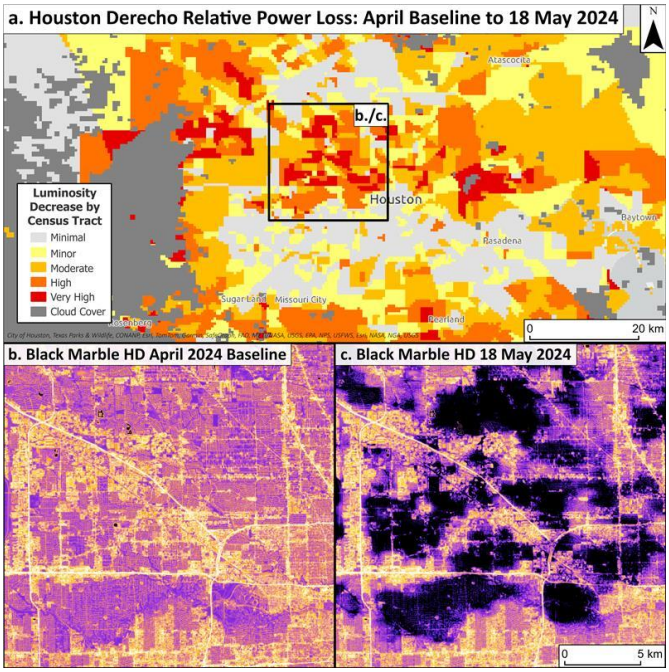

Figure 2. (a) A comparison of luminosity decrease by census tract observed by VIIRS over Houston following the derecho; (b) The Black Marble HD Baseline for April 2024, which averages luminosity over the month using cloud-free observations; (c) Black Marble HD imagery over Houston on 18 May 2024, two days after the derecho.

2.4.3. Los Angeles Fires

In early January 2025, severe drought conditions, extremely dry vegetation, and hurricane-force winds contributed to the rapid spread of two fires in heavily populated areas of Los Angeles County. By the end of January, the wildfires burned more than 57,000 acres, destroyed over 16,000 structures, and resulted in substantial loss of life and property damage.

Table 3. Selected products from the DRCS response to the Los Angeles Fires.

Request	Product Highlights
Active Fire Detection and Perimeters	Fire Information for Resource Management System (FIRMS) - Fire mapping and detection were provided through high-resolution VIIRS data to update active fire detections and perimeters every 12 hours. These timely updates significantly aided firefighting and evacuation strategies in rapidly evolving conditions.
Burned Area and Burn Severity	Normalized Burn Ratio difference (dNBR) maps from Sentinel-2 imagery, burned area perimeters, and detailed severity classifications from Sentinel-1 radar and Sentinel-2 optical imagery (OptiSAR method). These assessments distinguished between burned vegetation and damaged urban areas, providing additional context for damage evaluation and recovery planning.
Structure-level Damage Assessments	Damage analysis products from interferometric Sentinel-1 radar (InSAR) were compared with pre-disaster building footprint data and gain insight on potentially damaged areas and structures. Analysis by Corey Scher of CUNY Graduate Center and Jamon Van Den Hoek of Oregon State University.
Detection and Locations of Environmental Hazards and Health Risks.	Hyperspectral imagery from the Earth Surface Mineral Dust Source Investigation (EMIT), Greenhouse Gas Satellite (GHGSat), and the Airborne Visible and InfraRed Imaging Spectrometer 3 (AVIRIS-3) airborne instrument were analyzed for traces of methane leaks, though none were found. AVIRIS-3 hyperspectral data was also used to create an ash and char fraction map, showing where hazardous ash was located. Both analyses proved useful to CalGuard's field operations.

The DRCS responded to requests from a variety of local, state, and federal EM partners for multispectral satellite imagery and detailed burned-area assessments to inform ongoing firefighting and recovery planning as well as imagery to support damage assessment through change detection (Table 3). Additional requests included air quality and smoke plume analyses, active fire detections with regularly updated perimeter maps, and thermal imagery for hotspot identification. In response to these needs, NASA's DRCS produced and delivered over twenty remote sensing products, directly supporting operational decision-making (Figure 3).

While DRCS products effectively served the mid-to-late phases of disaster response (24+ hours after incident initiation), inherent satellite latency limited their impact in the critical initial hours. The incident represented a unique challenge as the fire heavily impacted the Jet Propulsion Laboratory (JPL) community, which includes DRCS team members and subject matter experts (SMEs). The incident also emphasized the importance of strong pre-incident relationships with state and local emergency management agencies. Prior relationships that established trust and familiarity with agencies increased the speed of the request and efficiency of product use. A key finding was the importance of streamlining and curating the products delivered to response teams. The large volume and variety of available datasets underscored the need for targeted, concise information tailored specifically to operational needs and decision-making contexts.

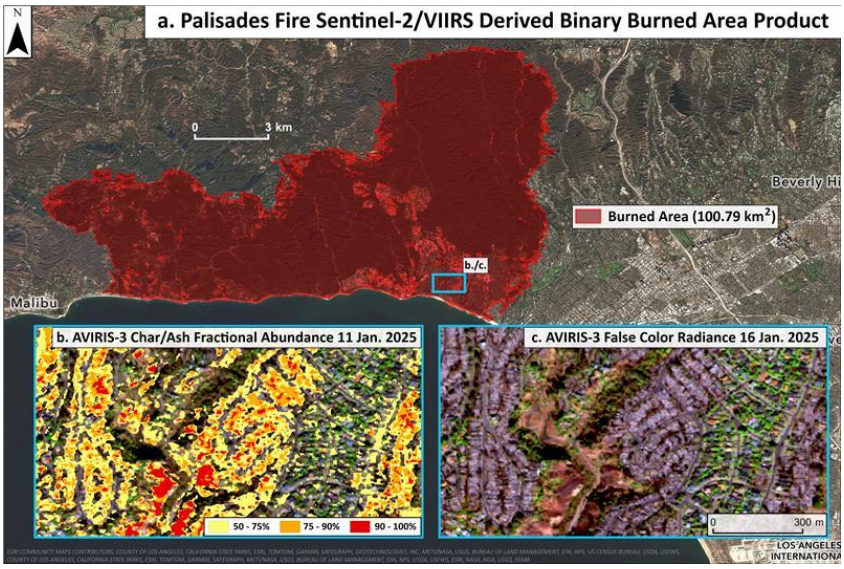

Figure 3. (a) A view of the estimated ~101 km^2 total burned area for the Palisades fire northwest of Los Angeles, CA derived from Sentinel-2 and VIIRS imagery; (b) AVIRIS-3 Char/Ash Fractional Abundance product for 11 January 2025; (c) AVIRIS-3 False Color Radiance on 16 January 2025. Contains modified Copernicus Sentinel data processed by ESA, 2024.

2.4.4. Brazil Flooding

From April 24 to May 2, 2024, a devastating flood and subsequent landslides heavily impacted southern Brazil and northern Uruguay. According to the Pan American Health Organization (PAHO), the flooding displaced nearly half a million individuals in Rio Grande do Sul alone and caused nearly 200 fatalities and 1,000 injuries (PAHO, 2024). Various agencies and organizations affected by the flooding and landslides requested data to support response activities. The DRCS responded to multiple data requests and provided imagery that helped show flooding, identify landslides, and give insights into power outage extent (Table 4). Beyond providing data, the DRCS used imagery taken before and after the incident to manually flag over 4,000 landslides in the affected region (Figure 4).

The DRCS after-action review process found that while many organizations valued the products provided, they were unsure how to best utilize and disseminate some of the resources in a timely and effective manner. Optical imagery for identifying landslides, isolated areas, environmental impact, and escape routes were among the most useful. When requestors were consumed with their response efforts, the DRCS struggled with whether to continue product creation without requestor input. Workflow improvements could also better define file formats and processing times to ensure that delivered products are available on a useful timeline in a digestible format.

Table 4. Selected products from the DRCS response to the Brazil flooding.

Request	Product Highlights
Locations of Flooding and Damage	The Advanced Rapid Imaging and Analysis (ARIA) and Observational Products for End-Users from Remote Sensing Analysis (OPERA) teams at NASA's Jet Propulsion Laboratory (JPL) and California Institute of Technology derived water maps and flood depth estimates from Harmonized Landsat Sentinel (HLS) data. Sentinel-1A SAR data was also used to create water extent maps.
Locations of Landslides	PlanetScope imagery taken before and after the event was used to manually flag over 4,000 landslides.
Power Outage Awareness	Black Marble nighttime lights product derived from the VIIRS Day/Night band on the Suomi NPP satellite.

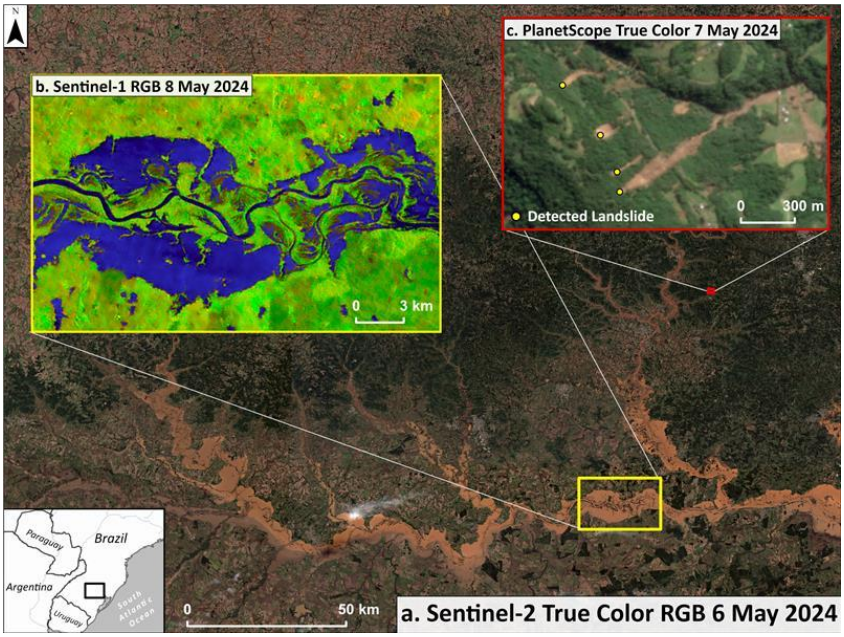

Figure 4. (a) A large-scale view of the extensive flooding in Brazil observed by Sentinel-2 on 6 May 2024; (b) A Sentinel-1 C-band SAR RGB observation of flooding from 8 May 2024; (c) An example of expert-labeled landslide detections in high-resolution PlanetScope optical imagery from 7 May 2024. Contains modified Copernicus Sentinel data processed by ESA and ASF DAAC, 2024. Includes copyrighted material of Planet Labs PBC. All rights reserved.

3. Gaps Between Earth Observation Data, Science, and Emergency Management Use

Despite a wealth of news articles, social media posts, and websites extolling the virtues of satellite remote sensing in disaster response, the DRCS's experience shows that emergency managers often remain dissatisfied with the availability and quality of remote sensing data products during disasters. This section describes how technical trade-offs, procedural complexity, and policies can limit the successful application of remote sensing data to support disaster response.

Success requires multiple decision-makers and operators having a shared understanding of end user needs and available technology. Remote sensing often falls short in meeting end user needs due to coordination failures inherent in this system (Picchione *et al*., 2024). When an incident occurs, relationships often must be established or reestablished due to employee turnover, the involvement of new organizations or assets, or technology upgrades. In addition, coordination failures are more likely when a disaster occurs in an area that has been disaster-free for some time, or when the disaster results from a less common hazard that requires different types of remote sensing products (e.g., oil spills). Constant communication, relationship building,

capacity building, and innovation are necessary to anticipate and mitigate coordination failures in this complex socio-technical environment.

3.1. Remote Sensing Trade-offs: Temporal Latency, Spatial Resolution, and Area Coverage

Three attributes influence the capabilities and use of a remote sensing instrument: spatial resolution, temporal resolution, and the areal footprint of the captured image (Tatem *et al*., 2008). Different spatial and temporal resolutions offer unique trade-offs (Tatem *et al*., 2008). Understanding these trade-offs and why they exist helps providers and end-users determine which geospatial data and tools best address emergency management needs.

Table 5. Assets frequently associated with disaster response. Data from assets in this table are published publicly during disasters or routinely available from public assets.

	Asset	Number of Satellites	Orbit	Approximate resolution	Constellation Revisit Rate	Area coverage	Narrative
Multispectral Imaging Assets	Landsat	2	Polar SSO	30m	8 days	185 km swath width	Detect flood, landslides, active fires, burned area, and vegetation change over several counties within a week.
	Sentinel-2	2	Polar SSO	10m	5 days	290 km swath width	Detect flood, landslides, active fires, burned area, and vegetation change over several counties within 4–5 days.
	PlanetScope*	130+	Polar SSO	3m	24 hours	24x8km to 32x19km	Detect landcover change over towns and cities, may observe severe damage to structures.
	MODIS	2	Polar SSO	250m	24 hours	Global, daily	Global daily low-resolution imagery shows landcover change at the city-block scale.
	VIIRS	3	Polar SSO	375m	24 hours	Global, daily	Global daily low-resolution imagery shows landcover change at the city-block scale.
	GOES-R	2	Geostationary	500m	10 min	Western Hemisphere	Low-resolution, low-latency data shows active fires, standing water for severe floods, and some damage from severe weather in real time.
Synthetic Aperture Radar (SAR)	Sentinel-1	2	Polar	10m	6 days	250 km swath width	Detect flood and landcover change over several counties within a week.
	NISAR **	1	Polar	10m	12 days	240 km swath width	Detect flood and landcover change over several counties within a week.

*PlanetScope data is provided under contract through the NASA Commercial Satellite Data Acquisition (CSDA).

**NISAR launched on July 30, 2025.

Timing is considered in two ways: collection timing and processing time. The frequency, or revisit rate, of satellite overpasses impacts the date and time of data collection. Delivery is also influenced by data downlink and post-processing time. Raw data or simple band combinations can give insights, but some end users may require processed data such as maps that identify flooding or landslides. These requests increase the value of the data but also lengthen delivery times.

Satellites maintain stable orbits around the Earth, but differences in orbital characteristics influence the application of an instrument. Sun-synchronous orbits (SSO) align with areas of the Earth illuminated by sunlight and cover the entire planet in relatively high or moderate spatial resolutions, but the revisit rate is limiting. Geostationary orbits keep satellites positioned over a fixed point by maintaining an orbital velocity that matches the Earth's rotation. This allows for continuous or nearly continuous observations of the AOI but sacrifices spatial resolution (Tatem *et al*., 2008).

There is an inverse relationship between the spatial resolution and area covered by an instrument. As the level of detail an instrument captures increases, the area imaged decreases (Table 5). For example, sun synchronous instruments such as the Landsat and Sentinel constellations have spatial resolutions of 10–30 m and image 185–290-km-wide swaths. Geostationary satellites such as the Geostationary Operational Environmental Satellite (GOES) constellation have a much lower spatial resolution of 500 m or higher, depending on the instrument, but offer near real-time coverage of the Western Hemisphere.

The spatial resolutions of satellite-based instruments vary but are theoretically limited by atmospheric turbulence and distortion of light near the surface to around 10 cm (Evvard, 1965). Some commercial satellites have high-resolution data under 1m, while federal civilian agencies' satellites range from 10 m to 1 km per pixel. Depending on the use-case, higher spatial resolution may not always be needed — for example, large-scale trends across a landscape can be tracked with coarser resolution imagery, but a single small landslide may be missed. Each instrument offers a unique perspective on Earth and its atmosphere. Understanding the technological nuances helps providers and requestors understand how these tools can deliver the most impact.

3.2. Geographic Nuances

Regional variations also influence the use of remote sensing in disaster response. Emergency management agencies across the globe operate under diverse geographic environments that shape their specific information needs and challenges. While the designs of EO products often consider broad applicability, they may not perform equally well across all geographic regions or align with localized priorities. These misalignments create operational challenges for integrating EO data into state and local decision-making processes.

In Alaska, for instance, emergency managers rely heavily on sea ice data to support maritime search and rescue and monitor coastal hazards. However, common optical EO systems are limited in high-latitude regions due to persistent cloud cover and long periods of darkness. While SAR offers a potential workaround, its effective use requires not only increased technical capacity but also tailored products that account for ice type, motion, and hazard potential; needs that are often unmet by standard products.

In desert regions, heavy rain often causes flash flooding with little warning. The terrain in these regions frequently creates problems for satellite detection of water (Garg *et al*., 2024). Dry soil, highly reflective surfaces in urban settings, and low vegetation cover challenge both optical and SAR-based flood detection algorithms to distinguish real flood signals from noise (Pierdicca *et al*., 2018). Automated products developed in wetter regions may not transfer well to these contexts, limiting their reliability and operational usefulness.

Machine learning is often seen as a universal solution to overcome these limitations; however, its effectiveness can be similarly challenged by geographic diversity. Training sets are typically created manually, making the process time consuming and arduous, thus limiting the geographic and temporal diversity of the input data. For example, a study evaluating an automated landslide detection system found that landslide classification is highly sensitive to regional terrain characteristics, vegetation cover, and imagery types. Although the model generates results much faster than manual mapping, its outputs often require manual correction and adaptation to local conditions (Pierdicca *et al*., 2018).

EO data products, even when technically advanced, must be grounded in the environmental and operational realities of their intended users. Emergency response agencies often serve as the first line of response, and their information needs are shaped by geography, infrastructure, and resource availability.

3.3. Interpretation and Application

Remote sensing instruments now downlink hundreds of terabytes of telemetry each day, yet these raw data offer little benefit to emergency managers upon acquisition; significant calibration, processing, and interpretation must occur before the raw sensor data become actionable geospatial products that can be mapped, queried, and integrated into operational decision-making frameworks (Voigt *et al*., 2016). The Data-Information-Knowledge-Wisdom (DIKW) hierarchy proposed by Ackoff (1989) illustrates that data alone hold limited intrinsic value; their utility increases as they are transformed into contextualized information, actionable knowledge, and ultimately the wisdom to effectively utilize knowledge for decision-making. Hodgson *et al*. (2013) emphasize that remote sensing products frequently fail to influence disaster response effectively when they arrive too late, in incompatible formats, or do not align with responder procedures. Understanding the processing latencies, product formats at various data levels, and their corresponding operational use cases help ensure that remote sensing outputs align more closely with emergency management requirements.

Table 6. Summary of NASA EOSDIS data processing levels, including descriptions, typical applications in disaster response, and representative MODIS data products.

	Description	Use in disaster response	Example data product from MODIS
Level 0	Time-ordered instrument telemetry reconstructed from downlinked packets; detector counts remain in raw engineering units.	Rarely used operationally. Engineers might revisit Level 0 after the fact (e.g., to recalibrate sensor drift).	MOD00F - Raw telemetry packets as downlinked from the instrument.
Level 1A	Uncalibrated detector counts together with synchronized attitude, ephemeris, and on-board calibration metadata.	Specialist pre-processing. Level 1A quick-look images from optical sensors can be used to spot smoke plumes or ash clouds before calibrated data arrive.	MOD01 - Digitized detector counts + all ancillary engineering data, still in instrument counts.
Level 1B	Radiometric calibration coefficients have been applied, converting counts to at-sensor spectral radiance (or reflectance); data is geolocated.	Rapid visual situational awareness. Near-real-time true-color or false-color images. Also, the base layer for automatic hotspot detection systems such as NASA FIRMS.	MOD021KM - Radiometric calibration & geolocation applied. Product shows at-aperture spectral radiance/ reflectance.
Level 2	Geophysical variables retrieved on a per-pixel basis at native sensor resolution via physics-based or statistical inversion of Level-1 radiances.	Single-hazard metrics ready for GIS. Examples include: land-surface temperature which gives insight into fire intensity & residual heat for active fires or heatwave response); aerosol/ash optical depth for aviation alerts.	MOD11_L2 – Per-pixel land-surface temperature & emissivity.
Level 3	Level-2 geophysical fields composited or mapped onto a uniform spatial–temporal grid (daily, 8-day, monthly, etc.) through averaging, maximum-value compositing, or optimal interpolation.	Change detection and time-averaged data. Examples include: NDVI/EVI composites to quantify drought stress, crop loss, or post-fire vegetation recovery. Surface displacement maps that compare post-incident land surface changes to pre-incident baseline.	MOD13A1 - 16-day, 500 m global NDVI/EVI grid (Level-2 vegetation indices composited onto a sinusoidal grid).
Level 4	Model output or analyses generated by assimilating multiple Level 1–3 data streams into numerical models or statistical frameworks; may provide variables not directly observed (e.g., damage proxy).	Multi-source data fusion & modeling for impact assessment and forecasting. Examples include ARIA Damage Proxy Maps that fuse InSAR coherence layers with modeling to produce a damage likelihood layer; LHASA Landslide Hazard v2 forecasting that uses modeling to estimate landslide probability.	MOD17A2H (GPP) – Terra/MODIS Gross Primary Productivity, an 8-day composite of gross primary productivity used in carbon- and water-cycle models.

NASA's Earth Observing System Data and Information System (EOSDIS) establishes a standardized hierarchy (Levels 0 through 4) for tracking the processing of data from raw sensor readout to higher-level decision-support and forecasting products. Level 0 is raw telemetry, Level 1 applies calibration and geolocation, Level 2 derives per-pixel geophysical variables at the native sensor resolution, Level 3 aggregates or resamples those variables onto uniform spatial-temporal grids, and Level 4 represents products derived through modeling by assimilating multiple lower-level data streams (NASA EOSDIS, 2020). As detailed in Table 6, operationally useful remote sensing products can emerge at many levels. For example, a Level 1B true-color image may detect an ash plume within minutes, whereas a Level 4 flood forecast might guide evacuation plans. However, each level also carries distinct operational vulnerabilities: delayed or missing ephemeris data can stall Level 1B outputs; retrieval algorithms may misclassify features at Level 2; expert quality-control steps can delay the release of higher-level Level 3 and Level 4 products; and finally, the data itself may not be presented in a way that emergency management and responders find operationally useful or interpretable. A disruption at any of these data processing steps risks rendering a technically sound product operationally ineffective.

Once a hazard layer is produced, its value for operational response often depends on how quickly it can be related to people and infrastructure. A common step is to vectorize single-hazard raster layers (flood water, burn scars, or low-coherence change layers) into closed polygons that bound homogeneous impact zones (UN-SPIDER, 2025). Vector features can be ingested directly into GIS platforms and intersected with ancillary layers such as census blocks, road networks, lifeline utilities, and critical facilities. Exposure statistics (e.g., miles of road inundated or the number of homes within a burn perimeter) can then be generated quickly after product delivery, giving incident responders evidence for resource allocation.

3.4. Data Delivery and Accessibility

The successful transfer of information between providers and end-users depends on effective data delivery and accessibility. Some of the weakest links in the process: interoperability, navigation, and symbology present major challenges that limit the use of remote sensing in disaster response.

To benefit from remote sensing, users rely on specialized software, subscription-based software services, or web interfaces to interact with data. The large size of imagery data requires sufficient computer memory and processing power and takes time to load and download. Data format also plays an important role in interoperability. Consistently delivering data in preferred formats increases their useability. Unfortunately, the options are plentiful and overwhelming, and the best available format varies depending on its application or user. If data are not intentionally delivered in interoperable formats, users may struggle to put it to use under the time constraints of a disaster (CEOS, 2008). In addition to software, these data often require specialized access which can be a problem for some agencies and end users. The numerous data platforms and portals hosting geospatial data from different sources further exacerbate this problem. Even if an end user knows exactly what data they need, locating it is not always a simple task and requires precious time that over-scoped EM or GIS professionals often don't have. The capacity challenge is exacerbated further when the practical limitations of there being a small handful of (or zero) geospatial professionals that are dedicated to supporting EM operations. Those who are dedicated to the EM mission often find themselves pressed for time, resources, and leadership expectations and often struggle to conduct more advanced geospatial analytics (Kumar *et al*., 2020). Finally, disasters that wipe out power and affect internet access make it difficult, or impossible for people in the field to utilize remote sensing data.

There is a significant gap between the ways geospatial specialists handle, analyze, visualize, and publish datasets and how users are equipped to receive them. Improving the ease of access to often cumbersome data portals, and strategic use of symbology and semiotics make it easier for end-users to convert data into action.

3.5. Complex and Rapidly Advancing Technology

Remote sensing and associated technologies advance rapidly with commercial and civil players releasing a steady stream of new instruments, platforms, and products (Tweedie, 2025). This causes an inundation of new capabilities that far exceeds what emergency managers can effectively utilize. Nevertheless, many of these developments present exciting and novel ways to harness remote sensing for disaster response. Advancements include improvements in machine learning and artificial intelligence, the fusion of products for analysis, and higher availability of analysis-ready products. Similarities between products with different data and analysis processes or nuanced use cases exacerbate the challenge of selecting the right tool.

Consequently, despite federal, state, and local responders seeking advantages to maximize response efforts, capitalizing on the cutting edge of remote sensing remains difficult.

4. Best Practices and Proposed Solutions

In its first year, the DRCS observed three categories of best practices that help bridge the gap between remote sensing scientists and emergency managers: cataloging capabilities, capacity building, and coordination calls. Together, these approaches allow both scientists and emergency managers to transcend the norms of their disciplines.

4.1. Curation of Capabilities

One tool the disasters science community can provide to end users is a detailed catalog or menu of available products with guidance on their use cases and comparative value. Useful menus are comprehensive yet concise, enabling emergency managers to quickly identify and request resources. Additional documentation must also be available for those who require in-depth technical details. Menus should focus on the derived data product that will be delivered, not the EO assets used.

Crafting a menu is as much an ontological challenge as a technological one. Catalogs are boundary objects; disambiguating terms such as “product”, “asset”, and “capability” (Table 7) improves communication and understanding regarding what is available and useful to meet response needs. Typically, emergency managers request products relevant to one or two hazard types at a time. The nature of the incident – or state of the environment, such as the presence of clouds – may narrow user needs down to a certain sensor type, like SAR or multispectral imagery. Detailed records of each component allow those providing remote sensing imagery to set clear expectations and help end users make informed requests.

The DRCS is developing a set of menus and technical documentation to catalog NASA’s EO assets available for disaster response. To date, the DRCS has cataloged nearly 200 unique data products that NASA can provide or has provided in the past to support disaster response.

Table 7. Proposed terminology and definitions.

Term	Proposed definition
Capability	All-encompassing terms for products, assets, subject matter experts, or other resources that provide clear value for disaster response.
Asset	Any sensing system (satellite, aerial, UAV, or ground), sensor, model, algorithm, workflow, software package, or other “tool” that used to acquire data or develop products. Assets may be tangible or intangible, hardware or software.
Product	Any reproducible, unique dataset, Web Map, web application, or document that meets user needs. DRCS products are often geospatial in nature and consist of or are derived from EO. Ideally, products are generated with the same methodology and workflow for different disasters. The term product may refer to both an individual dataset for a specific incident and the generalized form of that dataset which could be produced for any incident.
Product Groups or Suites	A collection of products organized use case, hazard, or asset. Deliberately malleable to adapt to the needs of user community.

4.2. Capacity Building and Training

Capacity building helps bridge the gap between satellite data products and their use in disaster response. Defined by the United Nations as “the process of developing and strengthening the skills, instincts, abilities, processes and resources that organizations and communities need to survive, adapt, and thrive in a fast-changing world,” capacity building must employ an approach for emergency managers that builds their awareness of, access to, and ability to rapidly request and apply EO during a disaster (UN, 2025). Emergency managers cannot be expected to be remote sensing experts in addition to their other responsibilities, nor can remote sensing scientists be expected to be experts in the emergency management field. This impasse highlights the need for a synergistic approach to the development of trainings, scenario and tabletop exercises, and co-development of products, tools, and portals to facilitate the continuous exchange of information and

each field's best practices. To facilitate the most effective use of EO in disaster response, relationships between data providers, remote sensing scientists, and emergency managers must be strengthened through continuous interdisciplinary exchange of information.

During a disaster, timely access to data and information is crucial and many emergency managers prefer "plug-and-play" data utilization services (Zheng *et al*., 2021; Kumar *et al*., 2020). Building skills in emergency managers to be better requestors and users of EO data requires a tailored approach compared to graduate students or academia as working professionals face time constraints, organizational barriers, and often limited technical capacity (Prados *et al*., 2019). Scenario exercises and data portal demonstrations can strengthen the uptake of synthesized and curated training information. By incorporating insights and feedback gleaned from engagement with emergency managers on available or in-development tools and data products, the usability and utility of remote sensing resources improve.

4.3. Collaboration and Coordination

Emergency managers and scientists must build a mutual understanding of needs and limitations to work together effectively. Given the logistical challenges and time-sensitive decisions disaster responses entail, it is not effective for emergency managers to build connections with scientists during a disaster (i.e., "gray sky" periods). Thus, effective collaboration and coordination begin outside of disasters (i.e., "blue sky" periods).

Emergency management revolves around highly effective collaboration between parties to provide lifesaving and life sustaining services (Waugh and Streib, 2006). Practitioners leverage conferences, virtual meetings, and in-person collaborative co-development opportunities to build communications pathways and critical familiarity. Intentional collaboration with scientists also offers the chance for emergency managers to share input that helps guide the production of value-added datasets, new algorithms, and models that address data gaps. Blue sky periods also serve as an optimal time to offer capacity building opportunities, such as demonstrations of data portals or training on emergency management principles.

Deliberate actions during gray sky periods establish a unified vision and set of objectives. An important mechanism for supporting response efforts comes through regular "geospatial coordination calls." These calls allow data providers critical opportunities to deconflict areas of interest, reconcile end user requirements, and identify opportunities and barriers to support broader incident response. They afford impacted EM personnel a structured opportunity to engage with NASA, USGS, FEMA and other agencies and ensure their needs are met. Geospatial calls also provide an opportunity to coordinate collaborative mapping with other agencies, especially for deployment of airborne instruments and the tasking of high-resolution private satellite products (between emergency management and science agencies).

5. Conclusions

Data scientists, technical experts, and geospatial professionals are highly effective at advancing and refining the quality and sophistication of EO data and information. These data have the potential to help emergency managers make more informed decisions, allocate scarce resources more efficiently, and better meet the needs of the communities they serve. Tragically, the data too often lose value between their production and application. Emergency managers at the public, private, and non-profit levels enable robust capabilities to rapidly scale matrixed organizations and provide lifesaving and life-sustaining care to those in need after incidents. These emergency managers often must position themselves to be a "mile wide" but an "inch deep" and serve as collaborators-in-chief, stitching together the otherwise disparate resources to mount effective incident response and recovery efforts. However, being an "inch deep" for understanding and utilizing the technical information available in remote sensing is inadequate. Similarly, it is insufficient for technical experts to focus their advancements for socialization within their professional circles. Instead, both the remote sensing and emergency management communities need to undergo a transformation of relatability. As described here, there are specific and tangible actions that science agencies can and should undertake to meet emergency managers where they are to improve the accessibility and usefulness of the data and science they provide. In turn, emergency managers should continue to build the networks in blue sky conditions to integrate remote sensing requirements, capabilities, and technical understanding. By both parties inching closer to one another, the true value that remote sensing has for supporting disaster response can come to fruition.

Funding: This material is based upon work supported by NASA Disasters Program through contracts 80LARC23FA024, 22003.T.0131.00, 80NM0018D0004, and cooperative agreement 80MSFC22M0004.

Data Availability Statement: Data are available at the NASA Disasters Mapping Portal: maps.disasters.nasa.gov.

Acknowledgment: Any mention of a commercial product, service, or activity in this material does not constitute NASA endorsement. Any opinions, findings, and conclusions or recommendations expressed in this material are those of the author(s) and do not necessarily reflect the views of the National Aeronautics and Space Administration and partner organizations.

This material contains modified Copernicus Sentinel data (2024-2025), processed by ESA and ASF DAAC.

This work utilized data made available through the NASA Commercial Satellite Data Acquisition (CSDA) Program.

Conflicts of Interest: The authors declare no conflicts of interest. The funders had no role in the design of the study; in the collection, analyses, or interpretation of data; in the writing of the manuscript; or in the decision to publish the results.

References

Ackoff, R. L. (1989). From data to wisdom. *Journal of Applied Systems Analysis, 16,* 3–9.

Amorim, R., Villarini, G., Czajkowski, J., & Smith, J. (2025). Flooding from Hurricane Helene and associated impacts: A historical perspective. *Journal of Hydrology X, 27,* 100204. https://doi.org/10.1016/j.hydroa.2025.100204

Ashley, W. S., & Mote, T. L. (2005). Derecho hazards in the United States. *Bulletin of the American Meteorological Society, 86*(11), 1577–1592.

Battersby, S. E., Hodgson, M. E., & Wang, J. (2012). Spatial resolution imagery requirements for identifying structure damage in a hurricane disaster: A cognitive approach. *Photogrammetric Engineering & Remote Sensing, 78*(6), 625–635. https://doi.org/10.14358/PERS.78.6.625

Canton, L. G. (2006). San Francisco 1906 and 2006: An emergency management perspective. *Earthquake Spectra, 22*(2_suppl), 159–182. https://doi.org/10.1193/1.2181467

CenterPoint Energy. (2024, May 23). CenterPoint Energy helps restore and support Greater Houston in aftermath of devastating May 16 storm. https://www.centerpointenergy.com/en-us/corporate/about-us/news/1757 Last access: 18 July 2025

Committee on Earth Observation Satellites. (2008). *Committee on Earth Observation Satellites Working Group on Information Systems and Services Interoperability Handbook* [Issue 1.1].

Cova, T. J. (1999). GIS in emergency management. *Geographical Information Systems, 2*(12), 845–858.

Denis, G., De Boissezon, H., Hosford, S., Pasco, X., Montfort, B., & Ranera, F. (2016). The evolution of Earth observation satellites in Europe and its impact on the performance of emergency response services. *Acta Astronautica, 127,* 619–633. https://doi.org/10.1016/j.actaastro.2016.06.012

Drabek, T. E., & Hoetmer, G. J. (1991). *Emergency management: Principles and practice for local government.* International City Management Association.

Evvard, J. C. (1965). *Limits on observational capabilities of aerospacecraft* (No. NASA-TN-D-2933).

FEMA. (2018). *Geospatial support for disaster operations guide.*

Garg, S., Dasgupta, A., Motagh, M., Martinis, S., & Selvakumaran, S. (2024). Unlocking the full potential of Sentinel-1 for flood detection in arid regions. *Remote Sensing of Environment, 315,* 114417. https://doi.org/10.1016/j.rse.2024.114417

Hodgson, M. E., Battersby, S. E., Liu, S., Sulewski, L., & Davis, B. A. (2013). Geospatial and remote sensing data use by states and counties in disaster response and recovery: A nationwide survey. https://doi.org/10.13140/RG.2.2.12854.51523

Huang, S., Tang, L., Hupy, J. P., Wang, Y., & Shao, G. (2021). A commentary review on the use of normalized difference vegetation index (NDVI) in the era of popular remote sensing. *Journal of Forestry Research, 32,* 1–6. https://doi.org/10.1007/s11676-020-01155-1

Kerle, N., Nex, F., Gerke, M., Duarte, D., & Vetrivel, A. (2019). UAV-based structural damage mapping: A review. *ISPRS International Journal of Geo-Information, 9*(1), 14. https://doi.org/10.3390/ijgi9010014

Kirschbaum, D., Molthan, A., Bell, J., Gutro, R., Soja, A., Glasscoe, M., Oliver, S., & Green, D. (2017). A view from above: Earth

observation. *Crisis Response Journal.*

Kumar, A. S., Camacho, S., Searby, N. D., Teuben, J., & Balogh, W. (2020). Coordinated capacity development to maximize the contributions of space science, technology, and its applications in support of implementing global sustainable development agendas—A conceptual framework. *Space Policy, 51,* 101346. https://doi.org/10.1016/j.spacepol.2019.101346

Macias, M., Cerovski-Darriau, C., Bilderback, E., Schefer, L., Palermo, L., Ellison, S., Kostelnik, J., West, J., Allstadt, K., Burgi, P., Schmitt, R., Baxstrom, K., Bedinger, E., Mirus, B., Martinez, S., Rengers, F., Einbund, M., & McBride, S. (2024, September 30). 2024 Hurricane Helene landslide hazards [United States Government]. https://www.usgs.gov/programs/landslide-hazards/science/2024-hurricane-helene-landslide-hazards. Last access: 21 July 2025

McCormick, S. (2012). After the cap: Risk assessment, citizen science and disaster recovery. *Ecology and Society, 17*(4). http://www.jstor.org/stable/26269217

NASA EOSDIS. (2020). *Earth Observation System Data and Information System (EOSDIS) Terminology Specification* (Nos. 423-SPEC-002, Rev A).

NCEI. (2025). *Costliest U.S. tropical cyclones* [Dataset]. NOAA National Centers for Environmental Information. https://www.ncei.noaa.gov/archive/accession/0209268

Pan American Health Organization. (2024). *Flooding in Brazil*—2024. https://www.paho.org/en/health-emergencies/flooding-brazil-2024 Last access: 25 July 2025

Picchione, K. R., Council, C. L., Anklam, S., & Legge, R. S. (2024). Satellite remote sensing in disaster relief: FY23 HADR technical investment program [Project Report].

Pierdicca, N., Pulvirenti, L., & Chini, M. (2018). Flood mapping in vegetated and urban areas and other challenges: Models and methods. In A. Refice, A. D'Addabbo, & D. Capolongo (Eds.), *Flood monitoring through remote sensing* (pp. 135–179). Springer International Publishing. https://doi.org/10.1007/978-3-319-63959-8_7

Prados, A. I., Carleton-Hug, A., Gupta, P., Mehta, A., Blevins, B., Schmidt, C., Barbato, D. G., McCullum, A. J., Hook, E., Podest, E., Follette-Cook, M., Hudson-Odoi, S., & Kinsey, T. (2019). Impact of the ARSET program on use of remote-sensing data. *ISPRS International Journal of Geo-Information, 8*(6), 261. https://doi.org/10.3390/ijgi8060261

Strupp, C. (2006). Dealing with disaster: The San Francisco earthquake of 1906. UC Berkeley: Institute of European Studies. https://escholarship.org/uc/item/9gd2v192

Tatem, A. J., Goetz, S. J., & Hay, S. I. (2008). Fifty years of Earth observation satellites: Views from above have led to countless advances on the ground in both scientific knowledge and daily life. *American Scientist, 96*(5), 390.

Tweedie, E. (2025, May 12). Trends in the geospatial market. https://www.satellitemarkets.com/trends-geospatial-market. Last access: 25 July 2025

United Nations. (2025). Capacity-building [www.un.org]. United Nations Academic Impact.

UN-SPIDER. (2025). Step by step: Flood mapping and damage assessment using S2 data. https://www.un-spider.org Last access: 28 July 2025

USGS. (2025). What is a geographic information system (GIS)? https://www.usgs.gov/faqs Last access: 1 August 2025

Voigt, S., Tonolo, F. G., Lyons, J., Kučera, J., Jones, B., Schneiderhan, T., Platzeck, G., Kaku, K., Hazarika, M. K., Czaran, L., Li, S., Pedersen, W., James, G. K., Proy, C., Muthike, D. M., Bequignon, J., & Guha-Sapir, D. (2016). Global trends in satellite-based emergency mapping. *Science, 353*(6296), 247–252. https://doi.org/10.1126/science.aad8728

Waugh, W. L., Jr., & Streib, G. (2006). Collaboration and leadership for effective emergency management. *Public Administration Review, 66,* 131–140.

Zheng, X., Wang, F., Qi, M., & Meng, Q. (2021). Planning remote sensing emergency services: Bridging the gap between remote sensing science and emergency practice in China. *Safety Science, 141,* 105346. https://doi.org/10.1016/j.ssci.2021.105346

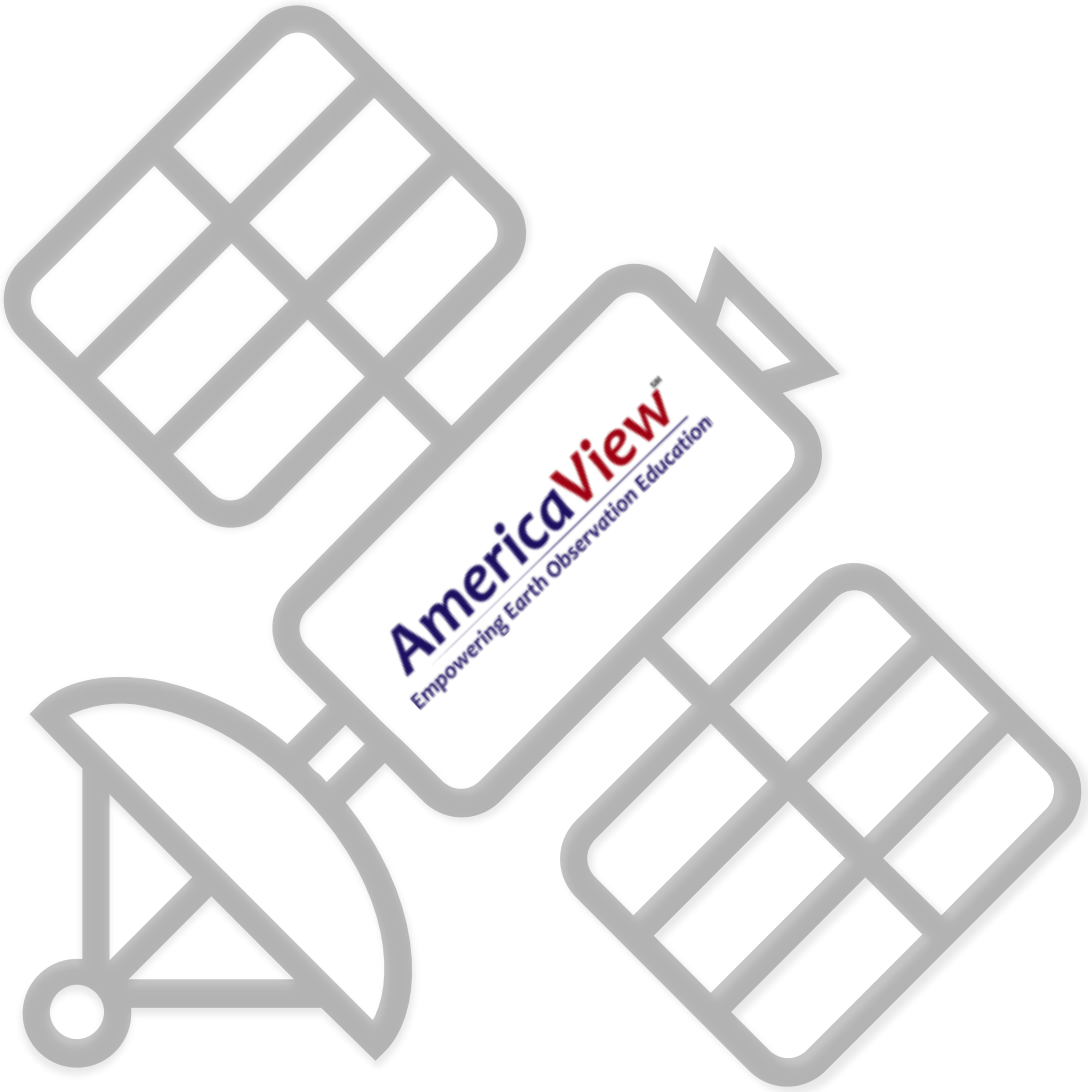

ISSN (online): 3070-3867

A Publication of AmericaView
https://AmericaView.org

Front Page Image:
Elizabethtown, New York
Landsat 9. October 2022
Credit: Joshua Stevens
NASA Earth Observatory

JEOGA Journal Home